

UNCLASSIFIED

AD NUMBER: ADB951671

LIMITATION CHANGES

TO:

Approved for public release; distribution is unlimited.

FROM:

Distribution authorized to U.S. Gov't. agencies and their contractors; Administrative/Operational Use; Jul 1951. Other requests shall be referred to Defense Atomic Support Agency, Washington, DC.

AUTHORITY

DNA ltr dtd 25 Apr 1980 (80-15)

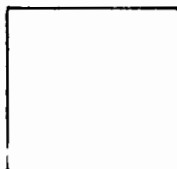
THIS PAGE IS UNCLASSIFIED

AD B951671

PHOTOGRAPH THIS SHEET

AD B951671

DTIC ACCESSION NUMBER



LEVEL

UNANNOUNCED

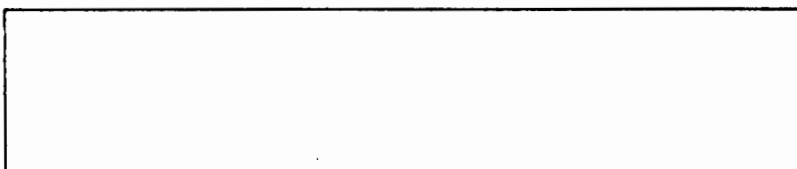


INVENTORY

AEC

WT-65

DOCUMENT IDENTIFICATION



DISTRIBUTION STATEMENT

ACCESSION FOR	
NTIS	GRA&I <input type="checkbox"/>
DTIC	TAB <input type="checkbox"/>
UNANNOUNCED	<input checked="" type="checkbox"/>
JUSTIFICATION	
BY	
DISTRIBUTION /	
AVAILABILITY CODES	
DIST	AVAIL AND/OR SPECIAL
2	

DISTRIBUTION STAMP

DTIC	
ELECTE	
S	D
MAY 2 1980	
D	

DATE ACCESSIONED

80 5 1 051

DATE RECEIVED IN DTIC

PHOTOGRAPH THIS SHEET AND RETURN TO DTIC-DDA-2

UNCLASSIFIED

~~CONFIDENTIAL~~

This document consists of 230 plus 4 pages  
(counting preliminary pages)

No. 5 of 150 copies, Series A

## Scientific Director's Report of Atomic Weapon Tests at Eniwetok, 1951

### Annex 8.2A

Effects of an Atomic Bomb Burst on Aircraft  
Structures on the Ground

[REDACTED]

~~CONFIDENTIAL~~

[REDACTED]

UNCLASSIFIED

UNCLASSIFIED

## Distribution

	Copy		Copy
<b>DEPARTMENT OF DEFENSE</b>		<b>AIR FORCE</b>	
Armed Forces Special Weapons Project (Sandia)	1-3	Director of Operations (Operations Analysis Division)	46
Armed Forces Special Weapons Project (Washington)	4-15	Director of Plans (AFOPD-P1)	47
		Director of Requirements	18-49
		Director of Research and Development	50-51
<b>ARMY</b>		Eglin Air Force Base, Air Proving Ground	52-53
Army Field Forces	16	Ent Air Force Base, Air Defense Command	54-55
Assistant Chief of Staff, G-3	17	Kirtland Air Force Base, Special Weapons Center	56-58
Assistant Chief of Staff, G-4	18-19	Langley Air Force Base, Tactical Air Command	59-60
Chief of Engineers	20-21	Maxwell Air Force Base, Air University	61-62
Chief of Ordnance	22-26	Offutt Air Force Base, Strategic Air Command	63-65
Operations Research Office (Johns Hopkins University)	27-28	1009th Special Weapons Squadron	66
		Rand Corporation	67-68
<b>NAVY</b>		Scott Air Force Base, Air Training Command	69-70
Bureau of Aeronautics	29-30	Wright Air Development Center	71-73
Chief of Naval Operations	31-32	Wright Air Materiel Command	74-75
Commandant, Marine Corps	33		
<b>AIR FORCE</b>		<b>ATOMIC ENERGY COMMISSION</b>	
Air Force Cambridge Research Center		Atomic Energy Commission, Washington	76-78
Air Research and Development Command		Los Alamos Scientific Laboratory, Report Library	79-83
Air Targets Division, Department of Intelligence (Phys.)		Sandia Corporation	84-85
Assistant for Atomic Energy	41-42	Technical Information Service, Oak Ridge (surplus)	86-149
Assistant for Development Planning	43	Weapon Test Reports Group. TIS	150
Assistant for Materiel Program Control	44		
Deputy Chief of Staff for Development (AFDRD)	45		

UNCLASSIFIED

**EFFECTS OF AN ATOMIC BOMB BURST  
ON AIRCRAFT STRUCTURES ON THE GROUND**

by

**DAVID L. GRIMES  
LLOYD J. BREIDENBACH**

and

**RALPH C. LENZ, JR.**

Approved by: **ROBERT E. JARMON**  
Col, USAF  
Director, Program 8

Approved by: **ALVIN C. GRAVES**  
Scientific Director

Aircraft Laboratory  
Aeronautics Division  
Wright Air Development Center  
Wright-Patterson Air Force Base  
Dayton, Ohio  
July 1951

**UNCLASSIFIED**

## Acknowledgments

The authors wish to acknowledge the contributions and generous cooperation of a number of individuals and organizations, who, through their efforts, assisted Project 8.2 to a successful conclusion.

The aggressive leadership of the Program Director, Col Robert E. Jarmon, USAF, and his comprehension of the problems involved were responsible for the accurate decisions and the expeditious manner in which staff functions were handled to render the maximum assistance to this project.

The direct staff support and coordination effected by Maj Robert E. Keegan is hereby acknowledged.

The close and continued support of Lt Col R. Nudenberg and E. H. Schwartz, of Wright Air Development Center (WADC), throughout the preparation and conductance of this operation is appreciated.

Through the excellent performance and cooperation of CDR J. R. Kirk, R. W. Newman, and D. F. Seacord, the data on overpressure variation with time were successfully measured on all four island test sites.

Capt Virgil E. Fieker, USAF, displayed an outstanding spirit of cooperation and initiative and, although time for preparations was extremely limited, assembled and conducted successful optical measurements in connection with the blast.

The ability and tenacity of 1st Lt Alan D. Sapowith as assistant chief of the Instrumentation Group contributed to the successful operation of the over-all instrumentation in spite of the use of experimental instruments under adverse conditions. He also ably assisted in the reduction of the instrument data.

Under the pressure of extremely limited time Carl K. Fredericks, WADC, developed a eutectic-alloy temperature-measuring device (Temp-Tape) and directed the fabrication of the large quantity required. He conducted the temperature survey with the Temp-Tapes and reduced the data reported in this volume.

Carl Doherty, of the Massachusetts Institute of Technology, designed the rigid-, structural-, and swept-wing models and as an overseas member of this project ably assisted in the erection of the test articles on the island test sites.

The authors wish to acknowledge with special appreciation the outstanding performance rendered by the airmen who constituted the main working force. It was due to their personal desire to accomplish the objectives of the project and to their willingness to work many consecutive hours at any time over a period of 1 year that brought this project to a successful conclusion.

It is also desired to express appreciation to the personnel of the J-Division of the Los Alamos Scientific Laboratory and of Holmes and Narver for their assistance and cooperation.

PRECEDING PAGE NOT FILMED

BLANK

UNCLASSIFIED

[REDACTED]

The assistance, cooperation, and support rendered by the ordnance personnel at the Aberdeen Proving Ground, and particularly by Capt Hollis Snyder, in conducting preparatory large-scale high-explosive tests were invaluable.

It is desired to commend the whole-hearted cooperation and rigorous efforts extended by the East Coast Aeronautics, Inc., organization in meeting the rigid overseas delivery schedule in the design and fabrication of a large portion of the test articles and supporting structures.



# CONTENTS

	Page
ACKNOWLEDGMENTS . . . . .	v
ABSTRACT . . . . .	1
CHAPTER 1 INTRODUCTION . . . . .	3
1.1 General Considerations . . . . .	3
1.2 Objective . . . . .	3
1.3 Background . . . . .	4
1.4 General Test Program . . . . .	4
CHAPTER 2 DESCRIPTION OF EXPERIMENTAL PROCEDURE AND TEST APPARATUS . . . . .	7
2.1 Selection of Test Articles . . . . .	7
2.2 Selection of Island Test Sites . . . . .	8
2.3 General Layout of Test Sites . . . . .	9
2.4 Description of Test Articles and Mounting Structures . . . . .	11
2.4.1 Rigid-wing Models . . . . .	11
2.4.2 Structural-wing Models . . . . .	12
2.4.3 Supporting Structure for Rigid- and Structural-wing Models . . . . .	13
2.4.4 Reinforced-concrete Base for Rigid- and Structural-wing Models . . . . .	13
2.4.5 Swept-wing Models . . . . .	13
2.4.6 Supporting Structure for Swept-wing Models . . . . .	13
2.4.7 Reinforced-concrete Base for Swept-wing Models . . . . .	14
2.4.8 Small Airfoils . . . . .	14
2.4.9 Small Cylinders . . . . .	14
2.4.10 Fighter Fuselage . . . . .	14
2.4.11 Fighter Wing Panels . . . . .	15
2.4.12 Airplane Control Surfaces . . . . .	15
2.5 Apparatus and Installation for Measuring Blast Phenomena . . . . .	15
2.5.1 Vane-type Angle-of-attack Indicators . . . . .	15
2.5.2 Optical-type Angle-of-attack Indicator (Fastax Camera) . . . . .	16
2.5.3 Electronic-chronograph Method of Determining Angle of Attack . . . . .	17
2.5.4 Overpressure Variation with Time; Measuring Apparatus and Installation . . . . .	17
CHAPTER 3 INSTRUMENTATION OF TEST ARTICLES . . . . .	19
3.1 General Problem of Instrumentation . . . . .	19
3.2 Recording System . . . . .	19
3.3 Selection of Sensing Elements for Wing Models . . . . .	22

vii  
UNCLASSIFIED

# UNCLASSIFIED

## CONTENTS (Continued)

	Page
3.4 Instrumentation of Wing Models . . . . .	23
3.4.1 Structural- and Swept-wing Instrumentation . . . . .	23
3.4.2 Rigid-wing-model Instrumentation . . . . .	23
3.5 Rigid- and Structural-wing Models: Camera Installation . . . . .	24
3.6 Temperature-measuring Devices and Installation . . . . .	24
3.6.1 Maximum Temperature Survey: Temp-Tapes . . . . .	24
3.6.2 Temperature Variation with Time: Electrical-resistance Gauges . . . . .	25
 CHAPTER 4 CALIBRATION . . . . .	 27
4.1 Rigid-wing Models . . . . .	27
4.2 Structural- and Swept-wing Models . . . . .	29
4.3 Calibration of Temperature Gauges . . . . .	30
4.3.1 Temp-Tape Maximum Temperature Survey . . . . .	30
4.3.2 Electrical-resistance Gauges and Temperature Variation with Time . . . . .	31
4.4 Vane-type Angle-of-attack Indicators . . . . .	31
4.5 Electronic Chronograph and Blast Switches . . . . .	31
 CHAPTER 5 TEST RESULTS . . . . .	 32
5.1 Re-entry and General Observation of Effects . . . . .	32
5.2 Visual Observation of Effects on Test Articles . . . . .	33
5.2.1 B-17 Elevator: Fabric-covered Control Surfaces . . . . .	33
5.2.2 F-47 Wings and Metal-covered Control Surfaces . . . . .	33
5.2.3 Rigid-wing and Structural-wing Models . . . . .	33
5.2.4 Swept-wing Models . . . . .	34
5.2.5 F-80 Fuselages . . . . .	34
5.2.6 Airfoils . . . . .	34
5.2.7 Cylinders . . . . .	35
5.3 Test Results from Model Wings . . . . .	35
5.3.1 Rigid-wing Models . . . . .	35
5.3.2 Structural-wing Models . . . . .	38
5.3.3 Rigid- and Structural-wing-model Cameras . . . . .	39
5.3.4 Swept-wing Models . . . . .	39
5.4 Results of Temperature Measurements . . . . .	40
5.4.1 Temperature Variation with Time: Electrical-resistance-type Gauges . . . . .	40
5.4.2 Maximum Temperature Survey: Temp-Tapes . . . . .	41
5.5 Blast Phenomena . . . . .	44
5.5.1 Angle-of-attack Variation with Time: Vane-type Indicator . . . . .	44
5.5.2 Angle of Attack: Optical Method (Fastax Camera) . . . . .	45
5.5.3 Angle of Attack: Electronic-chronograph Method . . . . .	46
5.5.4 Overpressure Variation with Time: Interferometer Gauges . . . . .	46
 CHAPTER 6 DISCUSSION . . . . .	 47
6.1 General Considerations . . . . .	47
6.2 Wing Models . . . . .	47
6.2.1 Rigid-wing Models . . . . .	48

## CONTENTS (Continued)

	Page
6.2.2 Structural-wing Models . . . . .	52
6.2.3 Swept-wing Models . . . . .	52
6.3 Instrumentation . . . . .	53
6.4 Angle of Attack of Blast Wave . . . . .	54
6.4.1 Vane-type Angle-of-attack Measurements . . . . .	54
6.4.2 Electronic-chronograph Angle-of-attack Measurements . . . . .	54
6.4.3 Optical Angle-of-attack Determination . . . . .	55
6.5 Venting of Aircraft Structures . . . . .	55
6.6 Ground Shock . . . . .	55
6.7 Fabric-covered Structures for Aircraft . . . . .	55
6.8 Temperature Variation with Time . . . . .	56
6.9 Re-entry . . . . .	58
 CHAPTER 7 CONCLUSIONS AND RECOMMENDATIONS . . . . .	 59
7.1 Conclusions . . . . .	59
7.2 Recommendations . . . . .	63

## ILLUSTRATIONS

### CHAPTER 1 INTRODUCTION

1.1 Typical Installation of the Rigid and Structural Models before Bomb Burst . . . . .	65
1.2 Rigid- and Structural-wing Models on Engebi, Range 4,020 Ft, after Detonation . . . . .	66
1.3 Typical Installation of Swept-wing Model before Bomb Burst, Engebi, Range 4,020 Ft . . . . .	67
1.4 Swept Model on Engebi after the Explosion . . . . .	68
1.5 Relative Locations of Project 8.2 Island Sites, Their Respective Ranges from the Shot Tower, and Other Related Data . . . . .	69
1.6 Aerial View of Engebi Illustrating the Relative Location of Project 8.2 Test Site and Other Test Installations . . . . .	70
1.7 Aerial View of the Test Site on Muzin . . . . .	71
1.8 Aerial View of the Test Site on Teiteir . . . . .	72
1.9 Aerial View of the Test Site on Bokon . . . . .	73
1.10 Aerial View of a Typical Test Array, Teiteir, after Bomb Burst, Range 12,000 Ft . . . . .	74
1.11 Rear Oblique View of a Typical Test Array, Muzin, Range 6,878 Ft . . . . .	75
1.12 Exterior View of the Instrument Room on Engebi before Bomb Burst, Range 4,020 Ft . . . . .	76
1.13 Typical Interior View of a Portion of a Submerged Instrument Room, Engebi . . . . .	77
1.14 Typical Interior View of a Portion of a Submerged Instrument Room, Engebi . . . . .	78
1.15 Typical Interior View of a Portion of a Submerged Instrument Room, Bokon . . . . .	79
1.16 View of the Two 7.5-kw Generators Installed on Engebi, Range 4,020 Ft, before Bomb Burst . . . . .	80
1.17 Same Generators as in Fig. 1.16, after Explosion, Engebi, Range 4,020 Ft . . . . .	81
1.18 View of 25-kw Generator Installation on Muzin before Bomb Burst . . . . .	82

UNCLASSIFIED

## ILLUSTRATIONS (Continued)

	Page
1.19 View of 25-kw Generator on Muzin, Range 6,878 Ft, after Detonation . . . . .	83
1.20 Split-triangular-vane-type Angle-of-attack Indicator, Engebi, before Bomb Burst . . . . .	84
1.21 Installation of the Split-triangular-vane-type Angle-of-attack Indicator (Engebi after Bomb Burst) on the Forward Strut of the Swept-wing Pylon . . . . .	85
1.22 Vane-and-slender-body-type Angle-of-attack Indicator, Muzin, Range 6,878 Ft, before Bomb Burst . . . . .	86
1.23 Installation of Vane-and-slender-body-type Angle-of-attack Indicator, Muzin, Range 6,878 Ft, before Bomb Burst . . . . .	87

### CHAPTER 2 DESCRIPTION OF EXPERIMENTAL PROCEDURE AND TEST APPARATUS

2.1 Schematic Diagram Illustrating the Division of Energies and Forces Released by an Atomic Bomb Explosion As Related to Project 8.2 Ground-test Program and the Aircraft Structures Problems . . . . .	88
2.2 Typical F-80 Fuselage Test Installation, Engebi, Range 4,020 Ft, before Bomb Burst . . . . .	89
2.3 Fuselage on Engebi after the Atomic Bomb Detonation . . . . .	90
2.4 Left Side of the F-80 Fuselage Nose on Engebi after Bomb Detonation . . . . .	91
2.5 F-47 Wing, Aileron, and Flap Installation and the Small Airfoils Set at $22\frac{1}{2}^\circ$ on Engebi, Range 4,020 Ft, before Bomb Burst . . . . .	92
2.6 F-47 Wing and Airfoils on Engebi, Range 4,020 Ft, after Detonation . . . . .	93
2.7 Portion of the F-47 Wing of Fig. 2.6 Showing Structural Damage, Engebi, Range 4,020 Ft, after Detonation . . . . .	94
2.8 B-17 Elevator on Muzin, Range 6,878 Ft, after Bomb Burst . . . . .	95
2.9 Typical Airfoil and Cylinder Installation before Bomb Burst, Telteir, Range 12,000 Ft . . . . .	96
2.10 Schematic Drawing Illustrating the Construction of the Rigid Wing . . . . .	97
2.11 Schematic Diagram of the Rigid-wing Model, Illustrating the Functioning of the Balance System . . . . .	98
2.12 Details of Failed Structural-wing Root Section on Engebi, Range 4,020 Ft, after Detonation . . . . .	99
2.13 View of the Failed Structural Model 104, Engebi, after Bomb Burst . . . . .	100
2.14 Structural Model (after Bomb Burst) with Top Cover Removed between Spars, Showing Installation of Temp-Tapes . . . . .	101
2.15 Location of Strain Gauges, Lead Masses, and Calibration Load Points for the Left-hand Structural-wing Models, Series -01 ( $6^\circ$ Angle of Incidence) . . . . .	102
2.16 Location of Strain Gauges, Lead Masses, Calibration Load Points, and Temperature Gauges for the Right-hand Structural-wing Models, Series -04 ( $9^\circ$ Angle of Incidence) . . . . .	103
2.17 Location of Strain Gauges, Lead Masses, and Calibration Load Points for the Swept-wing Models, Series -05 ( $8\frac{3}{4}^\circ$ Angle of Incidence) . . . . .	104
2.18 Airfoils Set at $0^\circ$ Angle of Incidence on Engebi, Range 4,020 Ft, after Bomb Burst . . . . .	105
2.19 Detailed View of the Airfoil Shown on Right in Fig. 2.18 . . . . .	106
2.20 Cylinders on Engebi, Range 4,020 Ft, after Detonation . . . . .	107
2.21 F-80 Fuselage Installation on Muzin, Range 6,878 Ft, before Bomb Burst . . . . .	108
2.22 F-80 Fuselage on Muzin after Detonation . . . . .	109

UNCLASSIFIED

## ILLUSTRATIONS (Continued)

	Page
2.23 B-17 Elevator Installation, Engebi, Range 4,020 Ft, before Bomb Burst . . . . .	110
2.24 Structural Damage Sustained by B-17 Elevator on Engebi after Detonation . . . . .	111
2.25 Spanwise View of B-17 Elevator from Engebi with the Fabric Removed from One Side (after Detonation) . . . . .	112
2.26 Crushed Internal Structure of the Inboard End of the B-17 Elevator, Engebi, 4,020 Ft, after Detonation . . . . .	113
2.27 Inboard Portion of the B-17 Elevator Showing Burned Fabric at the Leading Edge and Crushed Structure (after Detonation) . . . . .	114
2.28 Appearance of a Shock Front Photographed with Fastax Cameras during a 10,000-lb High-explosive Test at Aberdeen, 27 October 1950 . . . . .	115
2.29 Fastax Camera with Protective Canister (before Bomb Burst) . . . . .	116
2.30 Grid Suspended in Camera Field, Showing Vertical Pipe and Ping-pong Balls for Optical Angle-of-attack Determination, Teiteir, Range 12,000 Ft, before Bomb Burst . . . . .	117
2.31 View of Grid and Ping-pong Balls on Muzin, Range 6,878 Ft, after Detonation . . . . .	118
2.32 Typical Electrical Controls at Each Island Site for Cameras and Lights, before Detonation . . . . .	119
2.33 Installation of Angle-of-attack Blast Switch for Simultaneously Triggering Electronic Chronographs, Muzin, before Detonation . . . . .	120
2.34 Installation of Angle-of-attack Blast Switches for Stopping Individual Chrono- graphs (after Detonation) . . . . .	121
2.35 Four Electronic Counters Arranged to Facilitate Automatic Recording on a 4- by 5-in. Still Camera for Determination of Vertical Profile of Blast Front . . . . .	122
2.36 Signal from Four Electronic Counters As Recorded on a Still Camera for Easy Day Explosion . . . . .	123
2.37 Circuit Diagram for Automatic Operation of Electronic-chronograph Angle- of-attack System . . . . .	124
2.38 General Arrangement of Interferometer-gauge Elements . . . . .	125
2.39 Location of Interferometer Gauges at Each Test Site . . . . .	126

### CHAPTER 3 INSTRUMENTATION OF TEST ARTICLES

3.1 Perspective Interior View of an Instrumented Spanwise Station Typical for the Swept-wing and the Structural-wing Models . . . . .	127
3.2 Schematic Wiring Diagram for Strain-measurement Bridges on the Structural- and the Swept-wing Models . . . . .	128
3.3 Perspective View Illustrating Instrumentation Details of the Rigid-wing Model . . . . .	129
3.4 Location of Strain Gauges and Pressure Gauges for the Left-hand Rigid-wing Models, Series -02 (9° Angle of Incidence) . . . . .	130
3.5 Location of Strain Gauges and Pressure Gauges for the Right-hand Rigid-wing Models, Series -03 (6° Angle of Incidence) . . . . .	131
3.6 Rigid and Structural Models on Muzin, Range 6,878 Ft, after Detonation . . . . .	132
3.7 Drawing of Temp-Tape Components . . . . .	133
3.8 Outside-skin-surface Temperature vs Time Gauge Installed on Bottom Surface of a -04 Structural Wing . . . . .	134
3.9 Sketch Showing Location of Temperature vs Time Gauges in the Leading-edge Section of a -04 Structural Wing . . . . .	135

UNCLASSIFIED

## ILLUSTRATIONS (Continued)

	Page
3.10 Perspective View Illustrating Instrumentation Details of a Structural-wing Model . . . . .	136
 CHAPTER 4 CALIBRATION	
4.1 Calibration of Blast Switches . . . . .	137
 CHAPTER 5 TEST RESULTS	
5.1 Muzin Test Site after the Atomic Bomb Detonation, Range 6,878 Ft . . . . .	138
5.2 Engebi Test Site Approximately 6 Hr after the Atomic Bomb Detonation, Range 4,020 Ft . . . . .	139
5.3 F-47 Wing and Airfoil Installation on Teiteir, Range 12,000 Ft, before Bomb Burst . . . . .	140
5.4 Crushed Sheet-metal Covering of the Wheel Well of the F-47 Wing Installation on Teiteir, Range 12,000 Ft, after Bomb Burst . . . . .	141
5.5 Failed Airfoil with 1/4-in. Vent Holes on Engebi, Range 4,020 Ft, after Bomb Detonation . . . . .	142
5.6 Failed Airfoil with 1/4-in. Vent Holes on Engebi, Range 4,020 Ft, after Bomb Burst . . . . .	143
5.7 Partially Failed Airfoil with No Venting Holes, Engebi, Range 4,020 Ft, after Bomb Burst . . . . .	144
5.8 Variation of Lift with Time, Obtained from Balance-system Measurement for Rigid Wing 102 . . . . .	145
5.9 Variation of Lift with Time, Obtained from Balance-system Measurement for Rigid Wing 202 . . . . .	146
5.10 Average Variation of Lift with Time, Obtained from Balance-system Measurements for Two Wings . . . . .	147
5.11 Variation of Differential Pressure with Time at 5 Per Cent Chord of Rigid Wing 102 . . . . .	148
5.12 Variation of Differential Pressure with Time at 15 Per Cent Chord of Rigid Wing 102 . . . . .	149
5.13 Variation of Differential Pressure with Time at 20 Per Cent Chord of Rigid Wing 102 . . . . .	150
5.14 Variation of Differential Pressure with Time at 40 Per Cent Chord of Rigid Wing 102 . . . . .	151
5.15 Variation of Differential Pressure with Time at 80 Per Cent Chord of Rigid Wing 102 . . . . .	152
5.16 Variation of Differential Pressure with Time at 5 Per Cent Chord of Rigid Wing 103 . . . . .	153
5.17 Variation of Differential Pressure with Time at 10 Per Cent Chord of Rigid Wing 103 . . . . .	154
5.18 Variation of Differential Pressure with Time at 15 Per Cent Chord of Rigid Wing 103 . . . . .	155
5.19 Variation of Differential Pressure with Time at 10 Per Cent Chord of Rigid Wing 202 . . . . .	156
5.20 Variation of Differential Pressure with Time at 15 Per Cent Chord of Rigid Wing 202 . . . . .	157
5.21 Variation of Differential Pressure with Time at 20 Per Cent Chord of Rigid Wing 202 . . . . .	158

## ILLUSTRATIONS (Continued)

	Page
5.22 Variation of Differential Pressure with Time at 5 Per Cent Chord of Rigid Wing 203 . . . . .	159
5.23 Variation of Differential Pressure with Time at 10 Per Cent Chord of Rigid Wing 203 . . . . .	160
5.24 Variation of Differential Pressure with Time at 20 Per Cent Chord of Rigid Wing 203 . . . . .	161
5.25 Average Variation of Lift with Time Obtained from Differential-pressure Measurements for Rigid Wing 102 . . . . .	162
5.26 Average Pressure Distribution following Arrival of the Blast Front for Rigid Wing 102 . . . . .	163
5.27 Weighted Average Pressure Distribution following Arrival of the Blast Front, from Pressure Measurements for Four Wings Transferred and Combined to Give an Equivalent Pressure Distribution for a Rigid Wing . . . . .	164
5.28 Variation of Center-of-pressure Distance from the 25 Per Cent Chord Point with Time, Obtained from Differential-pressure Measurements for Rigid Wing 102 . . . . .	165
5.29 Variation of Moment about the 25 Per Cent Chord with Time, Compared to the Variation of Angle of Attack for Rigid Wing 102 . . . . .	166
5.30 Variation of Differential Pressure with Time at 10 Per Cent Chord of Rigid Wing 202 . . . . .	167
5.31 Comparison during Initial Stages of the Variation of Differential Pressure at Four Chord Points of Rigid Wing 202 . . . . .	168
5.32 Comparison during the Initial Stages of the Variation of Differential Pressure at Three Chord Points of Rigid Wing 203 . . . . .	169
5.33 Variation of Differential Pressure at 20 Per Cent Chord of Two Rigid Wings at Different Angles of Incidence . . . . .	170
5.34 Comparison of the Variation of Bending Moment with Time at Three Stations of Structural Wing 101 . . . . .	171
5.35 Variation of Bending Moment with Time at Station 1, Outboard, of Structural Wing 101 . . . . .	172
5.36 Variation of Bending Moment with Time at Two Stations of Structural Wing 104, Angle of Incidence $9^\circ$ , Compared with Bending Moment at One Station of Structural Wing 101, Angle of Incidence $6^\circ$ , to Indicate Time of Failure of Wing 104 . . . . .	173
5.37 Variation of Bending Moment with Time at Station 3, Inboard, of Structural Wing 101 . . . . .	174
5.38 Variation of Bending Moment with Time at the Intermediate Station of Two Structural Wings at Different Angles of Incidence . . . . .	175
5.39 Indication of Second-mode Bending Moment at the Intermediate Station of Two Structural Wings . . . . .	176
5.40 Variation of Shear with Time at Station 3, Inboard, Structural Wing 101 . . . . .	177
5.41 Variation of Shear with Time at Station 3, Inboard, of Structural Wing 101 . . . . .	178
5.42 Variation of Bending Moment with Time at Station 7, Inboard, of Swept Wing 105 . . . . .	179
5.43 Variation of Bending Moment with Time at Station 8, Intermediate, of Swept Wing 105 . . . . .	180
5.44 Variation of Bending Moment with Time at Station 9, Outboard, of Swept Wing 105 . . . . .	181
5.45 Variation of Shear with Time at Station 8, Intermediate, of Swept Wing 105 . . . . .	182

## ILLUSTRATIONS (Continued)

	Page
5.46 Variation of Shear with Time at Station 9, Outboard, of Swept Wing 105 . . . . .	183
5.47 Comparison during Initial Impulse of the Variation of Bending Moment with Time at Three Stations of Swept Wing 105 . . . . .	184
5.48 Comparison of the Variation of Bending Moment with Time at Three Stations of Swept Wing 105 . . . . .	185
5.49 Comparison of the Variation of Shear with Time at Two Stations of Swept Wing 105 . . . . .	186
5.50 Comparison of the Variation of Bending Moment with Time at Station 9, Out- board, for Two Swept Wings at Different Ranges . . . . .	187
5.51 Variation of Bending Moment with Time at Station 8, Intermediate, of Swept Wing 205 . . . . .	188
5.52 Variation of Temperature Change with Time of an Outside-skin-surface Point on Each of Two Structural Wings at Different Ranges . . . . .	189
5.53 Variation of Temperature Change with Time at a 25° Incidence Point on the Outside Skin Surface of Two Wings at Different Ranges . . . . .	190
5.54 Comparison of the Variation of Temperature Change with Time for Three Points of Structural Wing 204 . . . . .	191
5.55 Variation of Temperature Change with Time at Three Points of Structural Wing 204 . . . . .	192
5.56 Variation of Angle of Flow of the Advancing Air Mass with Time at 4,020-ft Range, Engebi . . . . .	193
5.57 Average Variation of the Angle of Flow of the Advancing Air Mass with Time at 4,020-ft Range, Engebi . . . . .	194
5.58 Enlargement of Two Frames from 35-mm Roll B-35-100-714 from Fastax Camera Film Taken Just prior to Passage of Blast Front, Muzin, Range 6,878 Ft . . . . .	195
5.59 Enlargement Same Film Roll As Fig. 5.60 Showing Probable Passage of Blast Front at Time That Shock Front Should Be Visible . . . . .	196
5.60 Enlargement from 35-mm Fastax Camera on Muzin, Range 6,878 Ft, Illustrating Clouds and Their Movement . . . . .	197
5.61 Vertical Profile of Blast Front As Determined by Electronic Chronographs and Blast Switches . . . . .	198
5.62 Variation of Blast Pressure with Time at Each of the Four Test Sites As Determined from Interferometer Gauges . . . . .	199
5.63 Variation of Blast Pressure with Time for the First 200 Msec at Each of the Four Test Sites As Determined from Interferometer Gauges . . . . .	200

### CHAPTER 6 DISCUSSION

6.1 Oscillograph Reproduction of the Magnetic-tape Record of the Lift for Four Wings . . . . .	201
6.2 Oscillograph Reproductions of the Magnetic-tape Record of the Variation of Differential Pressure with Time at Several Chordwise Stations of Rigid Wing 102, Angle of Incidence 9°, Range 4,020 Ft . . . . .	202
6.3 Oscillograph Reproductions of the Magnetic-tape Record of the Variation of Differential Pressure with Time at Several Chordwise Stations of Rigid Wings 103, 202, and 203 . . . . .	203
6.4 Oscillograph Reproductions of the Magnetic-tape Record of the Variation of Differential Pressure with Time at Chordwise Stations of Rigid Wings 202 and 203, Range 6,878 Ft . . . . .	204



## ILLUSTRATIONS (Continued)

	Page
6.5 Oscillograph Reproductions of the Magnetic-tape Record of the Variation of Bending Moment with Time at Three Stations of Structural Wing 101, Angle of Incidence 6°, Range 4,020 Ft. . . . .	205
6.6 Oscillograph Reproductions of the Magnetic-tape Record of the Variation of Shear with Time at Spanwise Stations of Structural Wings 101 and 204 . . . . .	206
6.7 Oscillograph Reproductions of the Magnetic-tape Record of the Variation of Bending Moment with Time at Spanwise Stations of Structural Wings 104, 201, and 204 . . . . .	207
6.8 Oscillograph Reproductions of the Magnetic-tape Record of the Variation of Bending Moment with Time at Three Stations of Swept Wing 105, Range 4,020 Ft . . . . .	208
6.9 Oscillograph Reproductions of the Magnetic-tape Record of the Variation of Shear with Time at Two Stations of Swept Wing 105; and of Bending Moment with Time at Two Stations of Swept Wing 205 . . . . .	209
6.10 Oscillograph Reproductions of the Magnetic-tape Record of the Variation of Bending Moment with Time at Station 4, Inboard, of Structural Wing 304; at Two Stations of Swept Wing 305; and of Shear with Time at Station 3, Inboard, of Structural Wing 201 . . . . .	210
6.11 Oscillograph Reproduction of the Magnetic-tape Record of the Variation of Angle of Flow of the Advancing Air Mass at the 4,020-ft Range. . . . .	211
6.12 Visual Reproductions of the Magnetic-tape Record of the Variation of Temperature Change with Time at Several Points on Structural Wings 204 and 304 . . . . .	212
6.13 Variation of Maximum Temperature Change with Range for Three Points on the Structural Wings. . . . .	213

## TABLES

### CHAPTER 1 INTRODUCTION

1.1 Table of Organization for Project 8.2 . . . . .	5
---	---

### CHAPTER 2 DESCRIPTION OF EXPERIMENTAL PROCEDURE AND TEST APPARATUS

2.1 Test Articles and Equipment at Each Island Test Site . . . . .	9
2.2 Project 8.2 Island Test Sites and Respective Data . . . . .	10
2.3 Airfoil NACA 65 <sub>2</sub> -015 . . . . .	12

### CHAPTER 3 INSTRUMENTATION OF TEST ARTICLES

3.1 Numbering Code and Description of the Quantities Measured by Each Instrument Channel . . . . .	20
--	----

### CHAPTER 4 CALIBRATION

4.1 Calibration Factors and Maximum Errors for Intelligence Channels by Test Site . . . . .	28
---	----

UNCLASSIFIED

## TABLES (Continued)

	Page
CHAPTER 5 TEST RESULTS	
5.1 Transposition of All Differential-pressure Data to 9° Rigid Wing at Engebi . . . . .	36
5.2 Maximum Temperatures on Aircraft Structural Components As Measured with Temp-Tapes . . . . .	42
CHAPTER 6 DISCUSSION	
6.1 Numbers of Figures in Which Are Plotted Curves for Lift, Pressure, and Angle of Air-mass-flow Functions . . . . .	49
6.2 Numbers of Figures in Which Are Plotted Curves for Bending Moment, Shear, and Temperature Functions . . . . .	50



## Abstract

This volume is the report of a test program to measure under carefully controlled conditions on the ground the effects of an atomic bomb on aircraft and missile structures. Some measurements of the blast and thermal phenomena peculiar to the USAF problem are included.

Automatic-recording-instrumented aerodynamic and structural models were erected at four different ranges from the shot tower to determine the forcing functions (actual loads) and the dynamic response when subjected to the blast wave. Other test articles, consisting of the following aircraft components: F-47 wings and control surfaces, F-80 fuselage sections with canopies, B-17 elevators, and cylinder- and airfoil-shaped overpressure models, were stationed at four ranges to determine mainly the destructive effect of the differential-pressure shock and also the over-all effect of the bomb. A survey of the highest temperature attained on

various portions of the test articles was conducted with an experimental temperature-measuring device. A limited number of measurements of temperature variations with time were made on portions of the test articles. The overpressure vs time at each of the four test ranges was measured using an interferometer gauge mounted level with the ground. Phenomena peculiar to the angle of attack of the blast wave were measured with three different types of instruments.

The results of the measured data are presented, including initial conclusions and recommendations. However, the intent or purpose of this operation was to gather data from which aircraft and missile structural design criteria could be evolved. Therefore conclusions will not be available until a more exhaustive evaluation can be conducted.

## Chapter 1

# Introduction

### 1.1 GENERAL CONSIDERATIONS

The over-all functions of Projects 8.0, 8.1, and 8.2 were to investigate, measure, and evaluate the effects produced on an aircraft flying in the region of an atomic bomb burst. The engineering data collected as a result of this test are to be utilized for (1) the establishment of aircraft and missile design criteria, (2) the determination of safe operating procedures for aircraft required to fly within the field of an atomic bomb burst, (3) the determination of hazards encountered by aircraft and missiles in the air and on the ground when in the field of an atomic bomb burst, and (4) the establishment of data required for the detail design of aircraft and missile structures, that is, choice of materials and type of construction.

Project 8.2 is the ground phase of the over-all aircraft program, and, as the name implies, all testing was performed on the ground of various islands of the Eniwetok Atoll. The ground tests provided an opportunity to gather data under closely controlled conditions (as compared to flight conditions) on simplified structures. This was extremely important since the use of simplified models rather than complex aircraft structures permits a correlation of theory and experiment with the minimum of problems due to superfluous details. In addition it provided an opportunity to make reliable observations of the effects on aircraft structures at a relatively short distance from the center of the burst. These observations are valuable in determining the effect and extent of local blast damage on secondary and primary structural components. This type of damage cannot be reliably predicted by methods of analysis; yet it may be an

important factor in the failure of certain types of aircraft structures.

It was apparent that, if failure were to occur in the structure of an aircraft operating within the field of an atomic bomb burst, it would be caused by blast or thermal radiation. Previous atomic tests and engineering data derived therefrom indicated that the blast effect was the phenomenon most destructive to the aircraft structure, although thermal radiation appeared to be critical in certain portions of the aircraft, and the requirement for temperature data became more important as studies of existing data progressed. The blast phenomena of an atomic bomb burst may be broken down into the following three divisions to clarify their relation to the aircraft structures problem and to the Project 8.2 test program: the aerodynamics of the shock wave, the air loads (lift, drag, and crushing) on the aircraft structure, and the response of the aircraft structure to these loads. The thermal-radiation problem does not need to be divided for the purpose of reporting the test results on aircraft structures. The Project 8.2 test program limited the investigation of the thermal problem to the measurement of the highest temperature encountered at a number of locations on the ground-test articles and included three temperature vs time surveys at each of the four test sites.

### 1.2 OBJECTIVE

In general, the objective of the Project 8.2 test program was to place definitely specified aircraft components and models at predetermined ranges in the field of the Easy atomic bomb burst and, under carefully controlled

[REDACTED]

conditions, to measure and evaluate the effects mainly of the blast phenomena and also of the thermal radiation on these test articles. The objective also included measurements of the blast phenomena peculiar to, and required by, the Air Force in order to obtain sufficient data about the aerodynamics and thermodynamics of the shock front and blast wave to make possible the establishment of aircraft design criteria.

Therefore the specific objective of Greenhouse Project 8.2 was to perform the necessary tests from which data of the following type could be assembled:

1. Air-load and air-pressure measurements on ideal rigid two-dimensional wing models to determine the actual loads which these wings experience (see Fig. 1.1). (An ideal two-dimensional rigid-wing model in this case refers to a small, very rigid (stiff) wing with no sweep backward or forward, no taper in either the leading or trailing edge, and no change in the size of the airfoil throughout the span).

2. Structural measurements of the dynamic response of ideal straight- and swept-wing models to an atomic bomb burst. (Ideal wing models in this case refer to small structural wings of simple design which behave structurally in a manner suitable to verify methods of dynamic-stress analysis.) The ideal models utilize the same airfoil section as the rigid model in order that the dynamic response can be correlated directly with known air loads. These ideal wing models shall be referred to hereafter as "structural" models and "swept" models (see Figs. 1.1 to 1.4).

3. Qualitative results on vented and unvented simple cylinders and simple airfoil shapes to determine the effect of the shock wave and the alleviation effect of venting holes (see Fig. 2.9).

4. Qualitative results of the over-all effect on canopies, pressurized-type cockpits, control surfaces, wing structures, etc.

5. A survey of the temperature rise of various elements of aircraft structures located stationary on the ground.

6. Measurements of pressure field vs time at each of the Project 8.2 test sites.

7. Measurements of the angle of the shock front relative to the chord of the wing models at all test sites.

### 1.3 BACKGROUND

The experience gained by members of Operation Crossroads and the reports therefrom furnished both practical and operational information.

The precedence enjoyed by being associated with Operation Greenhouse made available substantial amounts of engineering data (regarding the atomic bomb effects and phenomena) from other government agencies. This information, gathered from conferences and reports, advanced the general understanding of the aircraft and missile structures problem facing the USAF. Although this information was not available prior to the initiation of the Greenhouse Project 8.2, every effort was extended to digest the data and incorporate the latest conceptions in this project.

### 1.4 GENERAL TEST PROGRAM

To ensure accomplishment of the objectives, it was determined essential that a minimum of four test sites at specific ranges from the atomic bomb burst be established. The four islands selected as most nearly meeting the range requirement in this test were Engebi, Muzinbaarikku (Muzin), Teiteiripucchi (Teiteir), and Bokonaarappu (Bokon). Figure 1.5 is a sketch illustrating the relative locations of the island sites, their respective ranges from the shot tower, and other related data. Figures 1.6 to 1.9 are aerial views of each of the four island test sites.

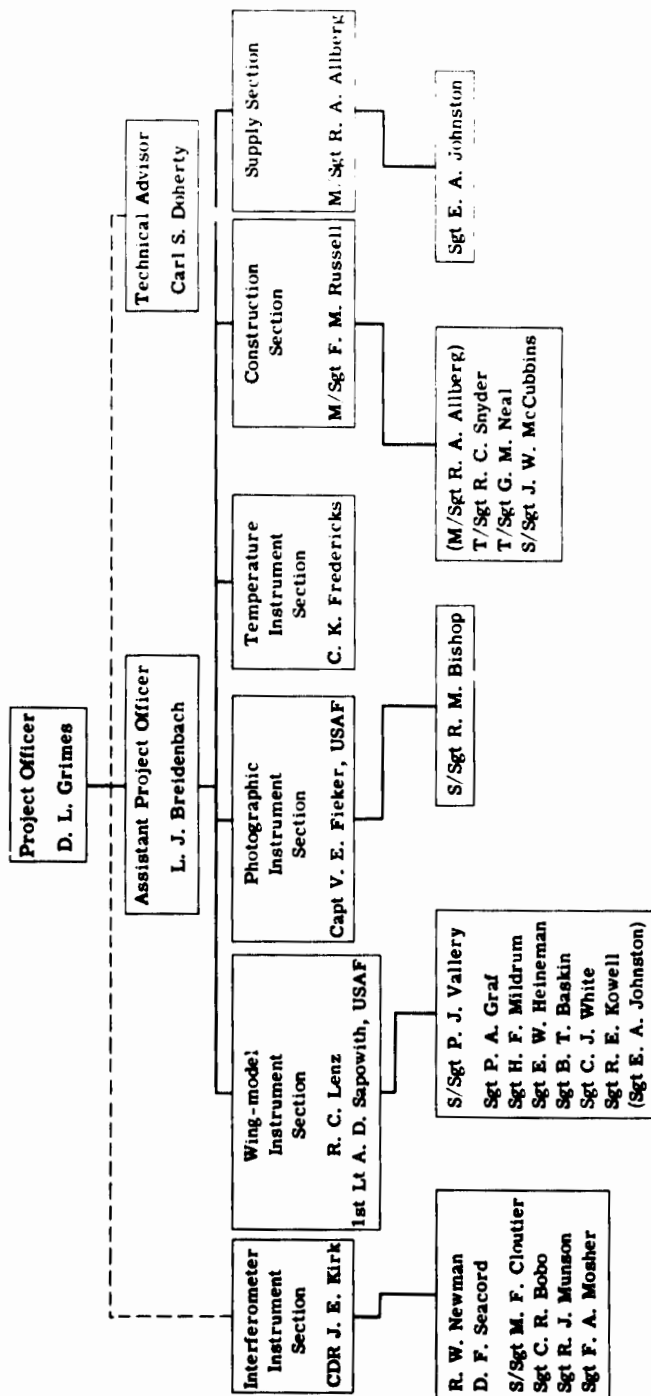
The array of test articles and equipment was practically identical for each of the four test islands. The test installations consisted of aerodynamic and structural models, F-80 fuselage sections, F-47 wing panels, B-17 elevators, cylindrically shaped and airfoil-shaped overpressure models, and angle-of-attack, temperature, and overpressure measuring equipment. Figure 1.10 is an aerial view and Fig. 1.11 is a rear oblique ground view showing a typical test array. On each island an instrument room was constructed of suitable design to house and protect the remotely controlled recording equipment, time-signal relays, stand-by battery and rectifier systems, and other equipment (see Figs. 1.12 to 1.15). These rooms or small buildings were all lo-

4

[REDACTED]

UNCLASSIFIED

TABLE 1.1 TABLE OF ORGANIZATION FOR PROJECT 8.2



cated partly below the ground and were 75 to 90 ft to the rear of the line of test articles. The instrument rooms on Engebi and Muzin were constructed of reinforced concrete with a heavy steel marine-type door. The large quantity of electric wires from the measuring devices in the test articles was conveyed to the ground inside the pylons and then underground in two large electrical conduits to the instrument house (see Fig. 1.15). Electrical power to operate the instruments was provided by central power sources operated by another group and by storage batteries. It was necessary to augment these sources with additional power on Engebi and Muzin. This was accomplished by the installation of portable generators (7.5 to 25 kw) below ground in prepared sandbag revetments (see Figs. 1.16 to 1.19). The dynamic response, which consists of bending, shear, and torsion loads, was measured on the structural- and the swept-wing models by strain gauges. The sensing elements for measuring total reactions, i.e., total lift, drag, and moment of the rigid model, were also strain gauges. Pressure transducers employing a variable-reluctance principle were used in measuring the pressure distribution over the rigid model. The temperature rise at various local areas in the structural models was measured by electrical-resistance-type temperature gauges. Vane-type angle-of-attack indicators attached to the supports of the swept-model pylons were utilized on Engebi and on Muzin to measure the angle of attack of the high-velocity air mass (positive pressure) immediately following the shock front (see Figs. 1.20 to 1.23). Two 24-channel magnetic-tape (Webster) recorders were used on each

island test site for remotely recording the data from the above-described sensing elements.

An electronic-chronograph system triggered by pressure switches was used to measure the angle of attack of the blast wave. This system operated from the auxiliary power source, and remote recording was performed by a photographic system. A method of measuring the angle of attack of the shock front through the use of high-speed motion pictures was attempted on all four test sites. This system consisted in photographing, with a Fastax camera, the optical phenomenon produced by refraction through the shock front of a break or discontinuity in straight lines suspended within the camera field.

The temperature survey of the highest temperature attained on various portions of the structural test articles was performed through the use of eutectic metal alloys with specific melting points.

Interferometer-type gauges were used in measuring the overpressure vs time at each of the test sites. These instruments contained their own battery power source and recording system.

The central-source time signal was used for remotely actuating all the Project 8.2 instrumentation. Additional timing or triggering systems were required in order to meet the full requirements of this project.

The organization of personnel for Project 8.2 is given in Table 1.1.

Detailed descriptions of the test, instrumentation, and equipment are contained in the following chapters.

## Chapter 2

# Description of Experimental Procedure and Test Apparatus

### 2.1 SELECTION OF TEST ARTICLES

The major portion of the test articles was utilized in obtaining data on the effects of atomic bomb blast phenomena on aircraft structures. A schematic diagram is presented in Fig. 2.1, illustrating the division of energies and forces released by an atomic bomb burst as related to the aircraft structures problem and the Project 8.2 ground-test program. For clarification of the cause of blast damage to aircraft structures the blast phenomena may be considered as two separate and distinct forces: On the arrival of the blast front the aircraft structure is subjected to a large crushing force due to the external-to-internal pressure differential; this is immediately followed by the movement of a large mass of high-velocity air over the structure, causing lift and drag. The effect of the latter force acting on an aircraft structure anchored in its path is similar to that of an outside wind tunnel in which the high-velocity air is caused by the atomic bomb burst. The functional requirements and a brief description of the test articles selected to obtain data on the effects of blast phenomena on aircraft structures are as follows:

1. The measurement of the actual total loads and the differential-pressure profile produced by the air-mass movement over a rigid-wing surface. To obtain these data, a small wing model of high inherent stiffness as compared to conventional wing structures was designed and fabricated. This rigid-wing model was oriented in the air-blast path and supported on a balancing system concealed within the supporting pylons. Two rigid models were mounted

horizontally at each island site between the pylons as illustrated in Fig. 1.1. The balance system was designed to make possible the isolation of the lift, drag, and moment forces so that measurements could be accomplished by strain gauges. Pressure-sensing elements were installed for pressure-profile measurements.

2. The measurement of the dynamic response of conventional wing structures under the applied load of the air-mass movement. This is the measurement of how a wing structure reacts to the dynamic load of the high-velocity air mass following the shock front. To reduce complications in the dynamic-stress analysis problem and to eliminate other influencing factors, it was determined advisable to design and fabricate both a straight- and swept-wing model for these data. The structural model, as the straight-wing design is hereafter named, and the swept model (see Fig. 1.3) were designed in a simple manner to permit a straight-forward dynamic analysis. Two structural models were mounted at each island site as horizontal cantilevers on the outer pylons (see Figs. 1.1 and 1.2). The structural model utilized the same airfoil section as the rigid model to permit direct correlation of the dynamic response with the measured air loads. Strain gauges were used as the sensing elements in both models.

3. The observation and evaluation of the effect of the shock front, or, more specifically, the destructive effect of the differential-pressure shock on various structural components. A number of factors influenced the selection of the structural components. These factors in-



cluded availability of the component from supply or salvage, size, type of construction, and the incorporation of several structural features in one test article, which in turn reduced considerably other problems, such as hold-down fixtures and logistics. Although the test articles are being described herein in accordance with the major reasons for their selection, it is desired to point out that practically all of them served at least a twofold purpose, such as a general qualitative test of various types of construction and the study of thermal-radiation effects. A list of the remaining test articles with major reasons for their selection follows.

1. The F-80 fuselage section was an available representation of typical fighter fuselage design. In addition to enabling investigation of effects of blast phenomena on fuselage-type aircraft construction, this component includes three other major test items of interest: a transparent canopy, a cockpit designed for pressurization, and a laminated-glass plastic radar dome (see Figs. 2.2 to 2.4).

2. The F-47 wing panels with ailerons and flaps installed were selected as typical wing construction and control-surface-type construction suitable for a qualitative observation of the over-all effect of an atom bomb. Of greater importance is the fact that they offered the opportunity to observe the differential-pressure effect upon, and behavior of, lightly constructed, completely closed metal-covered control surfaces (see Figs. 2.5 to 2.7 and 5.3).

3. The B-17 elevators were selected to study the behavior of typical fabric-covered control surfaces. This elevator was a particularly good article for this study since a large number of high-explosive tests had been conducted and evaluated on this same type of surface. Fabric-covered controls are still in general use and are particularly susceptible to the thermal effects following the detonation of an atomic bomb (see Figs. 2.8 and 2.23).

4. Vented and unvented cylinders and airfoils were designed specifically for this test as an initial attempt to derive a simplified, economical test article for use in qualitative investigation of the differential-pressure phenomena on closed aircraft structures (see Fig. 2.9).

A review of data to be collected by other organizations indicated that general engineering and scientific data on the thermodynamic and aerodynamic phenomena of the Easy Day atomic

bomb burst were sufficient to meet the requirements of the USAF with two exceptions. A requirement existed for the accurate measurement of the overpressure vs time at each of the four test sites. Also required was a determination of the angle of inclination of the blast front. An interferometer-type instrument (Buck gauge) was selected for the pressure-time measurement and was positioned about the test articles to give a pressure-field study.

The requirement for measuring the angle of the blast front with the chord of the models developed at such a late date that it was necessary to use only the equipment that was readily available. A high-speed motion-picture procedure was selected as most adaptable for each test site, and a mechanical system was devised in addition as a check at one of the most important sites.

The probability of the destruction of aircraft structures by the release of radiant energy due to an atomic bomb became more realistic with the opening discussions on the H-bomb. Therefore the temperature survey conducted under Project 8.2 was added at a later date as a feasible way to initiate some measurements from which the thermal problem could be more clearly understood and from which practical answers could be gained while theoretical studies were in process. Temperature measurements were made mainly by utilizing eutectic metal alloys. This method of instrumentation permitted the gathering of a large quantity of data regarding the highest temperature experienced by portions of aircraft structures of various types under many conditions. Several measurements of temperature rise vs time were made on the metal skin of the models, using fine-wire-type electrical-resistance gauges and the magnetic-tape recording system.

## 2.2 SELECTION OF ISLAND TEST SITES

In general the number of specific test articles and the repetition of tests at various ranges were limited by the economics and logistics of the situation. However, it was determined essential that a minimum of four ranges or test sites be established in order to derive suitable engineering data.

The selection of the range of the test articles or test sites with respect to the center of the

blast was based entirely on the overpressures as predicted for the estimated yield of the Easy Day atomic bomb. However, in anticipation of various errors in the theoretical knowledge of effects on aircraft structures up to the date of preparation for the Easy Day test and of the effect of terrain and in order to bracket the required data, identical test articles were placed at four ranges on four island test sites (Table 2.1).

and the fundamental data available prior to the test are given in Table 2.2.

### 2.3 GENERAL LAYOUT OF TEST SITES

The anticipated primary obstacle to the achievement of the objectives of the ground-test program was the possibility of error being introduced into the load and response measure-

TABLE 2.1 TEST ARTICLES AND EQUIPMENT AT EACH ISLAND TEST SITE

Test Articles and Equipment	Number on Each Site			
	Engebl	Muzin	Teiteir	Bokon
Instrumented kit articles:				
Rigid model	2	2	2	2
Structural model	2	2	2	2
Swept model	1	1	1	1
Uninstrumented test articles:				
F-47 wing panel	2	2	2	2
F-80 fuselage section	1	1	1	1
B-17 elevator	1	1	1	1
Airfoil section	6	6	6	6
Cylinders	2	2	2	2
Test equipment for measuring atomic bomb phenomena:				
Interferometer (Buck gauge)	2	4	4	4
Supersonic vane type (angle of shock front)	1			
Subsonic vane type (angle of shock front)		1		
Electronic chronograph (angle of shock front)		4		
Fastax camera system (angle of shock front)	1	1	1	1

After the desired range for each group of test articles was established, the specific islands were selected, based primarily on range from the shot tower and also on other prerequisites, such as boat-landing conditions, availability of electric power, and freedom from aerodynamic interference from natural or manufactured objects. The abbreviated names of the four island test sites selected as most nearly meeting these requirements were Engebl, Muzin, Teiteir, and Bokon. A list of Project 8.2 island test sites

ments owing to reflection and deflection of the shock front caused by beach, ground, or tree effects or change of the air-mass movement by test articles of other projects in the immediate area. Therefore every effort was extended to prevent or alleviate troubles of this nature. The array of test articles was located well forward on the islands (with the exception of Engebl) but at a great enough distance from the water's edge to minimize beach effect. Whenever it was required, trees and other natural objects were

TABLE 2.2 PROJECT 8.2 ISLAND TEST SITES AND RESPECTIVE DATA\*

Island Name and Symbol	Range (Test Articles to Point of A- bomb Burst) (ft)	Overpressure at Site of Test Articles (psi)		Estimated Elapsed Time from Bomb Burst to Arrival of Shock Front at Test Articles (sec)	Estimated Peak Gust Velocity (ft/sec)	Duration of Positive Phase (sec)	
		Observed for 50 kt	Estimated for 60 kt			Observed for 50 kt	Estimated for 60 kt
Engebi (E)	4,020	9.5	11.8	1.4	510	0.95	1.0
Muzinbaarikku (S)	6,878	3.4	4.2	3.5	210	1.01	1.4
Teiteiripucchi (Q)	12,000	1.5	1.75	7.7	93	1.40	1.75
Bokonaarappu (P)	16,614	0.9	1.15	11.6	60	1.73	1.95

\*Based on a predicted A-bomb size of 60 kt.

removed from all sides of the target array to a great enough distance to decrease possibilities of disturbance of the shock wave.

An area 200 by 300 ft about the test articles on all island test sites was stabilized with asphalt. This served the dual function of protecting the instrumentation from sand and dust prior to, and during, the atomic explosion and permitting ease of operation of the heavy erection equipment. To reduce the hazards to the test articles and equipment due to impingement of flying debris, all the ground area between the target array of each test site and the shot tower was thoroughly cleaned of all debris (driftwood, roots, and other foreign objects). Additional stabilization of the dust and fine sand was performed by spraying with an oil-salt-water emulsion. Figures 1.8 and 1.10 are views of Teiteir illustrating the preparation of the island terrain for the test site. It can be seen that the trees and brush were cleared from all sides of the test site. The very dark areas, one immediately in front of the asphalt paving around the test articles (the asphalt paving appears fairly light in the photographs) and another along the beach area, are the water-oil emulsion applied just prior to shot day. These strips were oiled to stabilize the deep fine sand which had been uncovered by grading. The area between the oil strips was fairly well stabilized by the vegetation.

Only a very limited amount of theoretical or empirical data was available and applicable at the initiation of this project to determine the heights above the ground at which it would be necessary to support the rigid, structural, and swept models to avoid ground interference and the lateral separation distance that would be required between test items to avoid mutual interference with the blast phenomena. Ten feet above the ground was selected as a practical height for the pylons to support the models. The pylons for these models were required to be extremely rigid, and therefore it was inadvisable to design the pylons to an increased height above ground. Many advantages were gained by arrangement of all the test articles of this project into one group at each test site. Some of the major advantages were economy and ease in the erection of test articles, a more choice selection of available terrain, and ease in the maintenance of a clear path to the shot tower. Because of the aerodynamic cleanliness of the

test articles and therefore the relatively small disturbance of the blast wave, 20 ft was selected as a practical distance to maintain between the anchor bases (see Fig. 1.10).

## 2.4 DESCRIPTION OF TEST ARTICLES AND MOUNTING STRUCTURES

The test apparatus being utilized on Project 8.2 included three types of wing models, rigid, straight-structural, and swept-back-structural, together with their instrumentation and recording equipment; small vented and unvented airfoils and cylinders; standard fighter fuselages and wing panels; and both fabric- and metal-covered control surfaces. Detailed descriptions are given below.

### 2.4.1 Rigid-wing Models


The rigid-wing models were specifically designed to determine the differential chordwise pressure distribution and to measure lift, drag, and moment forces. An NACA 65<sub>2</sub>-015 airfoil (see Table 2.3) was used with a 5-ft span and a 2-ft chord, supported between pylons which served as end plates for the flow (Fig. 1.1).

A wing of high rigidity was desired to reduce distortion of the airfoil section and to have a bending frequency high enough to be well separated from the frequency of the forcing function. High rigidity was obtained by utilizing cast nose and tail sections,  $\frac{1}{2}$ -in.-thick ribs, and  $\frac{1}{4}$ -in.-thick skin, all of aluminum alloy (see Fig. 2.10). The section moment of inertia was 22.6 in.<sup>4</sup> for the rigid wing. The wing weighed 151.5 lb, exclusive of the balance system.

The nose and tail sections of the model were both large castings, cored for weight reduction. Special cutters were employed to shape the castings to obtain uniformity and adhere to close clearances. Heavy 1-in.-thick spars were fastened to the castings, and six ribs were used to form an integral structure. The  $\frac{1}{4}$ -in. skin was fastened to the ribs and the two castings in order to add to the wing stiffness. The top skin or panel was removable for access to the pressure gauges contained in the model. The spars, located at 25 and 60 per cent of the chord, extended as a reduced section 7 in. beyond the wing surface and were designed to attach to the balance system inside the supporting pylon.

UNCLASSIFIED

The balance system was designed for the measurement of the dynamic response of the rigid wing to a forcing function with a frequency below 10 cps. The system was designed to facilitate separation of the lift, drag, and moment

TABLE 2.3 AIRFOIL NACA 65<sub>2</sub>-015\*


X (% C)	X (in.)	Y (% C)	Y (in.)
0	0	0	0
0.5	0.12	1.124	0.2698
0.75	0.18	1.356	0.3254
1.25	0.30	1.702	0.4085
2.50	0.60	2.324	0.5578
5.0	1.20	3.245	0.7788
7.5	1.80	3.959	0.9502
10.0	2.4	4.555	1.093
15.0	3.6	5.504	1.321
20.0	4.8	6.223	1.494
25.0	6.0	6.764	1.623
30.0	7.2	7.152	1.716
35.0	8.4	7.396	1.775
40.0	9.6	7.498	1.800
45.0	10.8	7.428	1.783
50.0	12.0	7.168	1.720
55.0	13.2	6.720	1.613
60.0	14.4	6.118	1.468
65.0	15.6	5.403	1.297
70.0	16.8	4.600	1.104
75.0	18.0	3.744	0.8986
80.0	19.2	2.858	0.6859
85.0	20.4	1.977	0.4745
90.0	21.6	1.144	0.2746
95.0	22.8	0.428	0.1027
100.0	24.0	0	0

\* Leading edge radius = 1.505 per cent of chord = 0.3612 where chord = 24 in.

reactions of the wing model (see Fig. 2.11). The wide range of loads predicted at the sites necessitated greater reduction of the spar ends on four of the rigid models to provide strains of measurable magnitude at the distant test sites.

The heavier spar ends were designed to have linear response up to a static load of 2,250 lb lift and 200 lb drag for installation at 4,020 ft (Engebi) and 6,878 ft (Muzin) from ground zero. The lighter spar ends were designed to have linear response for static loads up to 500 lb lift and 50 lb drag for installation at 12,000 ft (Teiteir) and 16,614 ft (Bokon).

#### 2.4.2 Structural-wing Models

The structural-wing models were mounted as cantilever wings (see Fig. 1.1) and were instrumented to obtain bending, shear, and torsion stresses at three spanwise stations.

The models were designed in a two-spar conventional sheet-stringer aluminum-alloy configuration utilizing the same NACA 65<sub>2</sub>-015 airfoil section as the rigid-wing models discussed previously. The two spars were located at 20 and 60 per cent of the chord and were formed from 0.091-in. aluminum alloy.

The spars were riveted to machined aluminum channels (Figs. 2.12 and 2.13) that extended 7 in. into the supporting pylon, which in turn fitted into a heavy steel root-fitting box. This box was adjustable and enabled the wings to be rotated to the 6° and 9° positions used in the test.

The structural-wing models had a constant chord and thickness, with a span of 84 in. and a chord of 24 in. The ribs were spaced 12 in. apart and were formed from 0.051-in. aluminum sheet. The trailing edge was milled from bar stock, and the skin was flush-riveted to it to retain an airfoil shape of close tolerance. The wing tip was formed from a single sheet of 0.051-in. aluminum-sheet stock. The section moment of inertia was 4.09 in.<sup>4</sup> for this wing.

A skin thickness of 0.051 in. was used to withstand crushing at an overpressure of 10 psi. This heavy skin resulted in a wing that was very stiff in bending; consequently lead weights were incorporated in the wing to reduce the first bending frequency to approximately 4.2 cps. These lead weights (see Fig. 2.14) were placed between the spars and grouped in three concentrated masses of 70, 70, and 150 lb at distances of 19, 43, and 73 in., respectively, from the root, as shown in Figs. 2.15 and 2.16. With the lead masses installed, the first bending frequency was approximately 4.3 cps, the second bending frequency was approximately 33

UNCLASSIFIED

cps, and the first torsion frequency was approximately 49 cps. The total weight of the wing was approximately 338 lb, including the 290 lb of lead masses.

The skin in the nose section and on the upper surface was removable to afford access to the interior of the wing. The remainder of the skin and the wing tip were flush-riveted to the spars and ribs.

#### 2.4.3 Supporting Structure for Rigid- and Structural-wing Models

The supporting structures for the rigid- and the straight-structural-wing models were given the name "pylons." The pylons were required to be very rigid in order to minimize any feedback from the deflection of one wing model to another. Since two rigid and two structural wings were to be installed at each site in order to provide complementary data at two different specified angles of attack, it was decided to mount the wings in a group of four, placed end-to-end spanwise and supported by three equally spaced pylons, each of which supported two wing ends. The rigid wings were mounted in the middle with a vertical stagger in order that the balance mechanisms could be enclosed within the pylons. The pylons also acted as end plates on the rigid wings. The structural wings were mounted as cantilevers on the outer pylons. Removable access panels were utilized to provide a means for installing the wing models and instrumentation leads. The composite installation of structural and rigid wings is shown in Fig. 1.1. The pylons were designed with three vertical steel columns (8WF34) covered with  $\frac{1}{2}$ -in.-thick steel plate. The leading and trailing edges were fabricated with aluminum-alloy sheet and ribs. The moment of inertia was 1,434 in.<sup>4</sup> for the pylons. Steel tie rods were employed to further increase the stiffness of the pylons.

#### 2.4.4 Reinforced-concrete Base for Rigid- and Structural-wing Models

A reinforced-concrete base was poured at each of the four island test sites to anchor and support the pylons. Two concrete deadmen were poured to anchor the outer tie rods. The main concrete base had a rectangular planform measuring 14 ft laterally, 10 ft longitudinally, and 3 ft in depth. The concrete mass was the

same for the two nearest sites, and the dimensions were slightly reduced at the two distant stations. Forty-two  $\frac{3}{4}$ -in. J-bolts, with the hooks under the lower reinforcing rods, were set in the concrete in a pattern to match the mounting holes in the bottom flanges of the pylons.

#### 2.4.5 Swept-wing Models

The swept-wing models were designed similarly to the structural-wing models but with increased length and a 35° sweepback. The swept-wing models were mounted at an 8 $\frac{3}{4}$ ° angle of incidence as cantilever wings (Fig. 1.3) and were instrumented to obtain bending, shear, and torsion stresses at three spanwise stations, as were the structural-wing models.

The construction of the swept wing was similar to that of the structural model, having the same section properties except for the two inboard bays. These two bays were heavily reinforced, and the root bay was cut to give the wing a 35° angle of sweepback. The root-fitting box was redesigned to allow for the sweepback but followed the same general design as in the structural model.

The swept-wing model used the same NACA 65<sub>2</sub>-015 airfoil with a 24-in. constant chord. The ribs and wing tip were placed perpendicular to the leading edge for ease of fabrication. The rib spacing was 12 in., and the two spars were located at 20 and 60 per cent of the chord. The spars were formed from 0.091-in. aluminum alloy.

The effective span of the swept wing and structural wing in the air stream was the same. Owing to the two added bays, however, the swept wing required the addition of fewer weights to reduce the stiffness to a desired value. The lead weights were grouped in three concentrated masses of 45, 45, and 90 lb at respective distances of 24 $\frac{3}{4}$ , 48 $\frac{3}{4}$ , and 91 $\frac{3}{4}$  in. from the root (Fig. 2.17) measured along the front spar. This addition of weight lowered the first bending frequency to approximately 3.8 cps and the second bending frequency to approximately 27.3 cps. The total weight of the wing was 250 lb.

#### 2.4.6 Supporting Structure for Swept-wing Models

The requirements for a rigid supporting structure also existed for the swept-wing

UNCLASSIFIED

models. At each site a single swept wing was mounted as a cantilever 10 ft above the grade level on a steel pylon similar to those previously described in Sec. 2.4.3. Cylindrical combination tension-compression struts were employed on the side opposite the wing model to provide additional rigidity. No tie rods were used on the swept-wing pylon.

#### 2.4.7 Reinforced-concrete Base for Swept-wing Models

A reinforced-concrete base was poured for each of the four swept-wing installations to anchor and support the pylon-and-wing assembly. The rectangular planform of the base measured 14 ft laterally and 10 ft longitudinally. The depth of the concrete varied from 3 ft thick at the nearest test site to 1 ft thick at the farthest test site. Two steel wide-flange beams (8WF67) were fastened to the top of the concrete with  $\frac{3}{4}$ -in. J-bolts hooked under the lower reinforcing rods within the concrete. The steel beams extended the entire width of the base and were utilized to distribute the loads into the concrete and also to maintain the high rigidity requirements for the supporting structure. The steel pylon and the cylindrical side bracing struts were bolted to the steel beams. The mounted wing-and-ptyon assembly is shown in Fig. 1.3.

#### 2.4.8 Small Airfoils

In order to observe the effectiveness of perforations in relieving the crushing effect of the pressure differential to which aircraft structures are subjected in the region of an atomic bomb burst, six small airfoils were installed at each of the four ranges. These airfoils were mounted as vertical cantilevers on top of the horizontal steel beams on which other test equipment was mounted. The six airfoils of 36-in. span and 18-in. chord located at each site consisted of three pairs with varying amounts of venting, one model of each pair being at 0° angle of incidence and the other member of the pair being at 22½° angle of incidence. One pair was unvented; the second pair was vented with three rows of  $\frac{1}{4}$ -in.-diameter holes, eight holes to the row, making the total open area in the upper and lower surfaces of

each of this pair 2.36 sq in.; and the third pair was vented with the same number and arrangement of  $\frac{1}{2}$ -in.-diameter holes, making the total open area of each of this pair 9.44 sq in. The ratios of vented area to internal volume were  $0.203 \times 10^{-4}$ , and  $81.9 \times 10^{-4}$ . The system of venting details of the small airfoils and the method of mounting are shown in Figs. 2.5, 2.9, 2.18, and 2.19.

#### 2.4.9 Small Cylinders

Similar observations were made of the effects of the differential pressures of the blast on small cylinders, both vented and unvented. These cylinders were fabricated of 0.051-in.-thick aluminum alloy. One pair of the cylinders was mounted at each test site. The vented cylinder was perforated with four axial rows of  $\frac{1}{2}$ -in.-diameter holes, four holes to the row, giving a total open area of 3.14 sq in. for an enclosed volume of 2.040 cu in. The ratio of vented area to volume was  $15.4 \times 10^{-4}$ . Installation and details of the vented and unvented cylinders are shown in Figs. 1.8, 2.9, and 2.20.

#### 2.4.10 Fighter Fuselage

Qualitative observations were made of the effects of the exposure of a conventional fighter fuselage section to thermal and nuclear radiation and blast pressures in the vicinity of an atomic bomb burst. The primary object of interest was the effect of the overpressures, together with thermal effects on the pressurized cockpit section and its transparent enclosure. The test articles selected were the joined nose and midsections of the F-80 aircraft. One fuselage section was installed at each of the four test sites. The fuselage was mounted horizontally on structural steel supports which were attached to heavy steel beams anchored to a reinforced-concrete base. The canopy was closed and locked, but the seals were not inflated. The tail section and the wings were not included in the installation. The noses of these fuselages contained a conventional radar dome consisting of cross-banded glass fabric laminated with polyester resin. The resin incorporated sufficient carbon to give the proper electrical properties, which in turn made the dome

UNCLASSIFIED

black in appearance. The test setup is shown in Figs. 2.2, 2.21, and 2.22.

#### 2.4.11 Fighter Wing Panels

Eight outer wing panels of fighter aircraft were exposed in pairs at each of the four ranges. The wings were standard stock items for the F-47 aircraft. The wings were mounted at the normal dihedral angle plus  $90^\circ$ , so that the installed position was nearly vertical. One of each pair of wing panels was vented internally in such a manner that pressure differentials were minimized within the wing. Wing guns were not installed, but the blast tubes were open on the leading edge. The wings were rigidly attached by means of steel brackets to heavy steel beams anchored to a reinforced-concrete base (Fig. 2.5). The rectangular surface of the base measured 16 ft laterally and 10 ft longitudinally, with the thickness varying (according to range) from 4 to  $2\frac{1}{2}$  ft.

#### 2.4.12 Airplane Control Surfaces

The effects of differential pressure due to an atomic bomb blast were observed on aircraft control surfaces, which are relatively fragile sections compared to the main structure of the aircraft. Both fabric-covered and metal-covered surfaces were exposed. The fabric-covered surfaces were B-17 elevators mounted vertically on tubular steel supports which were bolted to heavy steel beams anchored to a reinforced-concrete base (Figs. 2.23 to 2.27). The elevator consisted of an aluminum-alloy structure covered with aircraft fabric and doped with a silver finish. The part used was a standard B-17 elevator issued from Air Force stock. The metal-covered control surfaces consisted of standard Air Force stock ailerons and flaps mounted in a normal flight attitude ( $0^\circ$ ) on the trailing edges of the F-47 wing panels discussed in Sec. 2.4.11. Both the metal-covered and fabric-covered control surfaces were oriented parallel to the direction of blast propagation in order that any damage sustained would be due to differential-pressure crushing and not to side-on loading. The B-17 fabric-covered elevator was somewhat shielded from the high-temperature thermal radiation by the  $6\frac{1}{4}$ -in.-diameter supporting tube, as may be noted in Fig. 2.23.

### 2.5 APPARATUS AND INSTALLATION FOR MEASURING BLAST PHENOMENA

Although the original assumption was that the blast front (shock wave) would be practically vertical at the 10-ft elevation where the wing models were installed, it was later decided to attempt to measure the actual angle of attack. Owing to the time schedule, only existing available equipment could be considered for measuring the angle of attack. Three methods were used to measure this portion of the blast phenomena. These are described separately in subsequent paragraphs. A pressure-time survey was also made utilizing equipment that had been designed and used previously on other blast surveys.

#### 2.5.1 Vane-type Angle-of-attack Indicators

Two types of vane-operated angle-of-attack indicators were chosen to measure the angle of attack of the air mass behind the shock front. The first choice, installed at the Engebi site, utilized a split triangular vane mounted on a conical body containing the pivot point for the vane and the unbonded strain-gauge sensing element (see Fig. 1.20). This instrument, which was fabricated by Statham Laboratories, permits a minimum mass for the vane and has been tested for accuracy of response under supersonic conditions. The second choice, expedient because additional instruments of the first type were not available, consisted of a vane mounted at the rear of a slender body, pivoted at the center of mass (see Fig. 1.22). It is referred to as a "weather-vane-type angle-of-attack indicator." The pivot point, the cam movement, and beam on which strain gauges were bonded were contained in a cylindrical body with an elliptical nose. This instrument was installed at the Muzin site. Because of the relatively large mass of this instrument, its response to dynamic conditions is poor. The vanes or small wings of the split-triangular-vane instruments were restricted from flapping and were held in a position of  $0^\circ$  angle of attack by the installation of a fiberboard card which was easily removed by the first touch of the shock front. This improvisation was necessary to reduce the lag tendency and undesirable oscillations on first encounter with the high-velocity air. This temporary addition was



brought about by the late introduction of an instrument designed primarily for the measurement of the change in angle of attack while operating in a continuously moving air stream.

Although two different types of vane-type angle-of-attack indicators were utilized, one on Engebi and one on Muzin, their installations were similar. They were supported 65 in. above the ground by an arrangement of steel tubing welded to the large forward strut of the swept-wing pylon. Figures 1.21 and 1.23 illustrate the installation of the angle-of-attack indicators.

A third choice of angle-of-attack indicators was not employed because sufficient time was not available to design and complete the installation. However, this method will be described because of its inherently greater accuracy and its applicability to future tests of this nature. This method would consist in the fabrication of wedges in which differential-pressure gauges of the type used in the rigid wing would be installed, with orifices on opposite surfaces of the wedge. An arrangement of any number of these wedges at various angles of incidence over the expected range of angles would produce an equal number of data points at each interval of time, which would be plotted to indicate the angle of attack. By this method the frequency response is as high as the response of the pressure-sensing instruments. The multiple installation eliminates the necessity of correcting for air-mass velocity.

### 2.5.2 Optical-type Angle-of-attack Indicator (Fastax Camera)

An attempt was made to measure the angle of attack of the shock front in the vicinity of the aerodynamic and structural models located at the four selected islands. Because of an expected abrupt change of air pressure in the shock front, an attempt was made to use the principle of refraction to record an apparent discontinuity or break in a grid which was placed in the camera field. This phenomenon was photographed during a 10,000-lb high-explosive blast on 27 October 1950, at the Aberdeen Proving Ground. As shown in Fig. 2.28, at A and B there is a distinct discontinuity or break in ropes suspended in the camera field, which depicts the shock front. To photograph the shock front during the E-day bomb

test, a high-speed Fastax motion-picture camera with a 35-mm lens was used. The Fastax camera was operated at 2,000 frames per second. A protective canister for each camera was fabricated as shown in Fig. 2.29 for protection against the elements and possible flying debris. A sheet of plexiglas, covering the exit pupil of the canister, was automatically dropped out of the way before the camera started. On Engebi and Muzin the film was protected from radiation by placing lead bricks around the sides and over the top of the camera canister. On Engebi the lead bricks were stacked to form walls 8 in. thick on the end facing the shot tower, 6 in. thick on the top and the sides, and 4 in. thick on the end away from the tower. On Muzin the wall thickness was 6 in. on the end facing the shot tower and 4 in. on the top, sides, and the end away from the tower. Timing marks were placed on the film at  $\frac{1}{120}$ -sec intervals by the use of normal 60-cycle 110-v current supplied to the camera. A grid in the camera field was placed in front of the test articles or between the test articles and ground zero. The grid was constructed by suspending 1-in.-diameter 10-ft lengths of pipe on four cables as shown in Fig. 2.30. The four cables were mounted with a 1-to-3 slope from the ground to a B-17 elevator support and on a line which would project to ground zero. One pipe was plumbed and mounted at the midpoint of the sloping pipes, to be used as a vertical reference line. Two ping-pong balls were suspended between each of the grid pipes to give an additional indication of the passage of shock front and air movement.

Information was obtained previous to the atomic test that artificial lights would be required to light the target or grid on all test sites. This was accomplished by mounting two banks of high-intensity lights slightly below ground level. One bank consisted of six lights, the other of five. These 750-w lights were mounted and aimed as shown in Fig. 2.31.

Owing to the short running time of the camera at the desired speed, the starting time had to be carefully controlled. This was accomplished by using the -1 sec signal provided to start selected delay timers, which in turn, through a central control (see Figs. 1.10 and 2.32), started the Fastax camera 1.5 sec before the expected time of arrival of the shock front. In addition

to the above, the delay timers turned on the lights prior to camera starting time and turned off the camera and lights after the film was expended.

The location of camera and grid with respect to test articles is shown in Fig. 1.10. The angle-of-attack camera was mounted partly below ground to minimize possible bomb damage and was mounted at an angle so that the top of the picture frame was parallel with the grid which, as stated above, was set up with a slope of 3 to 1. The camera was mounted perpendicular,  $44\frac{1}{2}$  ft from the grid and 5 ft in front of the leading edge of the test articles. The two banks of lights used to illuminate the grid were mounted on a line between the grid and camera and approximately 24 in. from the grid.

### 2.5.3 Electronic-chronograph Method of Determining Angle of Attack

Owing to the possibility of irregular and unknown illumination adversely affecting the optical (photographic) method of angle-of-attack determination, it was decided to attempt to devise an additional method of making this measurement. It was necessary, because of the time limitation, to utilize available equipment for the supplemental method of angle-of-attack determination. The system selected incorporated mechanical diaphragm-type blast switches to trigger high-speed electronic counters to measure time differentials over a known geometric space pattern. A suitable electronic chronograph was found in the Potter Instrument Co. model 450, with slight modifications to provide for remote operation and to extend the total-count range. Since the electronic counters have no "memory," it was necessary to improvise a means of recording the indicated count prior to loss of electrical power to the system. A Speed Graphic still camera was employed to record the total count automatically.

The site on Muxin (8,878 ft from ground zero) was selected for the installation of this equipment. Four counters were in satisfactory working order just prior to E-day. The space pattern was established so that a single blast switch would start all the counters simultaneously, and four blast switches mounted on a vertical pole 38 ft downwind from the starting switch would stop individual counters. The starting switch was located 10 ft above the

ground. The stopping switches were located at 4, 10, 13, and 19 ft above the grade level. The installation of the common starting switch is shown in Fig. 2.33; the installation of the individual stopping switches is shown in Fig. 2.34. The two switches at the 10-ft elevation furnished the velocity component. The blast switches were set to trigger the counters at an overpressure of 1.8 in. of water (0.09 psi). This differential was considered necessary to prevent premature contact and triggering due to the prevailing climatic winds (up to 20 and 30 knots). (The predicted blast overpressure for this site was 4.2 psi.) Since continuous power could not be guaranteed from the central station following the detonation of the bomb, the power required for operation of the electronic counters, relays, and the two delay timers was obtained from a 25-kw 60-cycle 117-v portable generator (see Fig. 2.37). One delay timer was utilized to reset the electronic counters to zero just prior to shot time, and the other timer was set to trip the camera shutter after the blast wave had passed the test site. Time signals were furnished from a central control to operate relays on the site at -30 min, -5 sec, and -1 sec. The -30 min signal was used to turn on the electronic counters for warmup. The -5 sec signal triggered the delay timer for automatically resetting the counters to zero, and the -1 sec signal tripped the delay timer that controlled the camera-shutter solenoid. Triggering voltages for the electronic counters and for the camera solenoid were from dry-cell batteries. The electronic counters, signal relays, delay timers, and Speed Graphic camera were housed in the reinforced-concrete instrument room provided primarily for other instrumentation. Figure 2.35 shows the arrangement of the electronic counters as viewed from the recording-camera position (see also Fig. 2.36). The circuit diagram for automatic operation of the electronic-chronograph angle-of-attack system is shown in Fig. 2.37.

### 2.5.4 Overpressure Variation with Time: Measuring Apparatus and Installation

Interferometer-type pressure-time gauges, frequently termed "Buck gauges," were utilized to measure the actual overpressures acting on the test articles of this project. This gauge is

UNCLASSIFIED

of comparatively new design, utilizing a modified 35-mm Fastax high-speed camera to record the interference fringes produced by pressure acting on a thin, circular, optically plane fused-quartz diaphragm attached to a fixed, heavier, slightly concave, and partly mirrored quartz backing plate; the similar area on the thin diaphragm is completely reflecting. A monochromatic light (5,461 Å) is contained within the instrument and is directed through the backing plate to produce interference rings over the mirrored area. The general arrangement of the interferometer head is shown in Fig. 2.38.

The circular interference fringes are viewed by the camera through a slit, giving the appearance of a transverse series of light and dark spots, the exact displacement being a function of the pressure acting on the diaphragm. In normal operation the film is set in motion at a high rate of speed, and the spots are recorded as a series of lines (no camera shutter). As the pressure on the diaphragm is varied, the lines (spots) move laterally on the film. The total number of lines observed on the film at any instant, subtracted from the total number of lines observed with only atmospheric pressure acting on the diaphragm, is proportional to the pressure at that time. The time base was supplied by a 500-cps crystal-controlled oscillator used in conjunction with a small argon lamp to

produce known-frequency timing marks along the edge of the film. Power for all phases of the gauge operation was supplied from dry-cell batteries. Thus the unit was entirely self-sufficient. Delay-timer devices were necessary to actuate the gauges at the proper interval after the bomb detonation to record the arrival of the blast front and the history of the subsequent pressure variation. A total of 14 interferometer gauges was installed to make a pressure survey for Project 8.2. Bracketing of the individual test sites was accomplished by installing interferometer gauges in front of and behind the test installation, except at Engebi where only the two forward gauges were installed. These were displaced laterally at the forward edge of the site. Since the bracketing was very close compared to the range from the shot tower, pressure variations between gauges were expected to be small, and hence the malfunctioning of a gauge would not result in a complete loss of data at the test site since a weighted average could be used to compensate for the loss of results from a single gauge. All gauges were installed so that the quartz diaphragms were at the ground level, and the remainder of the gauge was enclosed in a steel box below the ground line. Lead bricks were used around the steel boxes to protect the film from radiation at the nearest test site. The locations of the individual gauges at each test site are shown in Fig. 2.39.

UNCLASSIFIED

[REDACTED]

## Chapter 3

# Instrumentation of Test Articles

### 3.1 GENERAL PROBLEM OF INSTRUMENTATION

In the original planning for this project the instrumentation problem consisted in the selection of measuring elements and an automatic recording system for recording the data measured by the elements. It was evident at the initiation of this project that approximately fifty assorted types of measurements would be required at each test site. A partial listing of the quantities measured is shown in Table 3.1.

The operational details included a number of abnormal requirements for the instrumentation. It was determined that the recording system and other elements of the instrumentation would need to be installed in a partially buried instrument house to the rear of the test articles. The sensing element or measuring device would have to be installed in the test articles, and information measured therefrom would have to be transmitted over a distance of approximately 90 ft to the instrument house. The entire instrumentation system had to operate automatically approximately 24 hr after the evacuation of all personnel. Thus it was necessary to provide a simple and reliable system that would energize all the elements of the instrumentation, initiate the recording cycle, and terminate at the conclusion of the record.

The necessity of maintaining and operating the instrumentation under very severe field conditions further emphasized simplicity, not only of each item of equipment but of the overall instrumentation plan as far as possible. Because of the geographic location of the test, it was necessary that the equipment be designed to operate at high temperatures, under environmental conditions of high humidity, and

in the presence of severe corrosive media and fungi. In the selection of the instrumentation for this test it was necessary to consider very carefully the ability of the instruments to sense and record, in a very brief time interval, the required data while being subjected to both severe shock and vibration. This was extremely important because of the nature of the shock and the fact that the shock effects on the equipment were likely to obscure the data at precisely the critical time.

All these requirements led to the selection and development of a basically electronic measuring and recording system.

### 3.2 RECORDING SYSTEM

The selection of the appropriate technique of recording for this project required considerable research. Initial advice indicated that the present standard method of recording, by means of bifilar-type galvanometers, would not give satisfactory service owing to the severe shock conditions. It was therefore necessary to select a recorder which was inherently impervious to shock. An expedient selection in this regard was the magnetic-tape recorder. A prototype of such a recorder had been recently completed by the Webster-Chicago Corp., and preliminary tests indicated several desirable features applicable to this project. Some of these features included sufficiently fast response characteristics, satisfactory operation with resistance-type sensing instruments, and good performance under adverse climatic conditions. Furthermore this type of recording system already had been selected and its procurement had been initiated for Project 8.1 and

TABLE 3.1 NUMBERING CODE AND DESCRIPTION OF THE QUANTITIES  
MEASURED BY EACH INSTRUMENT CHANNEL\*

Location	Number	Quantity Measured
Left-hand structural wing, Series -01:		
Station 1,† outboard	1	Bending
Station 1, outboard	2	Torsion
Station 1, outboard	3	Shear
Station 2, intermediate	4	Bending
Station 2, intermediate	5	Torsion
Station 2, intermediate	6	Shear
Station 3, inboard	7	Bending
Station 3, inboard	8	Torsion
Station 3, inboard	9	Shear
Left-hand rigid wing, Series -02:		
Strain measurement on spar extension	10	Drag
Strain measurement on spar extension	11	Lift
Strain measurement on spar extension	12	Moment
5% chord	13	Differential pressure
10% chord	14	Differential pressure
15% chord	15	Differential pressure
20% chord	16	Differential pressure
40% chord	17	Differential pressure
80% chord	18	Differential pressure
Right-hand rigid wing, Series -03:		
5% chord	19	Differential pressure
10% chord	20	Differential pressure
15% chord	21	Differential pressure
20% chord	22	Differential pressure
40% chord	23	Differential pressure
80% chord	24	Differential pressure
Strain measurement on spar extension	25	Drag
Strain measurement on spar extension	26	Lift
Strain measurement on spar extension	27	Moment
Right-hand structural wing, Series -04:		
Station 4, inboard	28	Bending
Station 4, inboard	29	Torsion
Station 4, inboard	30	Shear
Station 5, intermediate	31	Bending
Station 5, intermediate	32	Torsion
Station 5, intermediate	33	Shear
Station 6, outboard	34	Bending
Station 6, outboard	35	Torsion

UNCLASSIFIED

TABLE 3.1 (Continued)

Location	Number	Quantity Measured
Station 6, outboard	36	Shear
Station 10,† front spar web	37	Temperature
Station 11, inside skin surface	38	Temperature
Station 12, outside skin surface	39	Temperature
Swept wing, Series -05:		
Station 7, inboard	40	Bending
Station 7, inboard	41	Torsion
Station 7, inboard	42	Shear
Station 8, intermediate	43	Bending
Station 8, intermediate	44	Torsion
Station 8, intermediate	45	Shear
Station 9, outboard	46	Bending
Station 9, outboard	47	Torsion
Station 9, outboard	48	Shear
Front swept-wing-pylon cylindrical strut	41A‡	Angle of incidence to the ground of high-velocity air following blast wave

\* Number code and description were identical for each of the four test sites.

† Stations 1 to 9 are the spanwise stations for the structural and swept wings (Figs. 2.15 to 2.17).

‡ For stations 10 to 12, the locations of the temperature gauges are shown on Figs. 2.16, 3.9, and 3.10.

§ Installed only on Engebi and Muzin (Figs. 1.20 to 1.23).

**Program 3.** The procurement of this type of instrumentation therefore offered many logistic and operational advantages. Ten recorders, two for each test site and two spares, were procured from the Webster-Chicago Corp. and were used as the recording system for Project 8.2.

The magnetic-tape recording system operates on a phase-modulation principle. A 3,750-cps signal is impressed on a Wheatstone bridge sensing element, and the output signal is added to a voltage at quadrature to produce a signal which is shifted in phase with respect to a 7,500-cps reference signal. These signals are combined and then recorded as a single impression on magnetic tape to obtain one channel of data. There are 24 such channels on each magnetic tape used in this system.

Physically the recorder consists of the two units shown in Fig. 1.14. The first of these is

the amplifier unit, which contains the individual gauge circuits with the necessary controls for balancing and adjusting each circuit. The second unit is the recorder, which consists of a tape-transport mechanism, power supply, and control circuits.

The amplifier consists of the gauge-power-source generators and power components common to all channels, together with 24 separate plug-in amplifiers. These plug-in amplifiers are identical. They are standard amplifiers which provide a linear output response to frequencies from 0 to 500 cps. Controls are provided on the front surface of all amplifier units for resistance and capacitance balancing. This permits adjustment for variation in gauges and connecting circuits.

The recorder contains the power and starting circuits, along with the tape-transport mechanism. The tape is made of a plastic,

UNCLASSIFIED

UNCLASSIFIED

coated on one surface with ferric oxide. The tape is contained on a reel and is driven past the recording heads at a speed of approximately 24 in./sec. An automatic timer switch is provided to shut off the recorder at the end of a preset period of time. A centrifugal switch is provided which will turn off the recorder when the tape has been completely exhausted on the supply spool. Two means of starting the recorder are provided. By means of one receptacle, initiation of the recording cycle is accomplished by shorting two pins; through the other receptacle, the cycle is initiated by 24-v direct current applied from an external source.

The records obtained at the time of specific measurement, as discussed earlier, are in the form of an invisible magnetic orientation on the plastic tape. A two-channel reproducing system was used for transcribing the magnetic impressions on the tape into a visual presentation. The tape is transported through a recording head assembly similar to those in the recorder. In this head assembly the magnetic impressions are reproduced as electrical signals equivalent to the original signals used to form the impression. Two of the reproduced signals are selected for visual presentation and are transformed by amplifiers into output signals which are linear functions of the unbalance of the original Wheatstone bridge sensing element. These output signals are applied either to an oscillographic recorder employing bifilar-type galvanometers or to a chart recorder of the direct-inking type, thereby presenting visually the measured quantity as a function of time. The recorder was designed to have a linear signal output through the visual reproducing system up to approximately 140 per cent of a known reference signal, defined as the "calibrate" signal. For a typical gauge installation for the measurement of the bending moment, the 140 per cent signal level occurred in the region of the elastic limit of 24 ST aluminum alloy. The output of other gauge installations also produced a linear signal output to at least 140 per cent of the calibrate signal.

### 3.3 SELECTION OF SENSING ELEMENTS FOR WING MODELS

Strain gauges used on the test articles to measure lift, drag, moment, bending, shear,

and torsion loads were Baldwin-Southwark AX-5, A-7, and A-13 gauges, having a nominal resistance of 120 or 350 ohms. These gauges were selected because they are small and thermally stable and because they were known from previous experience to be very reliable. It was known from Operation Sandstone that the climatic conditions at the test site would have an adverse effect on strain gauges that were not given a protective coating. A contract was awarded to Purdue University to investigate commercial strain-gauge adhesive and protective coatings under conditions of high temperature, high humidity, and salt spray. From the tests conducted by Purdue University it was determined that gauge applications using General Radio Co. cement with a protective coating of Petrosene wax would endure the conditions of high temperature, high humidity, and salt spray better than applications using the other combinations of adhesives and protective coatings which were tested. All strain gauges installed in the test articles were applied and protected with these materials. The function and location of the various strain-gauge bridge circuits for each wing model are described in Sec. 3.4.

An extensive search was made for pressure transducers adequate to measure the differential-pressure distribution over the rigid-wing models. It was originally intended to use resistance-bridge-type sensing elements with resistance unbalance directly proportional to the imposed pressures and with negligible reactance unbalance so that complicated phase-shift problems would not exist when the sensing elements were employed with a phase-sensitive recording system. Several prototypes of such resistance-bridge sensing elements were constructed and submitted for test by leading instrument manufacturers. None of these prototypes satisfied all test requirements before the deadline date for awarding a production contract. Under these circumstances a pressure-sensing element employing a variable-reluctance principle, necessitating the use of an electrical coupling unit, was selected after being submitted for test by the Wiancko Engineering Company, Altadena, Calif. These transducers were of the differential type capable of measuring pressure differentials to 10 psi. The response to pressure was linear within  $\pm 3$  per cent up to 500 cps, with a maxi-

UNCLASSIFIED

to eliminate spurious signals caused by local buckling. Figure 3.2 shows the schematic wiring diagram for the bending, torsion, and shear channels. Figures 2.15 to 2.17 present the overall physical and electrical layout and numbering code for the structural and sweep wings.

### 3.4.2 Rigid-wing-model Instrumentation

The total lift, drag, and moment forces acting on the rigid wings were measured by an integral weighing system utilizing strain gauges mounted on the wing-spar extensions. The wing-spar extensions were attached to a balance system (Fig. 2.11) designed to eliminate restraint against rotation at the front spar and to furnish pin-ended supports at each end of the four spars to provide reaction against chordwise and normal force components. With this system the normal force component was measured as the output signal provided by a Wheatstone bridge composed of four A-13 gauges mounted to measure the strain at the top and bottom of the front spar extensions at the points of maximum stress. Inasmuch as the rear spar extensions comprised the only restraint against rotation of the rigid wing about an axis through the center of the front spar, the bridge composed of the gauges on the rear spar extensions provided an output signal proportional to the moment about this axis. The chordwise force component was measured by the output signal of a similar gauge installation on the front and rear surfaces of the front spar extensions. Although the rear spar also provided restraint against chordwise force components, the strain resulting in the front spar extensions provided a linear output signal accurately proportional to the chordwise force components applied to the wing.

Strain gauges were installed at each station to measure bending moment, torsion, and transverse shear. All strain gauges were installed on the front and rear spars since, by design, these were the primary load-carrying members for both wings. The strain-gauge arrangement on the wing spars was similar for all stations on both the structural and the swept wings. Three types of strain gauges were employed: the Baldwin-Southwark A-13, 300-ohm; AX-5, 120-ohm; and A-7, 120-ohm gauges. The last two types of gauges were used to produce low-resistance bridges for greater sensitivity where the test loads were expected to be small.

The measurement of the chordwise differential-pressure profile at midspan of the rigid wing was accomplished by the installation of the Wiancko pressure gauges within the rigid wing. Pressure orifices of  $\frac{1}{8}$ -in. diameter were drilled normal to the top and bottom surfaces of the wing at the 5, 10, 15, 20, 40, and 80 per cent chord stations. High-pressure tubing connected these orifices to the pressure chambers of the Wiancko gauges, except at the 40 per cent chord station where the wing structure permitted direct entry of the orifices to the pressure chambers (see Fig. 3.3). Measure-



ment of the differential pressures at the six chordwise stations as a function of time provided an alternate method of obtaining total lift, drag, and moment forces. Figures 3.4 and 3.5 show the instrumentation diagrams for the rigid wings.

### 3.5 RIGID- AND STRUCTURAL-WING MODELS: CAMERA INSTALLATION

In order to record any blast damage that might occur to the rigid- and structural-wing models and to photograph any debris hitting the models which could be correlated with any erratic readings of the recording instruments within the models, a high-speed Fastax motion-picture camera with a 35-mm lens was used. The Fastax camera was operated at 500 frames per second. The camera was mounted and protected in a similar manner as described in Sec. 2.5.2.

Information obtained before the atomic test indicated that artificial lights would be necessary. Seven high-intensity lights mounted slightly below ground level and in front of the rigid- and structural-wing models were installed as shown in Figs. 1.2 and 3.6. The lights and camera were turned on and off at the proper time through the use of the same type of electrical control as described in Sec. 2.5.2.

The location of the camera with respect to the rigid- and the structural-wing models is shown in Fig. 1.10. The camera was mounted 33 1/4 ft in front of the leading edge of the base of the pylons which supported the rigid- and structural-wing models, that is, between the wing models and ground zero.

### 3.6 TEMPERATURE-MEASURING DEVICES AND INSTALLATION

#### 3.6.1 Maximum Temperature Survey: Temp-Tapes

A device was developed for measuring peak temperatures, in either transient or steady state, by C. Fredericks of the Wright Air Development Center (WADC) for this temperature survey. This device, which is referred to as a "Temp-Tape," essentially consists of a series of low-melting-point alloy foils held in place on the adhesive side of a heat-resistant tape strip.

It may be installed at any convenient time prior to the temperature rise under investigation and can be examined for results at any convenient time after cooling.

The design of the Temp-Tape used by Project 8.2 consisted of two small strips of alloy foil, about 0.0025 in. in thickness, superimposed one on the other. The two strips are sandwiched between two sheets of aluminum foil or between a sheet of aluminum foil and one of thin paper, and this entire assembly is attached to the adhesive side of a strip of temperature-resistant adhesive tape (Fig. 3.7). The tape serves a dual purpose: it affords a means of holding the foil sandwich together and allows a method of attaching the foil sandwich to the surface to be measured. A temperature range of 117 to 511°F was covered in distinct steps of melting points, with a differential of approximately 20°F.

The Temp-Tape is a convenient device for measuring the maximum temperature attained on the back side (the side away from the radiation source) of a sheet-metal or opaque structure. However, when Temp-Tapes are installed on the front side (that is, facing the radiation source) or the back side of a transparent structure, the temperature measured is questionable owing to the influence of reflection and absorption of radiation by the gauge and by the transparent material prior to reaching the gauge and owing to other similar phenomena. Although the results from the latter type of installation are questionable, Temp-Tapes were utilized in this type of application. The Temp-Tapes are attached to the surface in a manner similar to that in which a Band-Aid would be applied. After the test the Temp-Tape is removed, and the protective covering is cut away from the alloy foil. The foil is then examined by eye or with the aid of a microscope for the melting and fusion, and a comparison is made with the calibration curves for the peak temperature attained.

Each of the four island test sites was instrumented for a temperature survey in exactly the same manner. An attempt was made to install the Temp-Tapes in positions such that each test article could be surveyed for maximum temperatures.

The test articles were instrumented with Temp-Tapes at the following locations:

1. F-80 fuselage:
  - (a) Aft of left inside sidewall of left-hand intake duct
  - (b) Inside windshield side windows
  - (c) Inside left nose access door
  - (d) Inside windshield glass
  - (e) Inside top of canopy plexiglas
  - (f) Forward face of nose compartment aft of wall
2. F-47 wing:
  - (a) Inside top wing surface in wheel-well area, first and second bay aft of bulb angle stringer
  - (b) Forward face of rear auxiliary spar in wheel well
  - (c) Rear face leading edge spar, wheel-well area
  - (d) Inside bottom wing surface, in aileron-inspection doors
  - (e) Outside top surface, just inboard of gun-inspection doors
3. Small airfoil sections, 4 in. aft of leading edge
4. Small cylindrical sections, 6 in. aft of leading edge
5. Rigid-wing model, inside of bottom skin, just aft of forward spar
6. Rigid-wing model, aft of face of forward spar
7. Structural-wing model, inside of bottom skin, just aft of forward spar
8. Structural-wing model, aft of face of forward spar
9. B-17 elevator:
  - (a) Inside leading edge fairing, 6 in. aft of leading-edge vicinity of tab-inspection door
  - (b) Inside of top surface on fabric, vicinity of tab-inspection door, placed at about 40 per cent chord

### 3.6.2 Temperature Variation with Time: Electrical-resistance Gauges

Only 3 of the 48 channels per site were assigned to measure the variation of temperature with time. With this limited number of channels the locations of measurement points were selected to obtain the best possible survey of the temperature conditions most likely to affect the structural characteristics of aircraft wings. This was accomplished by locating the temperature-measurement points on a structural

wing (right hand when facing tower) at each test site as follows: The lower external skin surface just aft of the leading edge, a corresponding point on the internal skin surface, and the forward surface of the front spar web.

In order to measure temperatures on both the inside and outside surfaces of the test articles, it was necessary that the temperature-sensing elements used on the outside surfaces should not affect the air flow around the test articles and that the sensing elements used on the inside surfaces should be easily mounted within a limited working space. Both types of gauges were also required to be durable, highly sensitive, and of matching impedance for the Webster recorder. The Trans-sonic S-101 surface-temperature gauge fulfilled the requirements for the internal gauge since it was easily installed with screws, but it was too large for external use. The Ruge-de-Forêt Stikon resistance thermometer fulfilled the requirements for the outside gauge since it had an applied thickness of only 0.005 in. Both gauges fulfilled the electrical requirements for this test.

Care was taken to ensure that the internal gauges were securely mounted in contact with the surface. In addition, silicon grease was placed between the gauges and the surfaces as recommended by the manufacturer for better heat conduction. The external-surface gauges were cemented to the wing with bakelite cement at 250 to 275°F temperatures, under 100 to 200 psi pressure. Leading-edge contour forms and clamping fixtures were designed and fabricated for this operation. After the gauges were affixed, holes were drilled through the wing skin to provide entrance for the gauge leads into the wing. The gauges were then covered with aluminum paint mixed to match the color of the wing models (Fig. 3.8).

Since both gauges were of the resistance type suitable for the active arm of a Wheatstone bridge, the completion of each bridge with three inactive arms was required. Trans-sonic 16-5 balancing bridges were used to complete the Trans-sonic gauges, and the bridges for the Stikon gauges were fabricated from resistance elements. The three arms required for completion of each bridge were not appreciably affected by changes in temperature. In addition, this part of each bridge was placed inside the

[REDACTED]

right-hand pylon for protection against thermal radiation.

Figure 3.10 shows the general location of the temperature gauges in the leading-edge section of the second bay of the right-hand structural wings. Figures 2.16 and 3.9 show the exact location of the gauges in this section. In Fig. 3.9 the distance from the right rib to the nearest edge of the external-surface gauge, station 12, was  $1\frac{1}{2}$  in. The corresponding distance to the internal-surface gauge, station 11, was 4 in. The spar-web gauge, station 10, was located 6 in. from the right rib. The design of the gauges prevented their emplacement on small

radii of curvature; however, the internal- and external-skin-surface gauges were located as close as possible to the leading edge, dimensionally,  $1\frac{3}{4}$  in., measured from the theoretical leading edge along the airfoil contour to the forward edge of the gauge. The angles of incidence of the thermal radiation on the external-skin gauge were  $24.6^\circ$  and  $25.6^\circ$ , respectively, for Muzin at 6,878 ft and for Teiteir at 12,000 ft. Since temperature is affected by the normal component of the thermal radiation, which varies as the sine of the angle of incidence, the assumption of  $25^\circ$  for both sites is sufficiently precise for calculation.

## Chapter 4

## Calibration

In order to achieve the maximum accuracy of the quantitative results obtained from the various instrumented test components, calibration procedures were established and conducted to determine the specific response to a known forcing function. Details of the calibration methods used for the different types of instrumentation are given in this chapter.

For those parts of the calibration involving the Webster recorder, the test points for the calibration curves, plotted as a function of applied load vs visual signal deflection in terms of percentages of the calibrate signal, closely followed straight-line patterns. Accordingly, all calibration curves were plotted as the best straight lines through the test points. The applied load required to produce a visual signal deflection equal to the deflection produced by the calibrate signal was defined as the calibration factor. These calibration factors are listed in Table 4.1.

## 4.1 RIGID-WING MODELS

The instrumentation of each of the rigid-wing models was calibrated for lift, drag, and moment forces in a specially designed jig constructed of steel I-beams. This jig was made very rigid to minimize distortion at the support points which held the chord plane of the model level for application of the calibration forces.

The lift calibration force was applied by means of lead-shot bags distributed on the model so that a uniform spanwise force acting downward through the 25 per cent chord line was produced. This force was applied in 250-lb increments from 0 to 1,500 lb.

The drag calibration force was applied horizontally through a system of three loading

trays, each supported by a cable led over a pulley to a bridle that rested against the leading edge of the model. The bridle design and spacing thus produced a distributed spanwise force acting in the chord plane of the model. This drag force was applied in 30-lb increments from 0 to 10 lb.

The moment calibration force was applied at midspan by means of a jig that clamped around the wing. This jig had two arms, one extending forward of the leading edge and one extending aft of the trailing edge. A cable fastened to the front arm led over a pulley to a loading tray. A similar loading tray was attached directly to the aft arm so that equal loading of the trays would produce a pure coupling force. This force was applied in 500 in.-lb increments from 0 to 3,000 in.-lb.

A 5-sec magnetic-tape recording of the drag, lift, and moment channels was made for each increment of the respective forces. Calibration curves of force vs deflection in terms of the percentage of the reference calibrate signal were plotted. These curves were approximate straight-line functions; similar gauge installations had similar calibration curves so that a limited number of calibration curves were sufficient for the reduction of drag, lift, and moment data.

The differential-pressure gauges for the rigid wings were calibrated prior to installation in the wings. Twelve gauges were attached to a pressure block equipped with a pressure-inlet tube and a mercury manometer. One pressure inlet of each gauge and of the manometer was left open to atmospheric pressure. After the zero and reference-calibrate-signal recordings were made, compressed air was allowed to flow through the pressure-inlet tube into the

TABLE 4.1 CALIBRATION FACTORS AND MAXIMUM ERRORS FOR INTELLIGENCE CHANNELS BY TEST SITE

Channel*	Calibration Factor†	Maximum Error by Percentage of Test Points			Unit
		99.7%	95%	67%	
E1	$32 \times 10^3$	3,200.0	2,100.0	1,100.0	in.-lb
E4	$32 \times 10^3$	3,200.0	2,100.0	1,100.0	in.-lb
E7	$32 \times 10^3$	3,200.0	2,100.0	1,100.0	in.-lb
E9	$39 \times 10^2$	390.0	260.0	130.0	lb
E11	$13.3 \times 10^2$	130.0	89.0	44.0	lb
E13	$58.9 \times 10^{-1}$	0.59	0.39	0.20	psi
E15	$54 \times 10^{-1}$	0.54	0.36	0.18	psi
E16	$54 \times 10^{-1}$	0.54	0.36	0.18	psi
E17	$54 \times 10^{-1}$	0.54	0.36	0.18	psi
E18	$44.2 \times 10^{-1}$	0.44	0.29	0.15	psi
E19	$54 \times 10^{-1}$	0.54	0.36	0.18	psi
E20	$49.1 \times 10^{-1}$	0.49	0.33	0.16	psi
E21	$54 \times 10^{-1}$	0.54	0.36	0.18	psi
E28	$-35.8 \times 10^3$	1,800.0	1,200.0	600.0	in.-lb
E31	$-32 \times 10^3$	3,200.0	2,100.0	1,100.0	in.-lb
E34	$-32 \times 10^3$	3,200.0	2,100.0	1,100.0	in.-lb
E40	$51.4 \times 10^3$	5,200.0	3,500.0	1,700.0	in.-lb
E41A	-10	2.9	1.9	0.97	°F
E43	$32 \times 10^3$	3,200.0	2,100.0	1,100.0	in.-lb
E45	$28 \times 10^3$	280.0	190.0	93.0	lb
E46	$-32 \times 10^3$	3,200.0	2,100.0	1,100.0	in.-lb
E48	$28 \times 10^3$	280.0	190.0	93.0	lb
S4	$32 \times 10^3$	3,200.0	2,100.0	1,100.0	in.-lb
S11	$11.75 \times 10^2$	110.0	72.0	36.0	lb
S14	$54 \times 10^{-1}$	0.54	0.36	0.18	psi
S15	$44.2 \times 10^{-1}$	0.44	0.29	0.15	psi
S16	$-54 \times 10^{-1}$	0.54	0.36	0.18	psi
S17	$58.9 \times 10^{-1}$	0.59	0.39	0.20	psi
S19	$54 \times 10^{-1}$	0.54	0.36	0.18	psi
S20	$-88.5 \times 10^{-1}$	0.66	0.44	0.15	psi
S22	$-49.1 \times 10^{-1}$	0.49	0.33	0.16	psi
S30	$-38.75 \times 10^2$	390.0	260.0	130.0	lb
S31	$32 \times 10^3$	3,200.0	2,100.0	1,100.0	in.-lb
S37	$11.27 \times 10$	6.3	4.2	2.1	°F
S38	$11.27 \times 10$	6.3	4.2	2.1	°F
S39	14.98	7.9	5.2	2.6	°F
S43	$32 \times 10^3$	3,200.0	2,100.0	1,100.0	in.-lb
S46	$32 \times 10^3$	3,200.0	2,100.0	1,100.0	in.-lb

TABLE 4.1 (Continued)

Channel*	Calibration Factor†	Maximum Error by Percentage of Test Points			Unit
		99.7%	95%	67%	
Q28	$32 \times 10^3$	3,200.0	2,100.0	1,100.0	in.-lb
Q39	14.98	7.9	5.2	2.6	°F
Q40	$51.4 \times 10^3$	5,200.0	3,500.0	1,700.0	in.-lb
Q43	$32 \times 10^3$	3,200.0	2,100.0	1,100.0	in.-lb
P	None				

\* Letters preceding the channel numbers indicate test sites: E, Engebi, 4,020 ft; S, Muzin, 6,878 ft; Q, Teiteir, 12,000 ft; P, Bokon, 16,614 ft.

† After reduction of test-data-signal deflections to percentages of calibrate-signal deflection, multiplication of the percentage values by the calibration factor converted the test data into units corresponding to the measured function. (The calibration factors may be applied to interpretation of the records presented in Figs. 4.1, 5.61, and 6.1 to 6.10.)

pressure block. The signal mechanism of each of the 12 gauges was deflected by this increase in differential pressure, and the electrical output from each gauge was recorded for 5 sec on the magnetic tape. The differential-pressure reading of the manometer was noted for each pressure increment applied. After the calibration had been completed, the deflections on the visual reproduction of the magnetic tape were compared with the manometer readings. Graphs of trace deflection in terms of percentage of reference calibrate signal vs manometer reading in inches of mercury were made. These plotted calibration curves were approximate straight-line functions. The gauges were sufficiently similar in electrical output to permit the use of only a few composite calibration values for the reduction of test data.

#### 4.2 STRUCTURAL- AND SWEEP-WING MODELS

The instrumentation of each of the structural and the swept wings was calibrated for bending moment, shear, and torsion. Each wing was supported as a cantilever structure by attaching the root-fitting box to a rigid steel framework.

The calibration forces for the three measured quantities were applied at the same time by the proper choice of six load points for each wing. Three of these points were located on the front spar and three on the rear spar. Three spanwise

load stations were chosen in such manner that a load station was located slightly outboard of each of the three instrumented stations. Thus a load point was located on each spar at each station. The structural-wing spanwise load points were  $31\frac{1}{2}$ ,  $52\frac{1}{2}$ , and  $73\frac{1}{2}$  in. from the root (Figs. 2.15 and 2.16). The swept-wing spanwise load points were  $20\frac{1}{2}$ ,  $44\frac{1}{2}$ , and  $86\frac{1}{2}$  in. from the root, measured along the 50 per cent chord line (Fig. 2.17).

The calibration forces were applied in 200-lb increments at each of the load points in succession. These forces were applied upward on the lower surface of the wings by means of a dynamometer and a loading jack. The jack and dynamometer were placed directly under one of the load points of the wing, with the jack resting on the dynamometer platform. The dynamometer scale was adjusted to compensate for the weight of the jack. The jack pad was then raised to the load point to apply upward forces, the magnitudes of which were read on the dynamometer scale.

For each load increment at each load point a 5-sec magnetic-tape recording was made of all the bending, shear, and torsion channels in the wing. The bending moment, shear, and torsion at each instrumented station were also calculated for each load increment at each load point. Thus with the visual reproduction of the magnetic-tape record a graph of bending moment, torsion, and shear vs the percentage of

[REDACTED]

calibrate signal could be made for each instrumented station. Since the wings were not loaded beyond the elastic limit and since the strain gauges and the recorders were designed to yield linear signals up to that limit, the plotted curves were approximately straight-line functions. These functions were found to be identical, within the limits of accuracy of the magnetic-tape recorder, for similar channels; therefore one function could suffice for several such channels. This was to be expected since all structural and swept wings were of like design and construction and since the gauge installations and calibration loadings were similar in many cases.

#### 4.3 CALIBRATION OF TEMPERATURE GAUGES

##### 4.3.1 Temp-Tape Maximum Temperature Survey

During the development stage of the Temp-Tape temperature-measuring devices, it was discovered that the melting points of the low-temperature alloys did not appear to correspond to the temperatures at which fusion of the alloy foils occurred. This indicated that a comprehensive calibration program would be necessary for accurate temperature determination. Accordingly the Engineering Department of the University of California at Los Angeles undertook the task of calibrating the instruments.

Before the calibration of the actual Temp-Tape was performed, a determination of the actual melting points of the alloys was made. It was found that each of the 14 alloys involved had sharp, although not precisely eutectic, melting points, the largest melting range being about 3°F.

The calibration was made by securing the Temp-Tape to a piece of sheet aluminum, irradiating the reverse side of the sheet with photoflood lamps, and checking the pieces of alloy foil for melting and fusion.

All temperature measurements in the calibration runs were made with the aid of thermocouples whose signals were amplified by d-c amplifiers and continuously recorded. The surface of the plate which was to be irradiated was blackened with dull-black brushing lacquer in order to increase its absorptivity. The radiating source was composed of two special 750-w

photoflood lamps. A thermocouple was welded to the surface of the plate in order to record the plate temperature.

In general, successive runs for any one alloy were taken by increasing the maximum plate temperature in 5 to 10°F increments. After each run the Temp-Tape was disassembled, and the amount of melting and fusion of the foils was noted. A calibration curve for each Temp-Tape was thus constructed, plotting percentage melting and percentage fusion against temperature in degrees Fahrenheit.

##### 4.3.2 Electrical-resistance Gauges and Temperature Variation with Time

The sensing elements of the BN Stikon and the Trans-sonic 16-1 temperature gauges and their respective balancing bridges were sufficiently precise to permit calibration of only one of each type of gauge. One of each type of the sensing elements of these gauges was placed on an aluminum plate, simulating the actual installation on a wing surface. This calibration sample was then placed in a small electric oven. The leads from the sensing elements to the balancing bridges outside the oven and the leads from the bridges to the magnetic-tape recorder were of the same length as those used for the actual test articles. Temperature readings during calibration were taken with a mercury thermometer extending into the oven.

Prior to calibration, zero- and reference-calibrate-signal recordings were taken on the magnetic tape. At this time the temperature of the closed oven was read and found to be slightly higher than room temperature. This temperature was used as the reference temperature throughout the calibration and was within 2°F of the ambient temperature at the time of the test.

The oven was then heated to various predetermined temperatures. At each of these temperatures the contents of the oven were allowed to reach equilibrium. When equilibrium was reached, a 5-sec magnetic-tape recording was taken, and the temperature reading was noted. Calibration at these temperature steps was continued until the maximum temperature of the oven was reached.

The magnitude of the deflection steps on the visual reproduction of the magnetic-tape record was compared with the mercury-thermometer readings, and a graph was made of the deflection

in percentage of the calibrate signal vs change in temperature, defined as  $\Delta T$ . The plotted curves were straight-line functions to  $\Delta T = 305^\circ\text{F}$  for the Stikon gauge and  $\Delta T = 228^\circ\text{F}$  for the Trans-sonic gauge.

#### 4.4 VANE-TYPE ANGLE-OF-ATTACK INDICATORS

Because of the lateness of the decision to measure the angle of flow of the air mass behind the shock front, the consequent time schedule for delivery and installation of the vane-type indicators at the Forward Area allowed only a hurried field calibration with improvised equipment.

Calibration of the split-triangular-vane indicator installed at the Engebi site was accomplished by calculation from the electrical characteristics furnished by the manufacturer. These characteristics permitted the calculation of the magnitude of the vane deflection producing a bridge unbalance equivalent to the bridge unbalance produced by placing a 50,000-ohm resistor in parallel with one arm of the bridge. This was in turn equivalent to the bridge unbalance introduced by the calibrate resistor of the Webster magnetic-tape recorder; therefore the calculated vane deflection would produce a signal equal to the calibrate signal. Since the bridge unbalance of this indicator varied as a linear function of the angle of vane deflection, the resultant calibration curve was a straight-line function from zero to the intersection of the calculated vane deflection (abscissa) with 100 per cent of the calibrate signal (ordinate). The magnitude, in degrees, of the calculated vane deflection was therefore the calibration factor for this instrument. For confirmation of the direction of vane movement with respect to the sign of the calibrate signal, the vane was placed in positions of slight and full displacement in each direction, and 5-sec magnetic-tape recordings were taken. The visual reproductions of these records were then checked to determine the direction of signal deflection.

Calibration of the weather-vane type of indicator installed at the Muzin site was accomplished by placing the vane at various angles as measured by a machinist's bubble-level protractor placed on the portion of the vane parallel to the center line of the vane. At each of these angles, a 5-sec magnetic-tape recording was taken. The magnetic-tape record was

compared with the protractor readings, and a graph was prepared of the deflection in percentage of the calibrate signal vs the change in angle of attack.

#### 4.5 ELECTRONIC CHRONOGRAPH AND BLAST SWITCHES

The accuracy specified for the high-speed electronic chronograph is such that calibration of these components is not required. A check was made to confirm that the performance was equivalent to that specified. This was done by comparison with a signal output frequency of radio station WWV, Washington, D. C. Satisfactory reliability was demonstrated by all the chronographs. The mechanical diaphragm-type blast switches, however, possessed sufficient inherent inertia to produce a definite lag time between the arrival of the blast wave and the following closing of the switch. This lag time is large compared to the accuracy of the electronic chronograph, and calibration is necessary to eliminate this unknown differential. The blast switches were calibrated individually by mounting them in a shock tube and subjecting them to a shock-pressure differential of 3.4 psi, the same magnitude as that recorded on the test site at 6,878 ft from ground zero (Muzin). This corresponds to a velocity of 1,250 ft/sec within the shock tube. The calibrations are shown in Fig. 4.1. Based on seven test runs, the time required for the shock to travel the 31-in. timed distance was found to vary by 21  $\mu\text{sec}$ , a deviation of 0.53 per cent. The individual blast switches showed maximum deviations as follows: starting switch, 30.9  $\mu\text{sec}$ ; 4-ft switch, very erratic, indicating unreliability (data from this channel have been eliminated); 10-ft switch, 45.4  $\mu\text{sec}$ ; 13-ft switch, 7.1  $\mu\text{sec}$ ; and 19-ft switch, 20  $\mu\text{sec}$ .

Since the chronographs were fabricated at a late date and were not received until shortly before Easy Day, calibration could not be scheduled until after the bomb detonation. A shock tube and electronic-timing components were necessary to calibrate the individual blast switches to determine the lag time between the arrival of the blast wave and the following closure of the blast-switch contact. The average lag time determined from a series of runs in the shock tube was obtained for each blast switch and applied to the readings obtained from Easy Shot.



## Chapter 5

# Test Results

### 5.1 RE-ENTRY AND GENERAL OBSERVATION OF EFFECTS

The detonation of the E-day atomic bomb at 0630 on 18 April 1951 was observed by Project 8.2 personnel from aboard the USS Sergeant Mower, anchored off shore of Parry Island. At 0730 the Project 8.2 re-entry party left Parry Island for the island test sites. The first stop was made at Bokon at approximately 1000. No damage of any type could be visually observed on any of the test articles. All the instruments had functioned, and all observations indicated that they had functioned properly. The only outward appearances that indicated that this site had been subjected to an atomic bomb explosion were a few burned portions of the fabric material of the sandbags. No monitor proceeded with this group to Bokon or to Muzin, the islands having previously been surveyed by Program 2 monitors. After Program 2 recovery operations were completed, it was necessary for the monitors to leave these islands instead of remaining to escort succeeding recovery teams. By the time a shuttle helicopter could be dispatched to furnish monitoring service, Project 8.2 had completed its inspections and proceeded to Engebi, where results of the initial survey were available. The radiation intensity at the time of re-entry was 1.0 r/hr.

The re-entry party departed from Bokon at approximately 1045 and proceeded to Muzin, where the inspection was started at approximately 1145. Here also very little disturbance to the Project 8.2 test articles was observed (see Fig. 5.1). Scorching of the paint and sandbags in a few spots and erosion of the temperature patches located close to the ground were noted. The 25-kw generator was still operating

in good order, although the sandbag revetment had caved in about it (see Fig. 1.19). Debris, such as sheets of metal from the buildings to the rear, littered the asphalt around the test articles. The interior of the instrument house showed no indication of bomb damage. All instruments had functioned and apparently in the proper manner and sequence. The small neon lights on the Potter counters were still lighted, permitting a direct reading of the total counts. The outward appearances of the Muzin test site showed only slight indications of having been subjected to the atomic bomb burst, although the power of the bomb was quite evident in the demolished buildings and debris of the surrounding projects. The radiation intensity determined by the initial survey was 0.3 r/hr.

The re-entry party departed from Muzin at approximately 1145 and proceeded to Engebi, where the inspection was started at approximately 1215. On this island test site, damage to various parts of test articles was evident, although no part of the installation was demolished (see Fig. 5.2). All instrumentation and recording systems had functioned, and all evidence indicated that they had functioned properly. At the Project 8.2 test site on Engebi the rate of radiation was approximately 0.1 r/hr.

The re-entry party departed from Engebi at approximately 1300 and proceeded to Teitel, where the inspection was started at approximately 1330. No damage was observed on the test articles at this site. Fires were observed around the test site in the deadwood that had been cleared from the site. The instrumentation and recording systems had all functioned properly at this test site except for the Fastax cameras. Power and relay troubles caused a malfunction of cameras and the lighting sys-

tem. The rate of radiation on the Teiteir test site at the time of re-entry was approximately 1.2 r/hr.

## 5.2 VISUAL OBSERVATION OF EFFECTS ON TEST ARTICLES

It appeared to be the opinion of practically all the people who inspected the test sites prior to the explosion and also of those who were familiar with Project 8.2 test installation that the aircraft test structures on Engebi would be completely demolished. In the breakdown of the observation of effects on test articles that follows, the details are practically all limited to the effect on the Engebi test articles since practically all cases of damage were confined to the Engebi test site, and this was difficult to photograph at times since the extent of damage was very limited or of a minor nature.

### 5.2.1 B-17 Elevator: Fabric-covered Control Surfaces

No effects of the explosion could be observed externally or internally on the B-17 elevators at Muzin, Teiteir, or Bokon (Fig. 2.8). The doped fabric was taut and showed no signs of deterioration.

The elevator on Engebi was damaged considerably, although the outward appearance belittled the actual damage that had occurred to the internal structure (Fig. 2.24). The doped fabric skin which was fairly well shielded by the supporting tube was scorched or burned through in places on the upper-surface leading-edge portion. The fabric skin on both sides was loose and wrinkled, with a small torn place on the upper surface between two ribs. This torn place may be directly attributed to the extension of a small hole ( $\frac{1}{8}$  in. diameter) that was in the fabric at this point prior to the test. Close examination of the contour of the elevator indicated that the shape was changed and therefore a probable crushing of the internal structure had occurred (ribs). The impression of the ribs on the metal skin of the trim tab was also evidence of damage due to crushing. The elevator was dismounted, and practically all the doped fabric skin was removed from one side to allow observation of the internal structure (see Fig. 2.25). The crushed metal ribs

of the internal structure and burned sections of skin may be seen in Figs. 2.26 and 2.27.

### 5.2.2 F-47 Wings and Metal-covered Control Surfaces

The F-47 wings and attached metal control surfaces (metal-covered flaps and ailerons) on Bokon, Teiteir, and Muzin showed no indication of damage whatsoever. Both of the F-47 wings on Engebi received superficial damage, consisting in a slight dishing of the metal skin on both sides inward between parts of the supporting internal structure (see Figs. 2.6 and 2.7). The supporting ribs and internal structure of the control surfaces and the wing proper were moderately impressed on the metal skin. The structure on the leading edge of the wing near the tip retained a visible permanent set from the crushing force of the differential pressure. Only infinitesimal damage due to thermal radiation could be observed. Several darkened areas which were caused by smoking of rubber seal strips were noted. Although the aerodynamic shape of the wing and control surfaces was impaired, the strength for all practical purposes was probably not lowered any appreciable amount.

As stated before, no damage was sustained by the F-47 wing structure proper on Teiteir; however, the sheet-metal covering placed over the wheel and strut well to give continuity to the airfoil section was dished in as shown in Figs. 5.3 and 5.4.

### 5.2.3 Rigid-wing and Structural-wing Models

The rigid-wing and the structural-wing models and the supporting system showed no evidence of damage in any form on Bokon, Teiteir, and Muzin. Only slight traces of erosion of the paint were visible on the leading edges of the nose section of the pylon on Muzin (see Fig. 3.6).

Structural-wing model 104, orientated at a 9° angle of incidence on Engebi, had definitely sustained damage. This wing had not broken free from the supporting pylon but was drooping severely, as shown in Fig. 1.2. The other structural model and two rigid models did not have any visible signs of damage. The nose sections of the pylons were the only portions of the supporting system that showed evidence

UNCLASSIFIED

N

of damage. The leading edges of these sections were scorched, and the aluminum skin showed the impression of the supporting ribs. When structural model 104 was disassembled, the following damage, illustrated in Figs. 2.12 and 2.13, was ascertained:

1. Shearing of the attachment rive's caused separation of the attachment fittings E from the spar roots (Fig. 2.13).
2. The upper spar caps buckled at the root section (points C in Fig. 2.13).
3. The upper and lower spar caps cracked and separated from the shear web in the root section as shown at points A and B in Figs. 2.12 and 2.13.
4. The intermediate stiffener D in the root section had failed (Fig. 2.13).

#### 5.2.4 Swept-wing Models

The swept-wing models and supporting system on Bokon, Teiteir, and Muzin did not sustain any structural damage. Their appearance was unchanged as a result of the bomb burst, except for a small amount of paint blistering on the forward 6-in. supporting struts and the nose sections of the pylons. The swept-wing model on Engebi showed no indication of damage. However, superficial damage did occur to the supporting system in that the nose section of the pylon had the internal ribs impressed on the aluminum skin and several shallow skin buckles were apparent. The paint on the leading edge of the nose section and on the large supporting strut was considerably burned. Some of these effects on the swept-wing model installation may be observed by comparing the before view, Fig. 1.3, with the after view, Fig. 1.4.

#### 5.2.5 F-80 Fuselages

The F-80 fuselage-section installation on Bokon, Teiteir, and Muzin showed no damage with the exception of a slight scorching of the finish on the radar dome and of the paint on the outside edge of the left intake duct on Muzin. Figure 2.21 is a before view, and Fig. 2.22 is an after view of the F-80 fuselage installation on Muzin. It can be seen in these photographs that the canopy, temperature gauges, radar dome, etc., are intact with no visible change.

Some superficial damage was sustained by the F-80 fuselage on Engebi. Structurally the damage was limited to shallow buckling of the

skin between internal supports. Some of these buckles can be observed in the nose section slightly forward of the 0 in the number 420 in Fig. 2.3. The dents in the right air scoop, as shown in the same photograph, were made previous to the explosion, as may be noted in the before picture, Fig. 2.2. Several shallow dished-in areas occurred on the left side of the fuselage nose. The largest area of damage of this nature, including the removable panel over the camera-window cutout, may be seen in the vicinity of the lower part of the F of the large black letters FT-42 of Fig. 2.4. The radar dome on the nose of the fuselage presented a charred appearance. The laminating resin down through the first layer of glass fabric was severely scorched. The canopy withstood the explosion with no outward appearance of damage. However, the rubber sealing strips around the edge of the canopy were burned. The windshield which faced directly into the blast was intact, but crazing and cracking within the laminate were observed.

#### 5.2.6 Airfoils

No effects of the explosion could be observed on the airfoils at Muzin, Teiteir, or Bokon. The three airfoils set at a  $22\frac{1}{2}^\circ$  angle of incidence on Engebi all failed in the same manner but in varying degrees. Figure 2.6 illustrates all three airfoils and their failure appearance with relation to the supporting system. The airfoil in the most prostrated position on the extreme left in Fig. 2.6 contains the larger  $\frac{1}{2}$ -in. venting holes. Details of this failure may be seen more clearly in Fig. 5.5. The airfoil containing the  $\frac{1}{4}$ -in. holes is on the immediate right side of the F-47 wing in Fig. 2.6, and the failure is illustrated in detail in Fig. 5.6. The remaining airfoil did not contain any venting holes, and, as illustrated in Fig. 5.7, its failure had progressed the least of the three airfoils set at maximum angle of incidence. The appearance of the failure indicated that the venting holes had not materially weakened the structure.

The three other airfoils on Engebi, which were set at a  $0^\circ$  angle of incidence, did not fail in any manner, as may be seen in Fig. 2.18. Fairly severe erosion from sand and dust had occurred on the temperature tapes that were

UNCLASSIFIED

on two of these airfoils. This also may be viewed in Figs. 2.18, 2.19, and 5.7.

### 5.2.7 Cylinders

None of the cylinders was damaged structurally on any of the four island test sites. The Temp-Tapes on the cylinder on Engebi were burned and sandblasted beyond any possibility of reading. Figure 2.20 is an illustration of the condition of the cylinders on Engebi after the blast.

## 5.3 TEST RESULTS FROM MODEL WINGS

### 5.3.1 Rigid-wing Models

Lift reactions were measured on the rigid-wing models at all four test sites. Drag and moment reactions at all four sites were obscured by the dynamic response of the rigid-wing models. On Engebi and Muzin (4,020 and 6,878 ft from ground zero) lift records were obtained from the wings set at a  $9^\circ$  angle of incidence, as plotted in Figs. 5.8 and 5.9. An average curve of the lift for each of these wings was obtained by a graphical elimination of the effects of wing-model dynamic response occurring at a frequency of 40 to 50 cps. These curves are presented for comparison in Fig. 5.10. As presented in this manner, the maximum lift for the wing model at a  $9^\circ$  angle of incidence at a range of 4,020 ft (Engebi) was 1,280 lb, occurring 55 msec after passage of the blast front, with a decrease to zero lift at 650 msec. The maximum lift was preceded by a lift of 1,140 lb at 20 msec. The maximum lift for the  $9^\circ$  wing model at the 6,878-ft range (Muzin) was 340 lb at 100 msec, with a prior peak of 300 lb at 15 msec. The lift decreased to zero at 900 msec for this wing model.

No significant signal was recorded for the rigid-wing models set at a  $6^\circ$  angle of incidence on Engebi and Muzin. On Teiteir and Bokon (12,000 and 16,614 ft from ground zero) lift records were obtained from the rigid-wing models at a  $6^\circ$  angle of incidence. However, the low magnitude of lift was considerably obscured by the dynamic response of the models, and consequently graphs of these functions are not presented. No signal was recorded for the wing models at a  $9^\circ$  angle of incidence on Teiteir and Bokon.

Differential-pressure profile data were obtained from all the rigid wings at Engebi and Muzin. As was predicted, the pressure differentials at the two farthest sites (Teiteir and Bokon) did not exceed the noise level of the recording system. The most complete pressure data were recorded at the 4,020-ft range (Engebi) from the rigid wing set at a  $9^\circ$  angle of incidence. Five of the six pressure-sensing elements on this wing operated satisfactorily. On the remaining three rigid wings at Engebi and Muzin, approximately 50 per cent of the pressure transmitters functioned properly. Individual graphs of the variation of these pressure differentials with time for the first 200 msec following the initial pressure disturbance are shown in Figs. 5.11 to 5.24. These graphs uniformly indicate that pressures exceeding 80 per cent of the maximum pressure recorded in each case were attained at approximately 3 msec after the first discernible pressure change.

Trapezoidal integration of the differential pressures, measured on the rigid wing at a  $9^\circ$  angle of incidence at the 4,020-ft range (Engebi), was conducted by tabular methods to give the variation of total lift with time as indicated by the chordwise pressure distribution. A graph of this function utilizing the average curve through insignificant variations is presented in Fig. 5.25. The maximum lift obtained by this method is somewhat questionable but is presented as 2,400 lb at 15 msec, decreasing to zero lift at 650 msec.

Each pressure-differential record for this wing was averaged over the first 20 msec and over the first 100 msec. Each of the average pressure-differential values was plotted at the proper place on a percentage of chord abscissa so that the curves connecting these points would present the chordwise pressure distribution for this airfoil. This distribution for 0 to 20 and 0 to 100 msec is shown in Fig. 5.26. The pressure-differential records for the remaining three wings were averaged in a similar manner, were multiplied by proper factors to raise the pressures for each wing to equivalent pressures for a  $9^\circ$  wing at a 4,020-ft range, and finally were averaged together with the average pressures for the  $9^\circ$  wing at 4,020 ft. These computations were conducted as shown in Table 5.1. The weighted average differential-pressure values were plotted on a per-

TABLE 5.1 TRANSPOSITION OF ALL DIFFERENTIAL-PRESSURE DATA  
TO 9° RIGID WING AT ENGEBI

Line*	(1) % of Chord	(2) Range (ft)	(3) Site	(4) Angle of Inci- dence (°)	Differential Pressure				
					(5) Av. Differ- ential Pressure (psi)	(6)† Adjust- ment Factor	(7)‡ Adjusted Av.	(8) Total of Adjusted	(9)§ Av. of Total Adjusted
First 20 Msec									
A	5	4,020	Engebi	9	4.81	1.0	4.81		
B	5	4,020	Engebi	6	3.41	1.1	3.75		
C	5	6,878	Muzin	6	0.33	14.6	4.82		
	5							13.4	4.46
E	10	4,020	Engebi	6	2.70	1.1	2.97		
F	10	6,878	Muzin	9	0.41	7.1	2.91		
G	10	6,878	Muzin	6	0.31	14.6	4.53		
	10							10.4	3.47
H	15	4,020	Engebi	9	2.37	1.0	2.37		
I	15	4,020	Engebi	6	3.18	1.1	3.50		
J	15	6,878	Muzin	9	0.51	7.1	3.62		
	15							9.4	3.16
K	20	4,020	Engebi	9	1.93	1.0	1.93		
L	20	6,878	Muzin	9	0.20	7.1	1.42		
	20							3.35	1.68
M	40	4,020	Engebi	9	1.65	1.0	1.65	1.65	1.65
N	80	4,020	Engebi	9	2.00	1.0	2.00	2.00	2.00

\*The letters in this column are used as coordinates with the column numbers in the computations below, e.g., A5 is the value on the first line in the column numbered 5 (average differential pressure), or 4.81.

†Computation of adjustment factors for first 20 msec for data from the following:

$$6^\circ \text{ wing, range 4,020 ft: } \frac{1}{2} \frac{A5}{B5} \frac{H5}{I5} = \frac{1}{2} \frac{4.8}{3.4} \frac{2.4}{3.2} = 1.1$$

$$9^\circ \text{ wing, range 6,878 ft: } \frac{1}{2} \frac{H5}{J5} \frac{K5}{L5} = \frac{1}{2} \frac{2.4}{0.5} \frac{1.9}{0.2} = 7.1$$

$$6^\circ \text{ wing, range 6,878 ft: } \frac{A5}{C5} = \frac{4.8}{0.33} = 14.6$$

Computation of adjustment factors for first 100 msec for data from the following:

$$6^\circ \text{ wing, range 4,020 ft: } \frac{1}{2} \frac{A5}{B5} \frac{F5}{G5} = \frac{1}{2} \frac{1.9}{2.8} \frac{1.6}{1.4} = 0.9$$

$$9^\circ \text{ wing, range 6,878 ft: } \frac{1}{2} \frac{F5}{H5} \frac{I5}{J5} = \frac{1}{2} \frac{1.6}{0.3} \frac{1.0}{0.3} = 4.5$$

$$6^\circ \text{ wing, range 6,878 ft: } \frac{I5}{K5} = \frac{1.0}{0.1} = 9.2$$

‡Values in the column numbered 7 were obtained by multiplying the value in column 5 by that in column 6.

§The values in the column numbered 9 are the final values used for graphs.

TABLE 5.1 (Continued)

Line*	(1) % of Chord	(2) Range (ft)	(3) Site	(4) Angle of Inci- dence (°)	(5)	Differential Pressure			
					Av. Differ- ential Pressure (psi)	(6)† Adjust- ment Factor	(7)‡ Adjusted Av.	(8) Total of Adjusted	(9)§ Av. of Total Adjusted
					First 100 Msec				
A	5	4,020	Engebi	9	1.90	1.0	1.90		
B	5	4,020	Engebi	6	2.88	0.9	2.59		
	5							4.49	2.25
C	10	4,020	Engebi	6	1.13	0.9	1.02		
D	10	6,878	Muzin	9	0.42	4.5	1.89		
E	10	6,878	Muzin	6	0.31	9.2	2.85		
	10							5.76	1.92
F	15	4,020	Engebi	9	1.64	1.0	1.64		
G	15	4,020	Engebi	6	1.39	0.9	1.25		
H	15	6,878	Muzin	9	0.28	4.5	1.26		
	15							4.15	1.38
I	20	4,020	Engebi	9	1.01	1.0	1.01		
J	20	6,878	Muzin	9	0.32	4.5	1.44		
K	20	6,878	Muzin	6	0.11	9.2	1.01		
	20							3.46	1.15
L	40	4,020	Engebi	9	0.86	1.0	0.86	0.86	0.86
M	80	4,020	Engebi	9	0.15	1.0	0.15	0.15	0.15

centage of chord abscissa, as shown in Fig. 5.27, to present the chordwise pressure distribution on the basis of the total amount of data available.

Tabular computation of the center-of-pressure movement was made on the basis of the five differential-pressure measurements from the rigid-wing model at a 9° angle at the 4,020-ft range. This center-of-pressure movement about the 25 per cent chord point was plotted as shown in Fig. 5.28. The moment about the 25 per cent chord point was similarly computed and graphically compared with the angle of attack in Fig. 5.29. The source and treatment of the angle-of-attack information on this figure is included in Sec. 5.5.1. The center-of-pressure computations and the moment computations, both originating in the same data, indicated an initial upward force acting aft of the 25 per cent chord point.

Variation of differential pressure with time measured at 10 per cent chord of the rigid-wing model set at a 9° angle of incidence at the

6,878-ft range (Muzin) is shown in Fig. 5.30 to indicate the small but abrupt variation in pressure occurring at 1,150 msec after passage of the blast front. This variation occurs within the time bracket of the change from positive to negative pressure established by the over-pressure data reported in Sec. 5.5.4. This phenomenon was observed on three of the seven differential-pressure records obtained at this site. In each of the other four records the record was not conclusive at this point, and measurements of other functions taken on the same magnetic-tape recorder had no similar indication. The record at 10 per cent chord of the 9° angle-of-incidence model is typical of the records for the other two pressure measurements where this variation was observed.

Another phenomenon occurring at the 6,878-ft range (Muzin) was noted on both rigid-wing models at this site. At the 20 per cent chord point of both models an initial negative pressure differential of approximately  $3\frac{1}{2}$  msec duration was observed. This represented a

function approximately 180° out of phase with other pressure measurements on the same wings at different chord points. No marked physical disparity, other than chordwise position, was apparent in this installation. The indication of predominantly positive differential pressure subsequent to the initial negative phase for these two pressure measurements is evidence of the correctness of the sign of the pressure measurements. Figures 5.31 to 5.33 present this phenomenon in various comparisons, and Figs. 5.21 and 5.24 provide supporting evidence.

### 5.3.2 Structural-wing Models

The bending moment was measured at three spanwise stations on the structural-wing models at Engebi and at one spanwise station on the structural-wing models on Muzin and Telteir. Failure in at least one component of the measuring and recording system eliminated measurements at two spanwise stations on Muzin and Telteir and at one station on Bokon. No attempt was made to measure the bending moment at the remaining stations on Bokon because of the very low magnitude of bending moment predicted.

The records of bending moment for the three spanwise stations on each of the two structural-wing models at the 4,020-ft range (Engebi) indicated high stresses during the first 20 msec of the positive-pressure phase (see Figs. 5.34 to 5.36). These stresses were imposed on the structures at frequencies higher than either the first- or second-mode bending frequencies of the wing models.

Following the initial indication of high-frequency stresses, the bending moments at the three spanwise stations of the structural wing at a 6° angle of incidence at the 4,020-ft range assumed characteristics equivalent to first-mode vibration of the structure, as shown in Fig. 5.34. The initial peaks of bending moment under first-mode conditions were 47,000, 8,500, and 5,500 in.-lb, respectively, for the inboard, intermediate, and outboard stations. These peaks occurred approximately 110 msec after the arrival of the blast front and were followed by successive first-mode vibrations of diminishing magnitude at a frequency of 4.3 cps. An expanded graphical presentation of the initial peak of the first-mode bending

moment at the inboard station of structural wing 101 is shown in Fig. 5.37.

As indicated in Sec. 5.2.3 the structural wing at a 9° angle of incidence at the 4,020-ft range failed structurally in the region of attachment to the root-fitting box. This failure was indicated by the records of bending moment for the intermediate and outboard stations of this wing model, as shown in Fig. 5.36. The time of failure is indicated in this figure by the abrupt change of frequency of the measured stress 81 msec after the arrival of the blast front. On the figure this change of frequency is emphasized by comparison with the bending moment from the outboard station of the 6° wing at this range. The frequency following failure was equivalent to the second-mode vibration of the model structure. Failure occurred on this wing model when the bending moments on the structural wing at a 6° angle of incidence at this site were 85 per cent of their eventual maximum value, which occurred 29 msec later. The magnitude of the bending moment at the inboard station of the 9° wing exceeded the full-scale range of the magnetic-tape recorder prior to the time of failure, so that no effective presentation of data for this station can be made.

The records of bending moment at the intermediate station of the two structural-wing models at the 6,878-ft range (Muzin) are presented in Figs. 5.38 and 5.39. No evidence of the high-frequency stresses recorded during the first 20 msec at the 4,020-ft range is apparent on these records. Both records of bending moment for these wing models indicate initial second-mode vibration superimposed on the first cycle of first-mode vibration, followed by simple first-mode oscillation. The initial period is presented in Fig. 5.39, and the continuing first-mode condition is shown by Fig. 5.38. Superposition of the second-mode vibration on the first-mode amplitude increased the magnitude of the initial peak bending moment at the intermediate station to 8,000 in.-lb for the 9° angle-of-incidence wing and to 5,000 in.-lb for the 6° angle-of-incidence wing. Two peaks of approximately equal magnitude occurred on each record, one near 90 and one near 125 msec after arrival of the blast front.

The one record of bending moment for the structural wing obtained at the 12,000-ft range

[REDACTED]

(Teiteir) was for the inboard station of the wing model set at a  $9^\circ$  angle of incidence. This station of this wing would, under theoretical consideration, record a larger bending moment than any other station on the structural wings at this range or at the 16,614-ft range (Bokon). The magnitude of the bending moment even at this station was so small that it scarcely exceeded that maximum error possible under conditions of normal distribution of error, as indicated in Table 4.1. For this reason the graphical presentation of this record has not been included, and a specific indication of peak bending moments has been omitted.

Shear loading on the structural-wing models was measured successfully only at the inboard station of the wing at a  $6^\circ$  angle of incidence at the 4,020-ft range (Engebi). Second-mode vibration is discernible superimposed on the initial cycle of first-mode vibration, although some irregularities tend to obscure the first oscillation of the second mode in Fig. 5.40. A maximum shear of 1,300 lb was measured at the peak of the first cycle of second-mode vibration at 15 msec after arrival of the blast front. This was followed by a small shear, 1,100 lb, for the maximum value of first-mode loading at 110 msec. Continuation of the first-mode vibration with diminishing amplitude is shown in Fig. 5.41. Wing failure, low shear-gauge output, and failure of components of the recording system combined to eliminate adequate records of shear at other stations, other wings, and other ranges. The excessive strength of the shear web of the wing spars was a major factor in limiting the bridge output of the gauges used for the shear-measuring installation.

No torsion loads were measured successfully on the structural-wing models. Contributing factors to this failure were the extreme torsional stiffness of the wing models, the excessive strength of the spar webs in resistance to torsional shear flow, and the incomplete pattern of gauges with respect to the problem of averaging the torsional shear flow in a cross section of the wing model.

### 5.3.3 Rigid- and Structural-wing-model Cameras

Film roll B-35-100-711, exposed in the Fastax camera and used to record damage to

rigid- and structural-wing models at Engebi, was not readable. It was overexposed by the fireball and was somewhat exposed by radiation in spite of protection afforded by lead bricks around the camera canister.

Film roll B-35-100-713, exposed at Muzin, was somewhat overexposed but was readable in part. There was no photographic evidence of any blast damage or of any object of sufficient size striking the models that might be correlated with an erratic reading from the instruments within the models. The beginning of the film was overexposed or washed out completely by the fireball. When the wing models could be seen, dust was present, and objects which probably were flakes of oil-impregnated sand could be seen moving through the camera field. Two floating sheets of iron were observed to the rear and on either side of the wing models. Since the camera started at  $H + 2$  sec and stopped at  $H + 11$  sec, it appears that most of the readable film was exposed during the negative phase of the pressure wave.

No film was exposed at Teiteir since a delay timer failed to start the camera.

A camera was not installed at Bokon since a short time prior to E-day a vehicle ran over the camera mount and canister, damaging them beyond repair.

### 5.3.4 Swept-wing Models

The bending moment was measured at three spanwise stations on the swept-wing model at Engebi and at two spanwise stations on the swept wings at Muzin and Teiteir. Shear loading was measured at two of the spanwise stations on the swept wing at Engebi. Failure of at least one component of the measuring and recording system eliminated one measurement of bending moment at Muzin and Teiteir and all measurements of shear loads at those two sites. Attempts to measure bending moment and shear at Bokon were canceled prior to the test when information became available which predicted very low air loads at this site. No torsion loads were successfully measured on the swept-wing models. As in the case of the structural models the factors contributing to this failure were the torsional stiffness of the model, excessive strength of the spar webs, and incomplete torsional gauge patterns for solution of the problem of average torsional



shear flow at the cross section of each span-wise station.

Each of the five records of stress, three of bending moment and two of shear, for the swept-wing installation at the 4,020-ft range (Engebi) indicated high stresses, similar to those of the structural wings at this site, during the first 20 msec following the arrival of the blast front. Figures 5.42 to 5.46 indicate the magnitude, frequencies, and relative times of occurrence of these initial stresses, and Fig. 5.47 indicates existing phase relations for the bending moments by comparison on an expanded time scale. Comparison of Figs. 5.42 to 5.46 with Figs. 5.34 to 5.36 indicates the similarity of these stresses in the swept- and the structural-wing models.

Following the initial high-frequency variations of the stress records, the bending and shear records of this swept-wing model at Engebi assumed the characteristics of a first-mode vibration of the structure, as shown by Figs. 5.48 and 5.49. Second-mode stresses are discernible in the first cycle of first-mode vibration shown in these records; however, it is not readily apparent whether or not the secondary stresses raise the peak magnitude of the first-mode stresses. The peak magnitude of the bending moment at the inboard station of this wing for first-mode vibration is unknown since the full-scale limit of the magnetic-tape recorder was exceeded. This is indicated in Figs. 5.42 and 5.48 by the omission of the curve of bending moment for the section from 82 to 147 msec. The initial peaks of the first-mode bending moments were 104,000 and 16,000 in.-lb, respectively, for the intermediate and outboard stations. The corresponding peak magnitudes of shear were 1,500 and 400 lb, respectively, for the intermediate and outboard stations. These peaks occurred approximately 110 msec after the arrival of the blast front and were followed by first-mode vibrations of diminishing magnitude at a frequency of 4.0 cps.

The records of bending moment at the intermediate and outboard stations of the swept-wing model at the 6,878-ft range (Muzin) are presented in Figs. 5.50 and 5.51. Evidence of minor second-mode loading is indicated at the beginning of the record of bending moment at the intermediate station of this wing, as shown in Fig. 5.51. This figure also indicates the in-

itiation and continuance of first-mode bending moment at this station, with a first-peak magnitude of 10,000 in.-lb at 100 msec, followed by lesser peak magnitudes at a frequency of 4.3 cps. As in the case of the structural wings, no evidence of the high-frequency stresses recorded during the first 20 msec at 4,020-ft range is apparent. The variation of bending moment with time at the outboard station is presented in comparison with the bending moment from the same station at the 4,020-ft range in Fig. 5.50. The comparison indicates equivalent conditions of second-mode vibration superimposed on the first cycle of first-mode bending at both ranges. The secondary stresses substantially increased the peak magnitude of the bending moment at the 6,878-ft range and bore a phase relation to the first cycle of the primary loading such that three peaks of approximately equal magnitude were recorded. These peaks indicated bending moments of approximately 4,000 in.-lb at 60, 95, and 130 msec. Cycles of first-mode bending moment continue with diminishing magnitude at a frequency of 4.4 cps. The initial 25 msec of each record is omitted in this figure because the high-frequency stresses of the record from the 4,020-ft range would obscure this section. These stresses were not evident on the record from the 6,878-ft range, as indicated by a similar comment on the measurement at the intermediate station.

The two records of bending moment at the inboard and intermediate stations of the swept wing at the 12,000-ft range (Teiteir) should, under predicted conditions, record larger bending moments than the remaining stations on the swept wings at this range and at 16,614 ft (Bokon). Even at these stations, however, the magnitude of the bending moment was so small that it scarcely exceeded the possible error, considered statistically, as indicated in Table 4.1. Thus the graphical presentation of these records has been omitted, and peak bending moments have not been specifically indicated.

#### 5.4 RESULTS OF TEMPERATURE MEASUREMENTS

##### 5.4.1 Temperature Variation with Time: Electrical-resistance-type Gauges

Of the 12 gauges for recording the temperature variation with time, installed in the struc-

tural-wing models, eight were operational on Easy Day. The external-skin-surface gauge at Engebi, range 4,020 ft, was intentionally eliminated because the skin temperatures expected at this range were calculated to be high enough to short out the gauge, causing electrical malfunction of the recorder. The two internal gauges at Engebi and the external-skin-surface gauge at Bokon, 16,614 ft, were eliminated because of the occurrence of electrical malfunctions with insufficient time for correction. Usable data were obtained from four of the eight gauges that were operational. The three gauges on Muzin (6,878 ft), the external-skin-surface gauge on Teiteir (12,000 ft), and the two internal gauges on Bokon functioned properly. Failure of at least one component of the measuring and recording system during the test eliminated measurements from the two internal gauges at Teiteir. The signals recorded by the two internal gauges at Bokon were insignificant. The ambient temperature at H-hour (approximately 80°F) was selected as the point of origin for all temperature-time data. Thus the data reported represent the increases in temperature of the structural-wing models caused by the thermal radiation of the 50-kt bomb. As the propagation of thermal radiation from the bomb is practically instantaneous, zero time on all temperature curves may be considered coincident with H-hour.

The maximum temperature increases recorded by the four operational gauges were, at Muzin, 87°F by external-skin-surface gauge, 43°F by internal-skin-surface gauge, and 12°F by front spar-web gauge; and, at Teiteir, 27°F by external-skin-surface gauge. Similarity of the temperature rise of the external-skin-surface gauges at Muzin and Teiteir was evident, as shown by Figs. 5.52 and 5.53. Each of these external-skin-surface gauges attained maximum temperature 0.4 sec after detonation of the bomb. These peak temperatures decreased rapidly; at the end of 2 sec the gauge at Muzin registered 47°F above the original ambient temperature, whereas the gauge at Teiteir indicated 17°F above the ambient temperature. At this time (2.0 sec) a slight increase in temperature was indicated by both gauges. This was followed by a moderate cooling rate, averaging, over the remaining 96 sec of the record, 0.3°F/sec at Muzin and 0.1°F/sec at Teiteir.

The internal-skin-surface gauge at Muzin exhibited an abrupt temperature rise of 21°F in approximately 1 sec, after which the rate of rise decreased, as shown in Fig. 5.54. The temperature indicated by this gauge continued to increase until at 11.5 sec the internal-skin-surface-gauge temperature equaled the external-skin-surface-gauge temperature which had cooled to 39°F above ambient (see Fig. 5.55). The internal-skin-surface gauge apparently continued to rise and reached a peak of 43°F above ambient at 22 sec. After 22 sec the internal-skin-surface-gauge temperature decreased at approximately the same rate as that of the external-skin-surface gauge.

The spar-web temperature at Muzin rose in 3 sec to a temperature of 6°F above ambient. After this time the temperature continued to increase at a lesser rate to a maximum of 12°F at 23 sec. From this point the temperature remained constant to the end of the record at 100 sec.

#### 5.4.2 Maximum Temperature Survey: Temp-Tapes

In general, the Temp-Tapes on Engebi which were mounted on the outside of the test article with an angle of incidence approaching normal to the blast were badly eroded by sandblasting. This caused piercing of the aluminum-foil protective covering, thus exposing the temperature-measuring alloy foil to extreme oxidation due to weathering. The edges of these adhesive tapes were also burned, but this burning did not reach the alloy patch in the center of the tape. In other locations the adhesive which held the tapes to the structure had softened; this caused a number of the Temp-Tapes to drop off the test article. The Temp-Tapes on the windshield and canopy of the F-80 fuselage had fallen to the floor of the cockpit owing to softening of the adhesive tape. None of these effects destroyed the temperature record except the oxidation of the alloys. No other Temp-Tapes on Engebi were affected by erosion or adhesive failure, and they performed in the intended manner.

All Temp-Tapes on Muzin, Teiteir, and Bokon were undamaged except for those installed on the cylinders on Muzin. These were burned and sandblasted, but they did not fall

TABLE 5.2 MAXIMUM TEMPERATURES ON AIRCRAFT STRUCTURAL COMPONENTS AS MEASURED WITH TEMP-TAPES\*

Temp-Tape Locations	Angle of Incidence (°)	Material under Test		Maximum Temperature at Indicated Test Site (°F)						
		Type	Thick-ness (in.)	Color	In	Out	Engelb	Muzin	Teiteir	Bokon
F-80 fuselage:										
Aft of left inside sidewall of left-hand intake duct, ap-proximately 265 in. aft of nose reference line		Aluminum	0.025	Aluminum metal	Aluminum metal	130	130	130	130	130
Inside of windshield side windows (3)	71.3	Plexiglas	0.375	Plexiglas	Plexiglas	220	175	145	162 (1)	
Inside of left nose access door (2)	80.0	Aluminum	0.032	Green	Aluminum metal	145	145	130	145 (1)	
Inside of windshield glass (3)	55.1	Glass	1.500	Glass	Glass	290	190	145	158 (1)	
Inside of top of canopy plexiglas (3)	73.6	Plexiglas	0.375	Plexiglas	Plexiglas	235	170	145	165 (1)	
Forward face of nose com-partment aft of wall		Aluminum	0.032	Aluminum metal	Aluminum metal	130	130	130	130	
F-47 wing:										
Inside of upper wing surface in wheel-well area	88.8	Aluminum	0.032	Light olive green	Aluminum metal	180	130	130	130	
On forward face of rear aux-iliary spar in wheel well		Aluminum	0.090	Light olive green	Light olive green	130 (4)	130	130	130	
On rear face of leading-edge spar, wheel-well area		Aluminum	0.090	Light olive green	Light olive green	130	130	130	130	
Inside of bottom wing sur-face on alleron-inspection doors	88.5	Aluminum	0.025	Light olive green	Aluminum metal	130	130	130	130	
Outside upper wing surface just inboard of gun-inspec-tion door	88.8	Aluminum	0.032	Light olive green	Aluminum metal	225	130	130	130	

Small airfoil sections, 4

In. aft of leading edge:

0° airfoil, side away from  
blast (left-hand side)

0° airfoil, side toward  
blast (right-hand side)

23½° airfoil, side away  
from blast

23½° airfoil, side toward  
blast

Small cylindrical section:

6 in. aft of leading edge

Rigid-wing models:

Inside of bottom skin, 2 in.  
aft of forward spar

Aft of face of forward spar

Structural-wing models:

Inside of bottom skin, 2 in.  
aft of forward spar

Aft of face of forward  
spar (2)

B-17 elevator:

Inside of leading-edge

fairing, 6 in. aft of leading  
edge, vicinity of tab-inspec-  
tion door

Inside of upper surface on  
fabric, vicinity of tab-in-  
spection door, placed at  
about 40 per cent chord

80.0	Aluminum	Aluminum metal	Aluminum metal	(5)	130 (6)	130 (6)	130 (6)
80.0	Aluminum	Aluminum metal	Aluminum metal	(5)	210 (5)	130 (6)	130 (6)
77.5	Aluminum	Aluminum metal	Aluminum metal	(5)	130 (6)	200 (6)	130 (6)
57.5	Aluminum	Aluminum metal	Aluminum metal	200 (6)	315 (6)	130 (6)	130 (6)
52.4	Aluminum	Aluminum metal	Aluminum metal	(5)	250 (6)	175 (6)	None taken
84.5	Aluminum	Aluminum metal	Aluminum metal		130	130	130
	Aluminum	Aluminum metal	Aluminum metal		130	130	130
84.5	Aluminum	Aluminum metal	Aluminum metal	132	130	130	130
	Aluminum	Aluminum metal	Aluminum metal	138	145	145	131
60.9	Aluminum	0.032	Light olive green	Fabric and aluminum metal	240	130	130
87.9	Cloth		Light olive green	Aluminum paint	130	130	130

\*The numbers found enclosed in parentheses throughout this table are placed herein for reference purposes in the explanation of these data in Sec. 5.4.2.

from their position on the cylinders. These particular Temp-Tapes were more normal to the blast than other exterior installations on Muzin.

All the temperature measurements made by the Temp-Tapes have been assembled in Table 5.2. The lowest melting alloy used in the Temp-Tape survey melted at 130°F. For reporting purpose, in all areas where no melting was observed, even on the 130°F alloy, the temperature was recorded as less than 130°F. The following comments regarding measured temperatures are numbered to correspond with the measured temperature bearing the same number, enclosed in parentheses, in Table 5.2.

1. As may be noted, the measured temperatures in these areas are higher on Bokon, range 16,614 ft, than those on Teiteir, range 12,000 ft. The explanation for the temperature being higher at a more distant range is not given. Theories are available and could be presented to try to explain this phenomenon, but it appears that they are premature and without sufficient foundation for presentation at this time.

2. The apparent consistency of temperatures measured in this region is perplexing. If it were due to a general rise in ambient temperature, it should have been indicated in several other areas, but there was no such indication. It is quite possible that the test articles involved were heated to these temperatures by the sun during days prior to E-day and the temperatures do not represent measured values from the test. However, these temperatures were not recorded by Temp-Tapes operating under similar conditions in the same locations on T-33 drone airplanes of Project 8.1.

3. It is apparent that some valuable data have been gathered from temperature measurements on these transparent areas; however, extensive calibration will be necessary before these data can be properly deciphered. Further investigation of this type of temperature measurements is in process.

4. The wheel-well area on the F-47 wing on Engebi was not covered during the test. A number of the Temp-Tapes were exposed to direct radiation and were burned and sandblasted beyond any possibility of reading. Those Temp-Tapes that were shielded by the forward section of the wing gave no temperature indication. Since the lowest-melting alloy was included in

this shielded group, it was apparent that the shielded area did not reach 130°F.

5. These Temp-Tapes were burned and sandblasted beyond any possibility of reading. The sand pierced the aluminum-foil protective covering, exposing the alloy foil to the atmosphere, which resulted in severe oxidation of the alloy foil; thus it was impossible to determine the temperature measurement.

6. These temperatures are listed as an indication that the areas under investigation did become heated. Little reliability should be accorded the actual values of temperature measured in degrees Fahrenheit because the Temp-Tapes were on the outside facing the radiation source (see Sec. 3.6).

## 5.5 BLAST PHENOMENA

### 5.5.1 Angle-of-attack Variation with Time; Vane-type Indicator

The angle of flow of the air behind the blast front, defined as the angle of attack and considered as zero when the flow was parallel to the plane of the earth, was measured only at the 4,020-ft range (Engebi). At the 6,878-ft range (Muzin) the dynamic response of the instrument described in Sec. 2.5.1 was such that no determination of the angle of attack could be made. This response was of the nature of a full-scale oscillation of the vane at a frequency of approximately 5 to 6 cps.

The measured variation of the angle of flow with time at 4,020 ft is presented in Fig. 5.56. This figure indicates rapid fluctuations of the angle of attack with an initial period of flow of negative angle, i.e., downward in the direction of movement of the air mass. This negative indication was succeeded by a positive flow, which in turn was succeeded by small oscillations about the zero point. The oscillations throughout this period were of irregular frequency in the general range of 100 to 150 cps. In Fig. 5.57 the curve of the angle of flow has been averaged to eliminate these oscillations and has been plotted for a longer period of time. A negative angle of flow with a peak magnitude of  $-6.6^\circ$  is indicated initially, followed by a positive maximum of  $1.1^\circ$ , subsiding at 125 msec to  $0.4^\circ$ . The angle of attack continued to decrease, reaching  $0^\circ$  at 400 msec,

followed by a period of considerable fluctuation as the positive-pressure phase weakened.

The use of the angle-of-flow information is indicated by Fig. 5.29. Here the angle of flow has been considered in its relation to the 9° angle of incidence of rigid wing 102 at the 4,020-ft range (Engebi). Initially, therefore, the flow about the wing started with a 9° angle of attack. Superficial fluctuations have been omitted, and the modified curve indicates a negative angle of attack of the wing within 3 msec after initiation of the air-mass flow. By 25 msec the flow was again at a positive angle of attack for this wing model, and by 65 msec the flow was reasonably stable and was such that the angle of attack of the wing was substantially the same as the established angle of incidence of the wing. A similar translation of the angle-of-flow data may be required for each wing model for the purpose of dynamic analysis and may be easily accomplished by adding the angle of incidence of the wing directly to the angle of flow of the air mass.

#### 5.5.2 Angle of Attack: Optical Method (Fastax Camera)

At each of four sites the camera and allied equipment operated successfully on E-day, with the exception of the camera at Teiteir. Owing to a malfunction of a delay timer, this camera failed to start. Of the lights used to illuminate the grids, approximately 66 per cent at Engebi and 33 per cent at Muzin were damaged.

Film roll B-35-100-718, exposed at Engebi, was not readable. The film was overexposed by the fireball and was somewhat exposed by radiation in spite of protection afforded by lead bricks around the camera canister.

Film roll B-35-100-714, exposed at Muzin, was somewhat overexposed by the fireball but was readable. There was no photographic evidence of the leading edge of a shock front, similar to the front photographed during a 10,000-lb high-explosive blast on 27 October 1950 at the Aberdeen Proving Ground which is described in Sec. 2.5.2 and illustrated in Fig. 2.28. The overpressure at Muzin (approximately 3.4 psi) was approximately the same as that at the camera in the Aberdeen test.

A thorough search was made for the shock-front phenomenon by viewing the film and by producing contact negatives of a number of

frames on a very high-contrast film (Kodalith) and enlarging two one-half frames to an 8- by 10-in. picture.

There was, however, an indication of the passage of a blast front, depicted by a change of film density of the ground in the lower right-hand corner of the frames. This is shown by comparing C in Fig. 5.58, recorded before blast-wave arrival time, with C in Fig. 5.59, recorded during the probable blast-front passage.

A sequence of events was observed when the film was shown with a motion-picture projector. The beginning of the film was overexposed or washed out completely, and, after the grid could be seen, the clouds in the background appeared to compress slightly toward the left in the photo and then moved to the left or away from ground zero. This movement was very pronounced and is shown pictorially by measuring from a vertical reference point at A to a cloud position at B in Fig. 5.58 and comparing the distance from A to B in Fig. 5.60.

The cloud position at B was found to have moved 3° 27' away from ground zero before it was obscured by dust. The indication of the cloud movement is included in this report since it may be of interest to some agency other than this project.

After passage of the blast front, the ping-pong balls, suspended between the grid wires, traveled to the left for a distance of approximately 5 in. The limitation on the travel of the ping-pong balls was due to the wires used to suspend the balls (see Fig. 2.31).

After the movement of the clouds and ping-pong balls the camera field was obscured by a heavy dust cloud. In the dust cloud objects which probably were flakes of oil-impregnated sand could be seen moving through the camera field and away from ground zero.

A study of film roll B-35-100-717, exposed during the test on Bokon, indicated that everything operated satisfactorily. The angle-of-attack grid and the ping-pong balls were illuminated brightly by the artificial high-intensity lights, whereas the background was quite dark. As was the case with the film on Muzin, there was no indication of the passage of a shock front as recorded in the 10,000-lb high-explosive test. The sharp movement of the ping-pong balls from right to left for an average distance of approximately 6 1/2 in. in the film

[REDACTED]

was evidence that the camera was operating when the blast front passed the camera and test site. No dust could be seen moving through the camera field on this film. From a study of the photography of the high-explosive tests at Aberdeen, it is felt that the photography was adequate on Muzin and Bokon to have indicated the passage of a sharp shock front if one had been present.

#### 5.5.3 Angle of Attack: Electronic-chronograph Method

The results obtained from the electronic chronographs approximate an isobar equivalent to an overpressure of less than 0.1 psi. Based on the original assumption that a shock front would be recorded as an abrupt discontinuity, that is, as having an infinite rate of rise from the ambient pressure to the peak overpressure, slight differentials in the minimum pressures affecting contact of the blast switches would not be evident in the final record. That this condition did not exist is evident from the results obtained with the interferometer gauges and with the high-speed motion-picture cameras; hence the configuration determined from the electronic counters is an isobar at some distance (time) following the blast front.

When the re-entry party arrived, the auxiliary gasoline-driven electric generator was still running. The chronograph equipment had operated automatically from the relay time signals, and a satisfactory record was obtained by the recording system. Since the generator was still running at full voltage, it was possible to take a visual reading of the chronographs. This reading was noted, and the later development of the recording negative proved the two to be identical. An enlargement from the recording negative is shown in Fig. 2.36. The corrected results are plotted in Fig. 5.61.

The data indicate a relatively large negative angle of attack shortly after the arrival of the blast wave, and the curvature is an indication that turbulence existed or that the initial portion of the blast wave did not form a uniform surface.

#### 5.5.4 Overpressure Variation with Time: Interferometer Gauges

The interferometer gauges used to determine the variation of overpressure with time were installed in a rectangular pattern, except on Engebi, where only two gauges were installed laterally, to bracket the test articles. This multiple installation provided data in such a manner that two to four records could be averaged at each site. Where only three records were obtained, owing to malfunctioning of one gauge, the weighted average was taken by assigning a double value to a single gauge reading. The average results at each test site are plotted on two separate time bases. Figure 5.62 shows the overpressure variations for the positive and negative phases (7 sec), and Fig. 5.63 shows the variations on an expanded time axis including only the first 200 msec.

The predicted overpressure values for the estimated 60-kt bomb on which preliminary plans were made and the values actually measured on Easy Shot are given in Table 2.2.

Of the 14 gauges installed for Project 8.2, 12 functioned properly. One of the four gauges (91e) at Muzin and one of the four (92c) at Bokon did not record satisfactorily. The results at Engebi are the averages of two records; those from Muzin and Bokon are the weighted averages of three readings each; and the results from Teiteir are the averages of four gauges. The plotted results have been smoothed out to eliminate reflection blips and other slight transient effects to portray the forcing function acting on the test articles.

## Chapter 6

# Discussion

### 6.1 GENERAL CONSIDERATIONS

The broad mission of Project 8.2 was satisfactorily accomplished. A large amount of data and experience was accumulated on the effects of an atomic explosion on aircraft structural components and instrumented test models mounted on the ground at various ranges from the point of bomb detonation.

In general, the actual damage sustained was far less than that predicted prior to the detonation. Even at 4,020 ft from ground zero, test articles were not demolished, although three small airfoils and one structural wing model were damaged. Original intentions were to bracket the optimum test range by having four identical installations at various distances from the shot tower. However, owing to the actual nature of the blast phenomena, the largest amount of data was accumulated on Engebl, range 4,020 ft. The decay of the forcing function at greater ranges was sufficient to limit the measurable responses of some of the instrumented test articles. Structural damage was apparent only at the nearest site (4,020 ft).

Qualitative observations indicated that from a 50-kt bomb the thermal radiation was sufficiently intense, at least up to 16,000 ft, to start fires in fabric and possibly other nonmetallic aircraft components at relatively low angles of incidence to the source. From an operational standpoint the hazard to the fabric-covered control surfaces is at once apparent. If low-altitude drops were attempted by bombardment aircraft, loss of the lower fabric on control surfaces, such as elevator and ailerons, would be expected. Also crew members exposed at transparent windows might be seriously affected. The effect of differential-pressure load-

ing of present aircraft at close ranges varied from moderately severe damage to bomber-type fabric-covered control surfaces to very slight panel buckling on fighter-type wings, fuselages, and metal-covered control surfaces at a range of 4,020 ft from ground zero. Even at this range the effects of differential pressure alone acting on an aircraft structural component at a zero angle of incidence were not sufficient to prevent further flight. However, it must be pointed out that the combined effects of side-on loading and differential pressure combined with the velocity and inertia of the aircraft may produce severe damage to major structural components under certain conditions. The point being emphasized is that overpressures up to 10 psi when applied progressively to conventional combat aircraft structures at zero incidence are not sufficient in themselves to cause the loss of the aircraft, although noticeable local damage will occur.

### 6.2 WING MODELS

Each item of measured data from the rigid-, structural-, and swept-wing models was considered separately for significant points, maximum values, frequency patterns, and spurious indications. Each item was then considered in relation to the other data, and multiple curves showing comparisons, combinations, averages, and integrations were plotted. The most important curves and combinations of curves were selected on a basis which included at least one direct graph of all the data considered accurate and of those combinations of graphs which appeared most significant. Various time scales were chosen as the abscissas of these



[REDACTED]

graphs, for most of which the units of time are in milliseconds, i.e.,  $10^{-3}$  sec. The more expanded time scales were selected to present the material in the most accurate manner for use in the dynamic analysis. The less expanded scales were chosen to show frequency relations, decreasing magnitudes through the end of the positive-pressure phase, and other characteristics having significant changes over a longer period of time. Whenever more than one requirement governed the selection of time scales, graphs of each were drawn; therefore duplication of certain items of data is noticeable in the group of figures presented. To facilitate cross reference, Tables 6.1 and 6.2 list the figures on which the time scales and other data are plotted for each quantity.

Except for the temperature data, time zero for each item of data has been chosen as the time of arrival, at the wing model containing the sensing unit, of the first measurable disturbances in the blast front. This, then, differs from time zero for detonation of the atomic bomb by the length of time required for the blast front to traverse the distance from the point of detonation to the location of the wing model in question. For the temperature data, time zero has been chosen as the time of the first measurable change in temperature of the outside-skin gauges. Because of the very low thermal inertia of these gauges and because of their direct exposure to thermal radiation, it is felt that this is equivalent to time zero for detonation of the atomic bomb within the limits of accuracy of the time base of the recording system, i.e.,  $\pm 1/2$  msec.

Although the information presented here includes all items of data which were successfully measured and represents a completed report of the measurements themselves, the information is preliminary in the sense that evaluation of its significance and of its conformity with theoretical concepts has not been completed. This evaluation will follow the completion of theoretical studies of the forcing functions based on overpressure data and on the analysis of dynamic loading of the structural and swept wings. These theoretical studies will be compared with the test results reported here for the observance of similarities and discrepancies. The exact form and distributions of this final evaluation are un-

known at the present time. The further statement may be made that the data, as presented here, give considerable promise of successful comparison with theoretical concepts and that considerable significance may be added to the data by this comparison.

One possible discrepancy in these data, not otherwise noted, is an abrupt positive or negative displacement of the record trace peaking at 34 to 35 msec, followed by an equally abrupt return of the trace to its previous position, which occurs on all records at the 4,020-ft range, except the record of lift on the  $9^\circ$  wing. It does not appear reasonable that any physical phenomena of the blast wave could have been responsible for this record displacement; therefore the most logical explanation for this occurrence is that it is a malfunction of the recording system at the 4,020-ft range. This affects only the part of each record at which the abrupt displacement occurs and therefore is not considered significant in the over-all reduction of the data.

#### 6.2.1 Rigid-wing Models

The rigid-wing models were designed with an inherent high stiffness so that bending deflections would be negligible during loading and records obtained would define the forcing function without complications introduced by bending deformations. The data obtained from these wing models indicated a more rapid build-up of the forcing function than was predicted prior to the test. Indications are that the response characteristics of the rigid-wing models, as determined by the balance systems and the spar extensions, were considerably affected by the excitation of the natural frequency of these components. This occurred because the natural frequency was not sufficiently separated from the hypothetical frequency of the forcing function (extrapolated from the first-quarter cycle of the forcing function indicated by the differential-pressure build-up). The fundamental frequency of the balance system, including the spar extensions, should be on the order of 10 times greater than that of the forcing function, and yet the system should be sufficiently flexible to produce a large strain-gauge output. Modification of spar ends and the balance system appears to be necessary to achieve these results.

TABLE 6.1 NUMBERS OF FIGURES IN WHICH ARE PLOTTED CURVES FOR LIFT, PRESSURE, AND ANGLE OF AIR-MASS-FLOW FUNCTIONS

Channel*	Type of Measurement	Measurement vs Time (20 msec/in.)	Measurement vs Time (200 msec/in.)	Comparison by Wing of Pressure Measurements on Rigid Wings at Muzin	Comparison of Two Pressure Measurements on Muzin	Av. Chordwise Pressure Distribution over Wing 102 during Two Periods	Mean Curve of Angle of Flow	Comparison of Lift (Mean Curves)	Shift of Center of Pressure on Wing 102	Mean Lift Curve on Wing 102 Determined by Chord- wise Pressure Distribution	Mean Chordwise Pressure Distribution Determined from All Pressure Measurements	Comparison of Moment about Chord Line and Mean Angle of attack Curve, Wing 102
E11	Lift	5.8						5.10				
S11	Lift	5.9						5.10				
E13	Differential pressure	5.11				5.26			5.28	5.25	5.27	5.29
E15	Differential pressure	5.12				5.26			5.28	5.25	5.27	5.29
E16	Differential pressure	5.13				5.26			5.28	5.25	5.27	5.29
E17	Differential pressure	5.14				5.26			5.28	5.25	5.27	5.29
E18	Differential pressure	5.15				5.26			5.28	5.25	5.27	5.29
E19	Differential pressure	5.16									5.27	
E20	Differential pressure	5.17									5.27	
E21	Differential pressure	5.18									5.27	
S14	Differential pressure	5.19	5.30	5.31							5.27	
S15	Differential pressure	5.20		5.31							5.27	
S16	Differential pressure	5.21		5.31	5.33						5.27	
S17	Differential pressure			5.31							5.27	
S19	Differential pressure	5.22		5.32							5.27	
S20	Differential pressure	5.23		5.32							5.27	
S22	Differential pressure	5.24		5.32	5.33						5.27	
E41	Angle of flow	5.56					5.57					5.29

\*Letters preceding the channel numbers indicate test sites: E, Engebi, 4,020 ft; S, Muzin, 5,878 ft; Q, Teitair, 12,000 ft; P, Bokon, 16,614 ft.

TABLE 6.2 NUMBERS OF FIGURES IN WHICH ARE PLOTTED CURVES FOR BENDING MOMENT, SHEAR, AND TEMPERATURE FUNCTIONS

Channel*	Type of Measurement	Measurement vs Time (20 msec/in.)	Measurement vs Time (100 msec/in.)	Spanwise Variation of Bending Moment with Time on Wing 105	Comparison by Wing of Temperature and Strain Measurements on Wings 101, 105, and 204	Comparison by Test Site of Bending Moment on the Structural Wings	Comparison of Temperature and Strain Measurements Recorded on Identical Channels of Two Test Sites	Comparison of Bending Moment at the Inboard Stations of the Struc- tural Wings on Muzin	Maximum Temperature Change vs Distance of Three Points on the Structural Wings
Y37	Temperature				5.55				6.13
Y38	Temperature				5.54				6.13
Y39	Temperature				5.55		5.52		6.13
B39	Temperature				5.54		5.53		6.13
R1	Bending		5.35		5.34	5.36	5.52		
R4	Bending				5.34		5.53		
R7	Bending	5.37			5.34		5.53		
R9	Shear	5.40	5.41						
R31	Bending					5.36			
R34	Bending					5.36			
Y4	Bending					5.38		5.39	
Y30	Shear								
Y31	Bending					5.38		5.39	
R40	Bending	5.42		5.47	5.48				
R43	Bending	5.43		5.47	5.48				
R45	Shear	5.45			5.49				
R46	Bending	5.44		5.47	5.48		5.50		
R48	Shear	5.46			5.49				
Y43	Bending		5.51						
Y46	Bending						5.50		

\*Letters preceding the channel numbers indicate test sites: E, Engebl, 4,020 ft; S, Muzin, 6,878 ft; Q, Teiteir, 12,000 ft; P, Bokon, 16,614 ft.

The forcing function, defined as "lift" throughout this report, was actually measured as normal chord force. The error introduced if the data are considered as lift force normal to the relative wind is of the order of 0.5 per cent, which is negligible in view of the overall accuracies indicated in Table 4.1.

The calculated lift for the 9° rigid wing at each range was approximately as follows: 2,160 lb at 4,020 ft; 345 lb at 6,878 ft; 56 lb at 12,000 ft; and 21 lb at 16,614 ft. For the 6° rigid wings, the equivalent figures were as follows: 1,440 lb at 4,020 ft; 230 lb at 6,878 ft; 37 lb at 12,000 ft; and 14 lb at 16,614 ft. The calculated times required to attain these lifts after the arrival of the blast front at each range were as follows: 47 msec at 4,020 ft; 67 msec at 6,878 ft; 120 msec at 12,000 ft; and 170 msec at 16,614 ft. These calculations were based on the overpressure data obtained from the interferometer gauges.

The record of lift for the 9° rigid wing at Engebi, presented in Fig. 5.8, has three areas in which the record is subject to question. These areas each have a large negative peak, which is seemingly impossible in view of present theories on the lift function. Therefore the function has been estimated for these areas, and this estimated curve has been included in Fig. 5.8 with the original curve. Both curves are dotted in the area of uncertainty. Since these areas coincide with the probable time of occurrence of the maximum lift, the magnitude of the maximum lift is also somewhat uncertain. However, no substantial alteration of the estimated curve seems justifiable on the basis of current information. The record of lift for the 6° rigid wing at Muzin, although somewhat obscured by excitation of the fundamental frequency of the balance system, presented a value of maximum lift (340 lb) closely approximating the maximum calculated lift (345 lb) although somewhat less than the originally predicted results.

The attempt to bracket the lift conditions at the test sites resulted in balance systems at Teiteir and Bokon with full-scale ranges of measurement from 700 to 1,400 per cent greater than the maximum lift conditions encountered at those ranges. This, together with the excitation of the balance-system frequency and the fact that winds of velocity sufficient to produce the same magnitude of lift existed in

the area, eliminated any conclusive interpretation of the record, except that the lift measurements were of the order of magnitude predicted.

The angle of flow of the air mass at the 4,020-ft range, as presented in Figs. 5.56 and 5.57, may be used to interpret, analyze, or modify the lift results presented. The definition of the lift functions thus obtained may be compared with calculated lift functions to check current theories and may further be used as the starting point for the calculation of the theoretical dynamic loads on the structural- and swept-wing models.

A qualifying occurrence in the differential-pressure records for the rigid wings at Engebi was the presence of excessive oscillation of the base, or zero-pressure-differential, line prior to and during the records. This occurred on only the one group of recorder channels at this one site and was determined to be a malfunction of the magnetic-tape recorder. Since these cycles were repetitive and were within the full-scale limits of the record-reproducing system, an adjusted zero line was drawn in the record section, and all displacements were measured from this line, as shown in the figures of the original records presented in the report. Admittedly this method is subject to error; however, the error is quite small in the region just after the arrival of the blast front, which is the most important region from the standpoint of dynamic analysis.

The one measurement of differential pressure at the 80 per cent chord point, namely, the record of that point on the 9° rigid-wing model at the 4,020-ft range, varied markedly from theoretical predictions and in so doing sharply affected most of the information based on the pressure-differential records. By being five times larger than predicted in the initial stages, this point increased the total lift measured by the pressure method since the single point of measurement controlled the envelope of the lift vectors aft of the 40 per cent chord point, i.e., over half the wing chord. Similarly this point, with its long moment arm about the 25 per cent chord point and with its large magnitude, exerted major influence both on center-of-pressure movement and on variation of pitching moment.

After 65 msec this differential pressure at the 80 per cent chord point assumed more reasonable values; so, in the picture of average

chordwise pressure distribution (Figs. 5.26 and 5.27), the pressure at the 80 per cent chord point eventually drops gradually when averaged over the first 100 msec, reaching predicted patterns of chordwise distribution.

The variation of lift with time, as determined by integration of the differential pressures, differed considerably from the lift function presented by the balance system. This was considered in view of the statements in the preceding paragraphs, giving rise to the belief that the balance-system lift is more accurate. However, it is felt that the pressure-system measurements may aid in the interpretation of the forcing functions as measured by the balance system.

### 6.2.2 Structural-wing Models

The purpose of the structural-wing models was to provide a dynamic test article having a fundamental natural bending frequency equivalent to that possessed by current fighter aircraft wings. The necessary design compromises for ease of fabrication and handling and for resistance to the maximum overpressure predicted (10 psi) resulted in a wing with a 7-ft span, a 2-ft chord, and a skin of 0.051-in. aluminum alloy. The combination of thick skin and short span resulted in a structural model with a higher natural frequency than desired. Consequently it was necessary to install 290 lb of lead weights inside the wing model to reduce the bending frequency to the desired magnitude (3.8 cps). These weights were distributed spanwise with their chordal centroids near the torsional neutral axis so as not to alter materially the torsional frequency.

The first noticeable deflections of the record traces from the structural wings at Engebi indicated large stresses at higher frequencies than either the first- or second-mode frequencies of the wing structure described in the preceding paragraph. Because of the irregularity in magnitude and frequency of these apparent stresses, no explanation drawn from present theory readily accounts for this phenomenon. The most logical interpretations of these deflections carry the implication that the deflections were spurious in the sense of being an accurate measure of bending stresses in the structure. These interpretations include a consideration of strain-gauge output based on

local, random deflections of the structure, induced by the overpressure effects at the beginning of the blast wave. These local deflections, if of unequal magnitude and/or if out of phase at the gauge locations of each bridge, will produce different strains at each gauge location, resulting in an unbalance of the strain-gauge bridge, which would be recorded as a deflection of the record trace. Since the local deflections of the structures would be of small radius and correspondingly of high frequency, this theory is at least plausible although unproved. Other equally plausible theories may be advanced for this characteristic of the record traces.

Except for the indications described in the preceding paragraph, the record trace deflections qualitatively indicated agreement with the theories of dynamic analysis with regard to the existence of first- and second-mode bending of the structures at predicted frequencies.

Although the maximum bending at the 12,000-ft range was too small to be evaluated quantitatively, the record indicated good agreement with theoretical predictions of the order of magnitude and the frequency of the bending stress.

The shear record at the inboard station of the 6° wing at the 4,020-ft range, presented as the only structural-wing shear successfully measured, is subject to question in its indication of the first cycle of second-mode vibration. The shear stress indicated in this cycle is much larger than would be possible when viewed in the light of a general knowledge of dynamic analysis. Further limitations affecting this record include those considerations which eliminated adequate records of shear at other stations.

### 6.2.3 Swept-wing Models

The purpose of the swept-wing models was to provide a test article for the determination of the effects of sweepback on the dynamic loading produced by the blast wave. To accomplish this purpose, it was required that the swept wing have natural bending frequencies equal to those of the structural-wing model. The same design compromises as in the case of the structural wing resulted in similar proportions for the swept wing, again requiring the addition of lead weights to the wing to reduce the first natural

[REDACTED]  
bending frequency to the desired magnitude (3.8 cps).

The first deflections of the record traces from the swept wing at Engebi exhibited high-frequency stresses similar to those observed for the structural wings. However, certain phase relations, possibly accidental, existed for these high-frequency stresses in the case of the swept wing. In spite of these phase relations, no applicable theory was found to justify the acceptance of these measurements as an indication of the actual stresses in the wing model. One of the seemingly logical explanations for this indication of stresses is the assumption of local deflections of the structure by the overpressure effects, as described for the structural-wing models.

As in the case of the structural-wing installation, the bending moments for the swept wing at Teitair were too small to be evaluated quantitatively. However, these records also indicated agreement with theoretical predictions of the order of magnitude and frequency of the bending moments.

The record of bending moment at the intermediate station of the swept wing at Muzin is lower than would be expected on the basis of general knowledge of dynamic loading. Therefore, although no apparent source of error exists, these data must be considered questionable until correlation with theory can be established. For this reason these data have not been presented in comparison with other similar quantities.

### 6.3 INSTRUMENTATION

The original visual reproductions of the magnetic-tape records have been photographed and are presented in reduced form in Figs. 6.1 to 6.12. In this manner the significant frequencies, variations, and characteristics of each measurement may be observed without the unavoidable small changes introduced by a manual transformation of the records into graphical form. The time scale has been indicated on each record. The ordinate scale is indicated by "calibrate-plus" and "calibrate-minus" designations. The magnitude of the measured quantity for a trace deflection equal to the displacement of the calibrate signal is presented in Table 4.1 for use with these records. A trace

deflection of any given percentage of the displacement of the calibrate signal indicates a corresponding percentage of the magnitude of the measured quantity at the calibrate signal, e.g., a  $\frac{1}{2}$ -in. trace deflection on a record with a calibrate-plus displacement of 1 in., being 50 per cent of calibrate plus where calibrate plus is equal to 1,000 lb, would indicate a loading of 500 lb. All records obtained are included in these figures, even in those cases where the records were not graphically reproduced.

The accuracy of the records and of the data reported therefrom is governed by the following considerations. A detailed study on the accuracy of the magnetic-tape recorder has never been made. The first recorders for this project did not arrive until mid-fall 1950; so no time was available to conduct such a study. However, an effort has been made to determine the approximate errors in the data presented in this report. A conservative estimate of the error was made in all cases, i.e., the maximum error was assumed.

A mechanical error of 1.5 per cent was assumed for the combination of recorder and visual reproducer (manufacturer's estimate, 1 per cent). The distinct operations of calibration with test loads, recording of test data, and the use of the ratio relation between the recorded signal and the calibrate signal result in a total mechanical error four times 1.5, or 6 per cent. The human errors involved in the reduction of the calibration and test records from the visual reproducer also had to be quadrupled to obtain the maximum human error. This error varied according to the actual deflections in the visual reproduction. The magnitude of the measured quantity, which was equivalent to 100 per cent of the calibrate signal, was multiplied by the total of these two errors, e.g., if the total of the two errors was 10 per cent and the measured quantity at 100 per cent of the calibrate signal was 2,000 lb, the error, 10 per cent of 2,000 lb, was 200 lb.

Following the above computations the assumption was made that a normal distribution of error occurred, i.e., that the maximum error as calculated above applies to 99.7 per cent of the results, defined as three  $\Sigma$ . Table 4.1 lists the maximum errors for one, two, and three  $\Sigma$ , equivalent to the maximum errors present in 67, 95, and 99.7 per cent of the test

[REDACTED]

data. All the calibration data points were not tabulated; so no valid statistical method existed for the determination of the maximum error of the calibration curves. However, these curves were the best straight lines through the test points, and it is felt that the maximum error in calibration was less than reported.

#### 6.4 ANGLE OF ATTACK OF BLAST WAVE

All the records obtained from the blast wave indicate initial turbulence. The vane-type indicators produced continuous records of the flow pattern, each at a specific point, whereas the electronic chronographs produced a vertical profile at a single time. The high-speed motion pictures showed no evidence of an abrupt shock front.

##### 6.4.1 Vane-type Angle-of-attack Measurements

The original assumption that the flow of the air mass behind the shock front was perpendicular to the shock front, which was in turn perpendicular to the plane of the earth, was not verified by the vane-type angle-of-attack measurements. Dubiousness concerning the validity of this assumption was actually the reason for the introduction of the vane-type angle-of-attack measurements in the last stages of the test program. Three major premises of the original assumption were not confirmed by the test data. The first premise lacking verification was the existence of a shock front, behind which the flow pattern would form. To support the remainder of the assumption, some isobar of the pressure front must be selected to replace the shock front. If the isobar selected is the one measured by the electronic chronograph, then the second premise, that the pressure front was perpendicular to the plane of the earth, was not confirmed. Then, if the flow immediately behind this pressure front is perpendicular to the isobar selected, several directions of flow at various angles to the plane of the earth are indicated. Since it is not reasonable that these directions could be maintained in the flow farther behind the pressure front, some degree of turbulence must be conceded. The indications of the split-triangular-vane indicator at Engebi confirmed the fact that the flow behind the blast front was not parallel to the plane of the earth and was con-

siderably turbulent. However, the average flow during the central part of the positive-pressure phase was nearly parallel to the plane of the earth.

Although no final analysis has been made of the effects and influence of these changes in the angle of flow on the wing models, an apparent correlation exists between the angle of attack and the pitching moment of the 9° rigid wing at Engebi, as shown in Fig. 5.29.

##### 6.4.2 Electronic-chronograph Angle-of-attack Measurements

Initially the electronic chronographs were adopted to serve as a check on the high-speed motion-picture method of determining the angle of attack when the exposure illumination appeared to be a critical factor in the photographic method. According to the information available during the planning phase of Operation Greenhouse, an abrupt shock front was supposed to precede the mass of high-velocity air, and the velocity vectors were assumed to be perpendicular to the shock front; hence it would be necessary only to determine the inclination of the shock front to find the true angle of attack of the wing models with respect to the flow.

The high climatic winds at the test site made it necessary to set a sufficient gap between the diaphragm and the contact point of the blast switches to prevent accidental triggering. Since the pressure rise at the shock front was theoretically instantaneous, this gap setting was not considered sufficient to compromise the test results.

Evidence from other ground-test instruments clearly indicates that a shock front did not exist in the immediate vicinity of the test sites.

The record from the electronic chronographs defines an isobar shortly behind the initial pressure rise. The positions of the measured points shown in Fig. 5.61 indicate substantial turbulence in the blast wave front and/or irregularities in the "spherical" blast envelope. Upon subsequent repeated test runs in a shock tube the blast switch from the 4-ft level was found to be excessively erratic, and therefore no value is given to the measurement at this height. It cannot be assumed that the true shape of the isobar is a regular smooth curve through the points measured since the large

[REDACTED]

vertical spread does not define local irregularities. Because of the slow rate of pressure rise, the precision of this method is subject to question.

To properly record turbulence in the blast wave, continuous-type records should be made in the immediate vicinity of the test articles to define properly the flow variations in the high-velocity air.

The desirability of a photoelectric triggering system for the electronic chronographs could not be realized owing to the time limitations when this method of angle-of-attack determination was introduced. It is possible that the rate of overpressure rise was too low to actuate photoelectric triggers had they been used. Further investigation is necessary to substantiate the limitations of photoelectric triggering systems.

#### 6.4.3 Optical Angle-of-attack Determination

The optical method utilizing high-speed motion-picture photography and refraction through the shock front was proved during high-explosive tests conducted by Project 8.2 at Aberdeen Proving Ground in 1950.

Results from Easy Shot of Operation Greenhouse indicated that no shock front existed in the vicinity of the ground. The film exposure and the image definition were sufficiently clear to portray the phenomenon if it had occurred. The passage of the high-velocity air was clearly indicated by the motion of ping-pong balls suspended in the camera field.

Additional investigations are required to establish the true nature of the blast phenomena at various altitudes.

#### 6.5 VENTING OF AIRCRAFT STRUCTURES

The evaluation of results of other blast tests with small high-explosive charges indicated that local structural damage would occur at relatively low overpressures, probably starting at about  $1\frac{1}{4}$  psi for large aircraft and at slightly higher overpressures for fighter aircraft. Operation Crossroads indicated the severity of side-on loading. The aircraft structural components exposed on Operation Greenhouse were oriented to minimize the effect of side-on loading in order to study the effects of overpressure.

The relieving effect obtained by venting the structural test articles was studied on three different configurations: small airfoils, small cylinders, and the outer wing panels of fighter aircraft (F-47). The small airfoils and cylinders were vented through the outer surfaces. However, the airfoils and cylinders were too rigid, and no blast effects were observed on these articles. The fighter wing panels were vented internally between all compartments and to the exterior through holes in the flap and aileron closing spars. No significant difference in damage was observed. Both the vented and unvented wings sustained slight local damage as evidenced by the inward buckling of the skin between ribs and stiffeners.

Because of the simplicity of the small airfoils and cylinders this method should be improved and expanded in future investigations.

#### 6.6 GROUND SHOCK

The adverse effects of ground shock on the models and the instruments were considered throughout the planning phase. The ground shock was expected to arrive at the test sites considerably ahead of the blast wave. Damage to the instruments was prevented by shock mounting on foam rubber in addition to the standard shock mounts integral with the instrument cases.

Since the recorders were started at H-hour minus 5 sec, if the ground shock was of sufficient strength, its effect on the test articles would be recorded on the magnetic tape.

When the records were played back in a visual form, it was found that only the moment channel (most sensitive) of rigid wing 102 at the 4,020-ft range (Engebl) showed the effects of the ground shock. The effects were of low magnitude, the peak value being 15 per cent of the moment reaction produced by the blast wave. The ground shock at the 4,020-ft range preceded the blast wave by 1.28 sec. The ground shock did not interfere with any of the test articles or instruments in the performance of their intended functions.

#### 6.7 FABRIC-COVERED STRUCTURES FOR AIRCRAFT

Fabric-covered aircraft structures are critical with regard to damage in the field of an



[REDACTED]

atomic bomb burst at ranges at least up to 16,600 ft (based on a 50-kt bomb) because of thermal effects. The minimum range at which no damage would occur was not determined since evidence at the farthest site of Project 8.2 (16,614 ft) showed that fabric combustion temperatures had been reached on sandbags. The screening of the supporting structure was sufficient to protect the low-incidence region of the fabric-covered (B-17) elevators at all sites, although at the 4,020-ft range (Engebi) the skin at a high angle of incidence, which projected beyond the supporting structure, was severely burned. If the large fabric surface had been normal to the incident radiation, severe thermal damage could be expected even at the 16,614-ft range (Bokon).

The overpressure (9.5 psi) at the 4,020-ft range severely crushed the ribs of the fabric-covered elevator without significant damage to the fabric except for one tear which propagated from a small ( $\frac{5}{8}$  in. diameter) hole which had accidentally been punched in the fabric prior to shot time. Although the structural damage was severe, the elevator might have been able to return an aircraft safely to the ground if no abrupt maneuvers were attempted. However, operational plans should include the effects of thermal radiation, side-on loading, gust loads, physiological capabilities of the crew, and the effects on volatile combustible liquids within the aircraft. Additional tests involving complete aircraft are necessary.

## 6.8 TEMPERATURE VARIATION WITH TIME

To obtain reliable data from the gauges for recording temperature variation with time, these gauges had to be balanced at a temperature equal to the ambient temperature at H-hour. A study of day-to-day temperature charts of the area revealed that the temperature for corresponding morning hours on consecutive days did not vary more than 1°F. Therefore all temperature gauges were balanced just 24 hr prior to H-hour.

The official weather record reported 81.7°F at 0800 on E-day. It has been assumed on the basis of available information that the ambient temperature at 0630 (approximately H-hour) was 80°F. Since the ordinate for all temperature curves was in terms of change in tempera-

ture, this ambient temperature, 80°F, must be added to the reported temperatures to obtain the total structural temperatures in degrees Fahrenheit.

Since the heat from the bomb passed from the outside skin surface to the inside skin surface and then to the spar web, the temperature records will be discussed in the same order. The events on each record will be considered chronologically following time zero.

The external-skin-surface gauges on both Muzin, 6,878 ft, and Teiteir, 12,000 ft, experienced irregular temperature rises during the first 0.2 sec, as shown in Fig. 5.53. The gauge on Muzin exhibited three distinct heating slopes, whereas that on Teiteir showed only two during this period. However, the following factors are worthy of consideration: actual fluctuation in the source, variation with time and distance of the transmissibility of the atmosphere, and the physical properties of the wing.

The time to reach maximum temperature for both the external-skin-surface gauges was 0.4 sec. Since these gauges were on structural wings, 6,878 and 12,000 ft from ground zero, it appears that the rise time to peak temperatures on the external skin surface was independent of range. This is, of course, reasonable in view of the known propagation characteristics of the thermal radiation. The maximum increases in temperature attained by the two external-skin-surface gauges were 87°F at Muzin, 6,878 ft, and 27°F at Teiteir, 12,000 ft. The ratio of these temperatures very closely approximated the square of the inverse ratio of their respective distances from ground zero. Therefore a graph of the variation of temperature with distance was plotted, and the curve following the inverse-square ratio was drawn through these test points (see upper curve, Fig. 6.13). From this curve the following peak changes in temperature may be read for the points of a 25° angle of incidence on the outside skin surfaces of the structural wings: 139°F at Engebi, 74°F at Muzin, 24°F at Teiteir, and 9°F at Bokon.

After the initial peak the temperature of the external skin surface dropped rapidly until at 2 sec the gauge at Muzin read 48°F and that at Teiteir read 17°F. Since the external-skin-surface gauges measure the temperature at the outermost layer of skin, it appears that this layer reaches considerably higher tempera-

tures than the main portion of the skin and then very quickly loses this high temperature through heat conduction to the cooler inside skin surface.

At approximately 2 sec both external-skin-surface gauges showed another rise in temperature (Figs. 5.52 and 5.54). The second increase at Muzin indicated a temperature rise lasting 1.7 sec with a peak increment of 3°F, whereas that at Teiteir indicated a temperature rise lasting 0.7 sec with a peak increment of 1°F. The magnitudes of these temperature rises are very small and are possibly insignificant, but they do exhibit a ratio similar to that of the peak temperatures measured by these gauges. The cause of these temperature rises is unknown; however, the realm of speculation includes the possibility of a variation in the thermal radiation of the fireball.

After 4 sec both external skin surfaces cooled at a steady rate until at the end of 100 sec the gauge at Muzin read 15°F above the original ambient temperature, i.e., 22 per cent of peak value, and the gauge at Teiteir read 6°F above ambient temperature, or 22 per cent of peak value. It is of interest to note the excellent correlation in both time and magnitude of these temperatures of the two external skin surfaces. In every case the heating and cooling slopes at Muzin were slightly steeper than the corresponding slopes at Teiteir, where the radiant energy per unit of area was less because of the greater range. In addition the ratio of the maximum temperature increases was in reasonable agreement with theory.

It is interesting to note that, since the thermal radiation of the bomb was directed against the leading edge of the wing models and since the angle of incidence to this radiation of the wing surface decreased from 90° to less than 10°, progressing aft on the chord, a sharp chordwise temperature gradient was developed. The effects of this gradient are unknown at this time. However, it is not believed that it appreciably affected the external-skin-surface temperature at the point of measurement during the first 2 sec.

The maximum temperature rise on the external skin surface probably occurred at the point where the surface was normal to the incident thermal radiation. However, no measurements were made at this point. In order to obtain these maximum skin temperatures at

each site, the temperatures for each range, given by the upper curve of Fig. 6.13, were divided by the sine of 25°. This division, in effect, transformed the angle of incidence to 90°. The maximum skin temperatures, as calculated by this method, were 329°F at Engebi, 175°F at Muzin, 57°F at Teiteir, and 21°F at Bokon.

The internal-skin-surface gauge exhibited a sharp rise to 21°F in 1 sec (Fig. 5.54). If this rate of rise had continued, the temperature on the inside skin surface would have equaled the temperature on the outside skin surface in approximately 2 sec. It is possible that the initial heating slope corresponded to that of a simple aluminum plate 0.051 in. thick at a 25° angle of incidence.

The rate of increase in the temperature of the internal skin surface was markedly reduced after the first second but continued to increase until at 11.5 sec the temperature of the internal and external skin surfaces were both equal to 39°F. After this point the temperature of the internal skin surface exceeded that of the external skin surface and finally reached a peak of 43°F at 22 sec. This peak is 65 per cent of the maximum temperature of the corresponding point on the external skin surface. A zero shift may have occurred at 13 sec in the record of the internal-skin-surface gauge. This possible variation was not considered significant since the general shape of the curve after 13 sec was believed to be valid and the maximum deviation in the magnitudes of the ordinates was a reduction of not more than 3°F. The middle curve of Fig. 6.13 was drawn through the peak temperature registered by the internal-skin-surface gauge and is intended to approximate this peak temperature for the wing models at the various test sites. Since no other readable records were obtained for the internal gauges, the ratio of internal to external peak temperatures at Muzin was projected to the other test sites.

It is noted that, after the maximum internal-skin-surface temperature had been reached, both the internal and external skin surfaces cooled at approximately the same rate, the internal temperature being slightly higher than the external temperature (Fig. 5.55). The external skin surface was exposed to the prevailing winds. The temperature of the internal skin surface at the end of 100 sec was 19°F, or 44

~~SECURITY INFORMATION~~

per cent of the peak temperature of this surface.

The spar-web temperature increased 6°F in 3 sec (Fig. 5.54). After this time the temperature continued to increase at a lesser rate until at 23 sec the increase was 12°F; thereafter the temperature remained constant to the end of the record. The lower curve in Fig. 6.13 was drawn through the peak spar temperature at Muzin. This curve was extended to include all sites by using the same ratio of peak spar temperatures to peak external-skin-surface temperatures as that measured by the temperature gauges at Muzin, thus representing an approximation of the spar-web temperatures of the structural-wing models at each site.

One of the important factors governing the low internal temperatures obtained from this test was the attitude of the wing models; i.e., the wing models were so positioned that the leading-edge section received the direct thermal radiation of the bomb. As a result there was a large area of relatively cool wing surface compared to the small area of heated wing surface.

Practically no correspondence existed between the locations of the Temp-Tapes and the locations of the temperature-vs-time gauges; however, such correlation as could be effected did not indicate conflicting data in any case. Two sets of Temp-Tape measurements were made on the structural wings: the lower internal skin surface 2 in. aft of the forward spar and the aft face of the forward spar web. The Temp-Tape measurements on the internal skin indicated no peak total temperatures higher than 132°F. The values of peak internal-skin-surface temperatures from Fig. 6.13, plus the ambient temperature of 80°F, did not conflict with these Temp-Tape records when transposed to the proper angle of incidence.

One set of internal- and external-skin-surface measurements from the Temp-Tapes was similar to the internal- and external-skin-surface peak temperatures obtained from the temperature-vs-time gauges. In this set the inside surface of the upper wheel-well area of the F-47 wing reached a peak temperature of 180°F, and the outside skin surface just inboard of the gun-inspection door registered 225°F, thus giving a ratio of the peak temperature of internal to external skin surfaces of 0.80, as compared to 0.65 obtained from the temperature-vs-time gauges.

## 6.9 RE-ENTRY

In order to provide information for future problems of re-entry into areas which have been subjected to an atomic bomb explosion, the experience of the re-entry party of Project 8.2 is cited here. Approximately 3 1/4 hr after the detonation of the Easy Day bomb the 16,614-ft test site was revisited, the data records were collected, and visual observations were made. No Project 8.2 test site was restricted by the radiological safety control group because of radiological hazards. The three other test sites were visited successively, and the collection of data and observation notes was completed. According to the film badges worn by each member of the re-entry party, the total dosage was approximately 1 r for an approximately 6-hr exposure; however, pocket electrosopes showed a dosage of 2 to 2 1/2 r. It is interesting to note that at the two greatest ranges, on opposite sides of the point of detonation, 12,000 and 16,614 ft, the residual radiation was greater than at the two nearer test sites, 6,878 and 4,020 ft. The test articles did not exhibit any greater radioactivity than the general background.

## Chapter 7

# Conclusions and Recommendations

### 7.1 CONCLUSIONS

The following conclusions are based on the test conditions as set forth in this report. The more important of these conditions are listed here in order that they may be foremost in mind when the conclusions are read:

1. An approximately 50-kt bomb was exploded 300 ft above ground on a steel tower.
2. All test articles were anchored to the ground and therefore were not subjected to flight loads.
3. All test articles were mounted with a small frontal area, normal to the incident radiation as compared to the considerably larger area parallel to the axis of propagation.

It is concluded that:

1. Even though the test articles were oriented to minimize the side-on blast loads, the damage sustained was considerably less than that predicted by all concerned.
2. The ground shock did not appreciably affect the functioning of the models, other test articles, or the electronic equipment.
3. Automatically operated (20 to 24 hr) portable generators can be successfully utilized as a primary power source at a range of 4,020 ft with relatively minor revetment installation. The portable generators utilized at ranges of 4,020 and 6,878 ft received only negligible damage.
4. In general, the singular effect of overpressure up to 9.5 psi applied to aircraft structures at zero angle of incidence (no side-on loading) does not appear to be sufficiently damaging to cause loss of present combat aircraft. Primary aircraft structures of conventional design, as exemplified by the F-80 fuselage, F-47 wing, and F-47 metal-covered control

surfaces, sustained limited damage that did not greatly reduce the load-carrying capacity but sustained extensive minor damage of the type which would require considerable maintenance to repair. The lighter type of construction, such as that employed in fabric-covered control surfaces (B-17 elevator), bomb-bay doors, and other large, relatively lightly stiffened areas, could be expected to sustain major damage that would greatly reduce the structural strength and in most cases would require complete replacement. However, when this crushing force is combined with the dynamic lift and drag loads due to the blast on aircraft components presenting relatively large surface areas to the blast wave, major damage to the aircraft involved may be expected.

5. Thermal damage to the test articles was minor and was confined to opaque nonmetallic aircraft components and to the paint of metal surfaces at ranges of 4,020 and 6,878 ft. No thermal damage of the test articles was observed at the 12,000- and 16,614-ft ranges.

6. Greater thermal damage would be expected on opaque nonmetallic components, such as fabric-covered control surfaces, if exposed with the maximum surface toward the point of detonation. Burned materials were observed at all test sites up through the 16,600-ft range (Bokon).

7. The effects of an approximately 50-kt bomb exploded 300 ft above the ground are sufficient to produce noticeable damage to structural components of combat aircraft located on the ground with a minimum angle of incidence at ranges up to 4,020 ft, but these effects most probably would not produce any blast damage at ranges of 6,878 ft and beyond. This is referring to damage to the structural

UNCLASSIFIED

component by the effect of the direct forces released by the atomic explosion and does not include other possibilities of damage due to flying debris, rotation, or translation of the complete aircraft.

8. The F-47 wings and metal-covered control surfaces, while sustaining some damage at the closest range, 4,020 ft, would have been operable or safe to fly if required, although the aerodynamic efficiency was most probably reduced. Considerable maintenance would have been required to restore these structural components to first-class condition.

9. The B-17 elevator, partly protected from the thermal radiation by the holding jig, was damaged considerably on Engebi by the overpressure. It appeared to retain sufficient strength to have supported at least a 1-g load and most probably could have operated sufficiently to return an airplane safely to the ground. It is also most probable that at all test sites the thermal radiation would have burned the fabric from the frame of the elevators had they been subjected to direct thermal radiation.

10. The F-80 fuselage sustained some damage at the 4,020-ft range, although it would have been operable if required. The thermal radiation apparently passed through the transparent methyl methacrylate canopy, causing little or no damage; however, the effects on an occupant would have been severe.

11. The strength of the small cylinders and airfoils was too great for the blast wave encountered; so they did not react in a manner that would permit a study and evaluation of differential-pressure alleviation effects.

12. The magnetic-tape recorders in the configuration used for automatically recording the measured test data given in this report did not possess sufficient accuracy, reliability, and flexibility.

13. The overpressure rise time as measured by ground-level interferometer gauges was of the order of milliseconds rather than microseconds, indicating a blast front appreciably thicker than that predicted.

14. The optical method for determining the inclination of the shock front, utilizing high-speed motion pictures, indicated that no shock front existed in the region of the test sites on Muzin and Bokon. Records were not obtained at Engebi or Teiteir.

15. The electronic-chronograph method of determining the inclination of the shock front resulted in the definition of an isobar, which was due to the relatively slow overpressure rise time.

16. None of the test articles were any more radioactive than the background radiation of their specific test site. Therefore as representative parked aircraft they were not dangerously radioactive for a long period of time but would have been available for limited operation shortly ( $3\frac{1}{2}$  hr or less) after detonation.

17. It is possible that fighter or bomber aircraft of all-metal construction might be lost owing to thermal-radiation injury to the operating personnel, even though direct structural or mechanical damage from the atomic bomb would not result in loss of the aircraft (this is for consideration in determining the range limitation criteria for aircraft operating in the vicinity of an atomic bomb burst from a structural, mechanical, and physiological viewpoint).

18. Insufficient data are available at this time to define clearly the blast-front characteristics and the flow of the high-velocity air in the vicinity of the ground.

The following conclusions apply to the rigid-wing model:

1. The rigid-wing model was sufficiently rigid for the purpose of measuring the airloads and the differential-pressure distribution; however, the natural frequency of vibration of the combination of wing-spar extensions and supporting balance mechanism was excited by the forcing function developed by the blast wave. Because of this excitation and because of insufficient damping to prevent continuance of vibration, the rigid-wing installation was not completely adequate.

2. Lift data, usable for the determination of the forcing functions required for dynamic analyses of the structural- and swept-wing models, were obtained from the rigid-wing models at a  $9^\circ$  angle of incidence at the 4,020- and the 6,878-ft ranges. Lift data confirming predicted low maximums of lift (of the order of magnitude of the lift produced by wind velocities normally occurring in the vicinity) were obtained from the rigid-wing models at a  $6^\circ$  angle of incidence at the 12,000- and 16,614-ft ranges. No drag and moment measurements were obtained because of the dynamic response of the rigid-wing-model installation.

UNCLASSIFIED

3. The maximum lift as measured by the balancing system on the 9° rigid wing at both the 4,020- and the 6,878-ft range was less than predicted, but the rate of increase to this peak was greater than predicted, and the rate of decrease following the peak was likewise greater than predicted.

4. The differential-pressure-sensing instruments and installation were only partly adequate for accomplishment of the objective. The survey of differential pressures in the region aft of the 40 per cent chord point was inadequate.

5. Differential-pressure data were obtained from all four of the rigid-wing models at Engebi and Muzin. Combinations of the differential-pressure data from these wings provided indications of lift, chordwise pressure distribution, center-of-pressure movement, and moment about the 25 per cent chord point. All these combinations are of limited credibility and usefulness for a dynamic analysis because of the absence of adequate duplication of measurements aft of the 40 per cent chord point. No differential-pressure data were obtained from the rigid wings at Teiteir and Bokon because of the small differential pressures at these ranges (of the order of magnitude of the differential pressure induced by wind velocities usually present in the area).

6. Variations of differential pressure with time at the chord points of the wings, as presented herein, individually possess certain distinctive features which may be of significance in detailed analyses to be conducted or which may be useful in other fields of atomic blast study.

The maximum lift on the 9° rigid wing at the 4,020-ft range, as obtained by combining the differential-pressure measurements from this wing, was approximately equal to the predicted magnitude. However, the rate of increase to this peak was much greater than predicted, and the lift force following the peak was less than indicated either by theoretical consideration or by the balance-system measurements. The chordwise pressure distribution for this wing and the weighted average distribution from all four wings at Engebi and Muzin averaged over the first 20 msec following arrival of the blast front were similar to the predicted distributions, with the notable exception that the differential pressure at the 80 per cent chord point was approximately five times greater than the pre-

diction. The average chordwise distribution for the 9° wing and for the combined wings during the first 100 msec was substantially in accordance with the predicted distribution, including the 80 per cent chord point.

Center-of-pressure movement on the 9° rigid wing at the 4,020-ft range was very great and considerably erratic, exceeding anything predictable by steady-state analyses. Variation of moment was similarly large and exhibited possible correlation with the variation of the angle of attack of the wing.

Turbulent air-mass flow, with noticeable vertical components, was present at the time of transition from the positive-pressure phase to the negative-pressure phase at the 6,878-ft range.

The phase relations of the differential pressures at the 6,878-ft range may affect the dynamic analyses and are of interest in connection with theoretical concepts of the circulation about the wing models.

From the structural-wing models it was concluded that:

1. The structural-wing models were adequately designed and instrumented for the measurement of first-mode bending stresses at the 4,020- and 6,878-ft ranges. The same design and instrumentation were not sufficiently sensitive to measure accurately the small bending stresses encountered at the 12,000- and 16,614-ft ranges. The design and instrumentation were inadequate for the measurement of shear and torsion loading at any of the ranges because of excessive strength in the shear webs of the spars.

2. Bending-moment data, suitable for comparison with the theoretical dynamic analyses to be conducted, were obtained from the structural-wing model at a 6° angle of incidence at Engebi and from both structural-wing models at Muzin. The 9° angle-of-incidence wing at the 4,020-ft range (Engebi) failed structurally at the root section before the dynamic loading conditions developed sufficiently to be used for analysis. Bending-moment data from the 9° structural wing at the 12,000-ft range (Teiteir) confirmed the prediction of low dynamic loading at this distance.

3. The bending-moment data have no major significance until compared with the theoretical dynamic analysis yet to be conducted. The maximum clearly defined stresses occurred at the

first peak of first-mode vibration of the wing models. The first-mode vibrations occurred at approximately the frequency predicted prior to the test. Second-mode stresses superimposed on the first-mode stresses increased the magnitude of the maximum bending moments at the 6,878-ft range (Muzin).

4. The bending moment measured at the intermediate station of the 6° wing at the 4,020-ft range appears to be much lower than preliminary calculations would indicate although without an apparent source of error. Therefore use of this item of data must be on the basis of possible gross error in measurement.

From the swept-wing models it is concluded that:

1. The swept-wing models were adequately designed and instrumented for the measurement of first-mode bending stresses at the 4,020- and 6,878-ft ranges (Engebi and Muzin). The same models and instrumentation were not sufficiently sensitive to measure accurately the small bending moments occurring at the 12,000- and 16,614-ft ranges (Teiteir and Bokon). Shear loading on the swept wing at Engebi was sufficiently large to overcome the insensitivity of the gauge installation induced by the relative stiffness of the spar webs. Except for this instance the model design and instrumentation were not adequate for the determination of shear and torsion at any of the ranges because of the proportions of the spar webs.

2. Measurements of bending moment, suitable for comparison with theoretical dynamic analyses, were obtained from the swept-wing models at Engebi and Muzin. Bending-moment measurements from the swept wing at the 12,000-ft range (Teiteir) agreed with the prediction of low dynamic loading at this test site. Shear measurements, acceptable for comparison with the dynamic analyses, were obtained only from the swept-wing installation at Engebi.

3. The measurements of bending moment and shear have no major significance except in comparison with the theoretical dynamic analysis, which is as yet uncompleted. The maximum stress recorded for each measurement usually occurred at the first peak of first-mode bending of the swept-wing models. The first-mode vibrations of the swept-wing models occurred at approximately the same frequency as the first-mode vibrations of the structural-wing models, as originally predicted for this test. Second-

mode bending moments superimposed on the first-mode bending moments increased the magnitude of the maximum stresses at the 6,878-ft range (Muzin).

From vane-type angle-of-attack measurements it is concluded that:

1. The split-triangular-vane-type angle-of-attack indicator installed at Engebi measured the variation of the angle of flow of the air mass behind the blast front with an unspecified degree of precision. The weather-vane-type angle-of-attack indicator installed at Muzin was inadequate for the measurement of the variation of angle of flow because of its tendency toward full-scale oscillation when subjected to the dynamic conditions of this test.

2. The specific characteristics of the angle of flow of the air mass at the 4,020-ft range, as given in the following paragraphs, are tentative, based on the results of one instrument, and are subject to investigation by other means in future tests.

3. The air mass was considerably and continuously turbulent at a level 65 in. above the ground.

4. The average flow, eliminating the higher frequency fluctuations, initially possessed a downward component that was replaced at approximately 25 msec by an upward component of smaller magnitude that decreased until at 65 msec no substantial vertical component remained. This flow was maintained until the waning positive-pressure phase introduced large angular variations in the flow.

5. The measurements of the angle of flow at the 4,020-ft range can be used to interpret, analyze, or modify the results of the lift, pressure, or stress measurements obtained.

From a study of the temperatures of structures it is concluded that:

1. The survey of temperature variation with time was extremely limited in scope but provided information on heat transfer through typical aircraft structural configurations.

2. The use of Temp-Tapes was an efficient method for measuring a large number of maximum internal temperatures on aircraft structures exposed to atomic explosions. These temperature measurements appeared to be sufficiently accurate to be used for verification of theories concerning aircraft structure temperatures produced by thermal radiations from atomic explosions. The Stikon and the Trans-

sonic temperature gauges provided a feasible method for measuring the variation with time of both internal and external temperatures of aircraft structures exposed to atomic explosions.

3. The maximum measured temperature rise of the structural-wing models, occurring at a point on the external skin surface where the angle of incidence of the thermal radiation was 25°, for the two sites of record was 67°F for Muzin, 6,878 ft, and 27°F for Teiteir, 12,000 ft. These temperatures were attained in 0.4 sec and were followed by a decrease to approximately 70 per cent of maximum in 2 sec. Equivalent computed temperatures for external-skin-surface points normal to the incident radiation for each site were 329°F for Engebi, 4,020 ft; 175°F for Muzin, 6,878 ft; 57°F for Teiteir, 12,000 ft; and 21°F for Bokon, 16,614 ft. To obtain total temperatures, the ambient temperature, 80°F, must be added to each of these temperature increases.

4. The maximum measured temperature rise of the inside skin surface of the structural wing was 65 per cent of the maximum temperature rise of the corresponding outside skin surface. The measured temperature rise of the spar web was of the order of 10 per cent of the maximum temperature rise of the point of the external skin surface having a 25° angle of incidence to the thermal radiation.

5. The temperatures induced by the thermal radiation of an approximately 50-kt bomb had negligible effect on the structural properties of the wing models while these models were under the dynamic loading of the blast wave.

## 7.2 RECOMMENDATIONS

It is recommended that:

1. The USAF utilize the data that were assembled to define the forcing function or loads imposed on aircraft wings, particularly the rigid-wing model; to perform a dynamic analysis of the structural and swept models, utilizing the forcing function measured on the rigid-wing model; and to check the validity of the method of dynamic analysis, utilizing the bending-moment and shear measurements made on the structural and swept models. The USAF should also utilize the temperature data presented in this report to check the validity of current theories

concerning the aircraft structural temperatures resulting from thermal radiations of atomic explosions.

2. Criteria be devised by the USAF and made a part of the specifications for the design of aircraft and missile structures that would participate in atomic bomb missions and for those likely to be exposed to an atomic bomb explosion. These criteria should restrict the use of exposed (exterior) materials that would be subject to burning, such as fabric used on control surfaces and other opaque nonconducting materials which can be effectively replaced. For components fabricated from nonreplaceable materials, such as rubber tires, sealing strips, deicing boots, and radar domes, other forms of protection should be devised, such as the complete coverage of tires with wheel-well doors, possibly a redesign and relocation of exposed sealing strips, and/or the requirement for reflecting or nonabsorbing (white) materials or coatings.

3. As a result of the data gathered on Operation Greenhouse a new evaluation be made of the effects of an atomic bomb on present military aircraft likely to be exposed in future operations to determine if modifications are warranted to minimize thermal and blast damage.

4. In the selection of the detail design of aircraft structures normally required to carry only small or insignificant loads over large surfaces, such as wing skins near the trailing edge, control surface skins, bomb-bay doors, landing gear, and access doors, consideration be given to the use of materials and combinations of materials (sandwich construction) which result in the greatest structural resistance to pressure differentials on the surface.

5. The minimum safe range from an atomic bomb explosion be determined for operation of conventional combat aircraft with the evaluation specifically including the critical physiological conditions resulting from thermal (and nuclear) radiation which would immediately incapacitate the pilot (and other crew members) to such an extent that loss of the aircraft would follow. It is further recommended that, if operations are restricted because of physical limitations of the crew, passive defense measures be developed.

6. Recording instruments for recording data of the type measured and reported here, with



[REDACTED]

particular attention to oscillograph types, be investigated and evaluated for use in future USAF ground-test programs. This evaluation should include, if at all possible, a complete shakedown test in the presence of an atomic bomb explosion prior to the acceptance of the instrumentation as a basic recording system.

7. After all Greenhouse reports have been prepared, a seminar or school be held for the project officers and their immediate staff wherein the latest fundamental information gained from this operation could be released and discussed. These people are normally responsible for future plans and operations within their own agency or branch of service and therefore should be in a position to formulate decisions based on the latest data to facilitate maximum utilization of the present knowledge.

8. A more detailed investigation be made of the blast-front characteristics and the flow of the high-velocity air in the vicinity of the ground; this should include a survey up to heights of 70 ft for purposes of USAF ground tests.

9. Additional tests of the effects of atomic bomb explosions on aircraft structures located on the ground be conducted. These tests should include, but not be limited to, the following:

- (a) An investigation of the problem of protection (revetments) of aircraft while in a ready position on the ground.
- (b) A more extensive test of the thermal-radiation effects, including a more in-

tensive temperature survey on materials and coatings utilized in aircraft and missile construction.

- (c) A test of aircraft structures, exposed with varying degrees of the largest projected area facing the atomic bomb explosion, to determine the effect of overpressures combined with the dynamic lift and drag loads.
- (d) An investigation of the variation of the angle of flow of the air mass behind the blast front by means of differential-pressure-wedge arrays.

10. In the event of future tests of the effects of atomic bomb explosions on similar aircraft model structures, the methods of instrumentation should include, but not be limited to, the following:

- (a) The omission of differential-pressure measurements at ranges experiencing less than 3 psi overpressure.
- (b) An improvement in the reliability and/or the quantity and distribution of the differential-pressure-sensing units.
- (c) A more adequate survey of differential pressures in the region aft of the 40 per cent chord point of the wing models.
- (d) An improvement in the balance and support system for wings of the rigid-model type to minimize the excitation of natural frequencies of the system.
- (e) The design of wing models of the structural and swept type in a manner facilitating the measurement of torsion and shear stresses.



Fig. 1.1 Typical installation of the Rigid and Structural Models before Bomb Burst. The rigid wings are mounted horizontally between the vertical pylons. The structural-wing models are mounted as horizontal cantilevers on the outer pylons. The diagonal rods increase the rigidity of the supporting pylons.

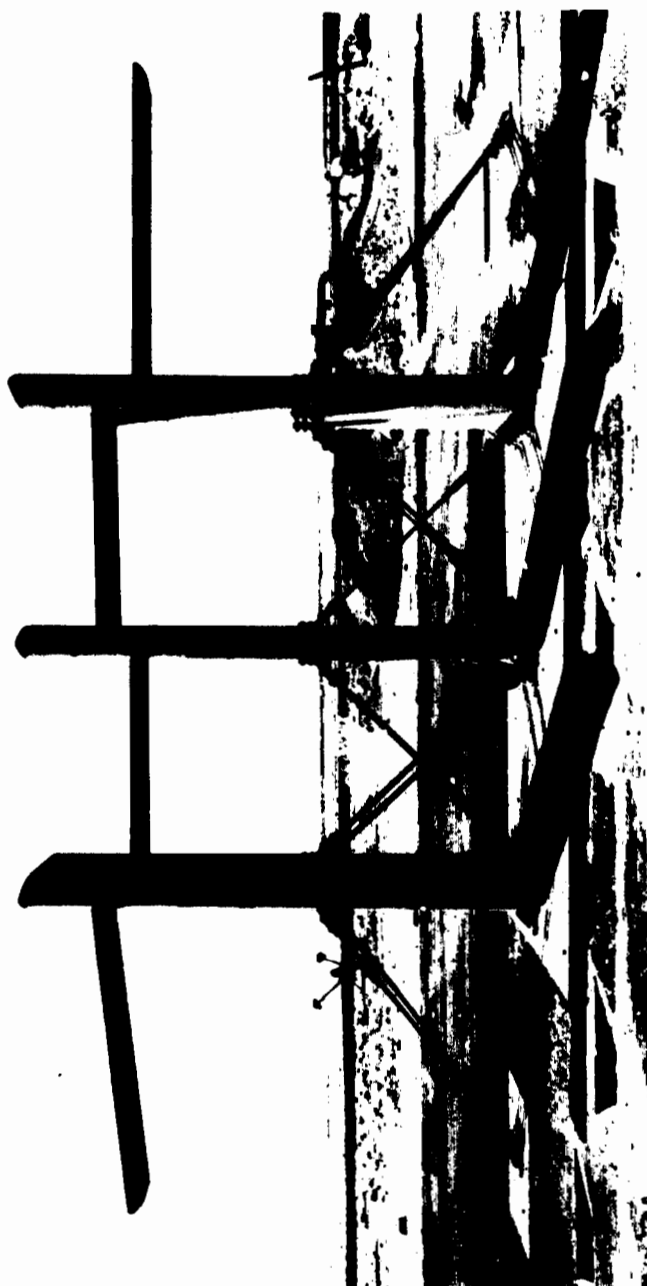
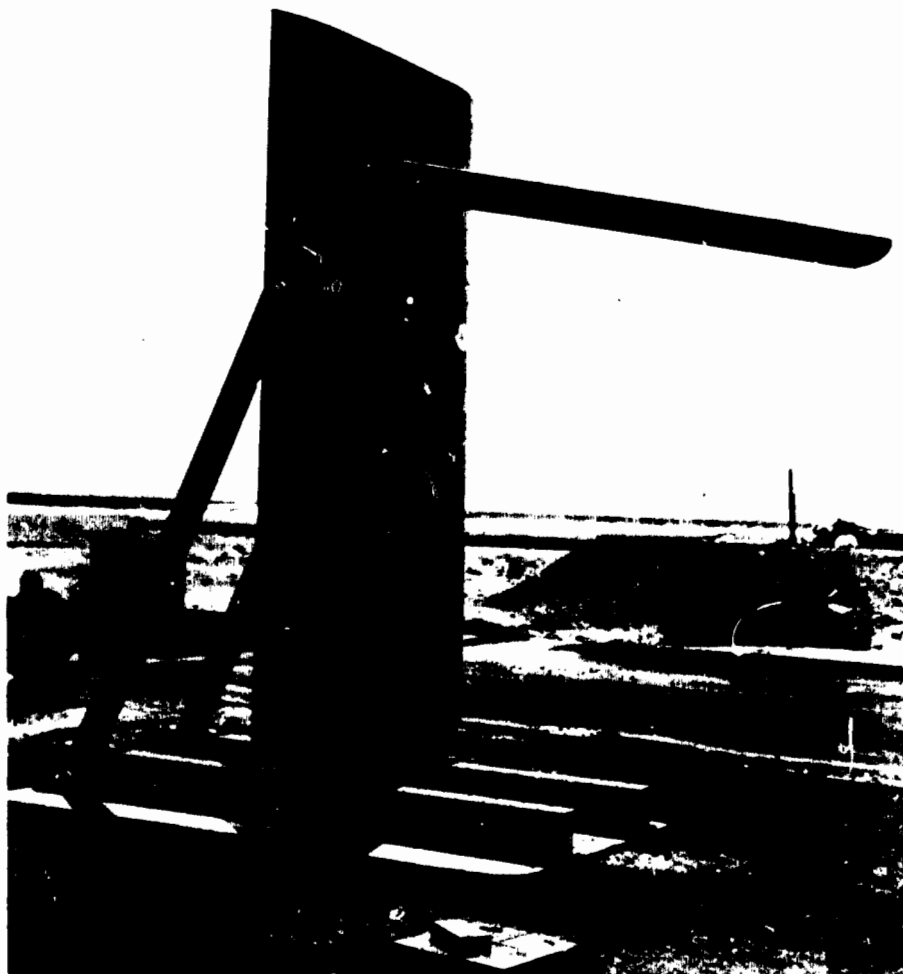


Fig. 1.2 Rigid- and Structural-wing Models on Engebi, Range 4,020 Ft, after Detonation. The structural model 104 at left failed at the root and is actually free to fall except for being wedged in place; note droop.



**Fig. 1.3 Typical Installation of Swept-wing Model before Bomb Burst, Engebi, Range 4,020 Ft. The vane-type angle-of-attack measuring device was not mounted on the pylon supporting strut at the time of this photograph.**

UNCLASSIFIED

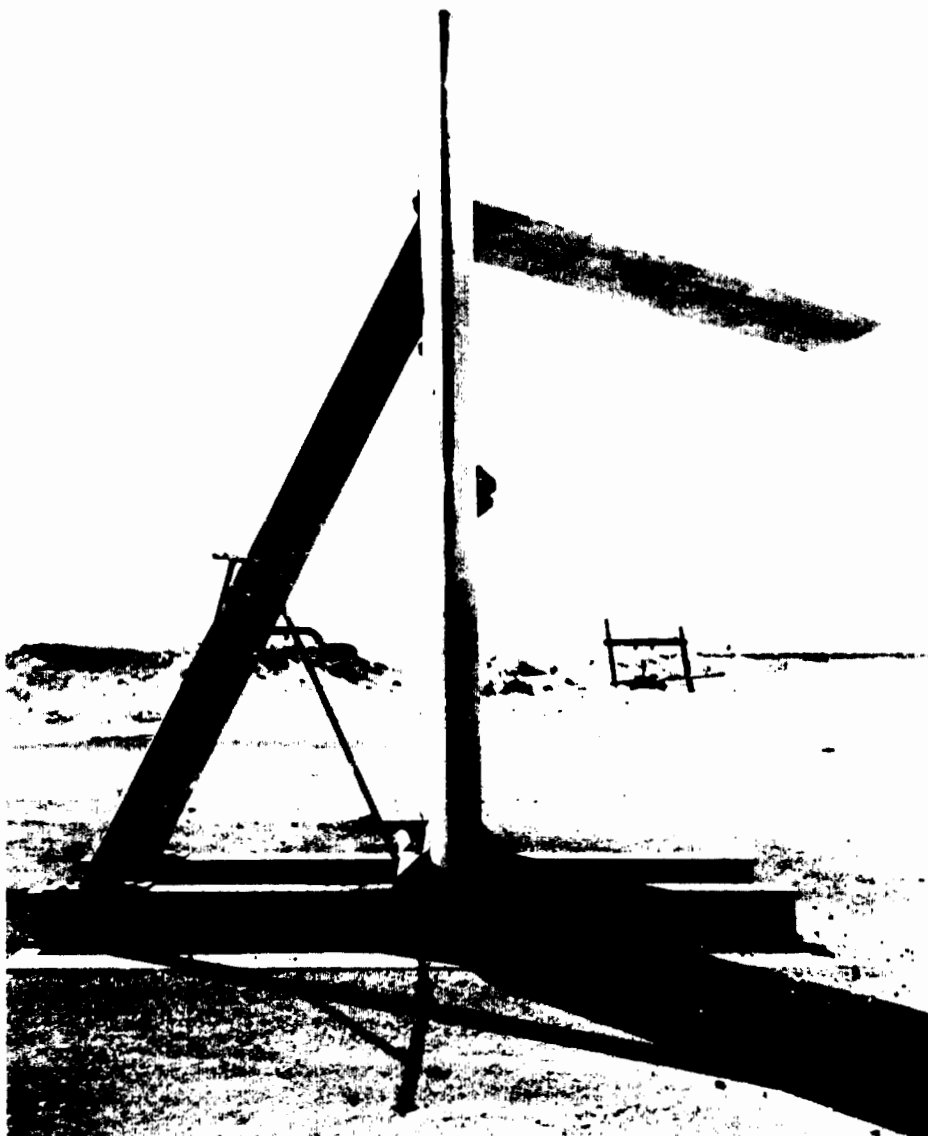


Fig. 1.4 Swept Model on Engebi after the Explosion. The scorched paint on the large strut and leading edge of the pylon is the only visible damage to this test installation (see Fig. 1.3).

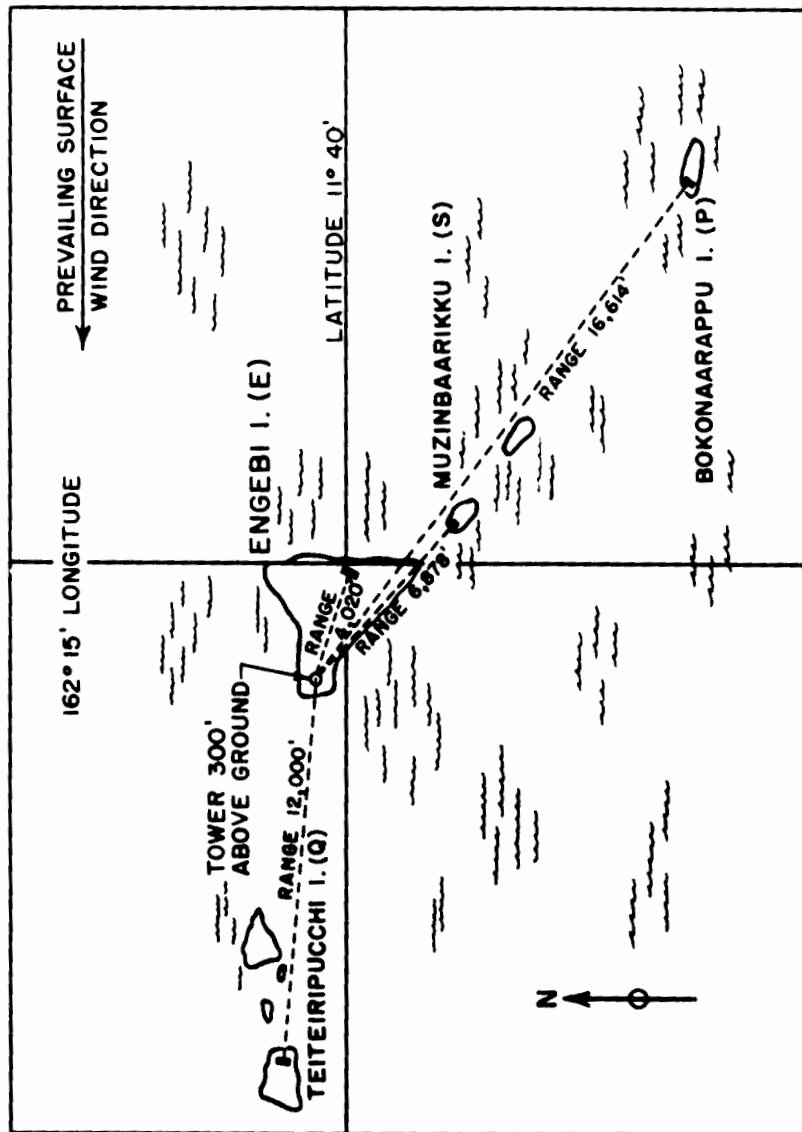


Fig. 1.5 Relative Locations of Project 8-2 Island Sites, Their Respective Ranges from the Shot Tower, and Other Related Data



Fig. 1.6 Aerial View of Engbel Illustrating the Relative Location of Project 8.2 Test Site and Other Test Installations. The test site appears in the left foreground 4,020 ft from the tower near upper center. Ground has been graded relatively flat and the final clearing of debris is in process. Teletiripucchi Island may be seen in the distance as the third island from the tower.

UNCLASSIFIED

2

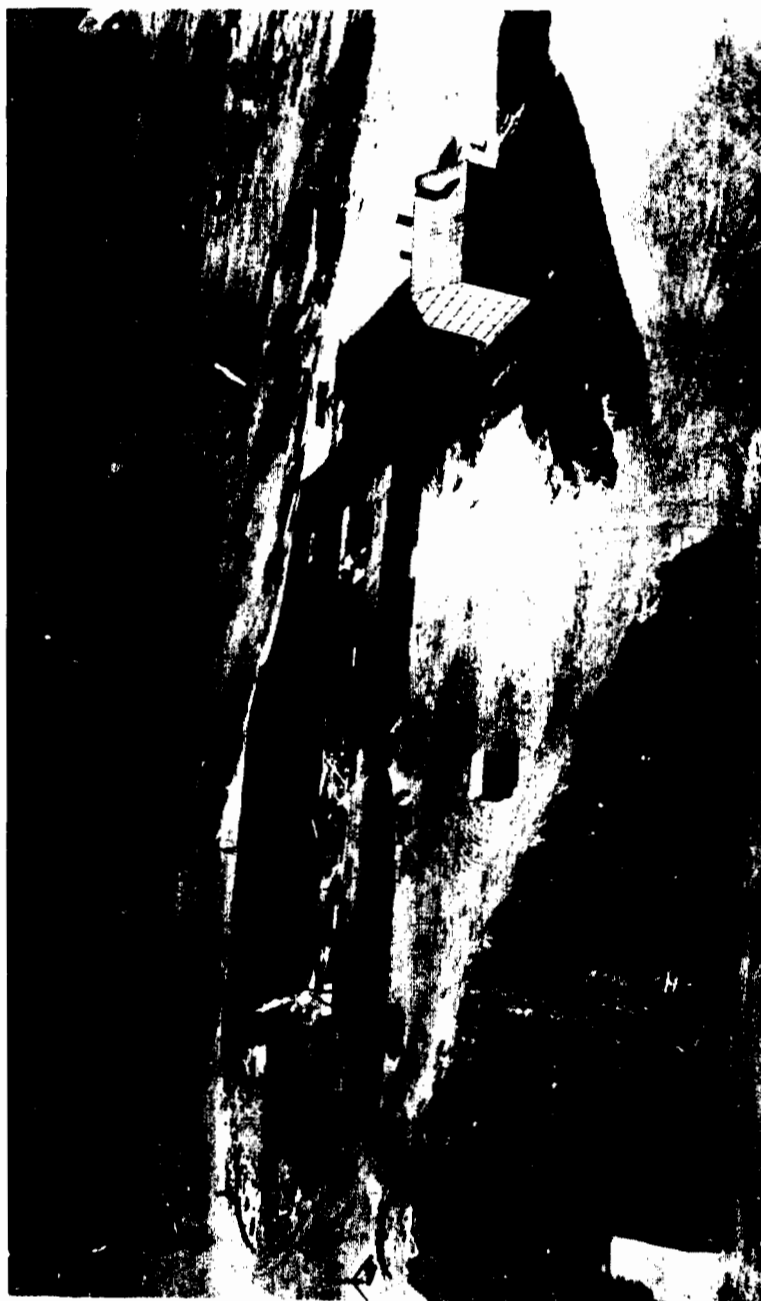


Fig. 1.7 Aerial View of the Test Site on Muzin. The photograph was made from the rear toward the shot tower on Engebi. The 25-kw generator in the submerged sandbag revetment and the partially submerged instrument house may be seen in the approximate center of the photograph. The Project 8.2 test site extended from these articles forward to the beach. The stabilization of sand about with an oil emulsion is apparent. Relative size and distances to other test buildings may be noted.

UNCLASSIFIED





Fig. 1.8 Aerial View of the Test Site on Teiteir. The photograph was made from the rear toward the shot tower on Engabl. For orientation the shot tower may be seen in the distance. The oil emulsion for stabilization of the sand, having been freshly applied, appears exceptionally dark in this photograph. The partially submerged instrument house may be seen in the rear of the test articles.



Fig. 1.9 Aerial View of the Test Site on Bokon. The photograph was made from the rear toward the shot tower on Engabl. The shot tower can be distinguished in the upper right corner of the photograph.

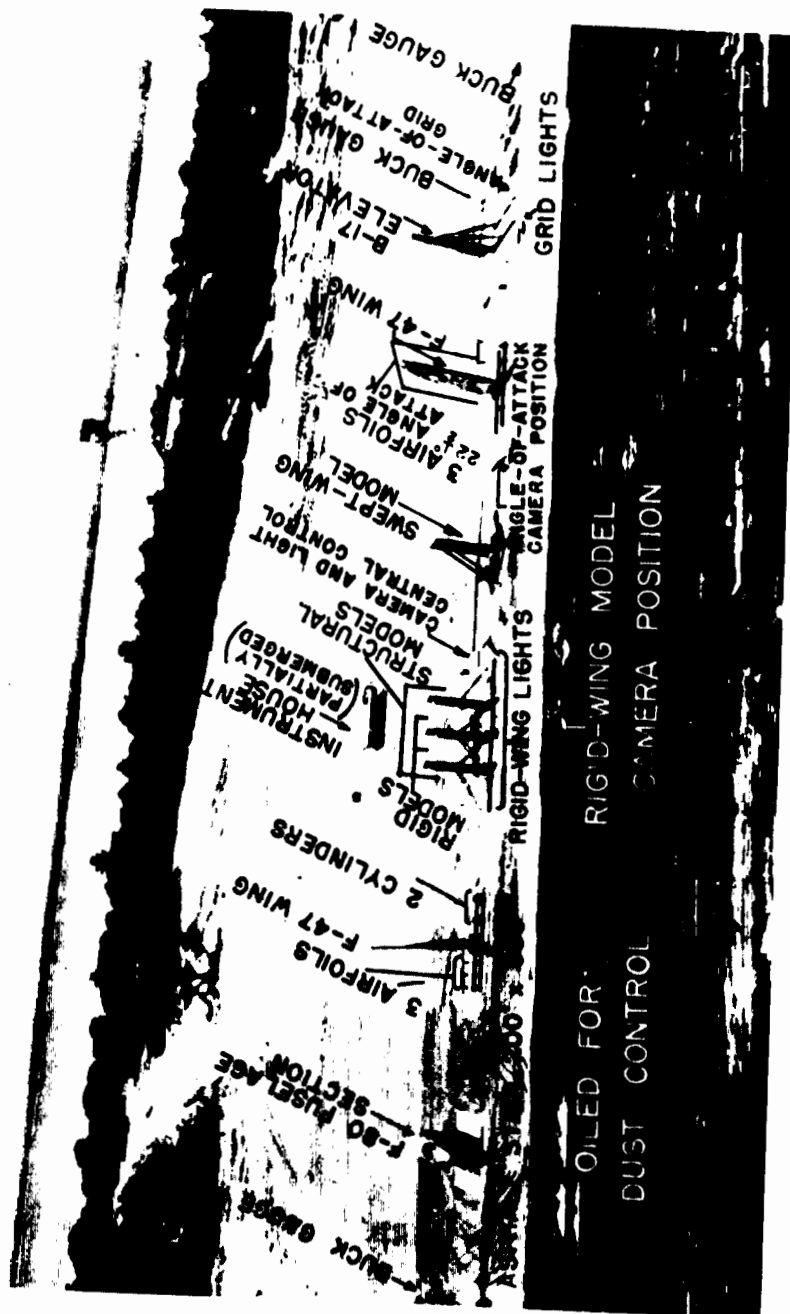


Fig. 1.10 Aerial View of a Typical Test Array, Teiteir, after Bomb Burst, Range 12,000 Ft. Notations have been added to the photograph indicating location of test articles and equipment.



Fig 1.11 Rear Oblique View of a Typical Test Array, Muzin, Range 6,878 Ft



Fig. 1.12 Exterior View of the Instrument Room on Engebi before Bomb Burst, Range 4,020 Ft. The cement dam inside the door was necessary to keep water out of the room at high tide.



Fig. 1.13 Typical Interior View of a Submerged Instrument Room, Engebli. The rectifiers and batteries for the recorder system are supported on the wooden stand in the center of the picture. The time-signal relays are on the bench at the right. Ducting at the top of picture was part of the forced-air system to cool and remove fumes from the instrument room.

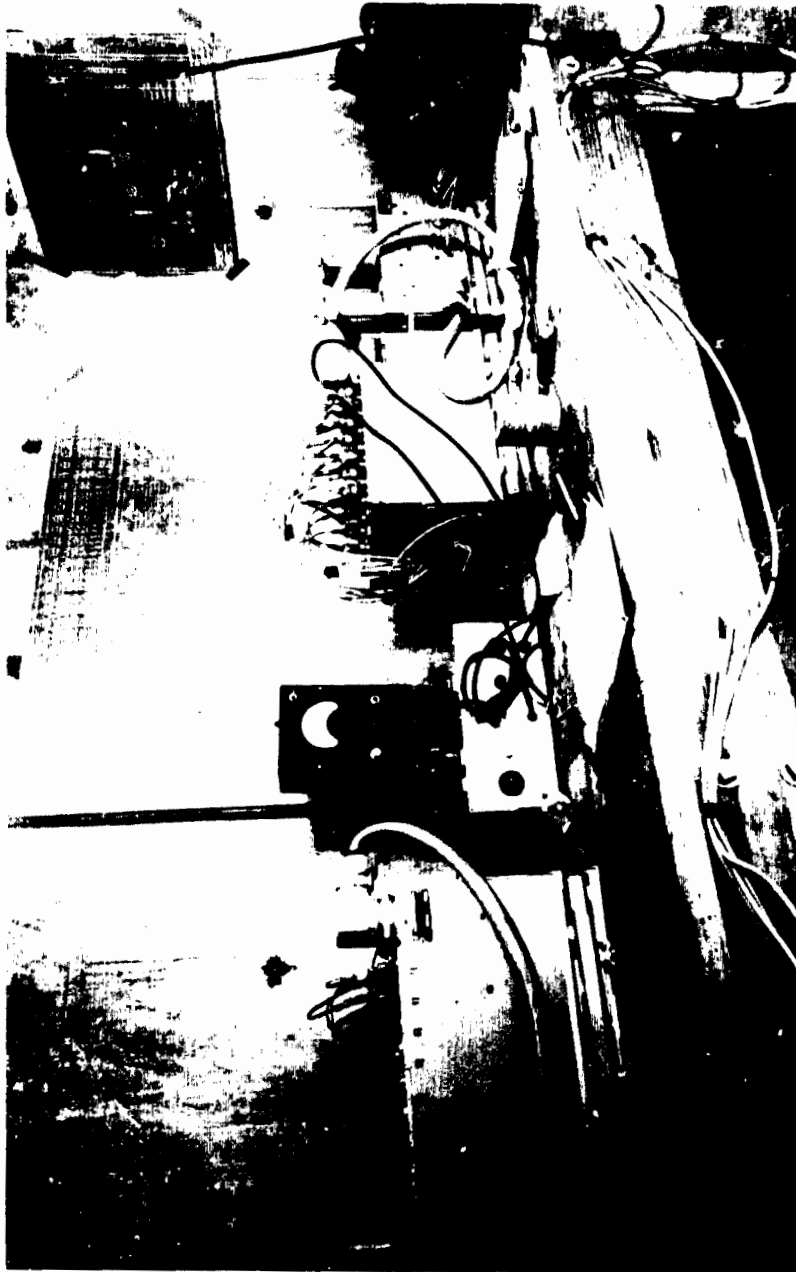


Fig. 1.14 Typical Interior View of a Submerged Instrument Room, Engebii. The amplifier and recorder units comprising one of the 24-channel recorders may be seen on the right side of the bench. The amplifier unit of the second recorder system can be seen at the left. The test unit in the center of the photograph is between the two recorder systems.



Fig. 1.15 Typical Interior View of a Portion of a Submerged Instrument Room, Bokon. The wires from the structural, rigid, and swept models were conveyed underground in the two conduits and are shown here entering the instrument room.



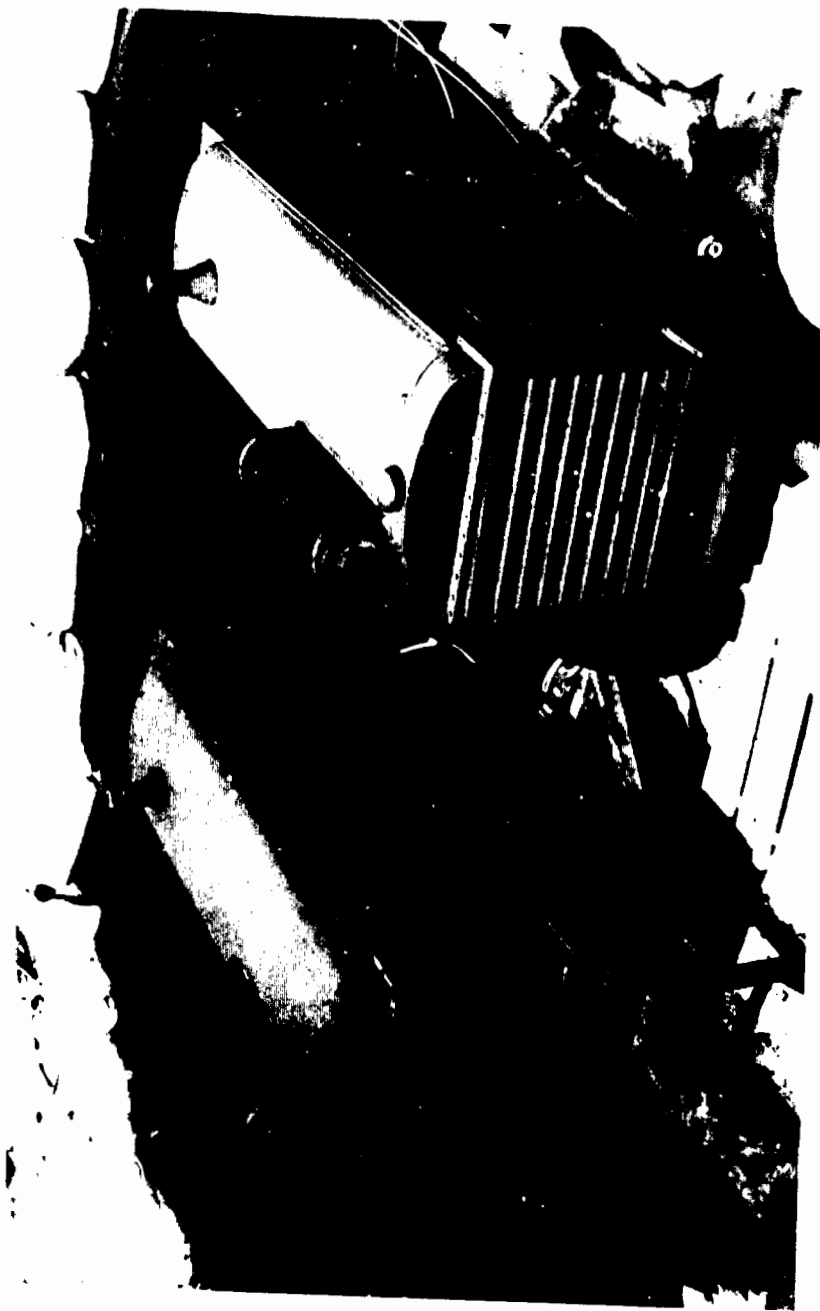


Fig. 1.16 View of the Two 7.5-kw Generators Installed on Engebii, Range 4,020 Ft, before Bomb Burst



Fig. 1.17 Same Generators as in Fig. 1.16, after Explosion, Engebi, Range 4,020 Ft. These generators both functioned successfully unattended through the atomic explosion and were turned off manually after approximately 21 hr of continuous automatic operation.



Fig. 1.18 View of 25-kw Generator Installation on Muzin before Bomb Burst. Auxillary 55-gal drum for extension of unattended operating time can be seen to rear of generator.



Fig. 1.19 View of 25-kw Generator on Muzin, Range 6,878 Ft., after Detonation. This generator operated successfully through the atomic explosion and was turned off manually on return of personnel after approximately 20 hr of continuous automatic operation.

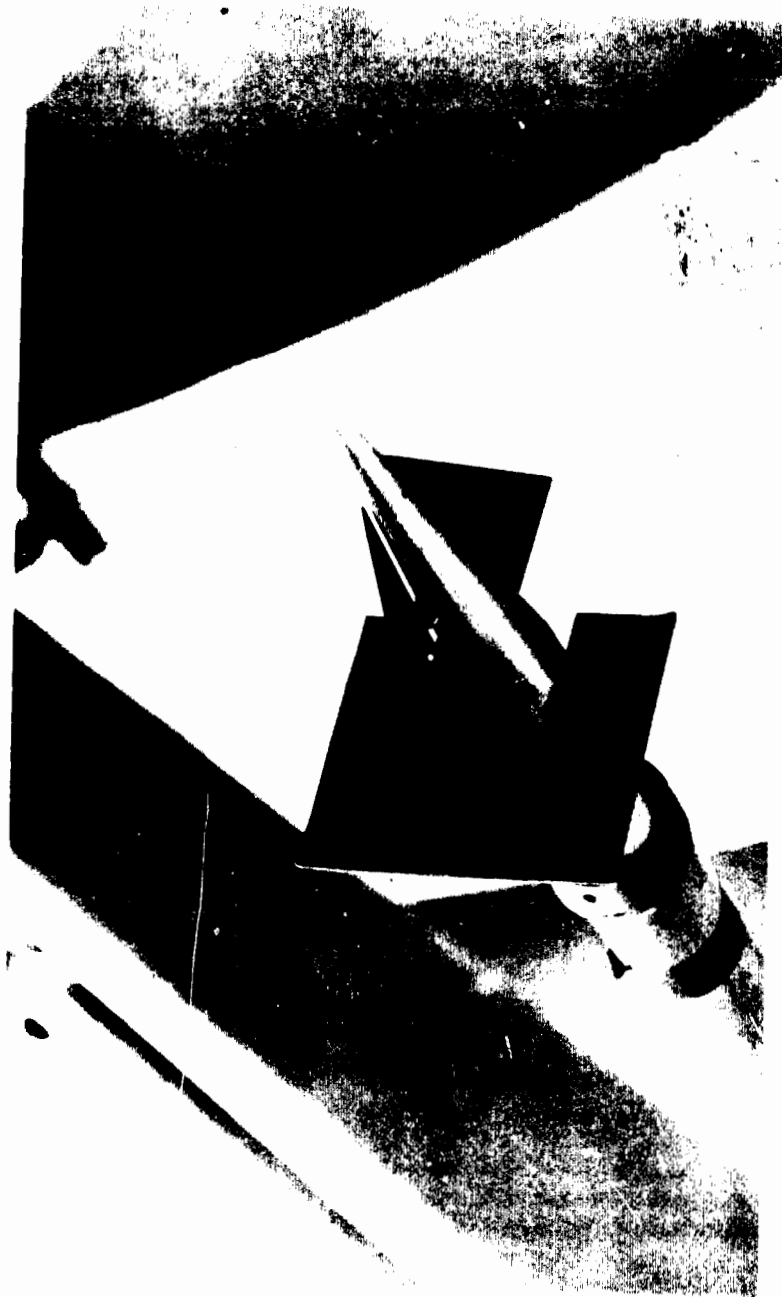


Fig. 1.20 Split-triangular-vane-type Angle-of-attack Indicator, Engebi, before Bomb Burst. The fiber-board card holding the triangular vane at zero displacement was blown off by the blast front.

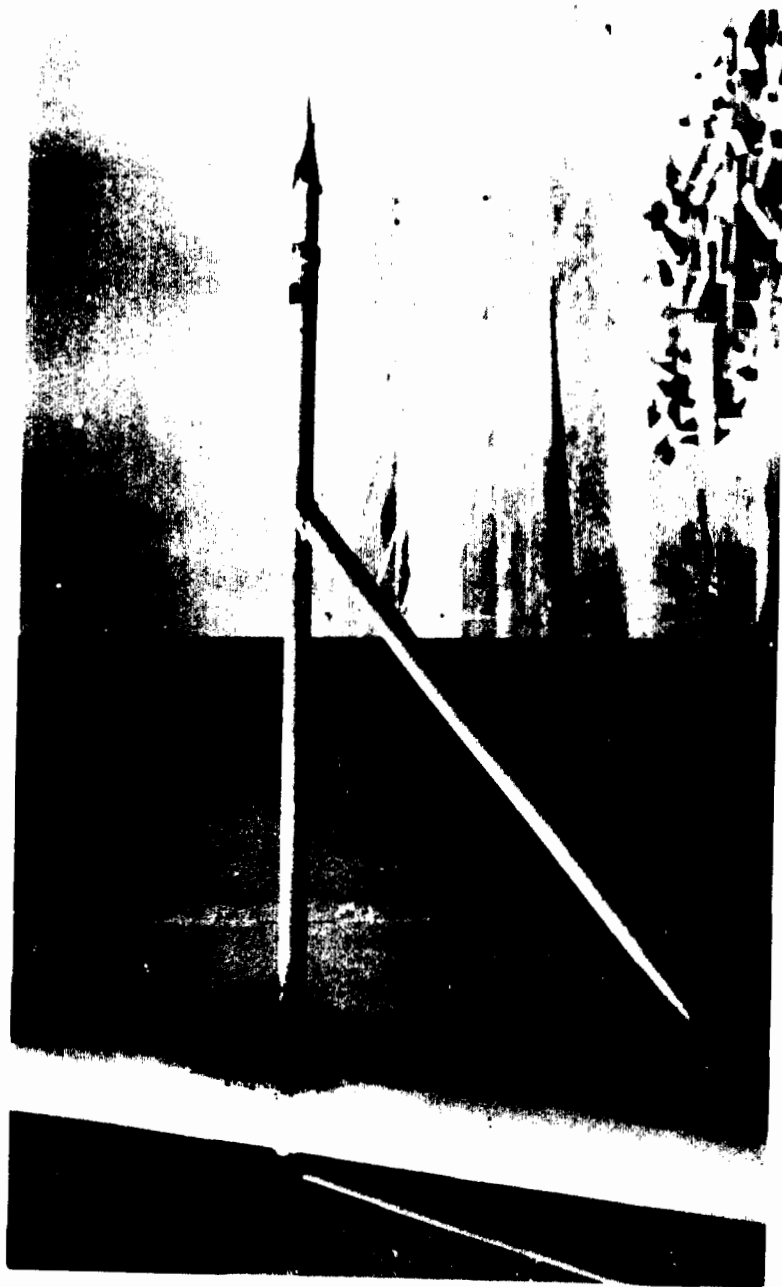


Fig. 1.21 Installation of the Split-triangular-vane-type Angle-of-attack Indicator (Engebi after Bomb Burst) on the Forward Strut of the Swept-wing Pylon. The only visible effects of the atomic bomb explosion are the burned paint on the front faces of the structure, the ribs impressed on the skin of the forward section of the pylon, and the absence of the fiberboard card from the indicator.

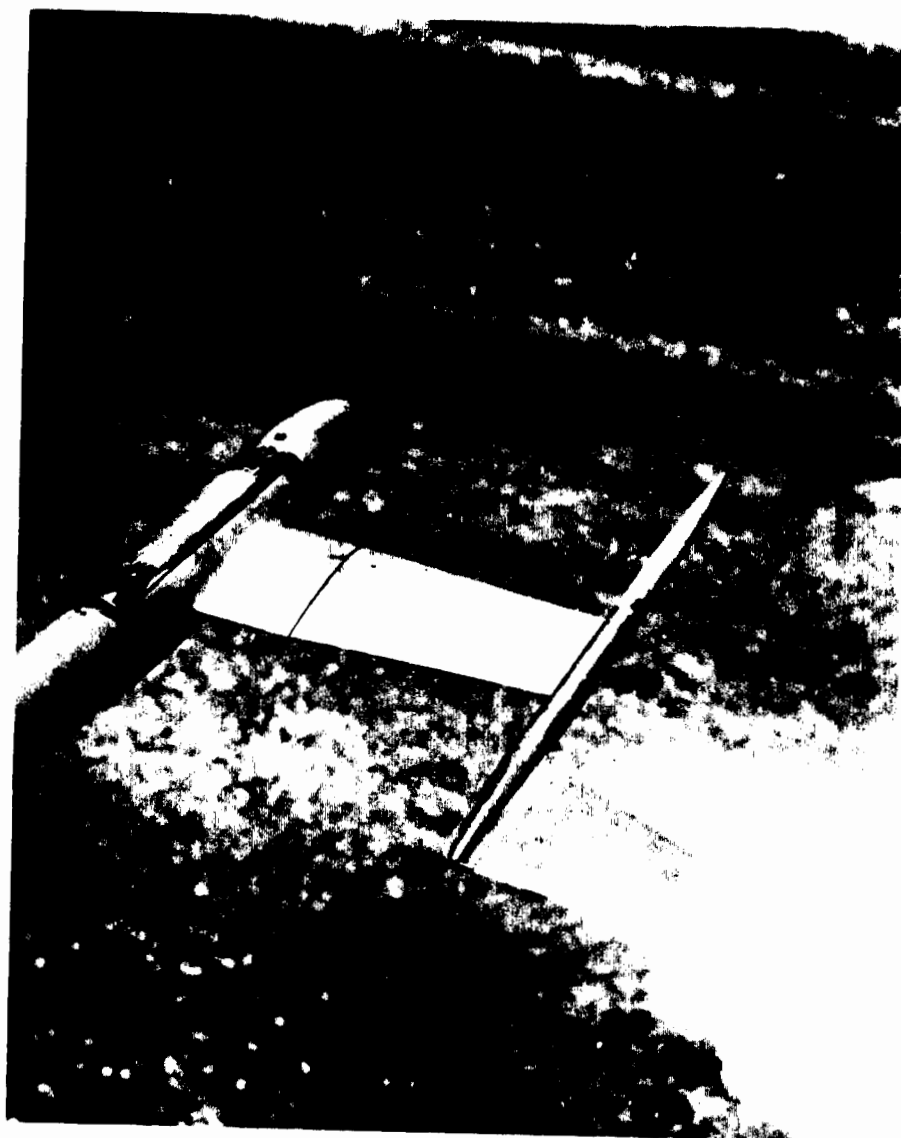


Fig. 1.22 Vane-and-slender-body-type Angle-of-attack Indicator, Muzin, Range 6,878 Ft, before Bomb Burst

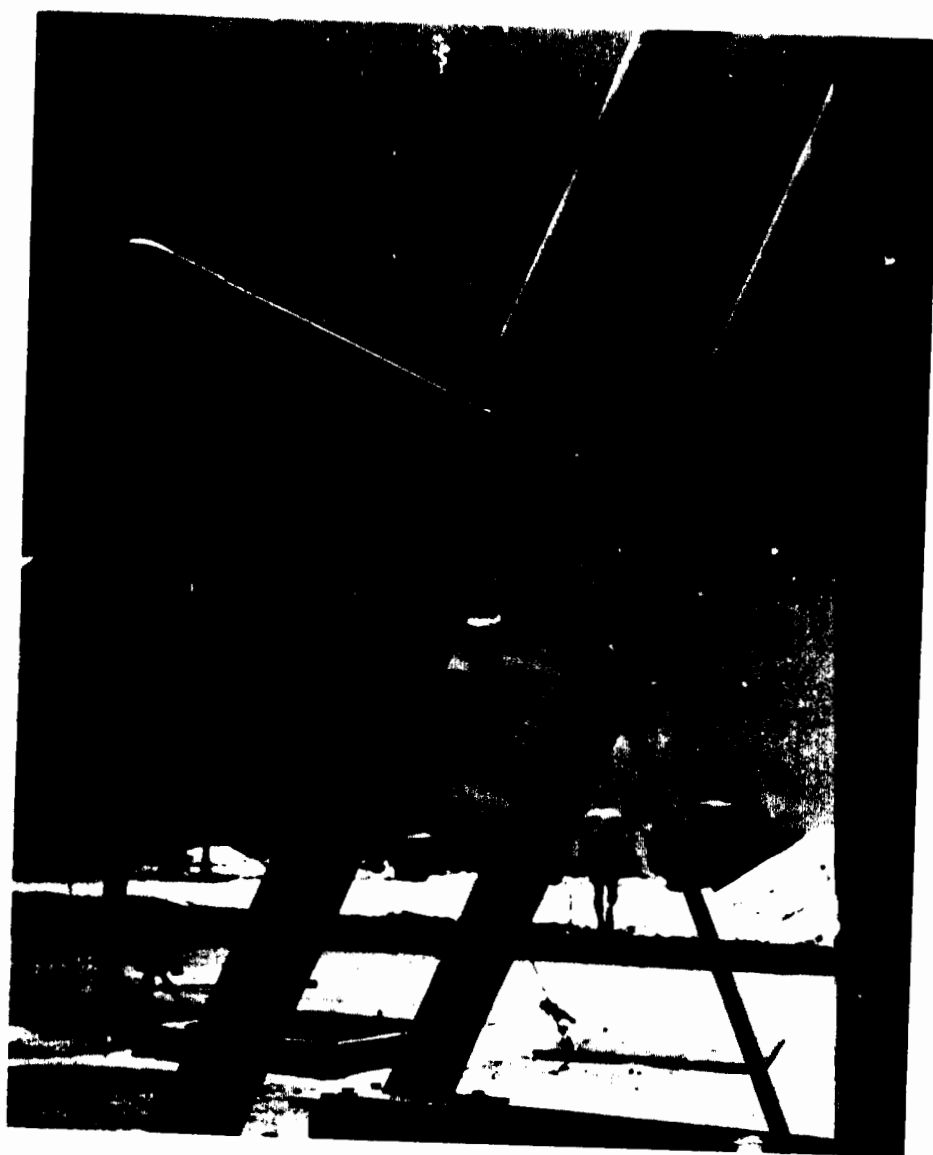


Fig. 1.23 Installation of Vane-and-slender-body-type Angle-of-attack Indicator, Muzin, Range 6,878  
Ft, before Bomb Burst



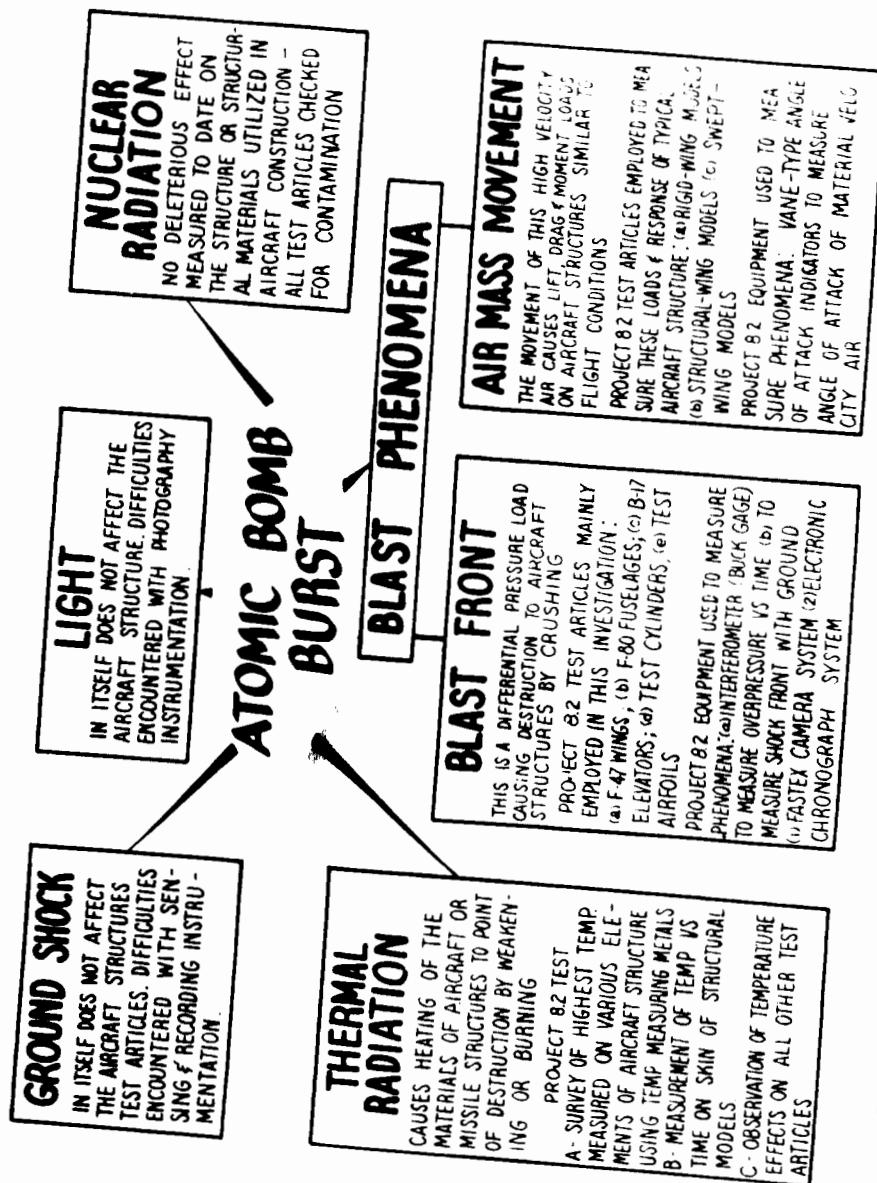


Fig. 2.1 Schematic Diagram Illustrating the Division of Energies and Forces Released by an Atomic Bomb Explosion As Related to Project 8.2 Ground-test Program and the Aircraft Structures Problems

UNCLASSIFIED



Fig. 2.2 Typical F-80 Fuselage Test Installation, Engeli, Range 4,020 Ft, before Bomb Burst. The Temp-Tapes can be seen on inside surface of the canopy. The dark portion of the fuselage nose is the laminated-glass plastic radar dome.



Fig. 2.3 Fuselage on Engebl after the Atomic Bomb Detonation. Note absence of Temp-Tapes from canopy, wrinkle in fuselage skin near the nose, and the burned appearance of the radar dome.



Fig. 2.4 Left Side of the F-80 Fuselage Nose on Engibi after Bomb Detonation. The shallow dished area about the removable panel under the large F, range 4,020 ft, is shown.

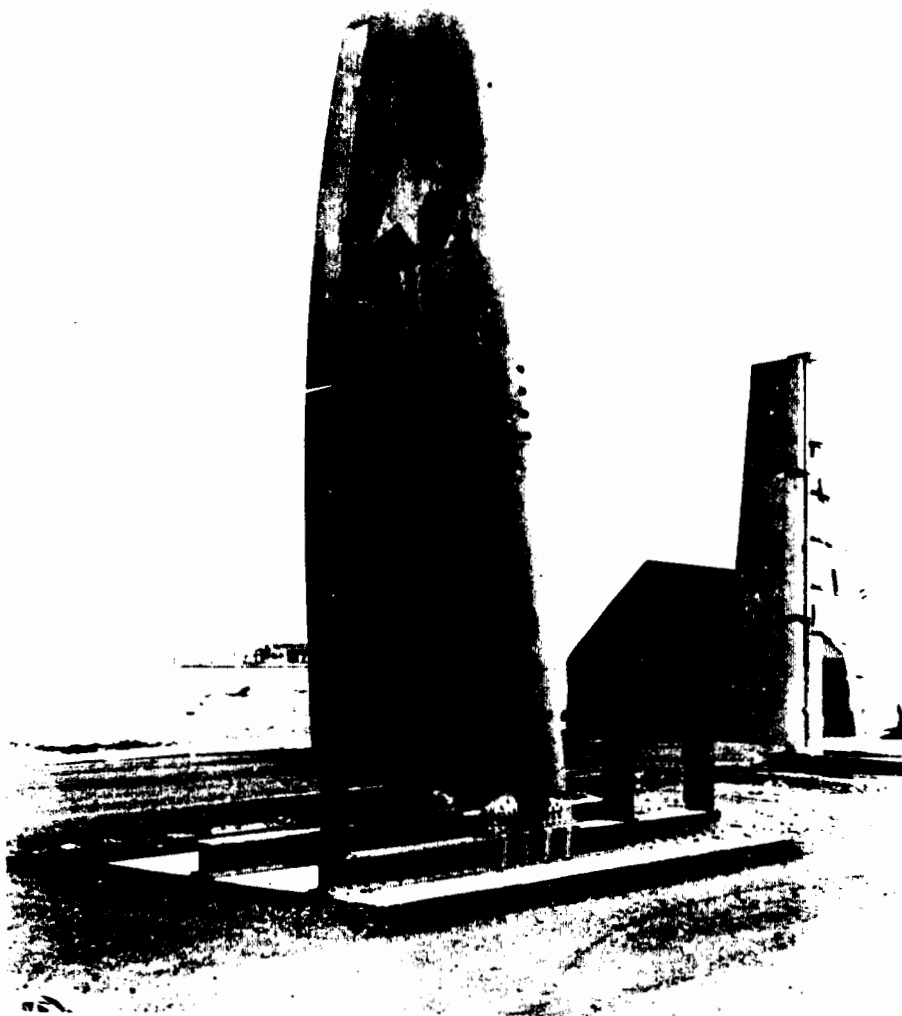


Fig. 2.5 F-47 Wing, Aileron, and Flap Installation and the Small Airfoils Set at  $22\frac{1}{2}^{\circ}$  on Engebi, Range 4,020 Ft, before Bomb Burst

UNCLASSIFIED

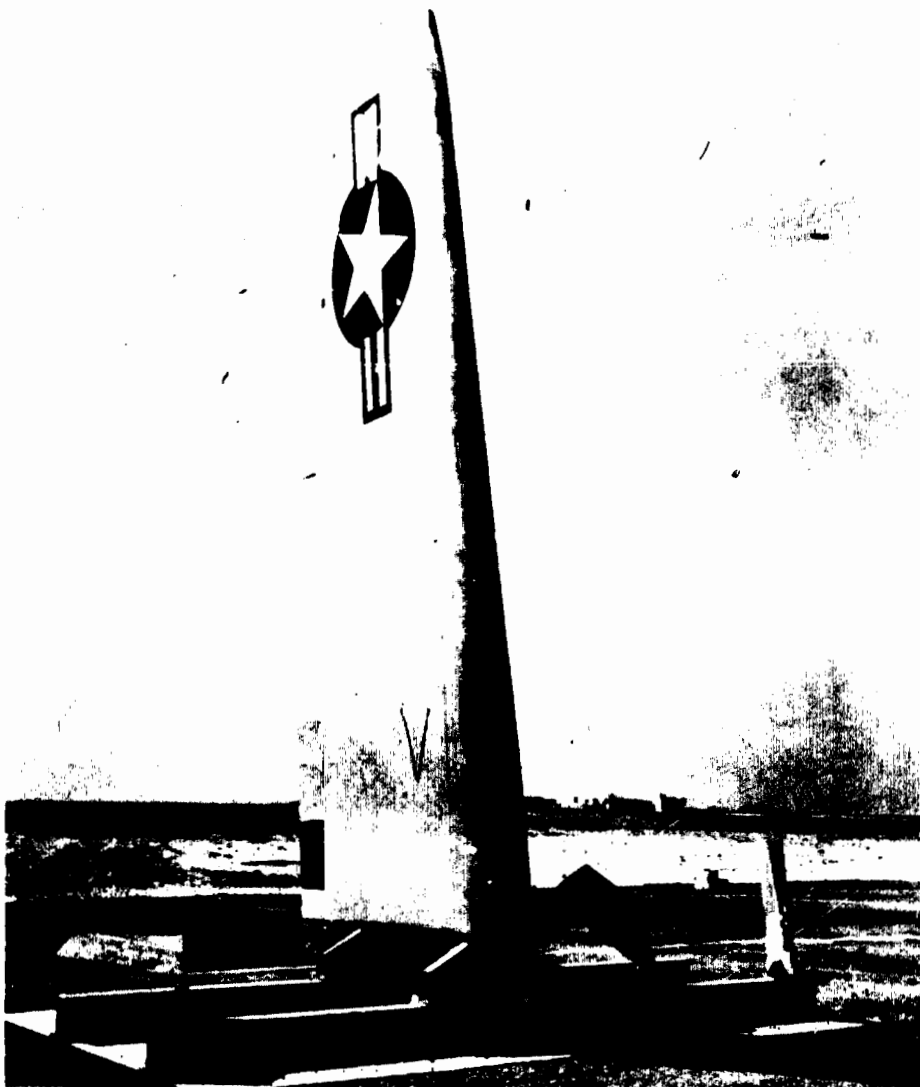


Fig. 2.6 F-47 Wing and Airfoils on Engebi, Range 4,020 Ft, after Detonation. The impression of the internal structure on the skin and the depression of the skin between the ribs is evident. The skin dents on the leading edge near the tip may be seen. The airfoils failed under combined bending and torsion loads.

UNCLASSIFIED

UNCLASSIFIED

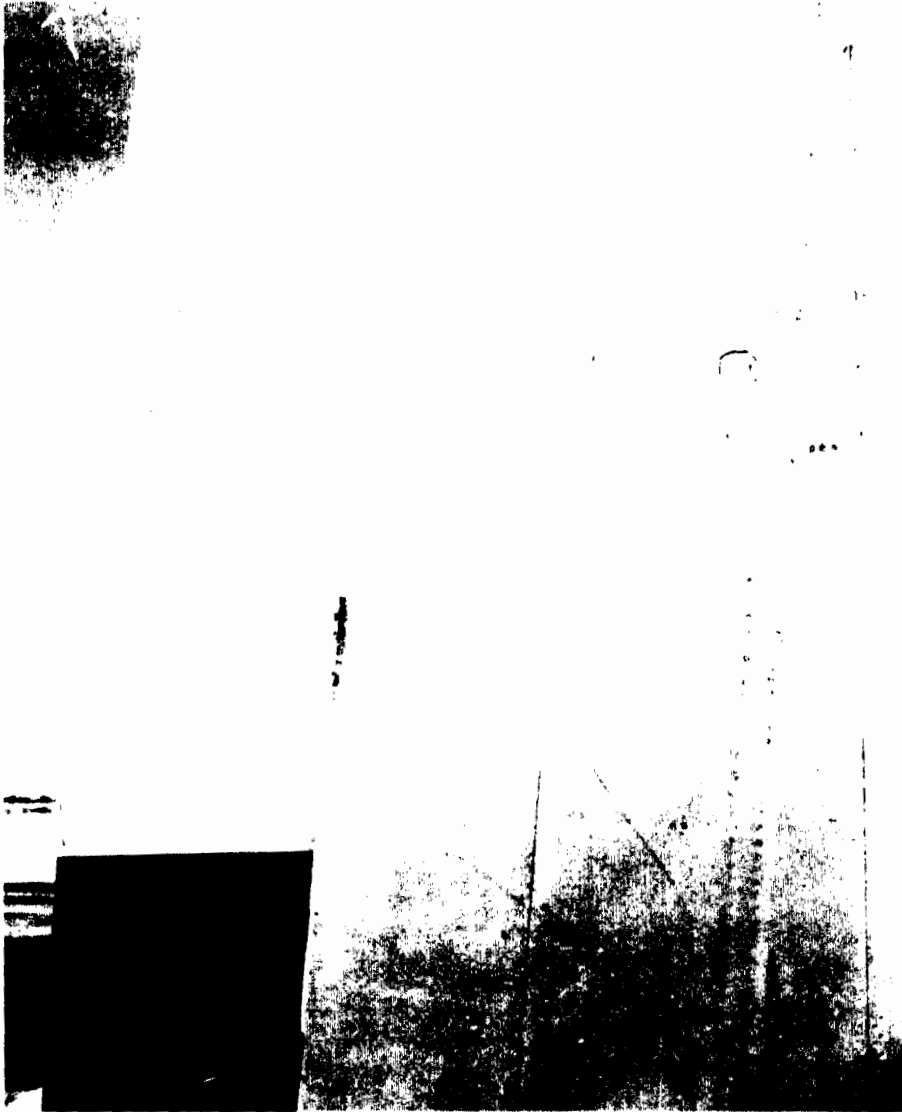


Fig. 2.7 Portion of the F-47 Wing of Fig. 2.6 Showing Structural Damage, Engebl, Range 4,020 Ft, after Detonation

UNCLASSIFIED

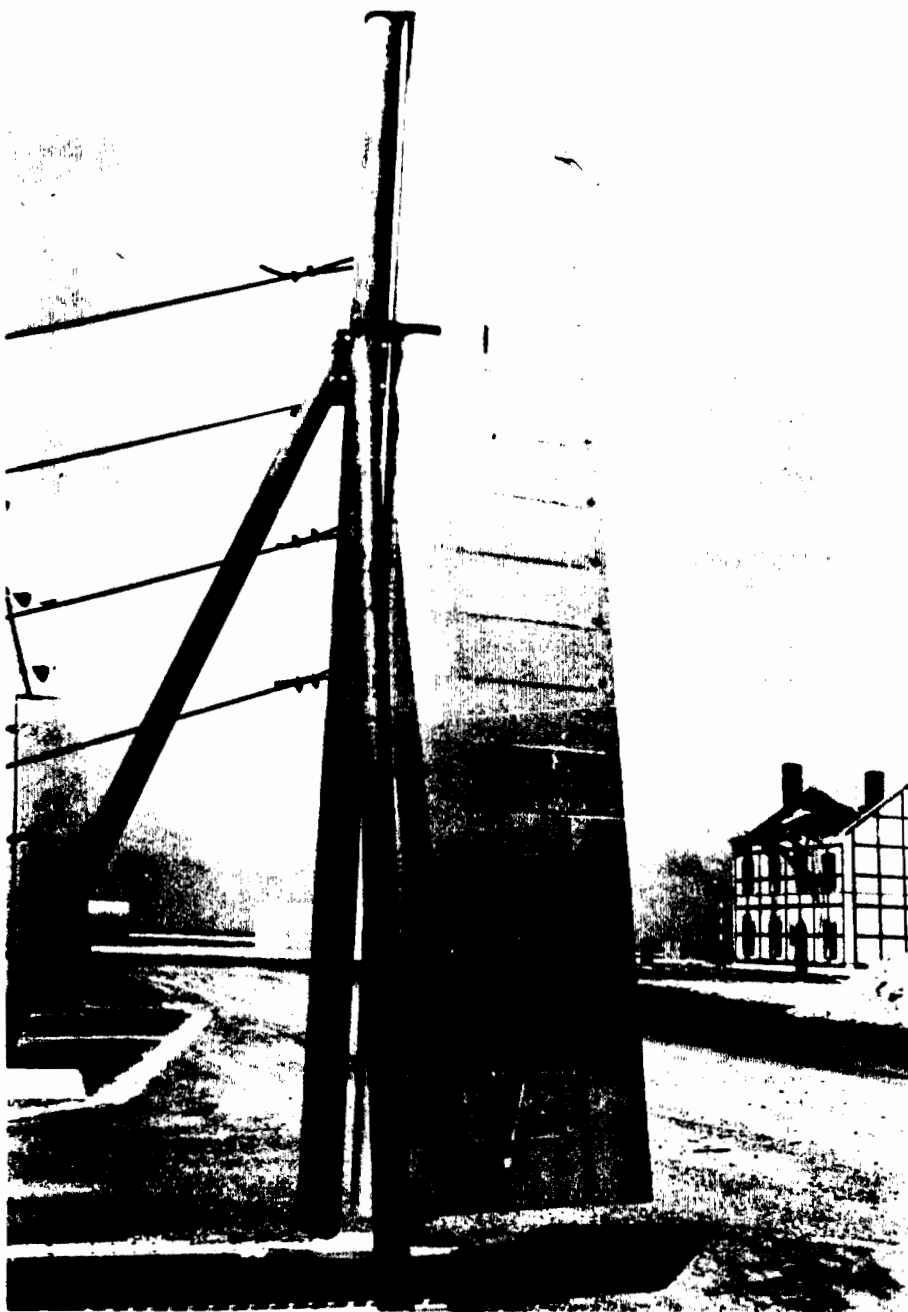


Fig. 2.8 B-17 Elevator on Muzin, Range 6,878 Ft, after Bomb Burst. No damage of any type was sustained.



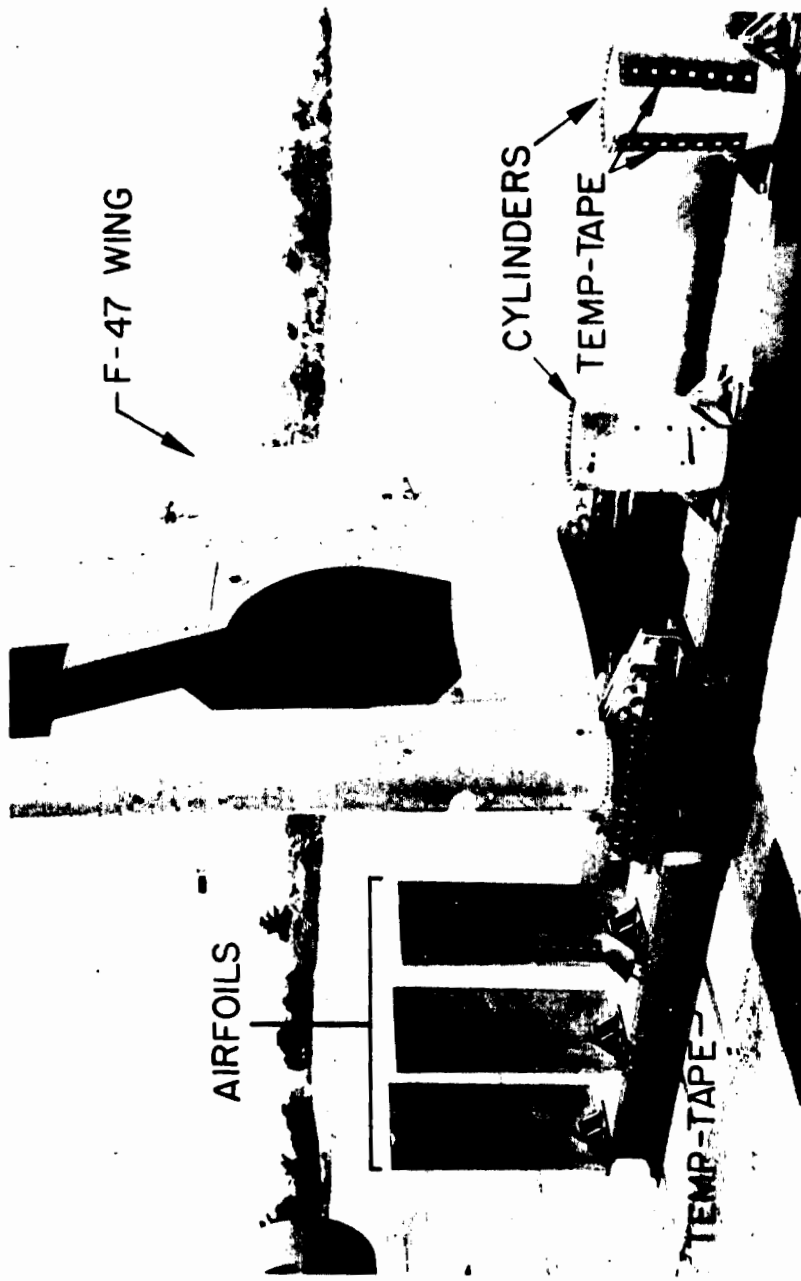


Fig. 2.9 Typical Airfoil and Cylinder Installation before Bomb Burst, Telteir, Range 12,000 Ft. These airfoils are set at 0° angle of incidence.

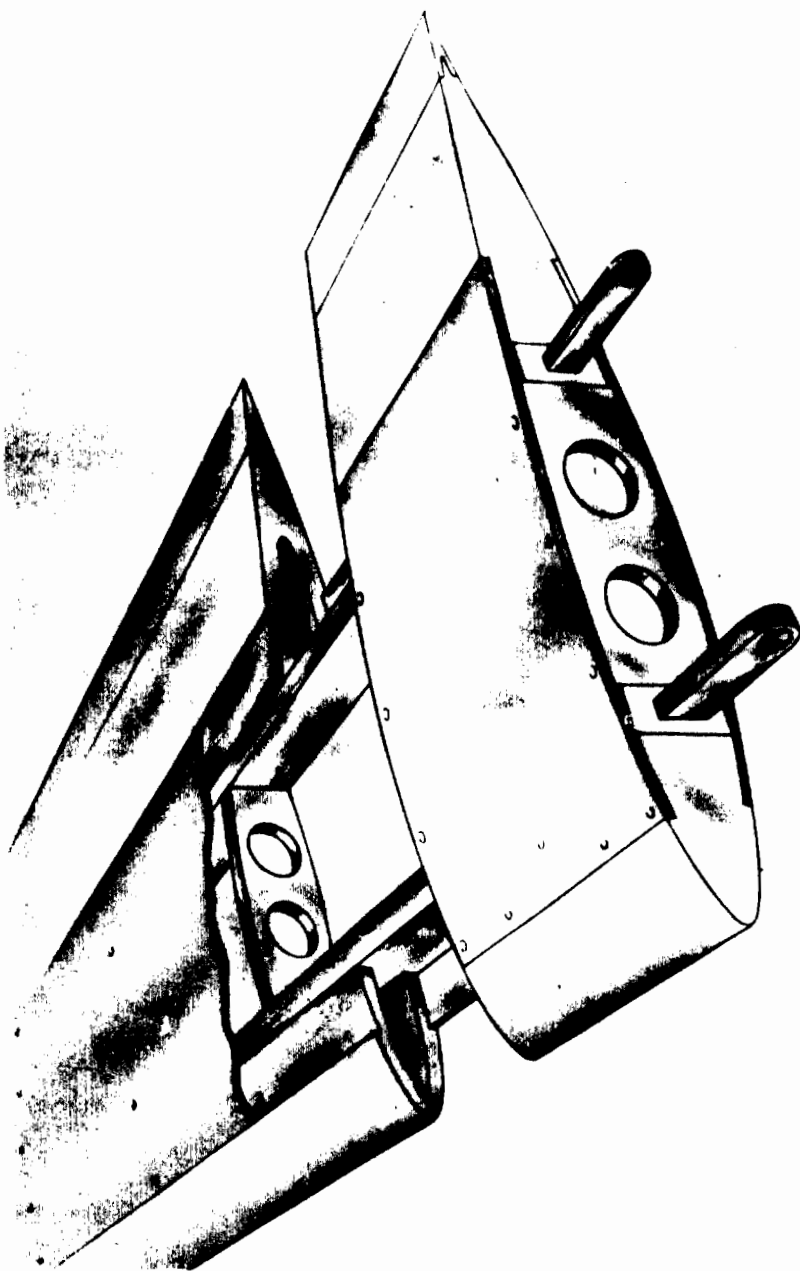


Fig. 2.10 Schematic Drawing Illustrating the Construction of the Rigid Wing

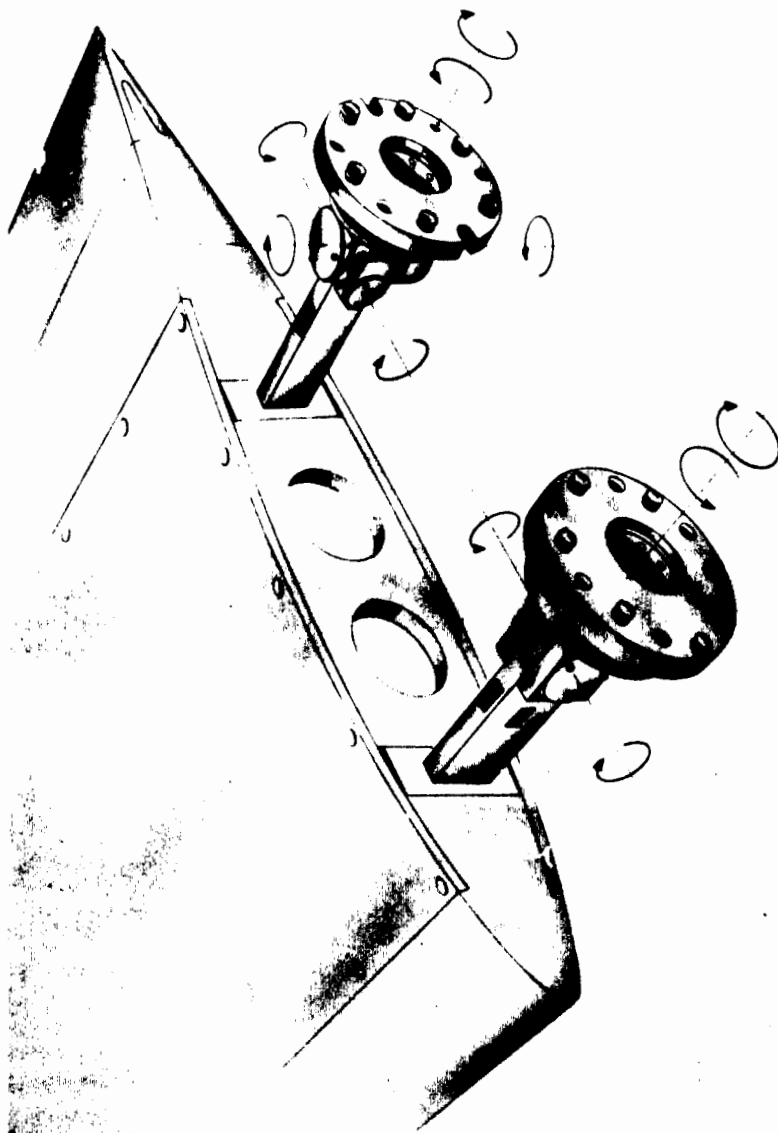


Fig. 2.11 Schematic Diagram of the Rigid-wing Model, Illustrating the Functioning of the Balance System

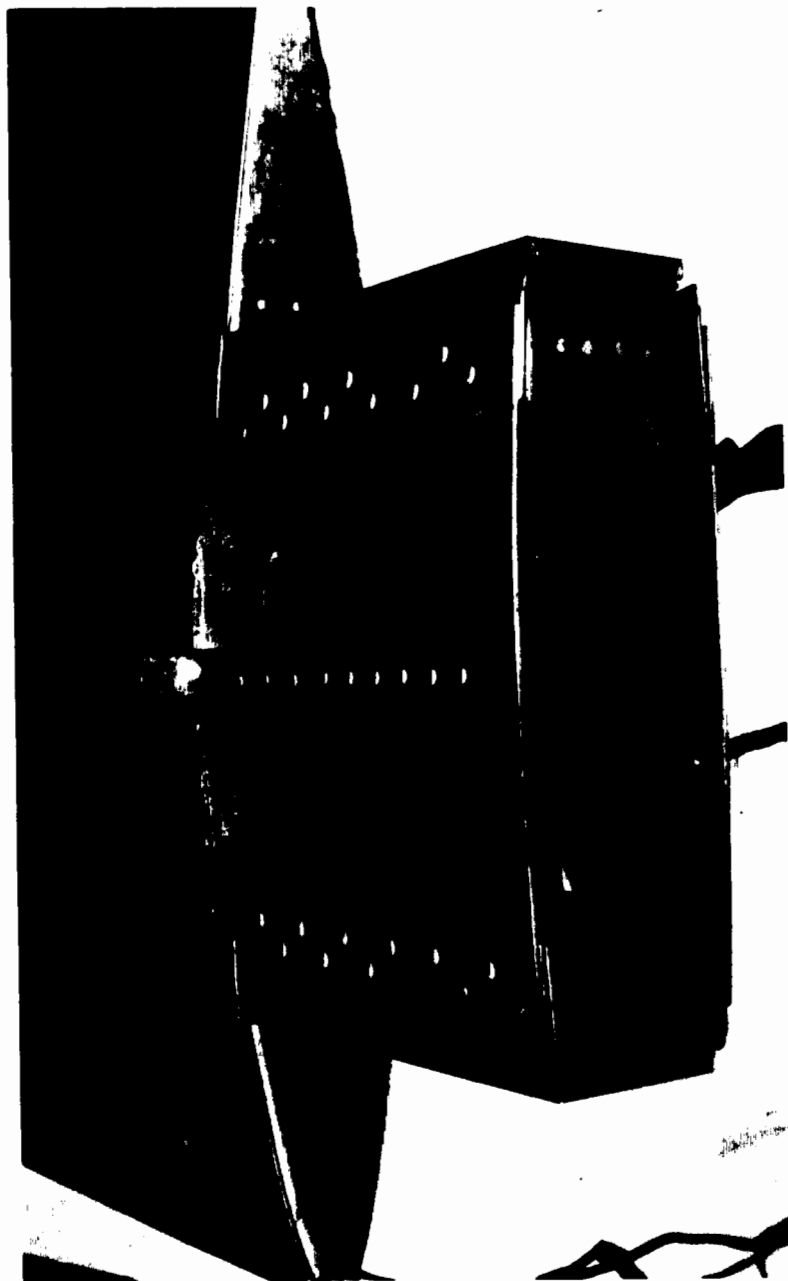


Fig. 2.12 Details of Failed Structural-wing Root Section on Engebi, Range 4,020 Ft, after Detonation. Cracking of both upper and lower spar caps of the root attachment may be seen at A and B. Completely failed intermediate stiffener has been suspended on two wires to show normal position.

UNCLASSIFIED



Fig. 2.13 View of the Failed Structural Model 104, Engabi, after Bomb Burst. Sheared rivets at parting face of root fitting E from spar web, bent spar caps at points C, and failed intermediate stiffener D are shown.



Fig. 2.14 Structural Model (after Bomb Burst) with Top Cover Removed between Spars, Showing Installation of Temp-Tapes. They are on aft face of forward spar and on inside of bottom skin.

N.A.C.A. 652-05 AIRFOIL SECTION

SECTION MOMENT OF INERTIA,  $I = 4.09 \text{ in}^4$

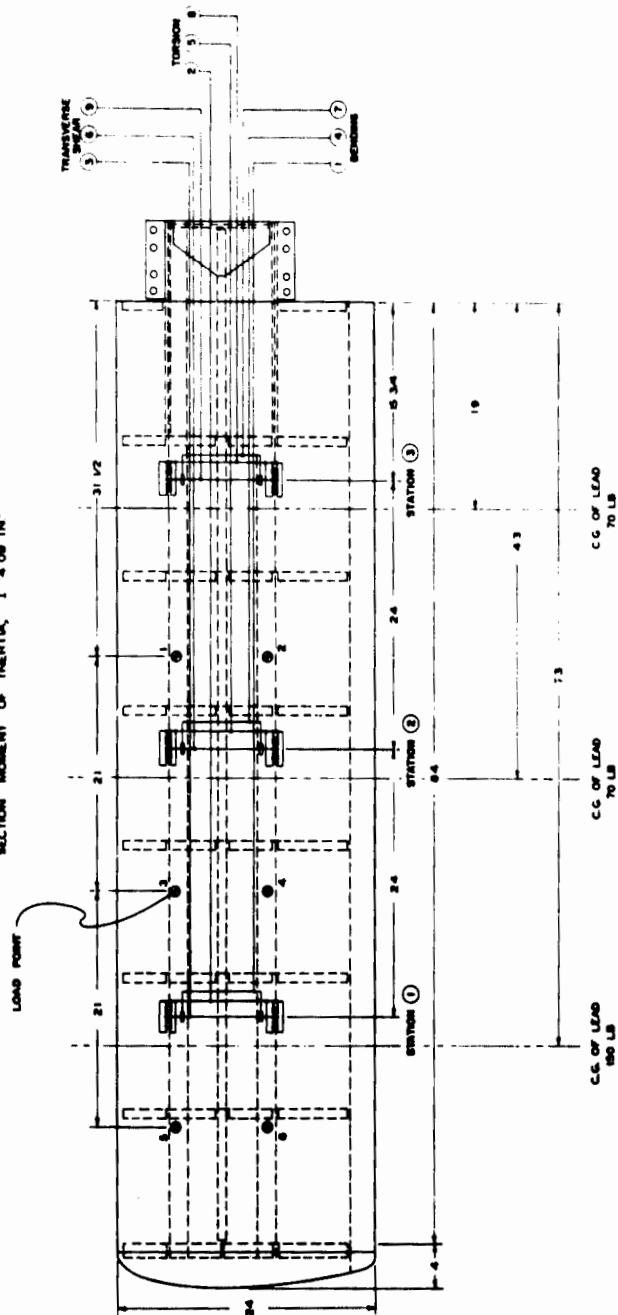
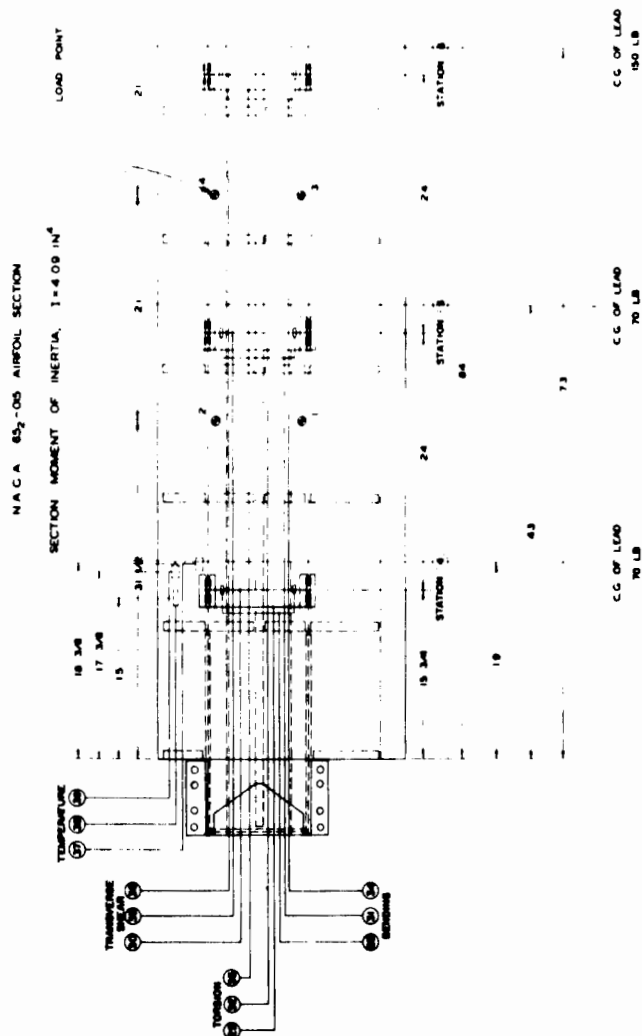


Fig. 2.15 Location of Strain Gauges, Lead Masses, and Calibration Load Points for the Left-hand Structural-wing Models, Series -01 (6° Angle of Incidence)





70 5/16

34 5/16

11 5/8

STATION ⑦

20 1/2

24 3/4

44 1/2

48 3/4

STATION ⑧

STATION ⑨

LOAD POINT LOCATIONS

INTERSECTION OF ROOT LINE AND 50% CHORD LINE

CG OF LEAD

45 LB

91 3/4

102 3/4

CG OF LEAD

43 LB

88 1/2

CG OF LEAD

90 LB

**Fig. 2.17 Location of Strain Gauges, Lead Masses, and Calibration Load Points for the Swept-wing Models, Series -05 ( $8\frac{3}{4}^\circ$  Angle of Incidence)**

**UNCLASSIFIED**



Fig. 2.18 Airfoils Set at 0° Angle of Incidence on Engbel, Range 4,020 Ft, after Bomb Burst. No damage was evident except for slight erosion on leading edge.

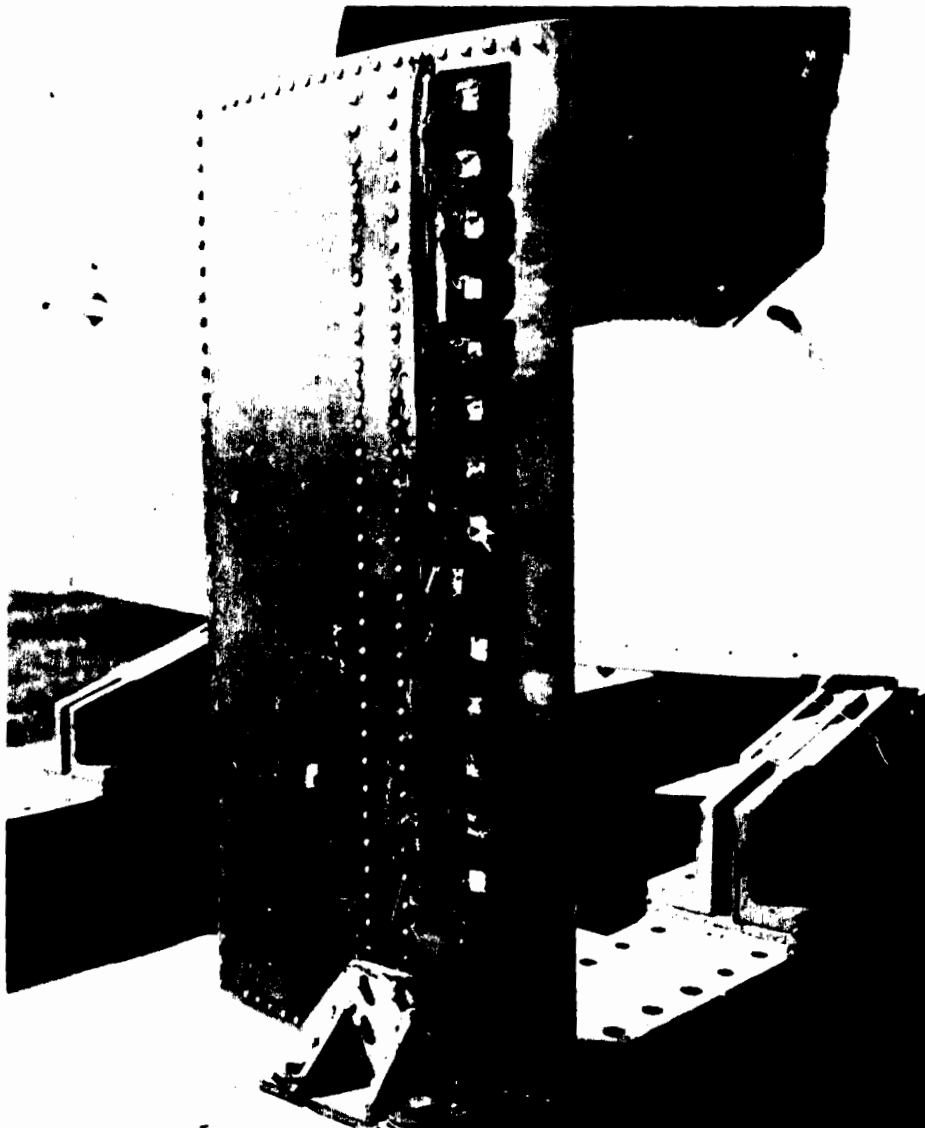


**Fig. 2.19 Detailed View of the Airfoil Shown on Right in Fig. 2.18. Note the severe erosion of the Temp-Tapes.**



Fig. 2.20 Cylinders on Engebli, Range 4,020 Ft, after Detonation. No structural damage was evident. Traces of superficial damage due to erosion and thermal radiation can be noted. The severely eroded Temp-Tapes had been removed.



Fig. 2.21 F-80 Fuselage Installation on Muzin, Range 6,878 Ft, before Bomb Burst



Fig. 2.22 F-80 Fuselage on Muzin after Detonation. Scorching of the radar dome and paint on leading edge of air scoop was the only perceptible damage.



**Fig. 2.23 B-17 Elevator Installation, Engebi, Range 4,020 Ft, before Bomb Burst**

UNCLASSIFIED

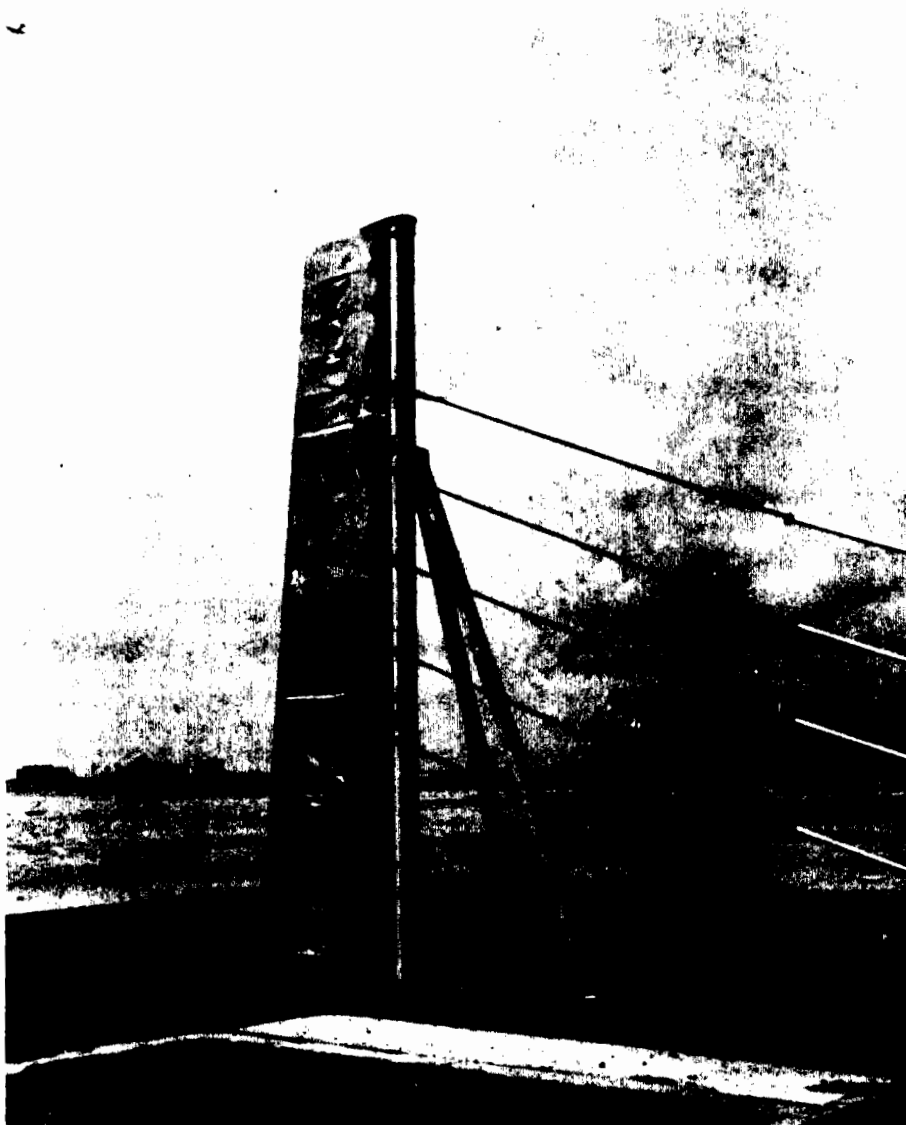


Fig. 2.24 Structural Damage Sustained by B-17 Elevator on Engebí after Detonation. Compare with Fig. 2.23. Note small hole in fabric in Fig. 2.23 in same bay where fabric is torn in this picture.

UNCLASSIFIED



~~SECRET~~ ~~NO FORN DISSEM~~



Fig. 2.25 Spanwise View of B-17 Elevator from Engeb1 with the Fabric Removed from One Side (after Detonation). The concave appearance of all the crushed ribs is shown.

~~SECRET~~ ~~NO FORN DISSEM~~



Fig. 2.26 Crushed Internal Structure of the Inboard End of the B-17 Elevator, Engebl, 4,020 Ft, after Detonation



**Fig. 2.27 Inboard Portion of the B-17 Elevator Showing Burned Fabric at the Leading Edge and Crushed Structure (after Detonation)**

UNCLASSIFIED

~~SECRET~~

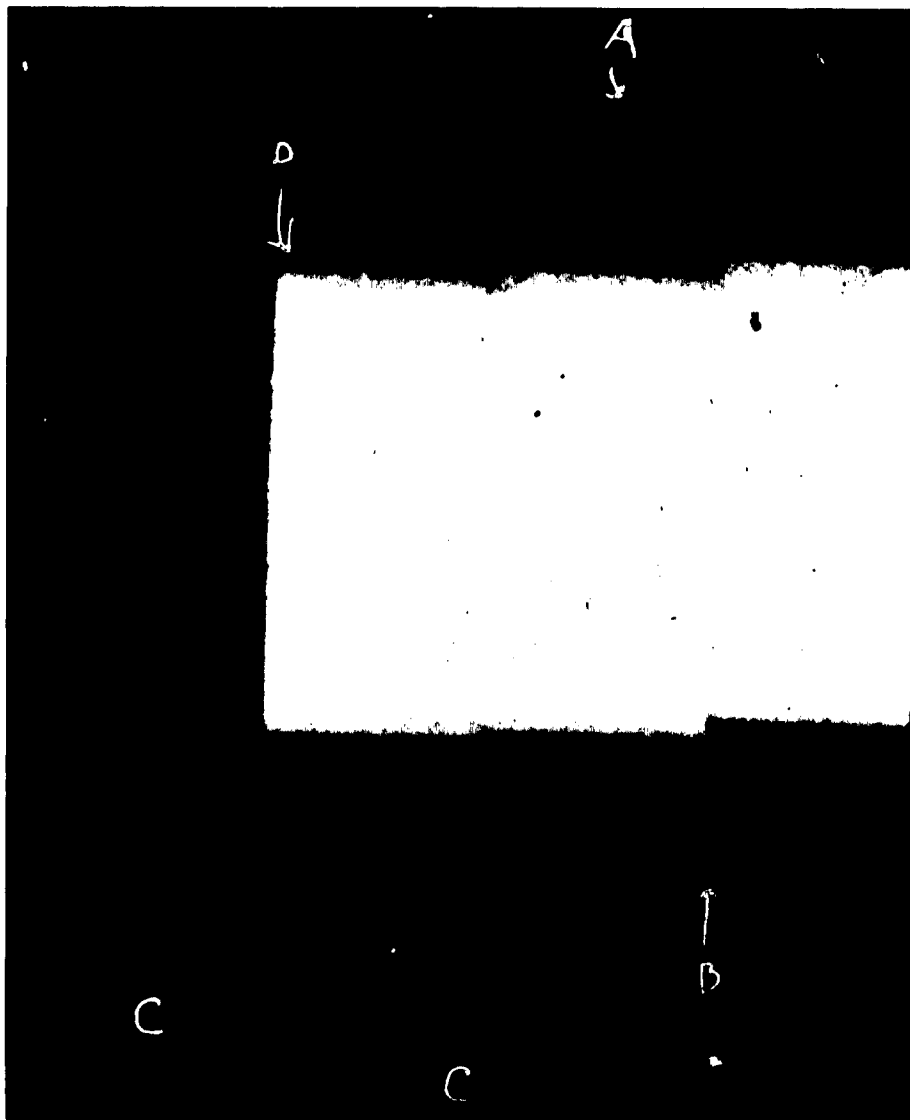


Fig. 2.28 Appearance of a Shock Front Photographed with Fastax Cameras during a 10,000-lb High-explosive Test at Aberdeen, 27 October 1950. Note discontinuity of ropes C at A and B.

~~SECRET~~  
UNCLASSIFIED



**Fig. 2.29** Fastax Camera with Protective Canister (before Bomb Burst). Plexiglass cover exit pupil and the placement of some lead bricks are shown.

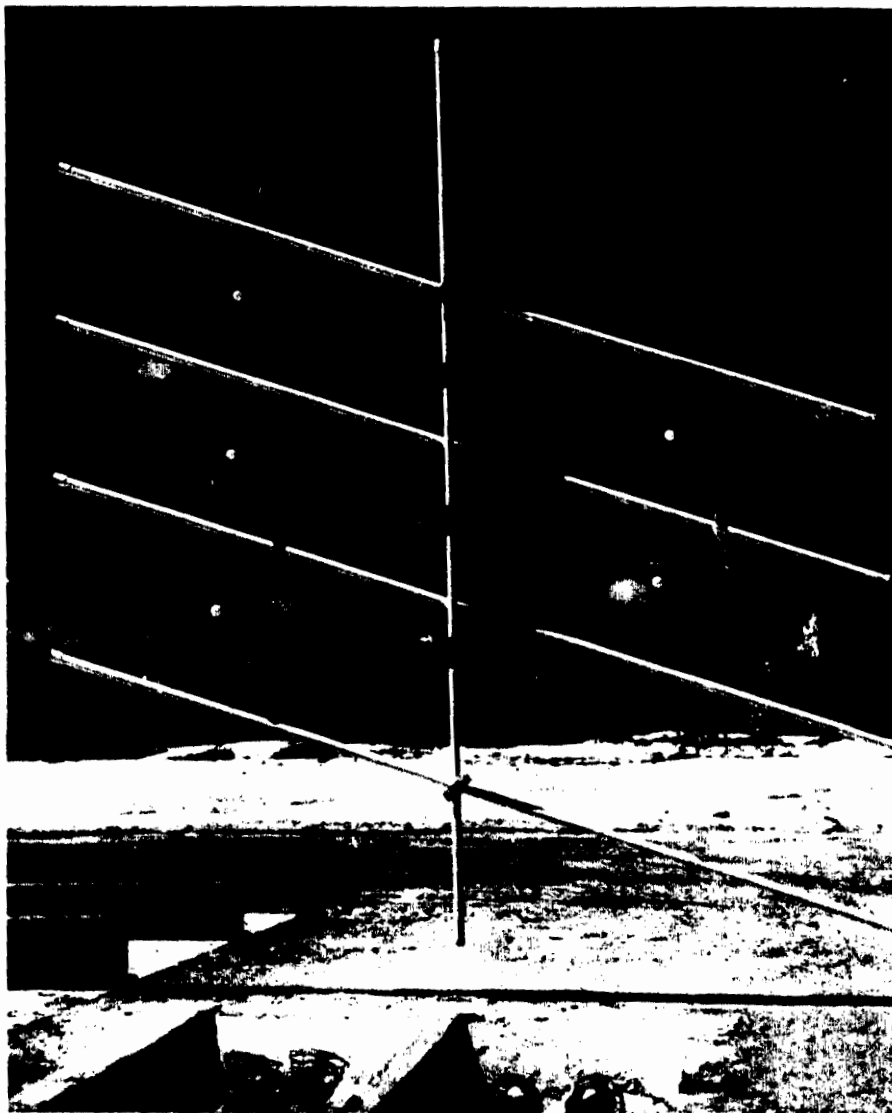


Fig. 2.30 Grid Suspended in Camera Field, Showing Vertical Pipe and Ping-pong Balls for Optical Angle-of-attack Determination, Teltels, Range 12,000 Ft, before Bomb Burst. The vertical pipe was used as reference line, and the ping-pong balls were used as reference points.



Fig. 2.31 View of Grid and Ping-pong Balls on Muzin, Range 6,878 Ft, after Detonation. The lights to illuminate the grid are visible in foreground.



Fig. 2.32 Typical Electrical Controls at Each Island Site for Cameras and Lights, before Detonation





**Fig. 2.33** Installation of Angle-of-attack Blast Switch for Simultaneously Triggering Electronic Chronographs, Muzin, before Detonation. The chronographs were housed in submerged concrete instrument shelter.

UNCLASSIFIED

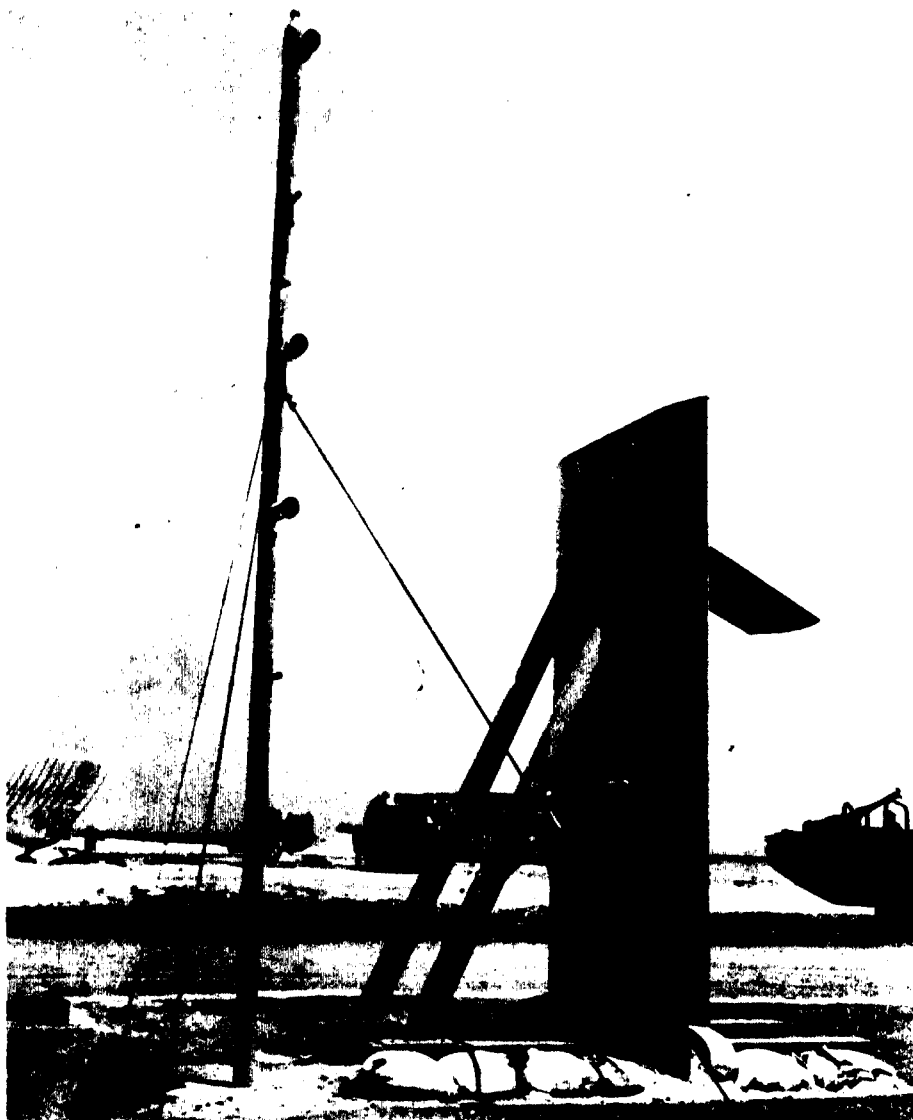


**Fig. 2.34 Installation of Angle-of-attack Blast Switches for Stopping Individual Chronographs (after Detonation). Remains of white tissue paper used to protect diaphragms from thermal radiation can be seen at 10- and 13-ft elevations.**

UNCLASSIFIED

UNCLASSIFIED

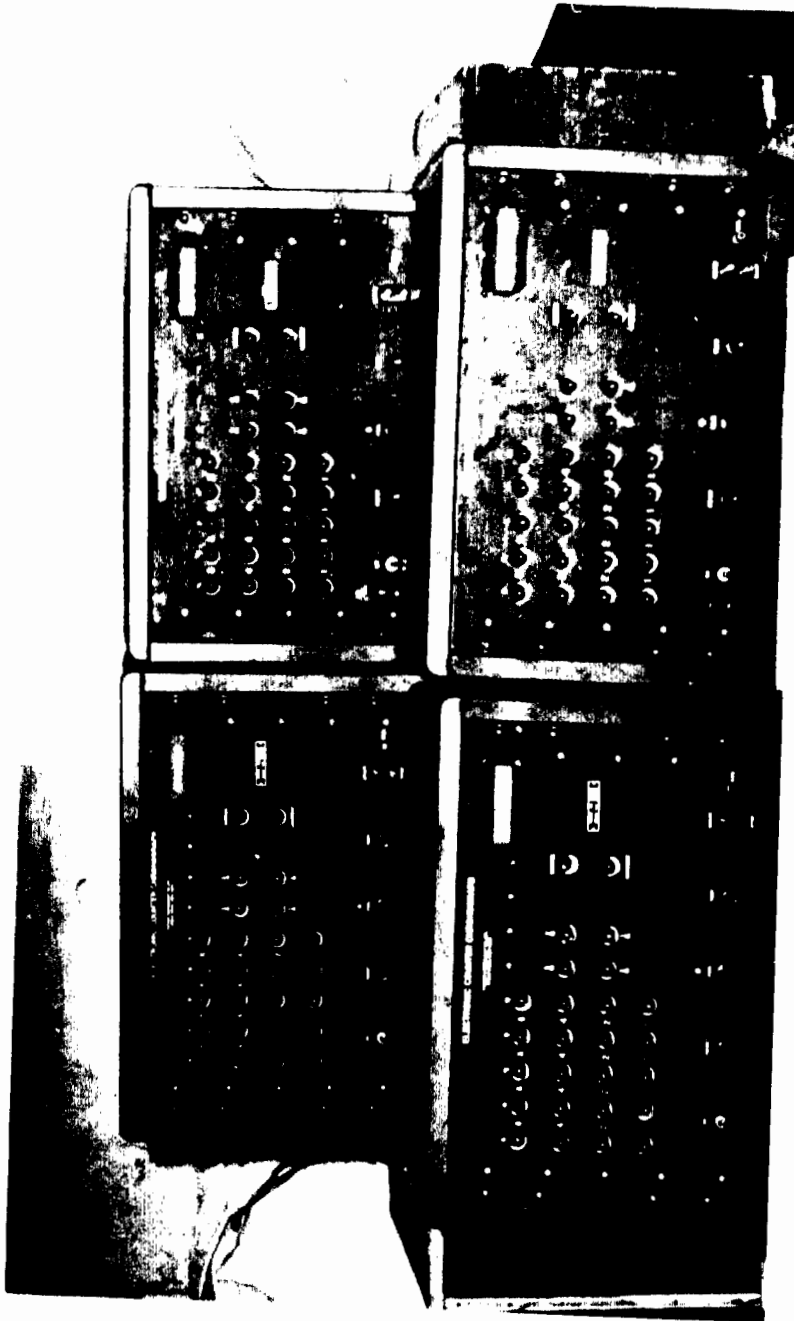


Fig. 2.35 Four Electronic Counters Arranged to Facilitate Automatic Recording on a 4- by 5-in. Still Camera for Determination of Vertical Profile of Blast Front. Equipment was located in concrete instrument shelter on Muzin.

UNCLASSIFIED



Fig. 2.36 Signal from Four Electronic Counters As Recorded on a Still Camera for Easy Day Explosion.  
Compare with total-neon-light pattern in Fig. 2.35.

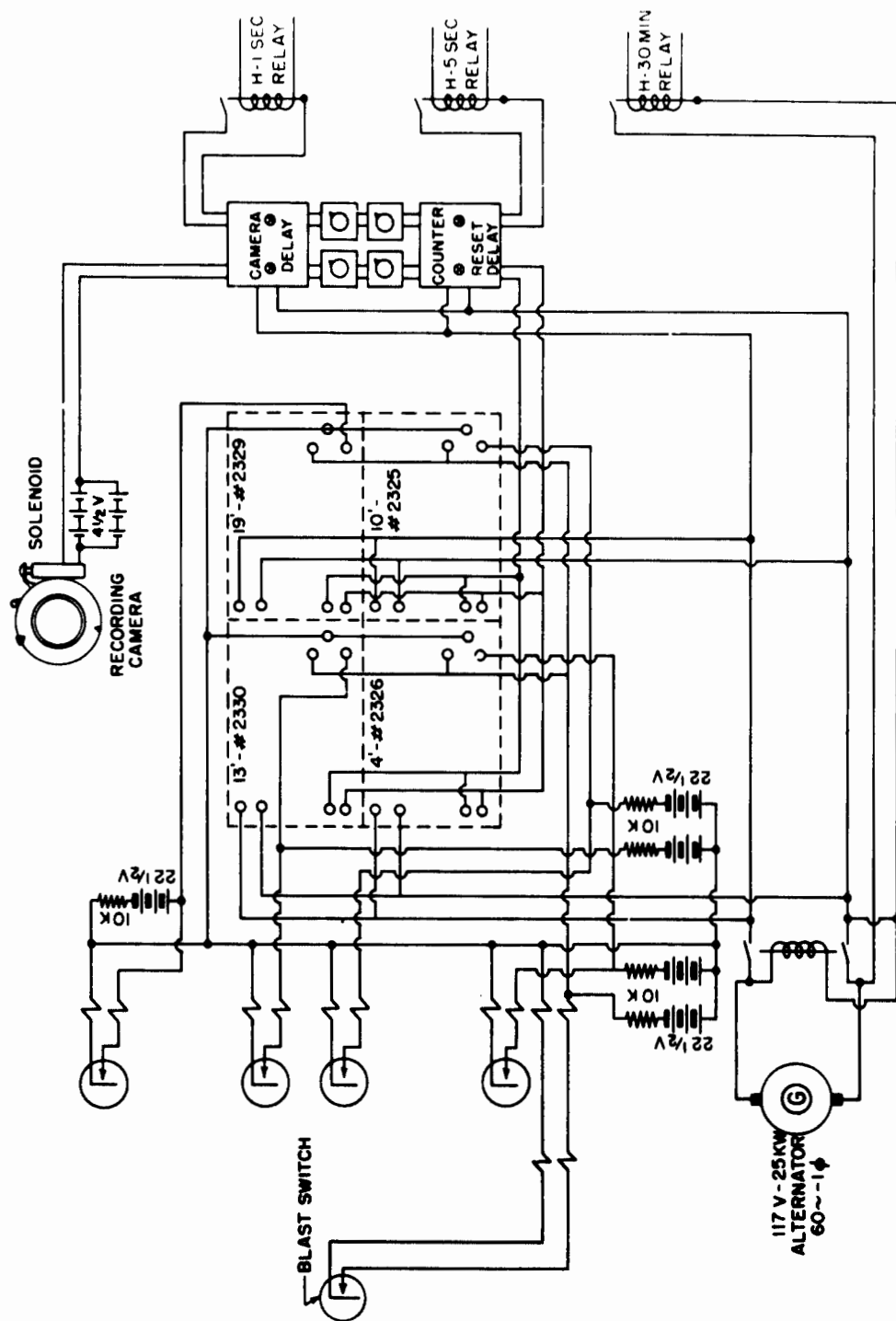


Fig. 2.37 Circuit Diagram for Automatic Operation of Electronic-chronograph Angle-of-attack System

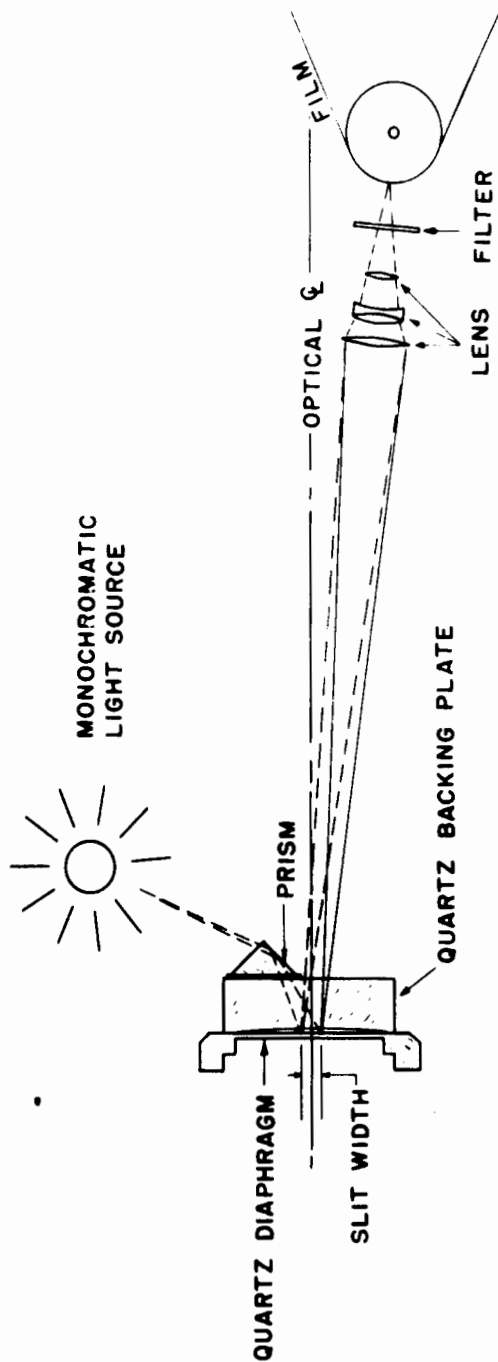


Fig. 2.38 General Arrangement of Interferometer-gauge Elements

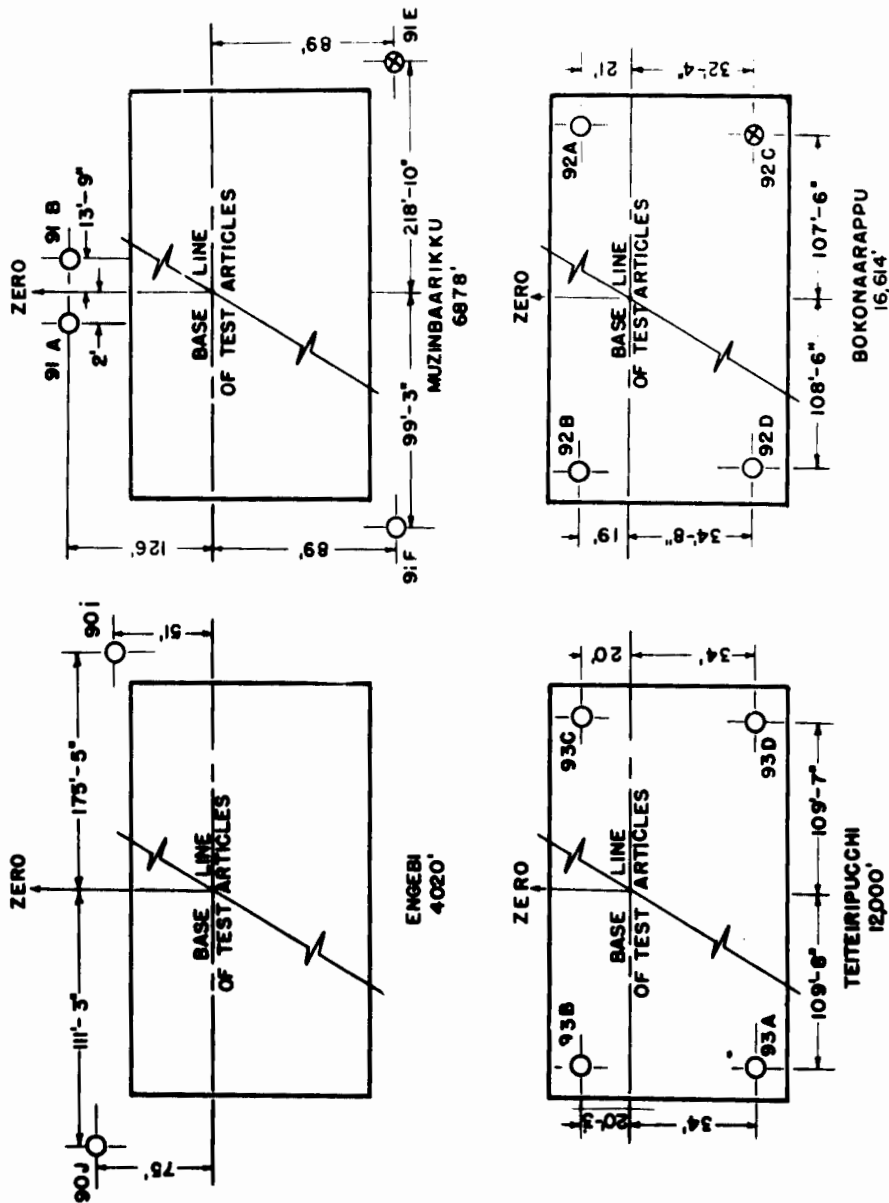


Fig. 2.39 Location of Interferometer Gauges at Each Test Site

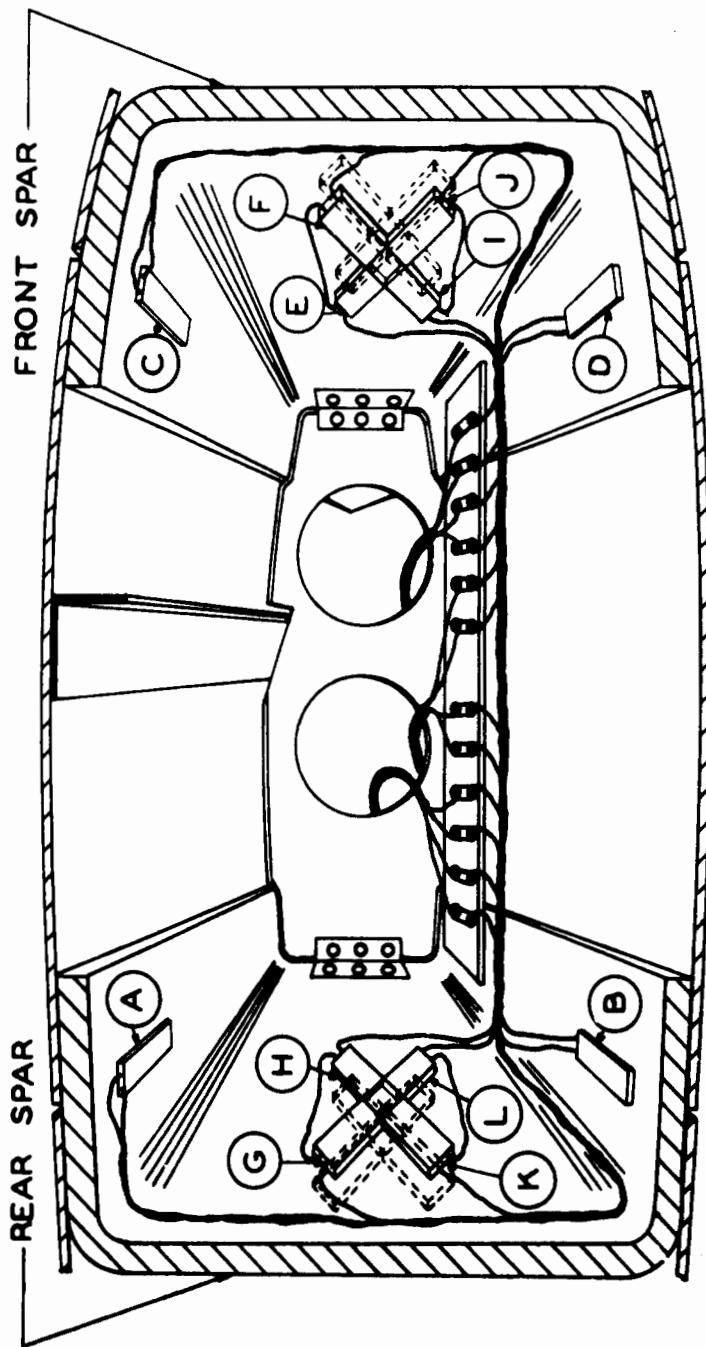


Fig. 3.1 Perspective Interior View of an Instrumented Spanwise Station Typical for the Swept-wing and the Structural-wing Models. Letters denote gauges (see text for explanation).



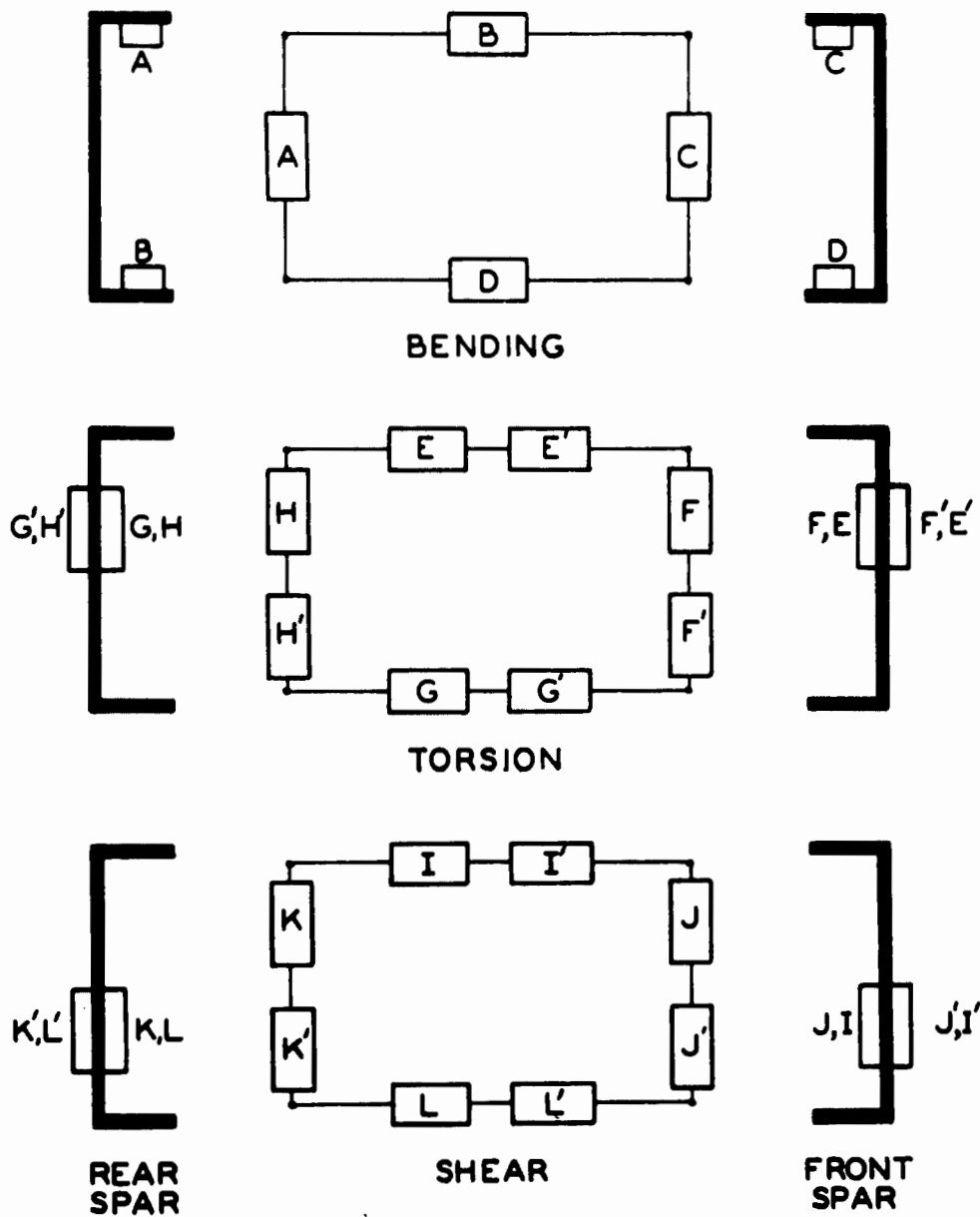


Fig. 3.2 Schematic Wiring Diagram for Strain-measurement Bridges on the Structural- and the Swept-wing Models

[REDACTED] INFORMATION

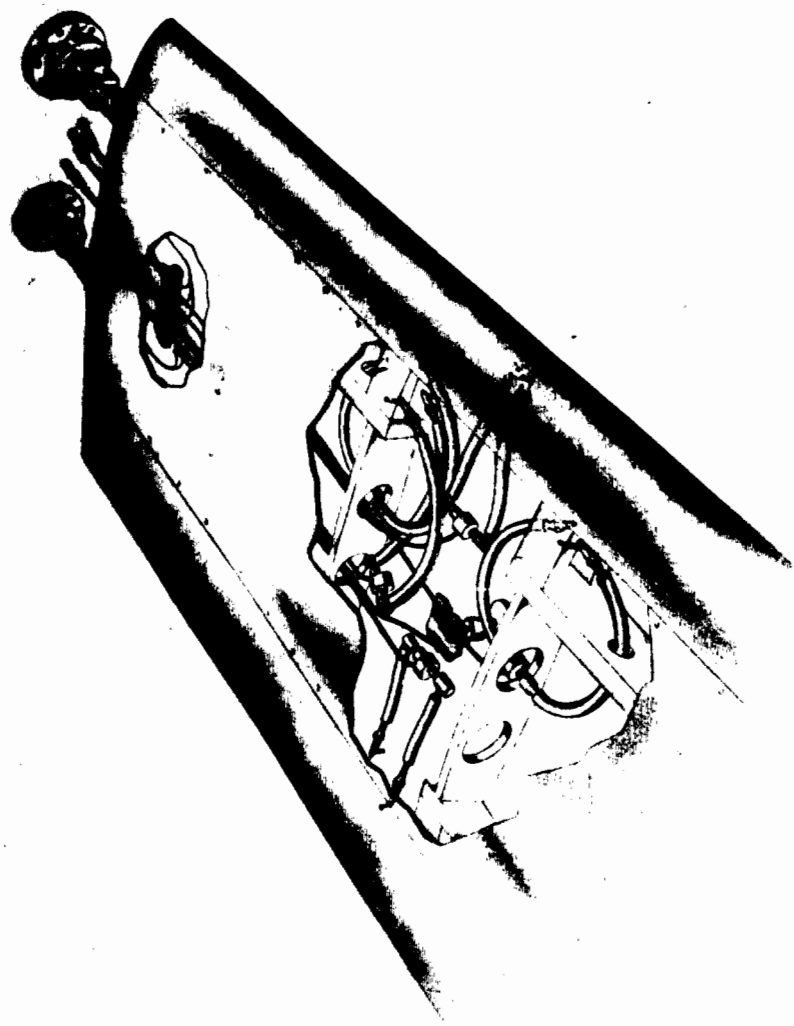


Fig. 3.3 Perspective View Illustrating Instrumentation Details of the Rigid-wing Model

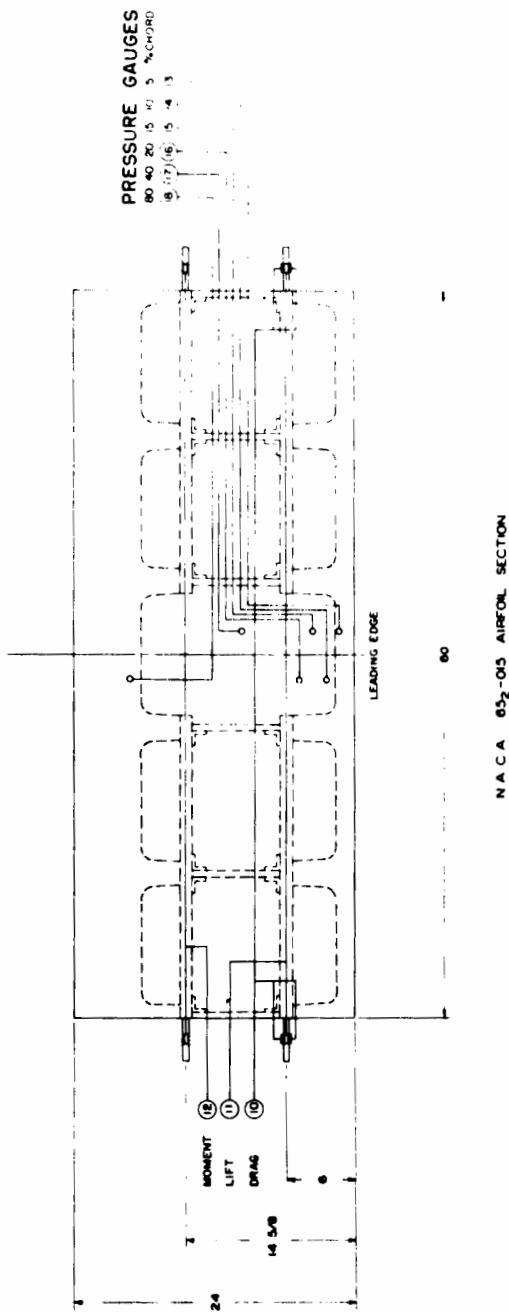
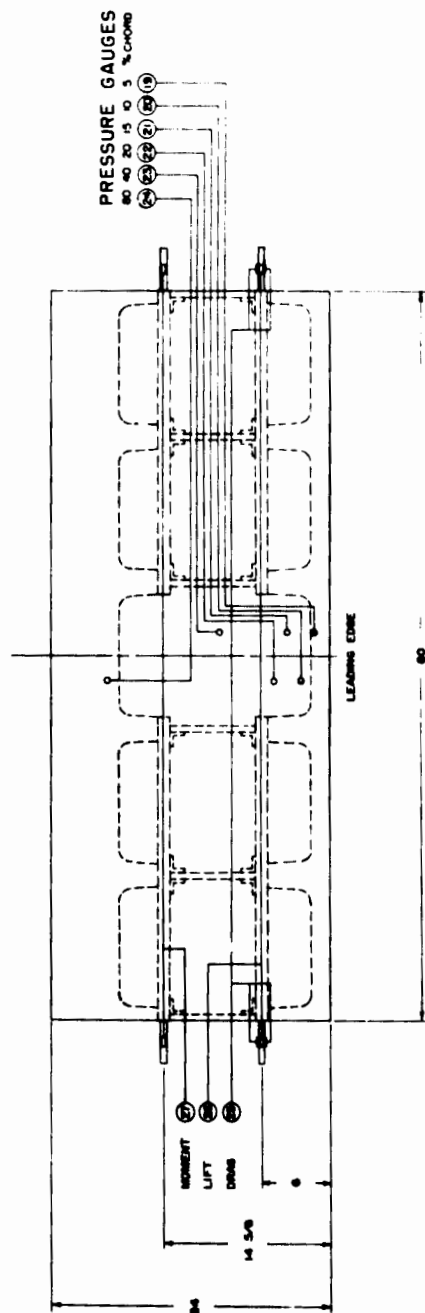


Fig. 3.4 Location of Strain Gauges and Pressure Gauges for the Left-hand Rigid-wing Models, Series -02 (9° Angle of Incidence)



N.A.C.A. 652-015 AIRFOIL SECTION

Fig. 3.5 Location of Strain Gauges and Pressure Gauges for the Right-hand Rigid-wing Models, Series -03 ( $6^\circ$  Angle of Incidence)

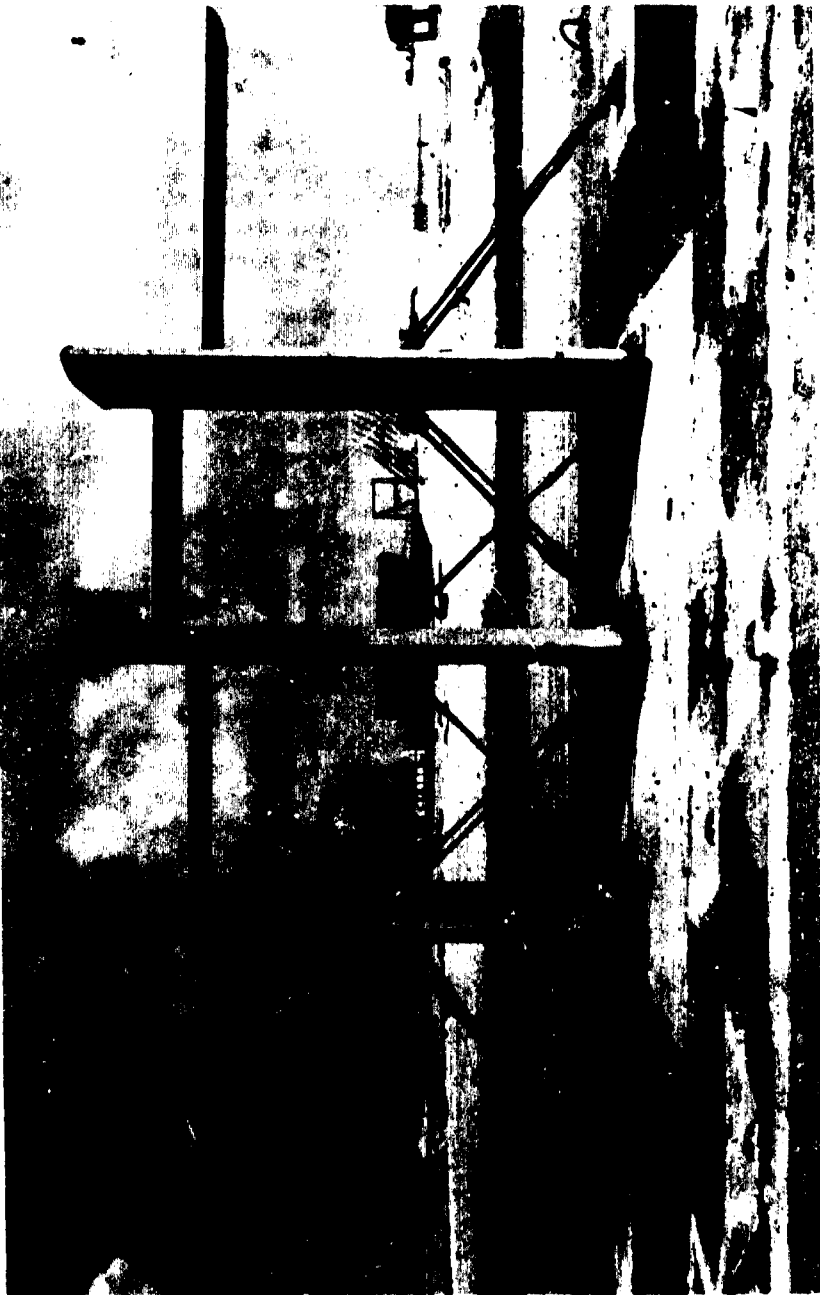


Fig. 3.6 Rigid and Structural Models on Muzin, Range 6,878 Ft, after Detonation. There was no perceptible damage of any type to this test installation.

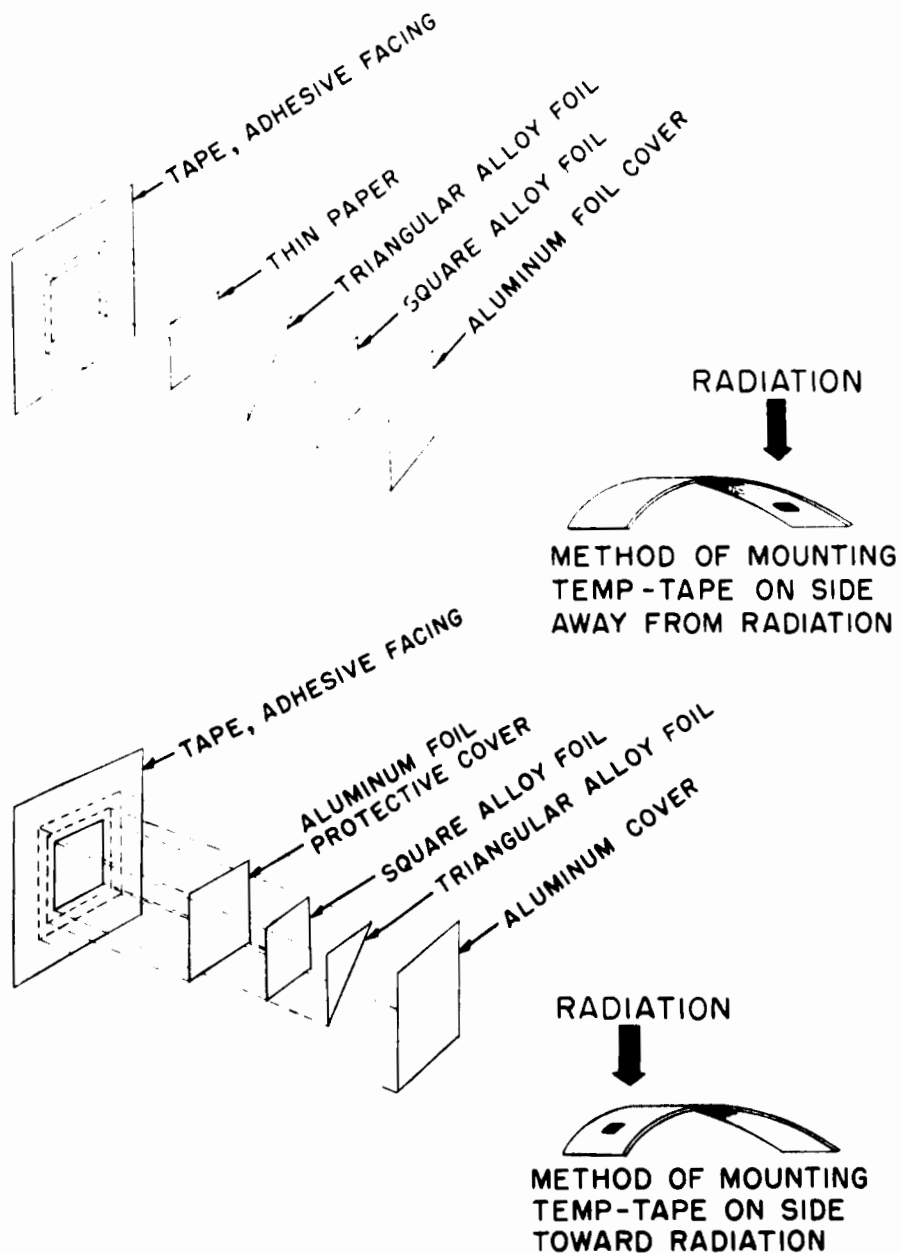


Fig. 3.7 Drawing of Temp-Tape Components



Fig. 3.8 Outside-skin-surface Temperature vs Time Gauge Installed on Bottom Surface of a -04 Structural Wing. See pencilled rectangle. Gauge sensing element, to the right of the dark patch, was covered with aluminum paint. Relative absorptivity of gauge and wing skin is indicated by their relative shading.

UNCLASSIFIED

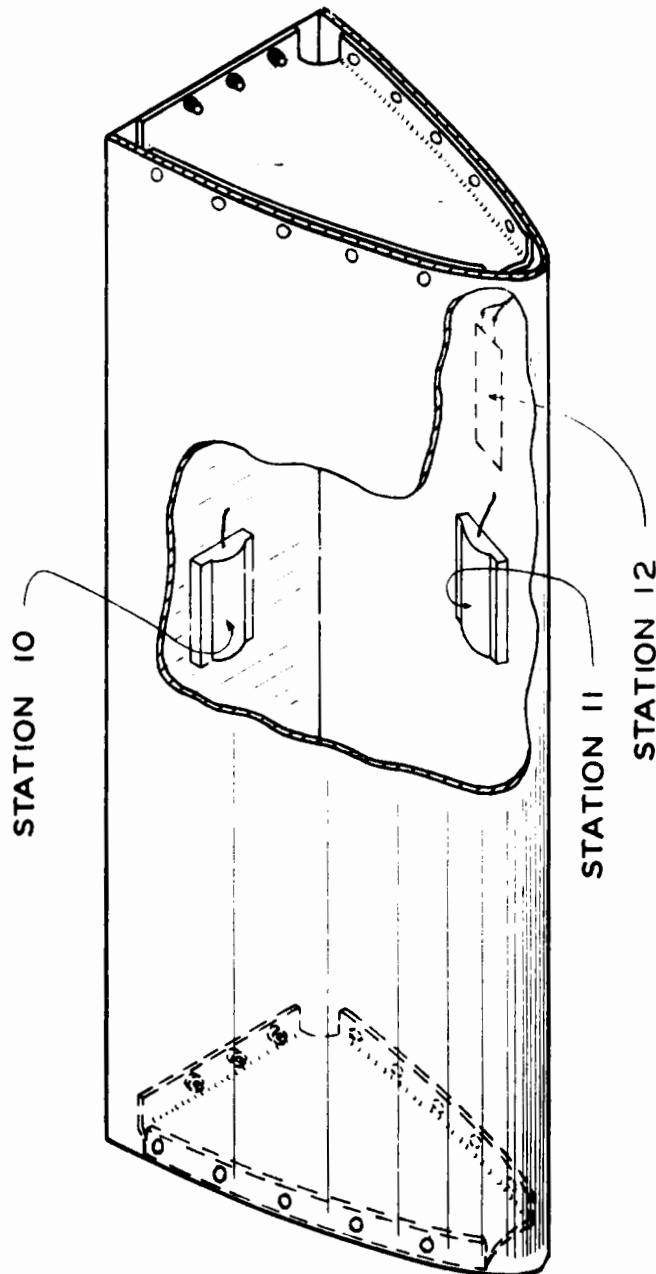


Fig. 3.9 Sketch Showing Location of Temperature vs Time Gauges in the Leading-edge Section of a -04 Structural Wing. Front spar-web gauge, Station 10; internal-skin-surface gauge, Station 11; and external-skin-surface gauge, Station 12.

UNCLASSIFIED



STRAIN GAUGES ON TOP  
AND BOTTOM (INSIDE) OF SPARS\*

STRAIN GAUGES ON FACE SIDE  
(OUTSIDE) OF SPARS\*

STRAIN GAUGES  
ON FACE SIDE  
(INSIDE) OF SPARS\*

TEMPERATURE  
PATCH  
TEMPERATURE  
GAUGE

\*NOTE: ALL THE STRAIN GAUGES  
ARE LOCATED AT EACH  
OF THE THREE STATIONS

Fig. 3.10 Perspective View Illustrating Instrumentation Details of a Structural-wing Model

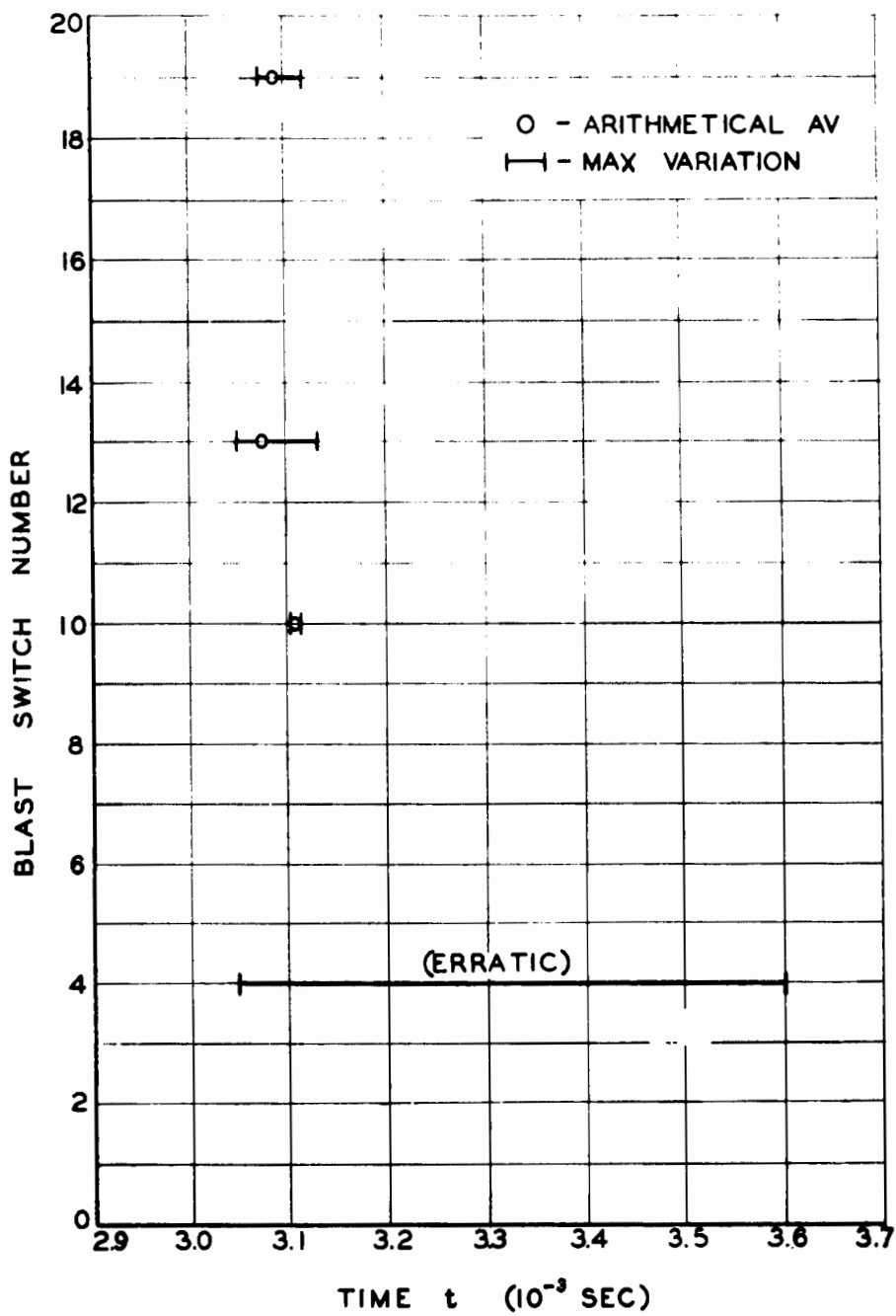


Fig. 4.1 Calibration of Blast Switches

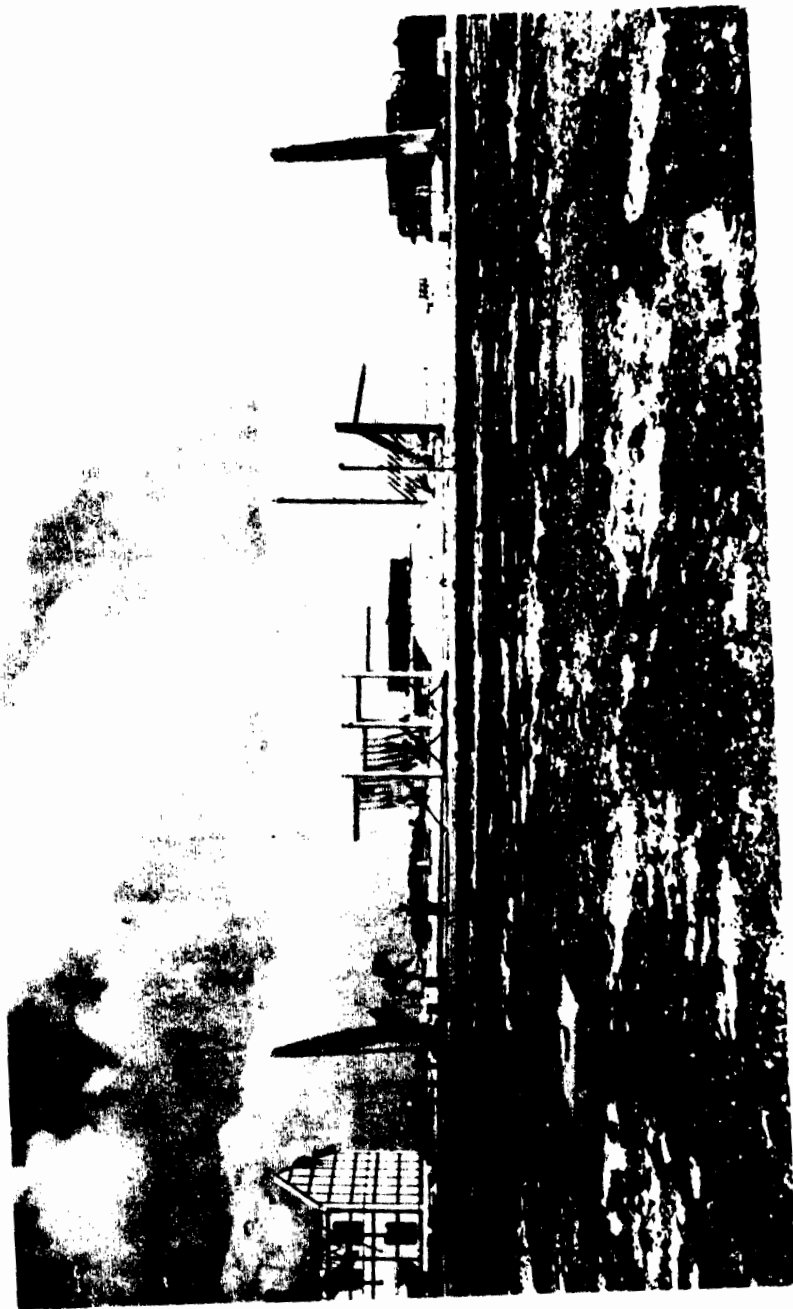


Fig. 5.1 Muzin Test Site after the Atomic Bomb Detonation, Range 6,878 Ft. The F-80 fuselage and B-17 elevator, which were undamaged, are at the extremities of the test site and are not visible.



Fig. 5.2 Engebi Test Site Approximately 6 Hr after the Atomic Bomb Detonation, Range 4,020 Ft

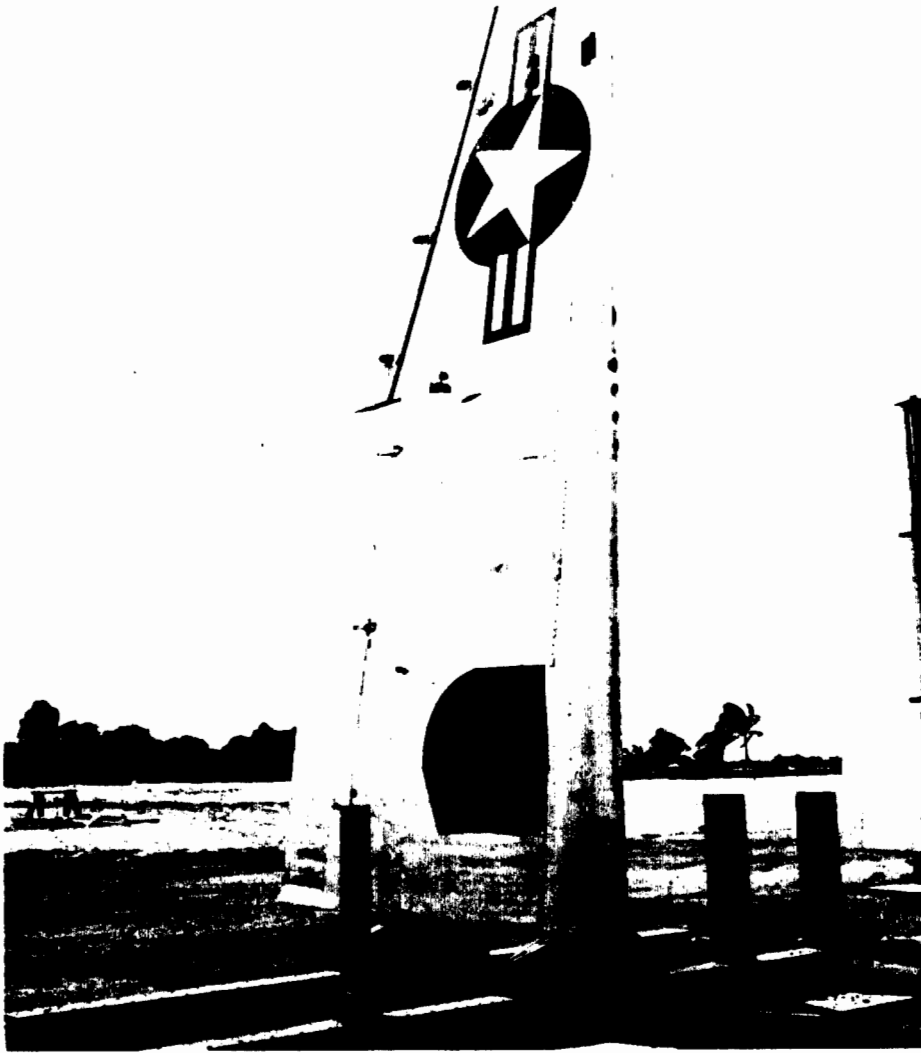


Fig. 5.3 F-47 Wing and Airfoil Installation on Testair, Range 12,000 Ft, before Bomb Burst. This view illustrates the simple sheet-metal covering placed over the gear strut and the wheel well for comparison with Fig. 5.4.

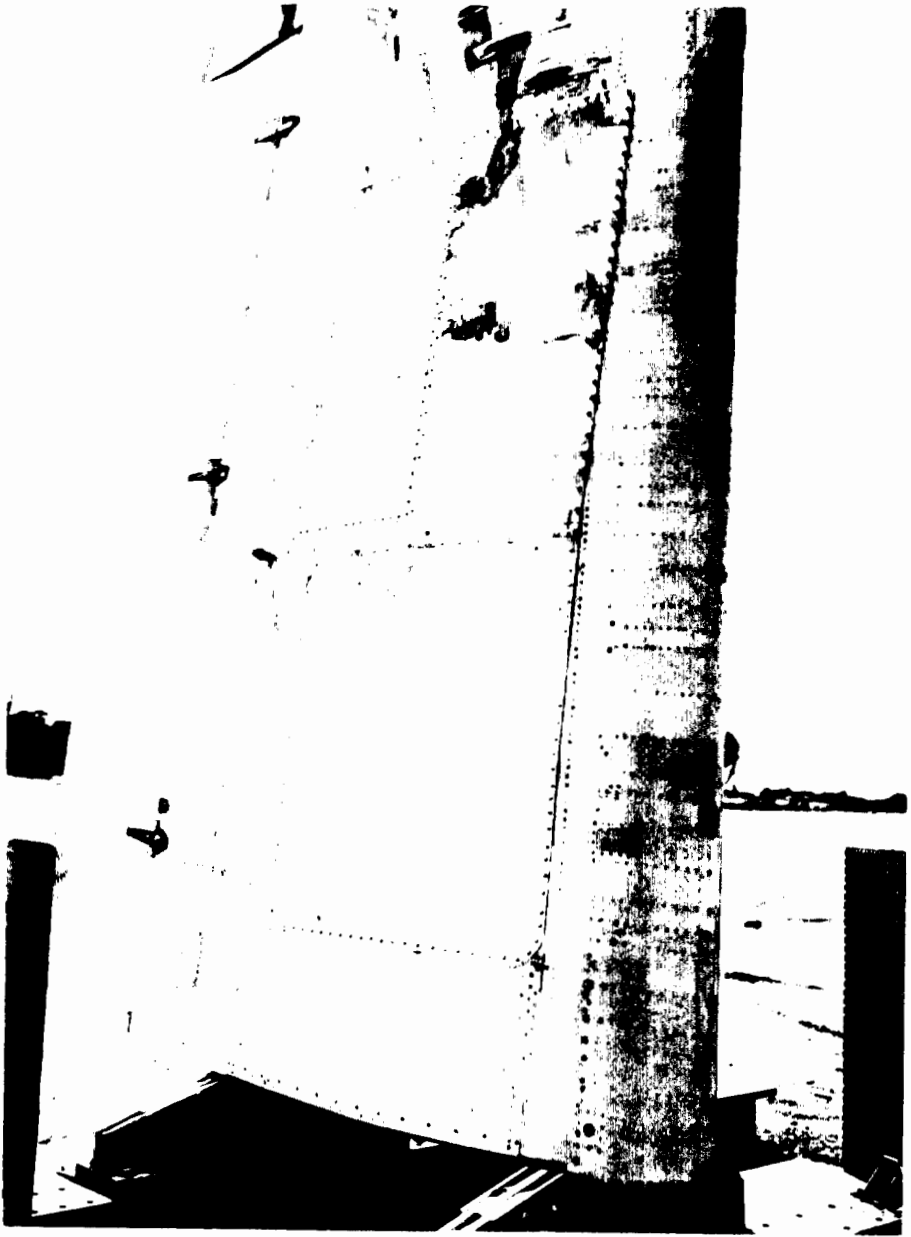


Fig. 5.4 Crushed Sheet-metal Covering of the Wheel Well of the F-47 Wing Installation on Teiteir, Range 12,000 Ft, after Bomb Burst. Peak pressure was approximately 1.5 psi. No damage to the basic wing was noted.



Fig. 5.5 Failed Airfoil with  $\frac{1}{8}$ -in. Vent Holes on Engebi, Range 4,020 Ft, after Bomb Detonation. This is the airfoil on the extreme left in Figs. 2.5 and 2.6. Originally set at  $20.1^\circ$  angle of incidence.



Fig. 5.6 Failed Airfoil with  $\frac{1}{4}$ -in. Vent Holes on Engebli, Range 4,020 Ft, after Bomb Burst. The airfoil was originally set at a  $22\frac{1}{4}^\circ$  angle of incidence. This is the airfoil on the immediate right of the F-47 wing in Figs. 2.5 and 2.6.



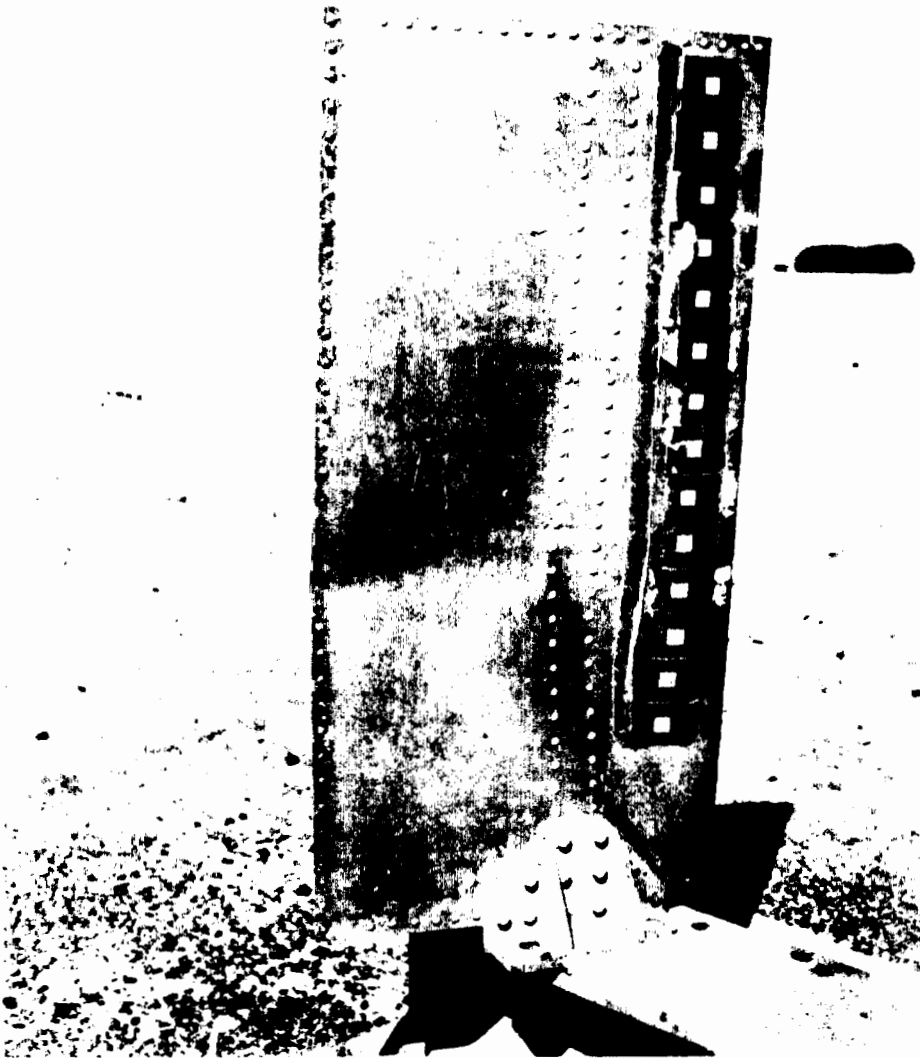


Fig. 5.7 Partially Failed Airfoil with No Venting Holes, Engebi, Range 4,020 Ft, after Bomb Burst. This is the airfoil on the extreme right in Figs. 2.5 and 2.6, originally set at  $22\frac{1}{4}^\circ$  angle of incidence. The Temp-Tapes on this side were partially protected by the nose of the airfoil during the positive phase, and they show only medium effect of erosion and thermal radiation.

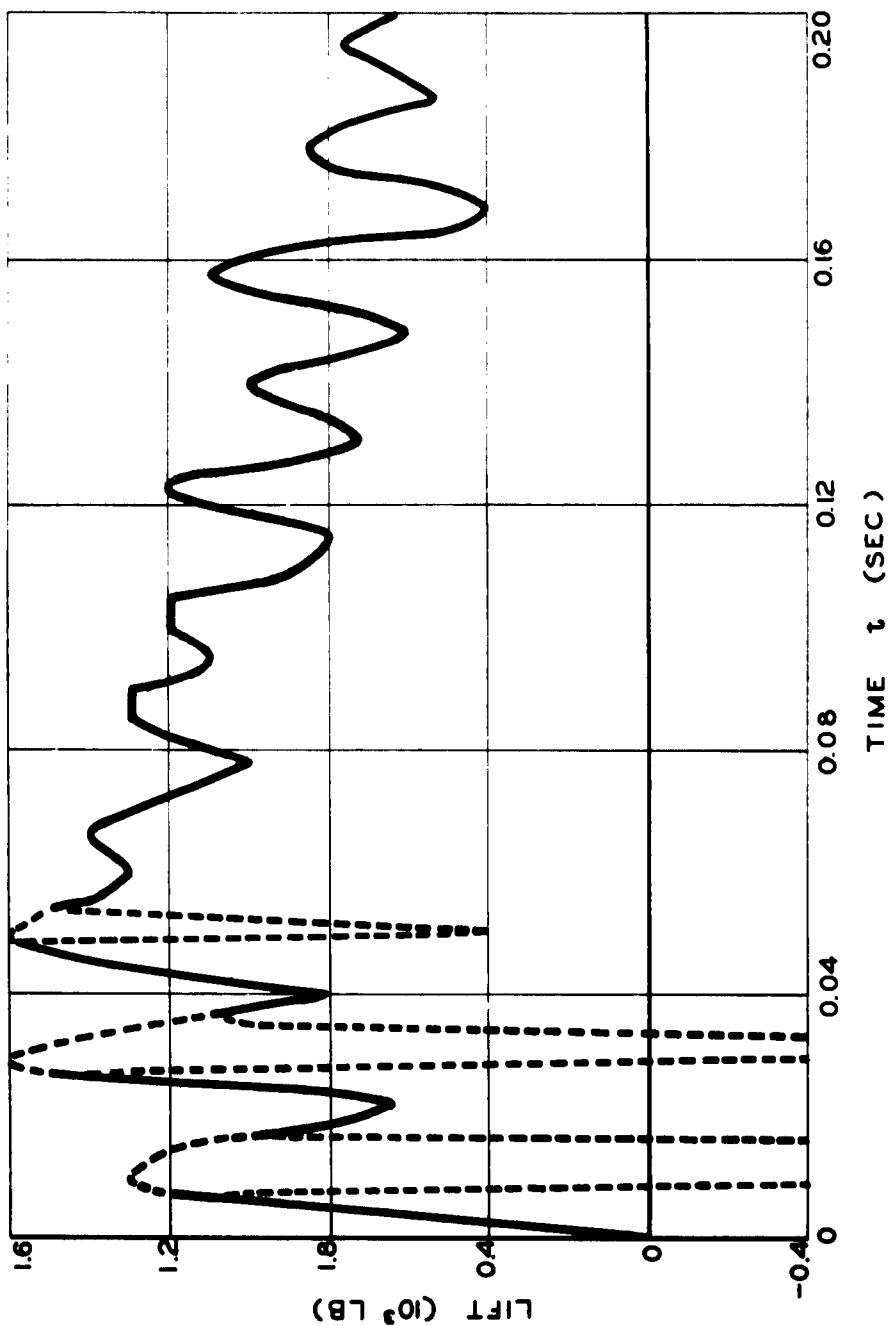


Fig. 5.8 Variation of Lift with Time, Obtained from Balance-system Measurement for Rigid Wing 102.  
The angle of Incidence was  $9^\circ$ , and the range was 4,020 ft, Engbl.

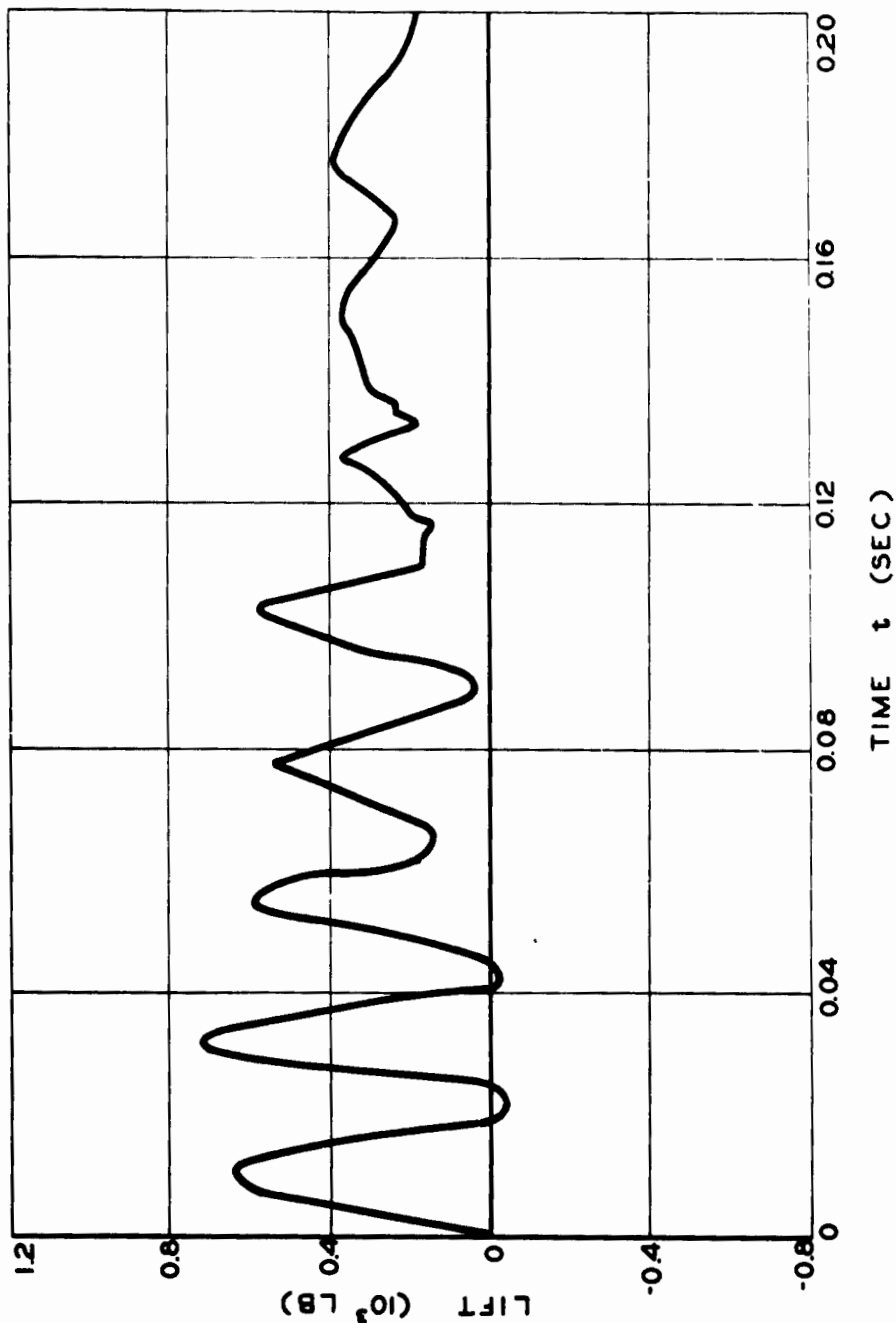


Fig. 5.9 Variation of Lift with Time, Obtained from Balance-system Measurement for Rigid Wing 202.  
The angle of incidence was  $9^\circ$ , and the range was 6,878 ft, Muzin.

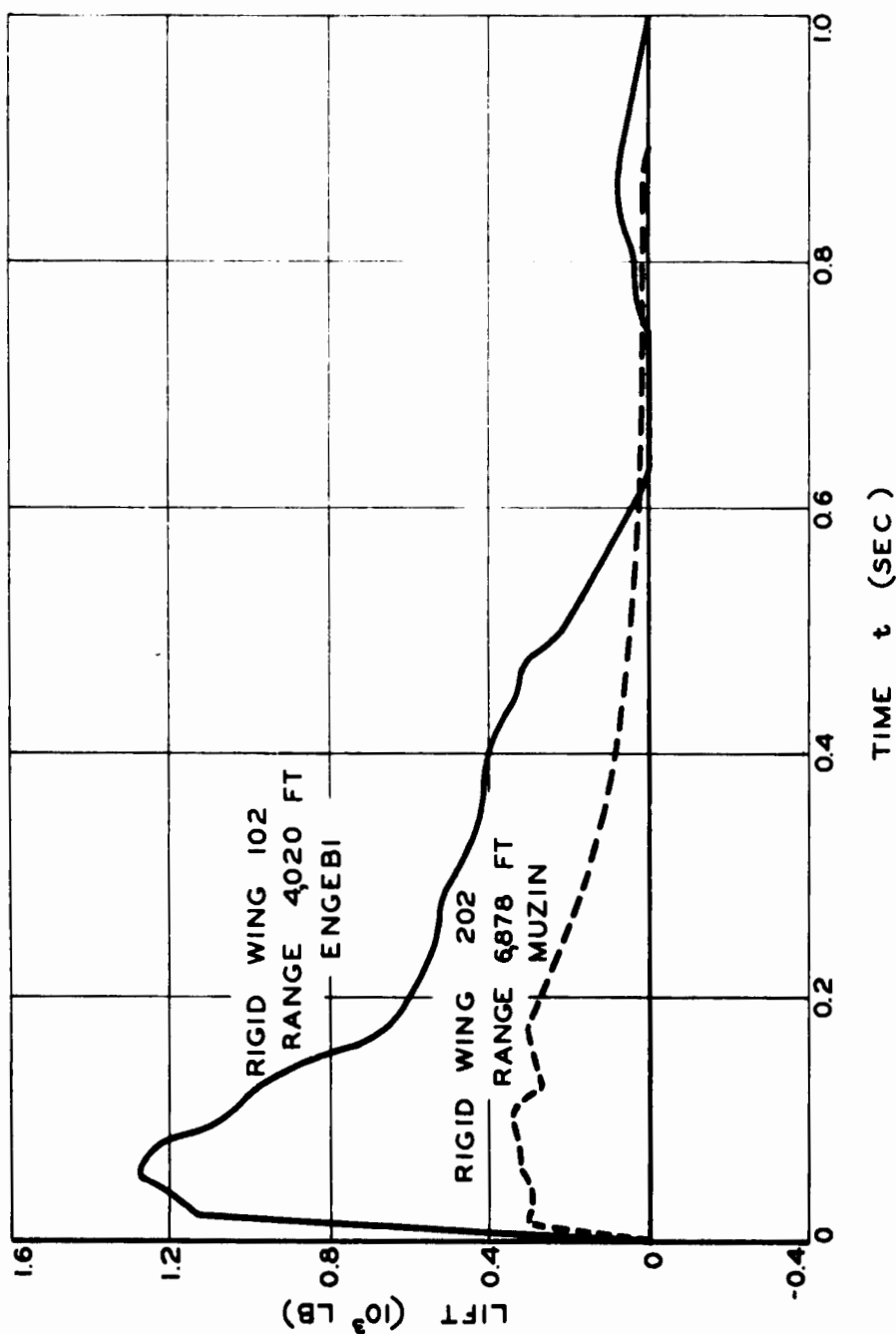


Fig. 5.10 Average Variation of Lift with Time, Obtained from Balance-system Measurements for Two Wings. Each had  $9^\circ$  angle of incidence, at different ranges.

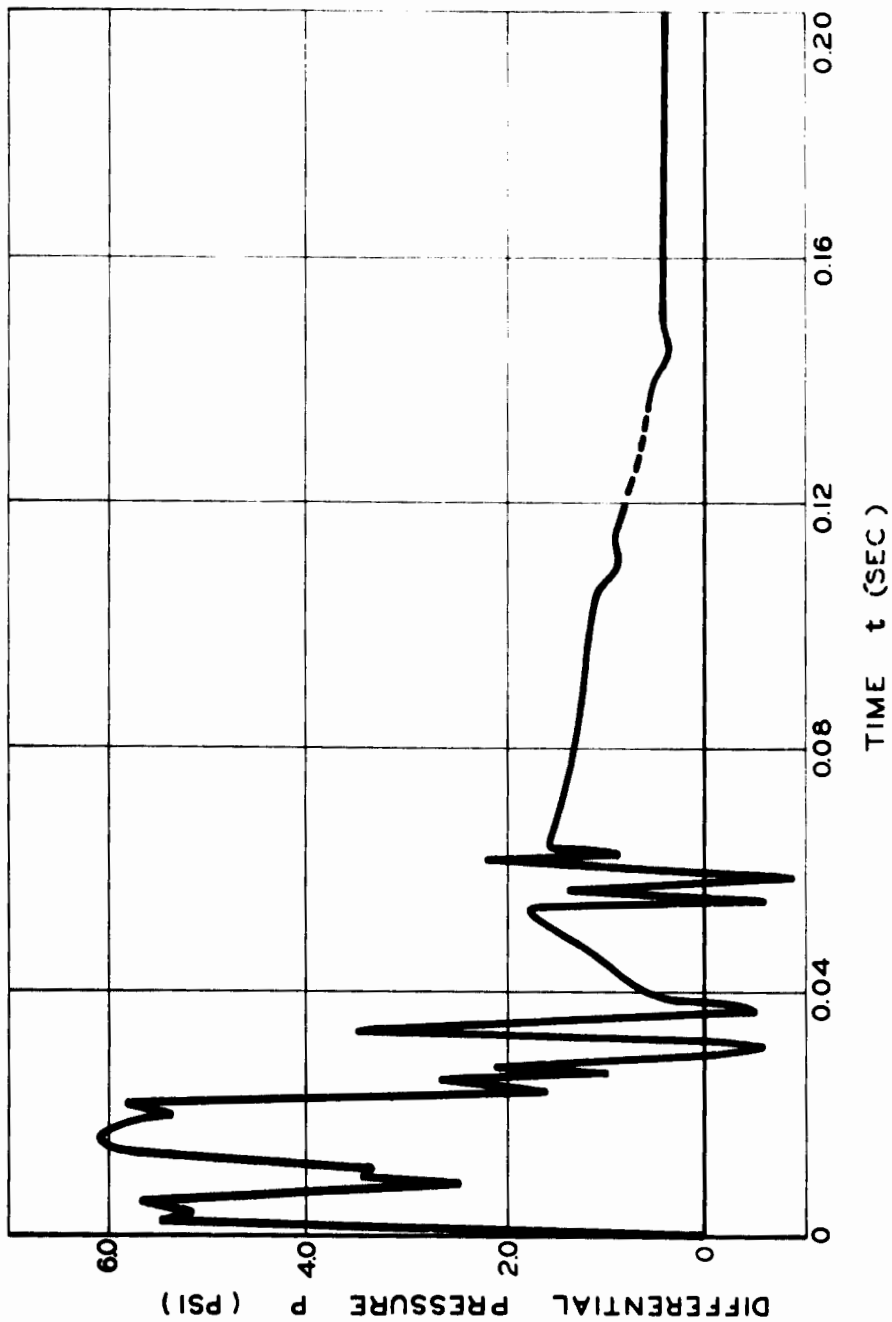


Fig. 5.11 Variation of Differential Pressure with Time at 5 Per Cent Camber of Rigid Wing 162. The angle of incidence was  $4^\circ$ , and the range was 4,000 ft, Engbl.

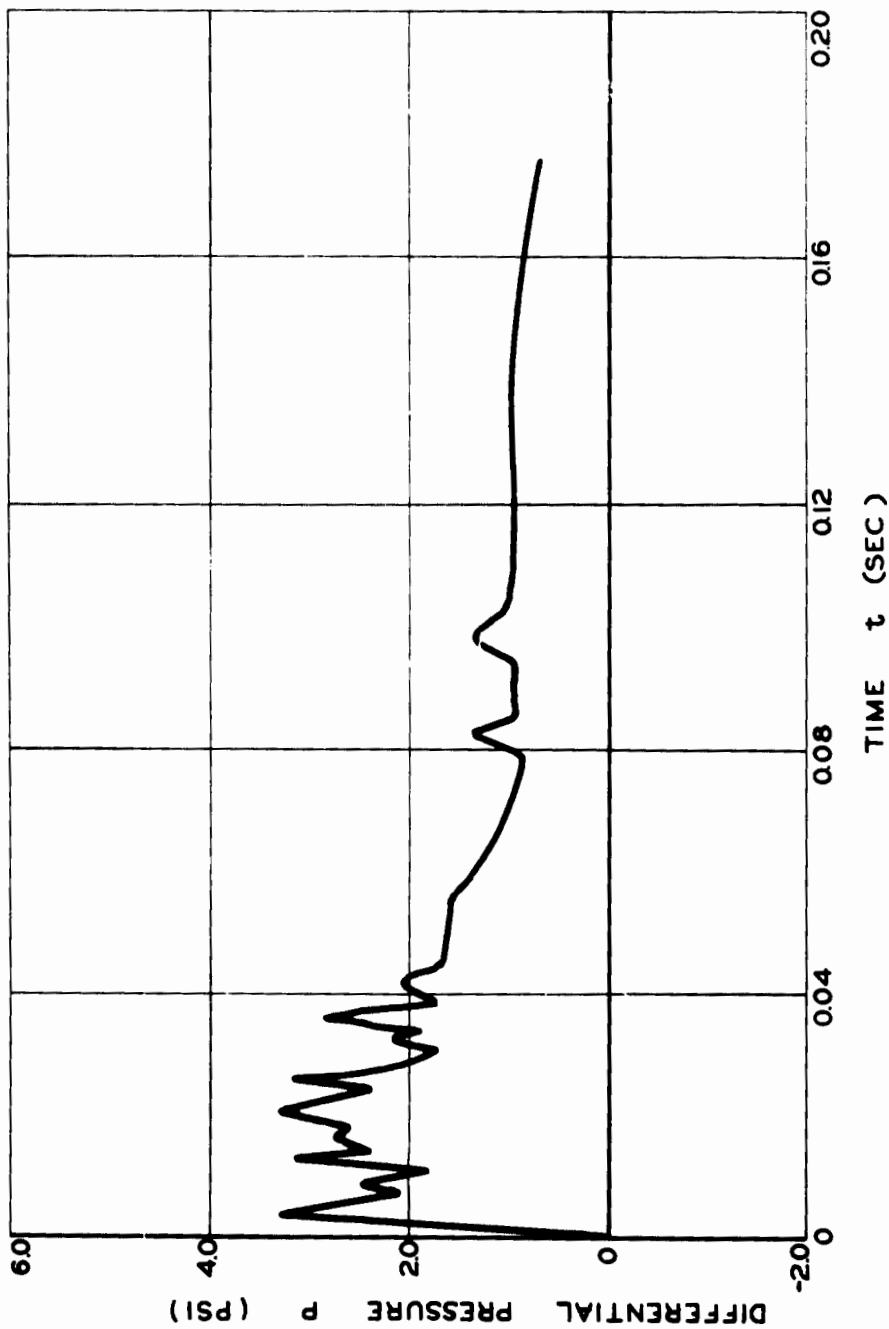


Fig. 5.12 Variation of Differential Pressure with Time at 15 Per Cent Chord of Rigid Wing 102. The angle of incidence was  $9^\circ$ , and the range was 4,020 ft, Englebi.

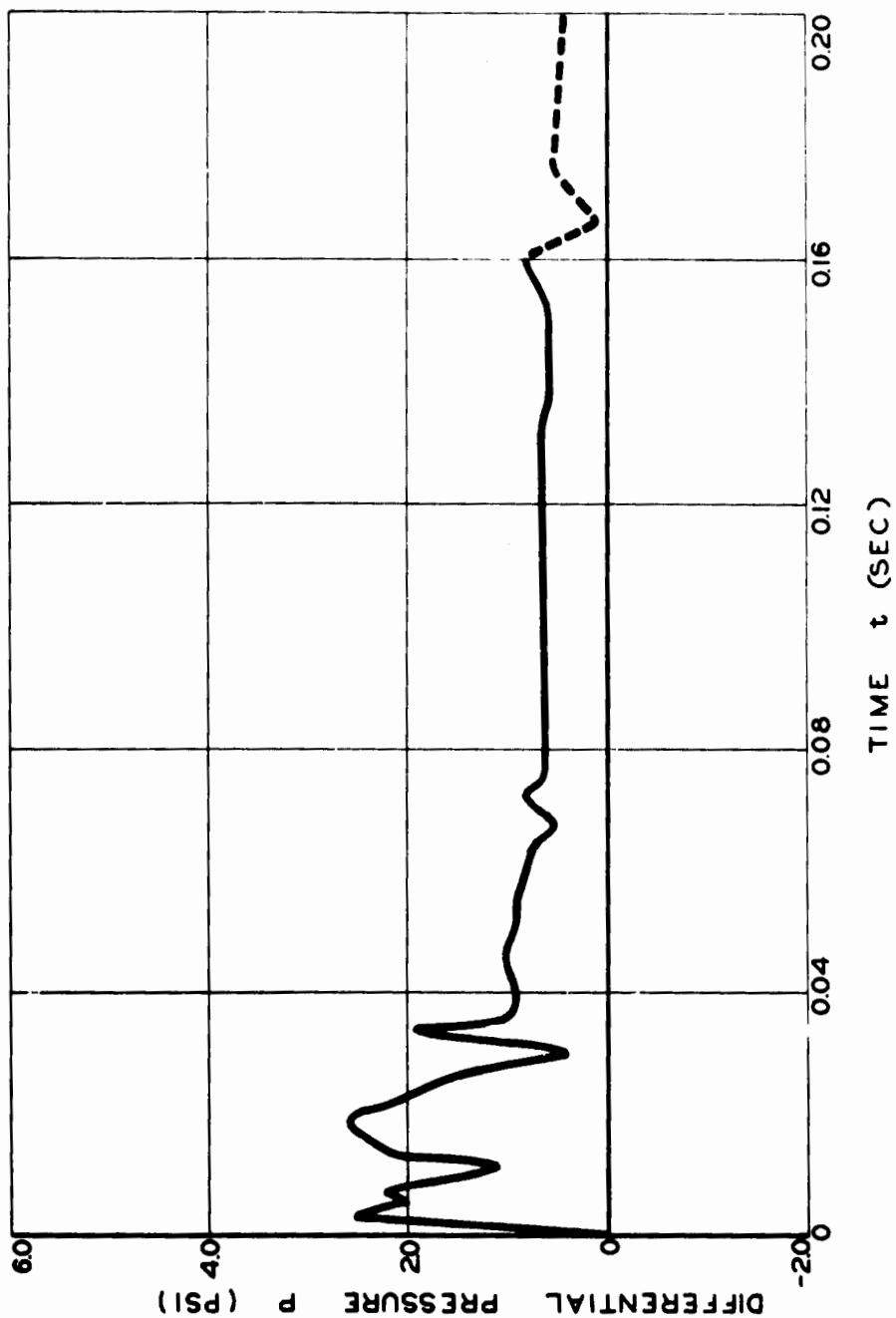


Fig. 5.13 Variation of Differential Pressure with Time at 20 Per Cent Chord of Rigid Wing 102. The angle of incidence was 9°. The range was 4,020 ft, Engbl.

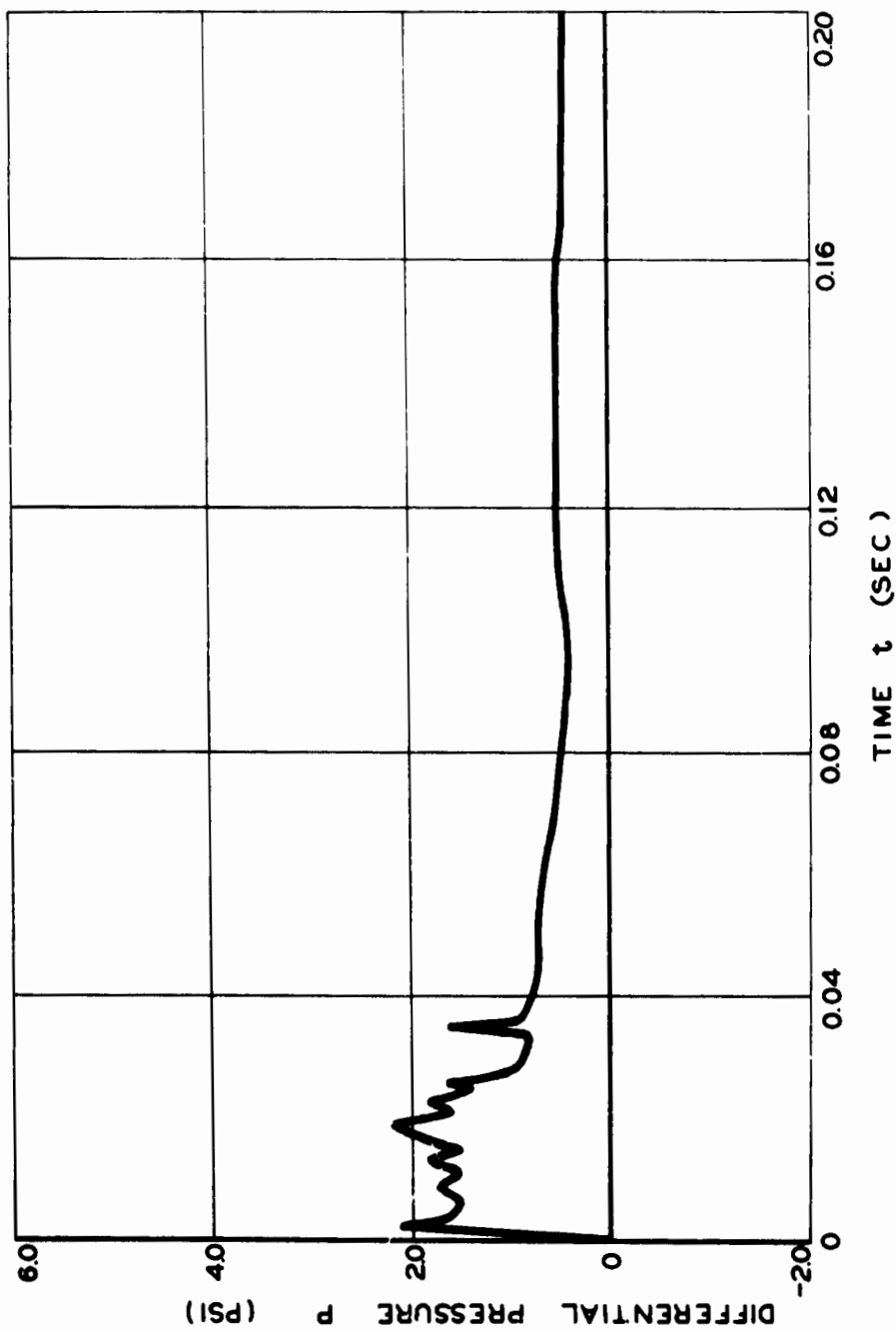


Fig. 5.14 Variation of Differential Pressure with Time at 40 Per Cent Chord of Rigid Wing 102. The angle of incidence was 9°, and the range was 4,020 ft, Engel.



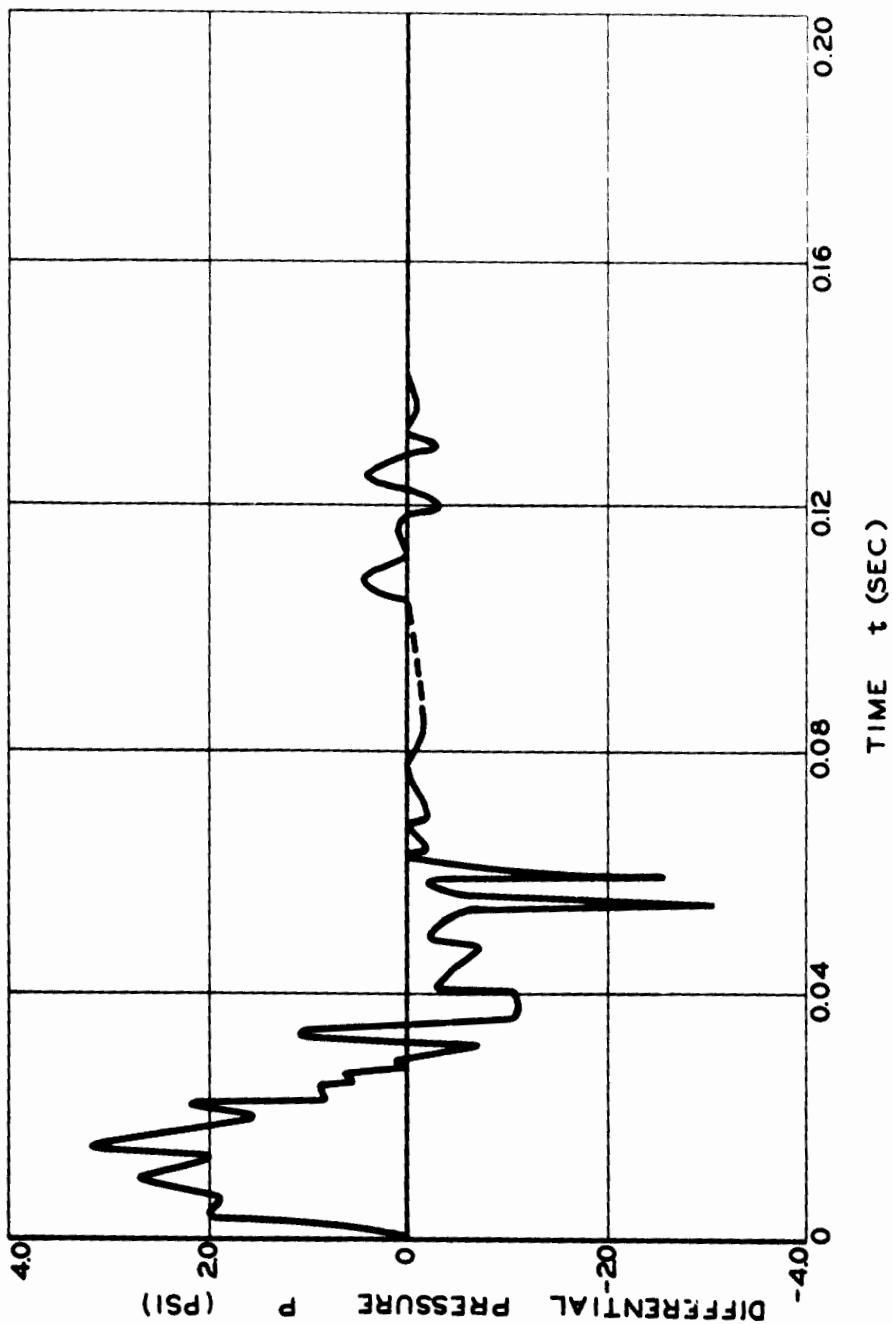


Fig. 5.15 Variation of Differential Pressure with Time at 80 Per Cent Chord of Rigid Wing 102. The angle of incidence was 9°, and the range was 4,020 ft, Englebi.

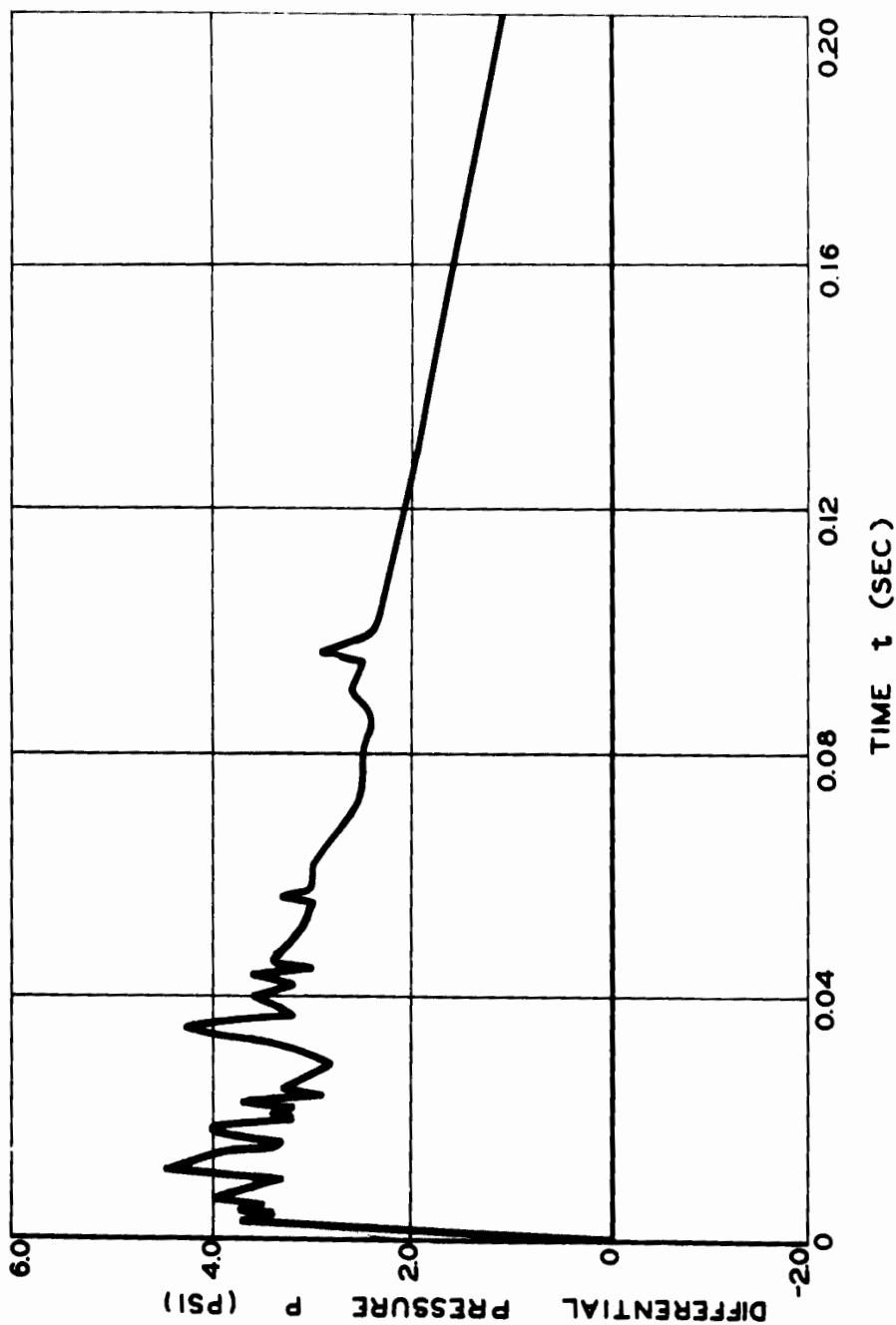


Fig. 5.16 Variation of Differential Pressure with Time at 5 Per Cent Chord of Rigid Wing 103. The angle of Incidence was  $6^\circ$ , and the range was 4,020 ft, Engelbl.

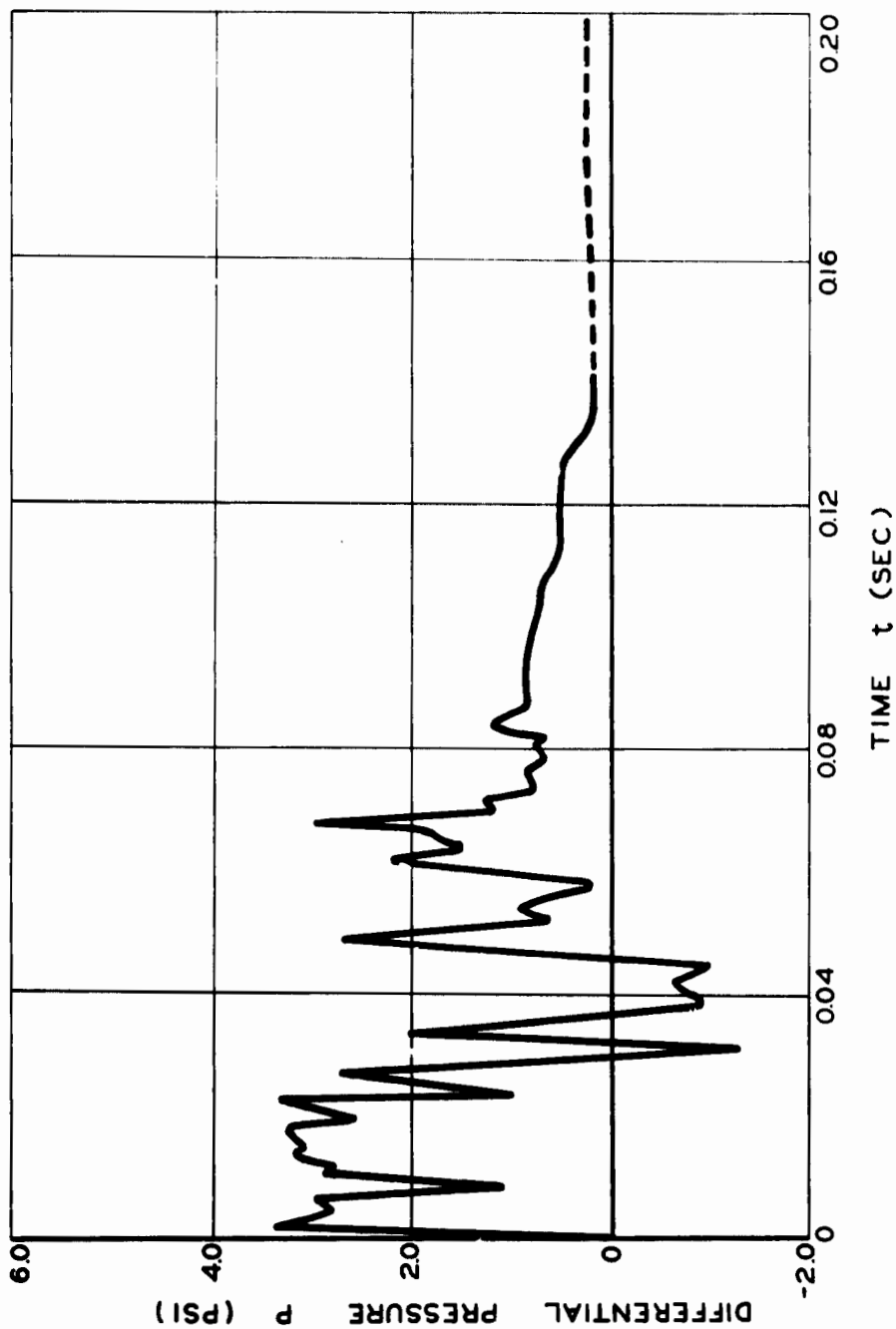


Fig. 5.17 Variation of Differential Pressure with Time at 10 Per Cent Chord of Rigid Wing 103. The angle of incidence was  $6^\circ$ , and the range was 4,020 ft, Englebi.

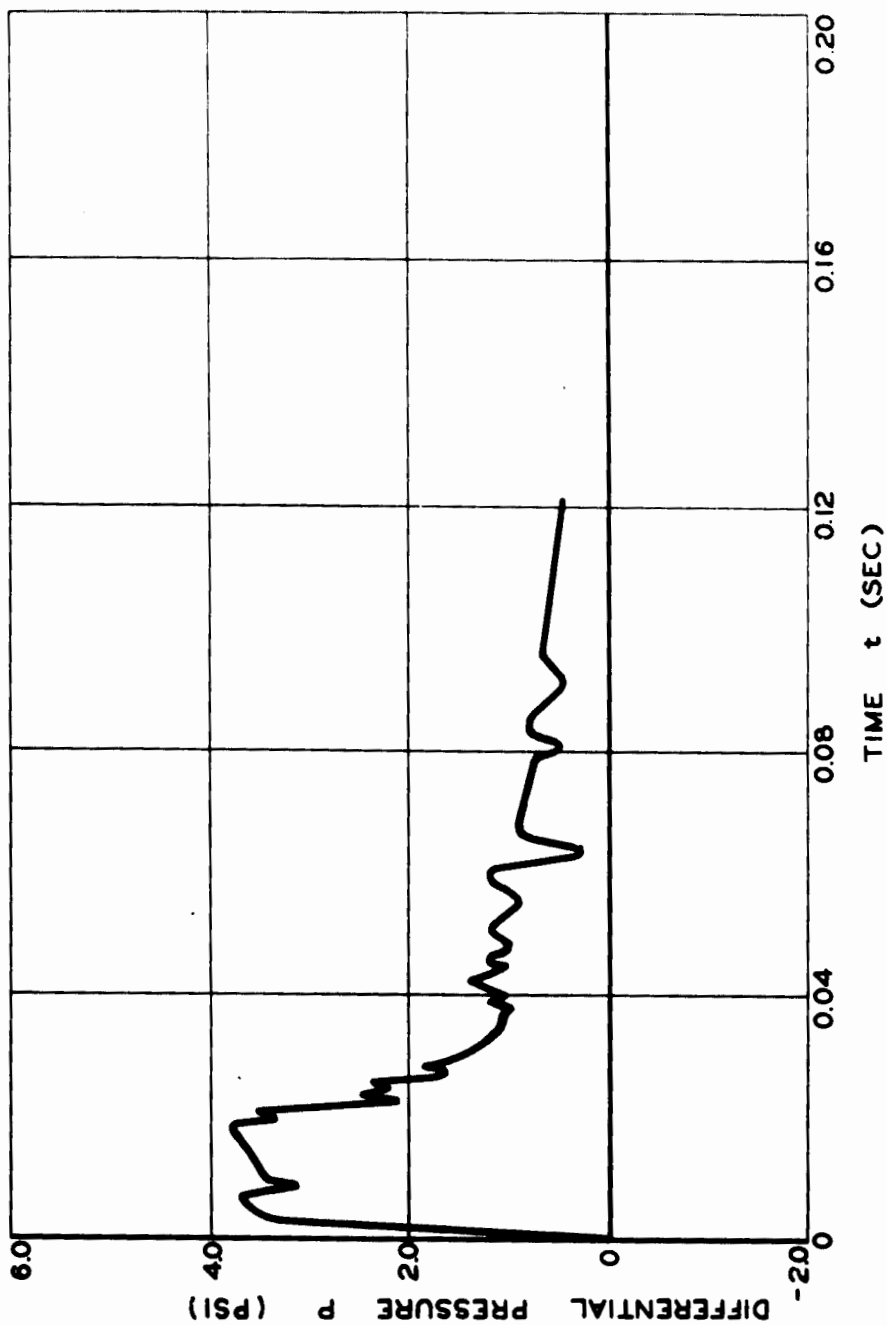


Fig. 5.18 Variation of Differential Pressure with Time at 15 Per Cent Chord of Rigid Wing 103. The angle of incidence was 6°, and the range was 4,020 ft, Engelb.

UNCLASSIFIED

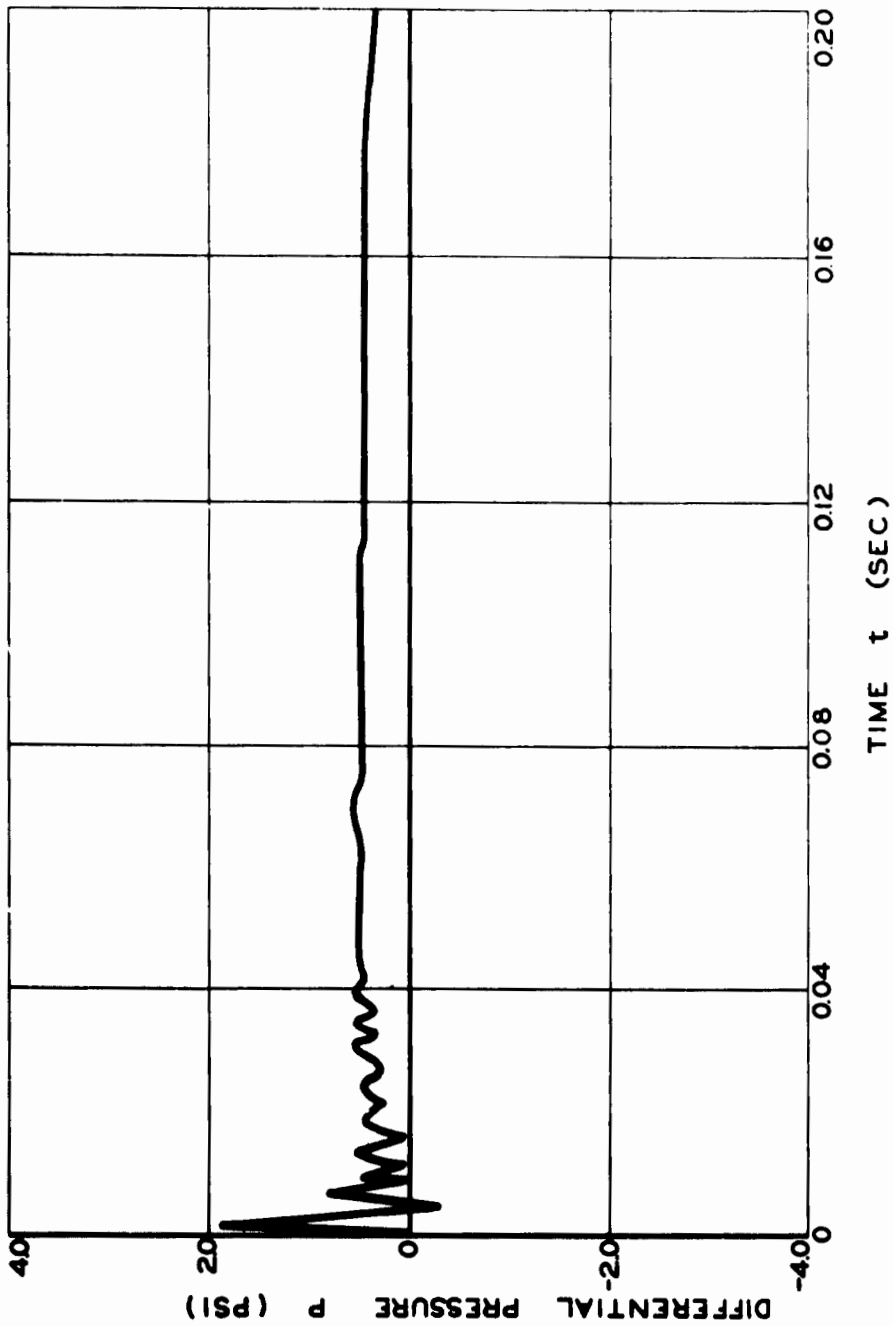


Fig. 5.19 Variation of Differential Pressure with Time at 10 Per Cent Chord of Rigid Wing 202. The angle of incidence was  $9^\circ$ , and the range was 6,878 ft, Muzlin.

UNCLASSIFIED

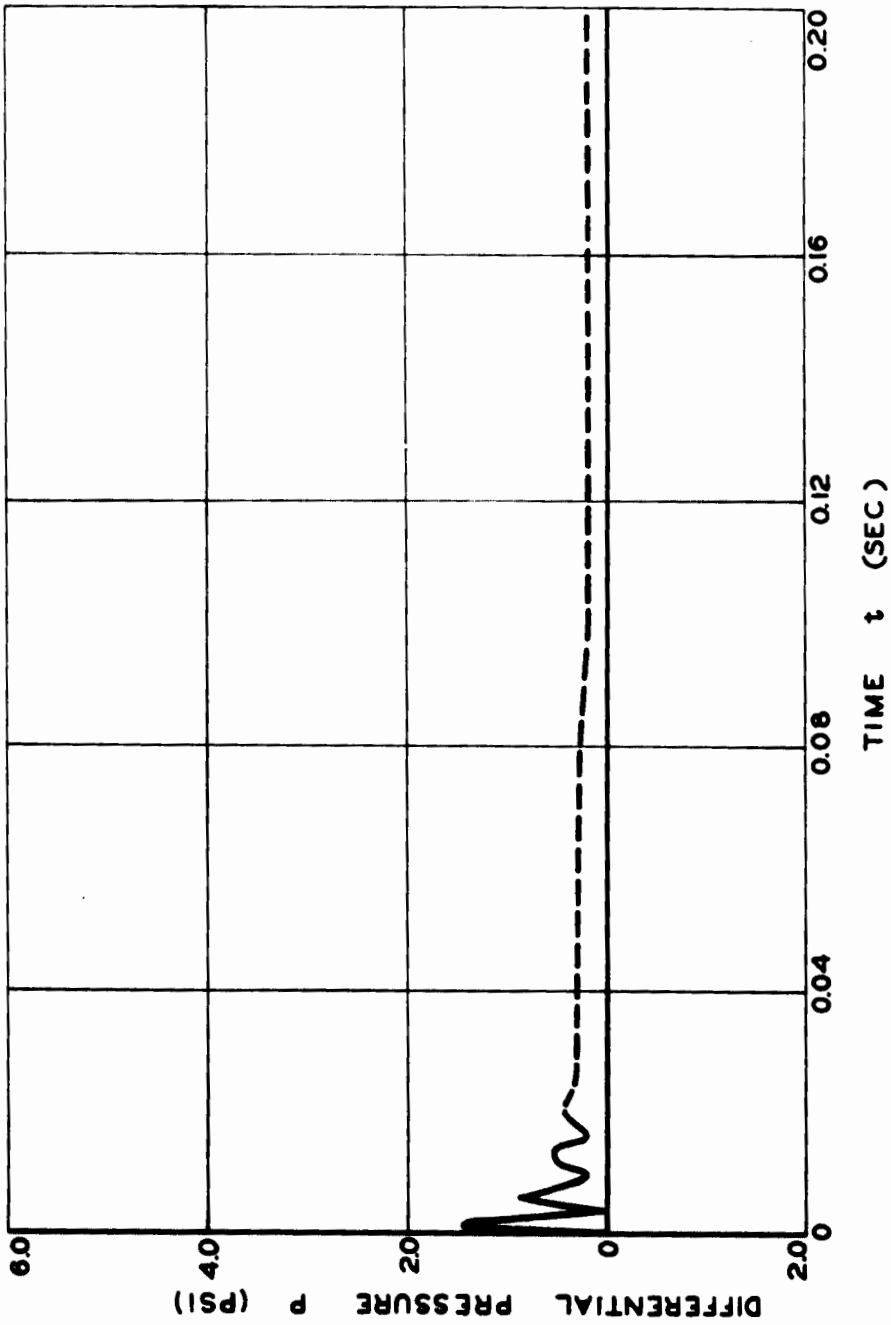


Fig. 5.20 Variation of Differential Pressure with Time at 15 Per Cent Chord of Rigid Wing 202. The angle of incidence was  $9^\circ$ , and the range was 6,878 ft, Muzin.

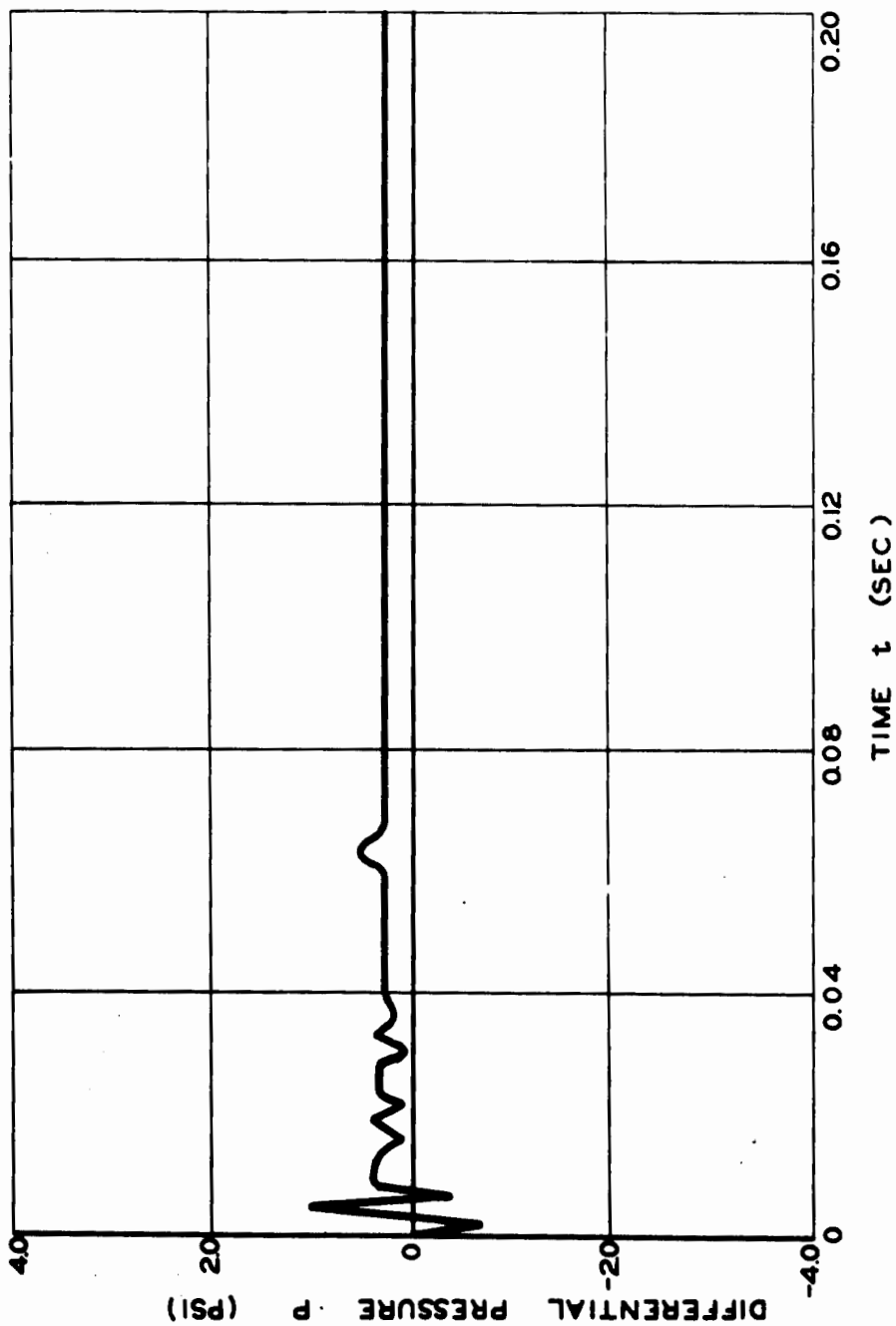


Fig. 5.21 Variation of Differential Pressure with Time at 20 Per Cent Chord of Rigid Wing 202. The angle of incidence was  $9^\circ$ , and the range was 6,878 ft, Muzin.

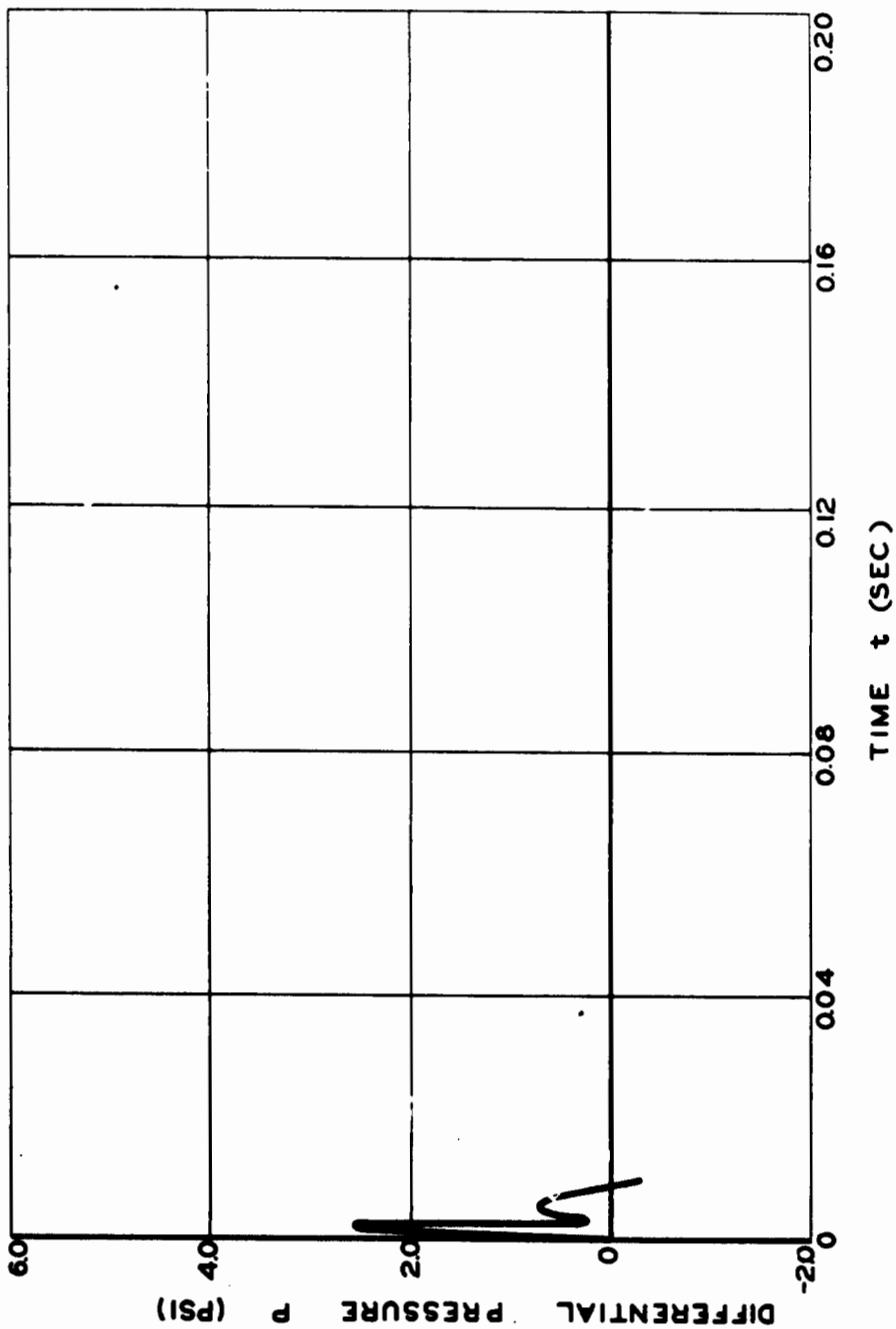


Fig. 5.22 Variation of Differential Pressure with Time at 5 Per Cent Chord of Rigid Wing 203. The angle of incidence was  $6^\circ$ , and the range was 6,878 ft, Muzin.



UNCLASSIFIED

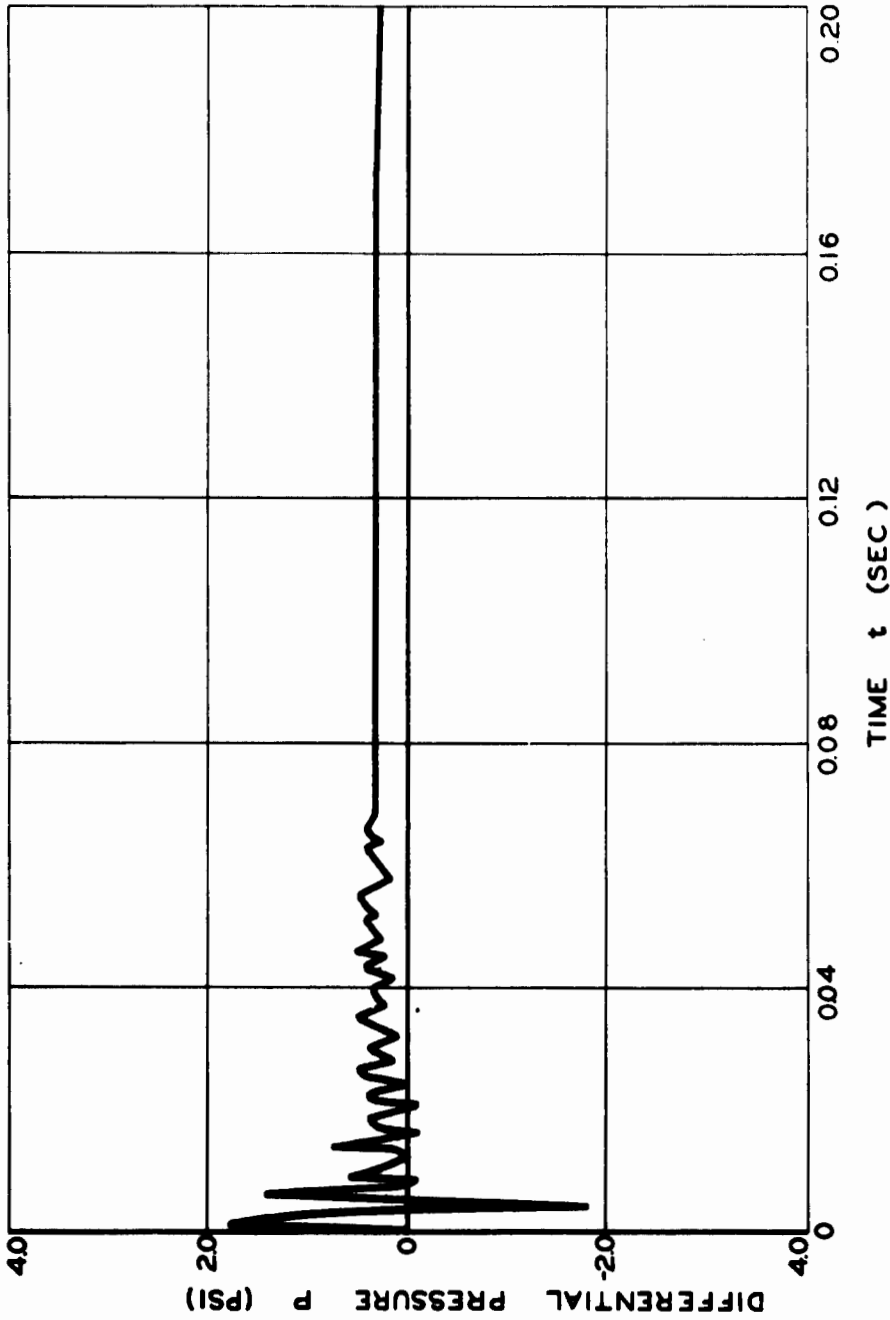


Fig. 5.23 Variation of Differential Pressure with Time at 10 Per Cent Chord of Rigid Wing 203. The angle of incidence was 6°, and the range was 6,878 ft, Muzin.

UNCLASSIFIED

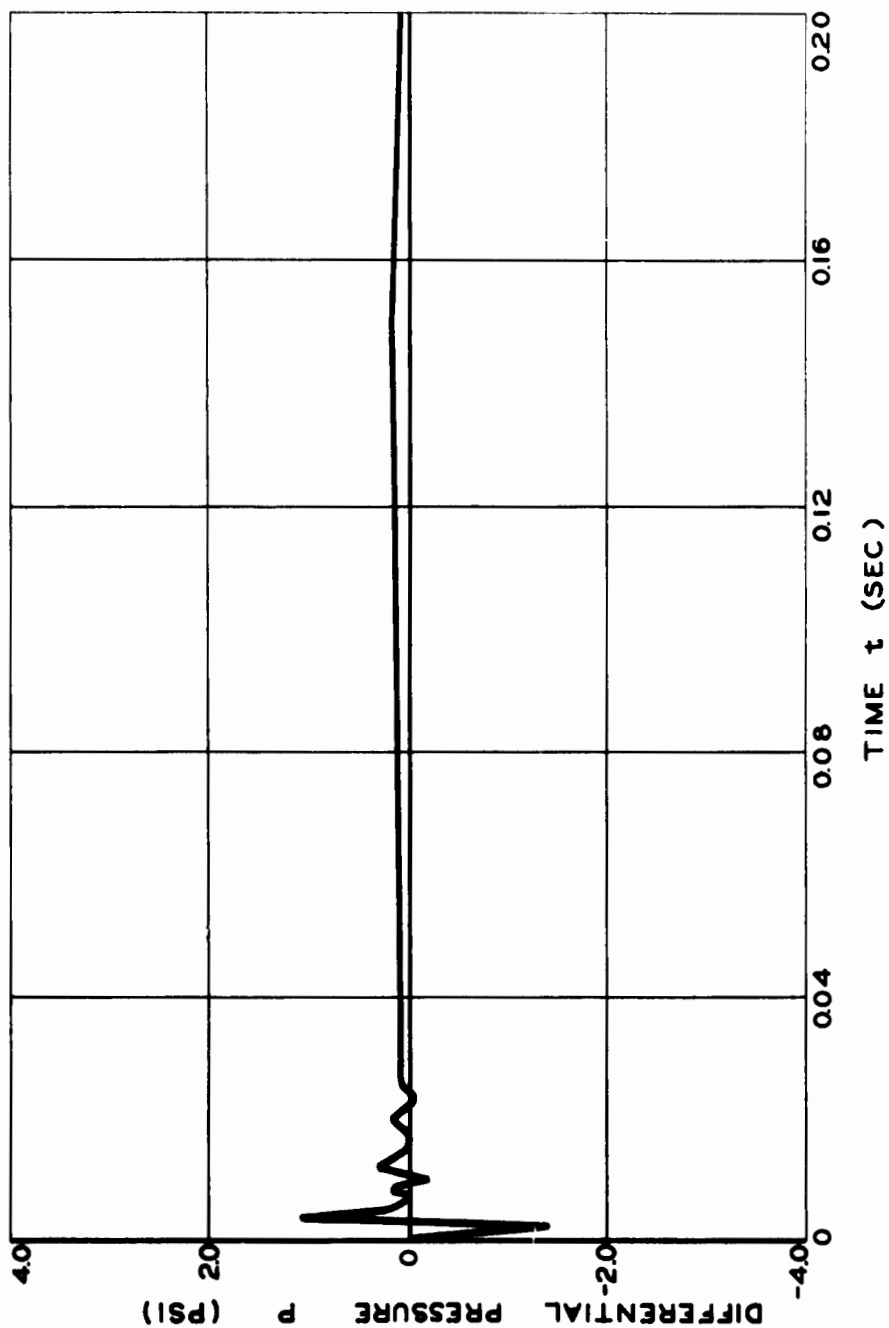


Fig. 5.24 Variation of Differential Pressure with Time at 20 Per Cent Chord of Rigid Wing 203. The angle of incidence was  $6^\circ$ , and the range was 6,878 ft, Muzin.

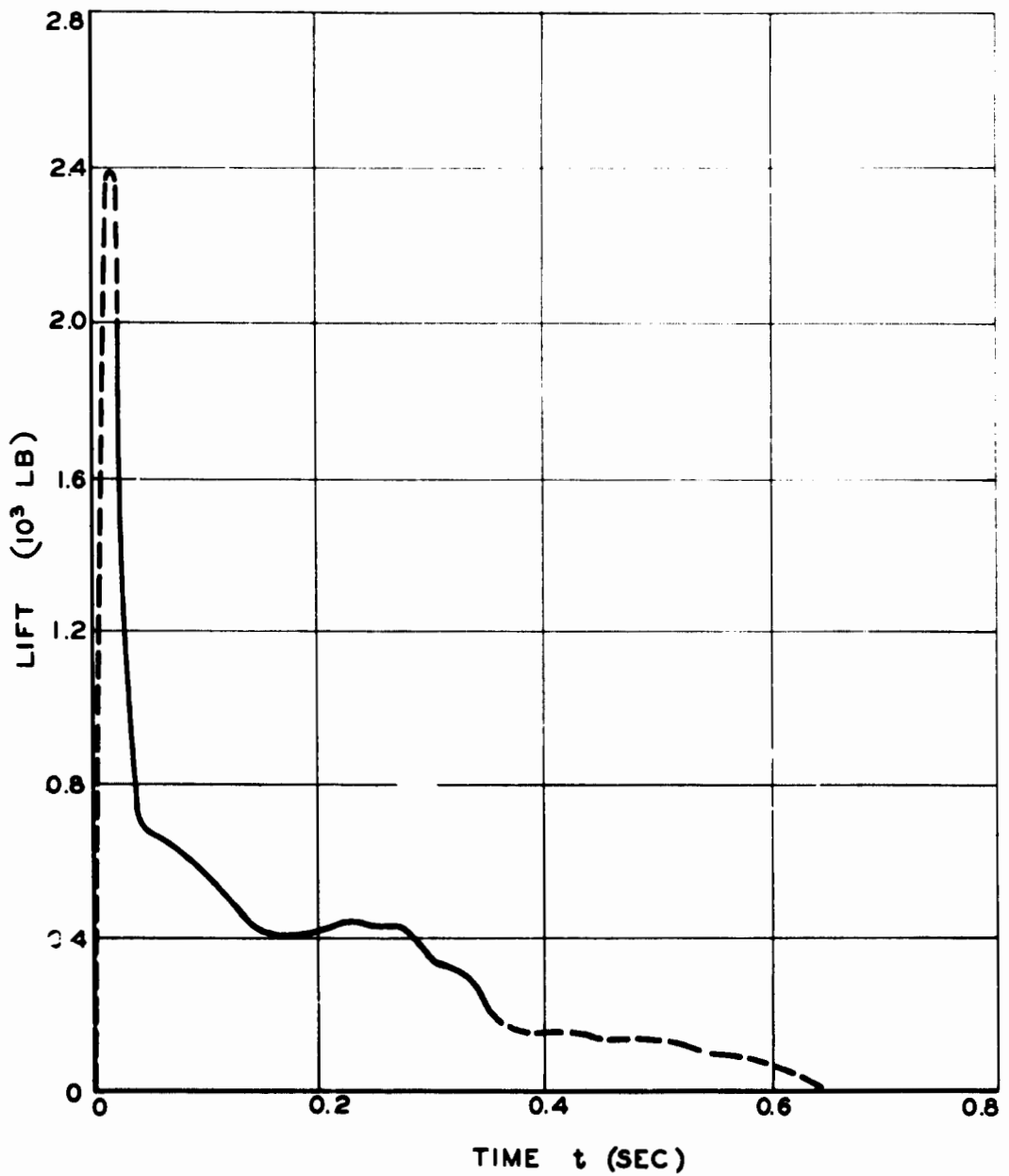


Fig. 5.25 Average Variation of Lift with Time Obtained from Differential-pressure Measurements for Rigid Wing 102. The angle of incidence was  $9^\circ$ , and the range was 4,020 ft, Engel.

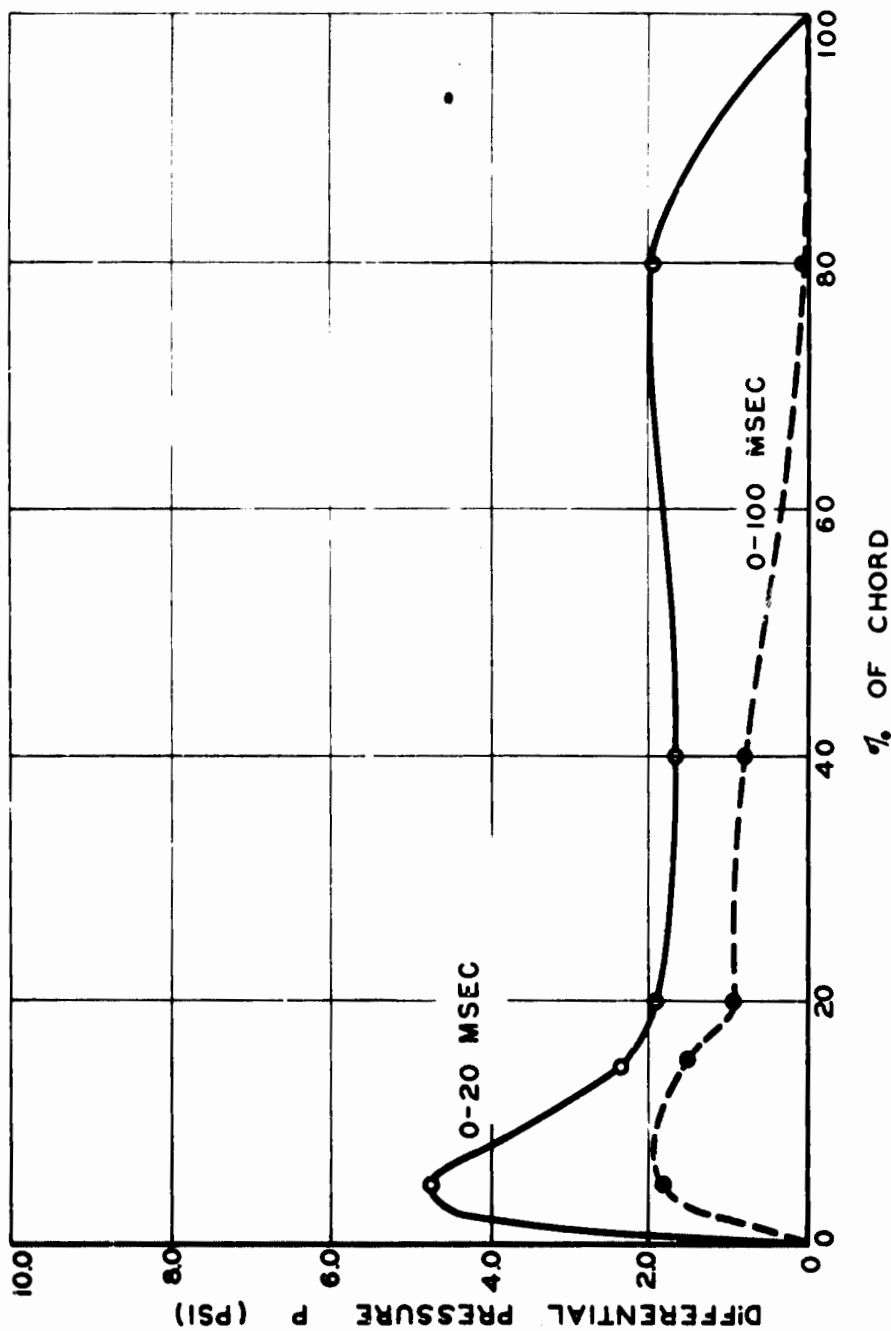


Fig. 5.26 Average Pressure Distribution following Arrival of the Blast Front for Rigid Wing 102. The angle of incidence was 9°, and the range was 4,020 ft, Engbl.

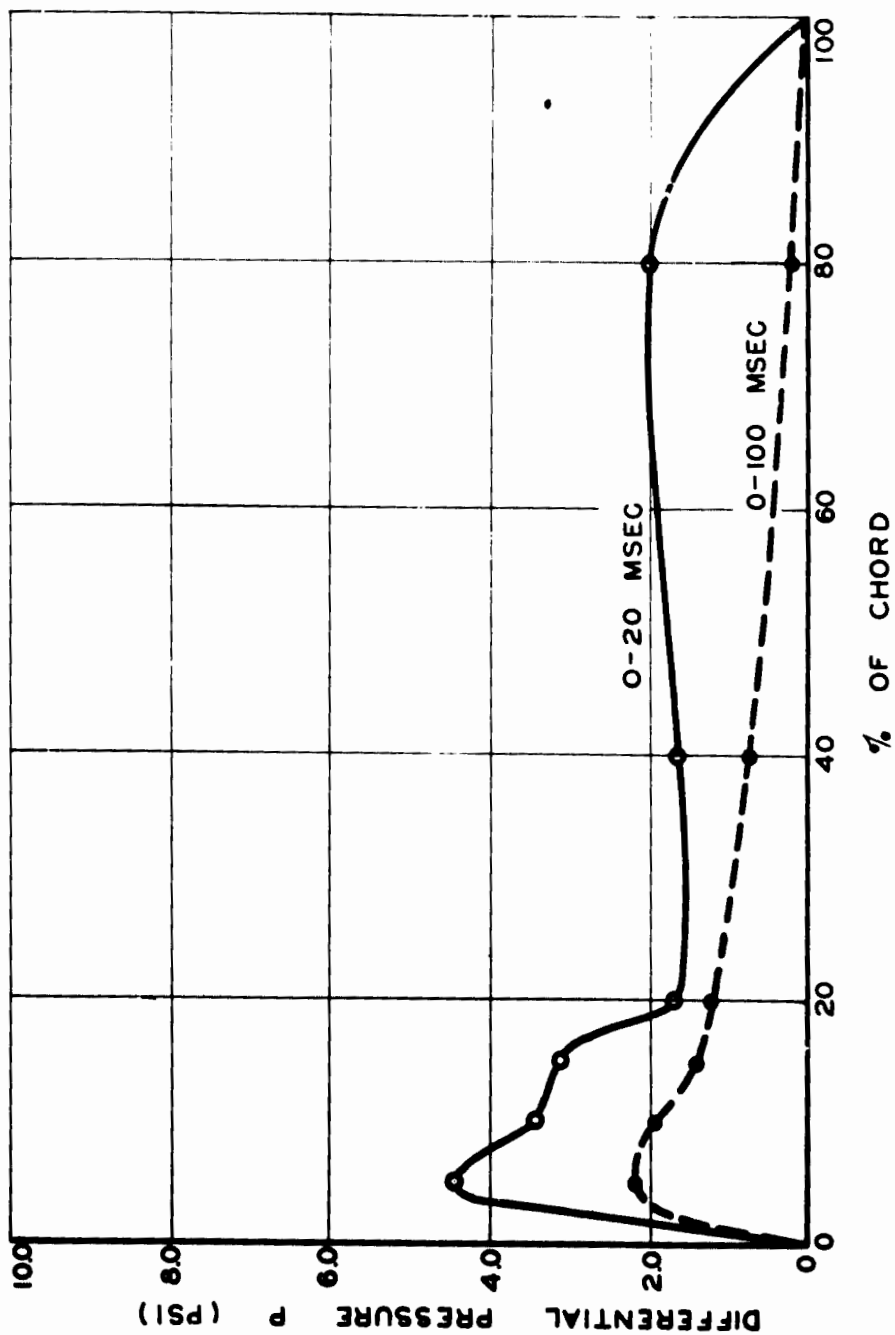


Fig. 5.27 Weighted Average Pressure Distribution following Arrival of the Blast Front, from Pressure Measurements for Four Wings Transferred and Combined to Give an Equivalent Pressure Distribution for a Rigid Wing. The angle of incidence was  $9^\circ$ , at a range of 4,020 ft.

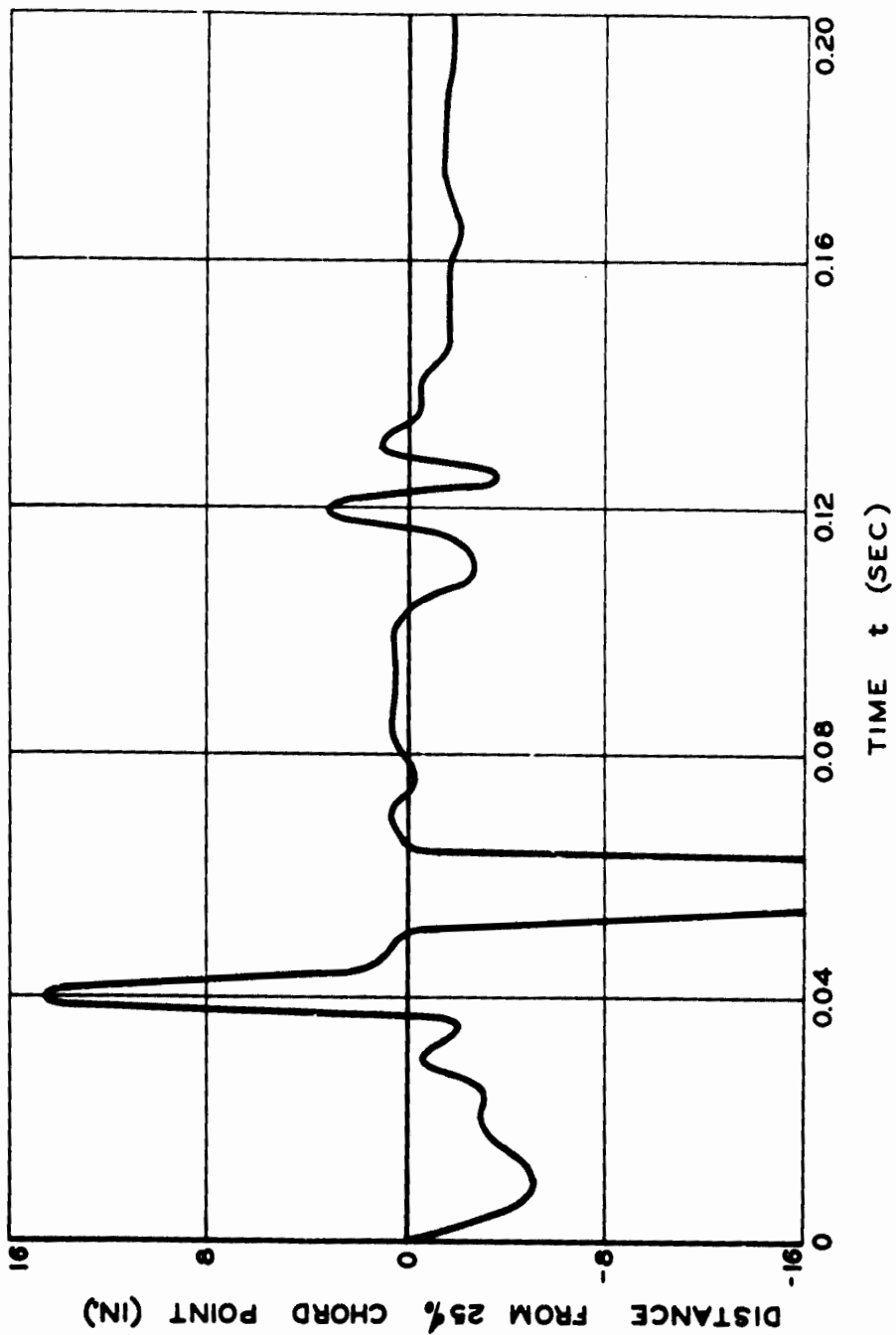


Fig. 5.28 Variation of Center-of-pressure Distance from the 25 Per Cent Chord Point with Time, Obtained from Differential-pressure Measurements for Rigid Wing 102. The angle of incidence was  $9^\circ$ , and the range was 4,020 ft, Engelb.

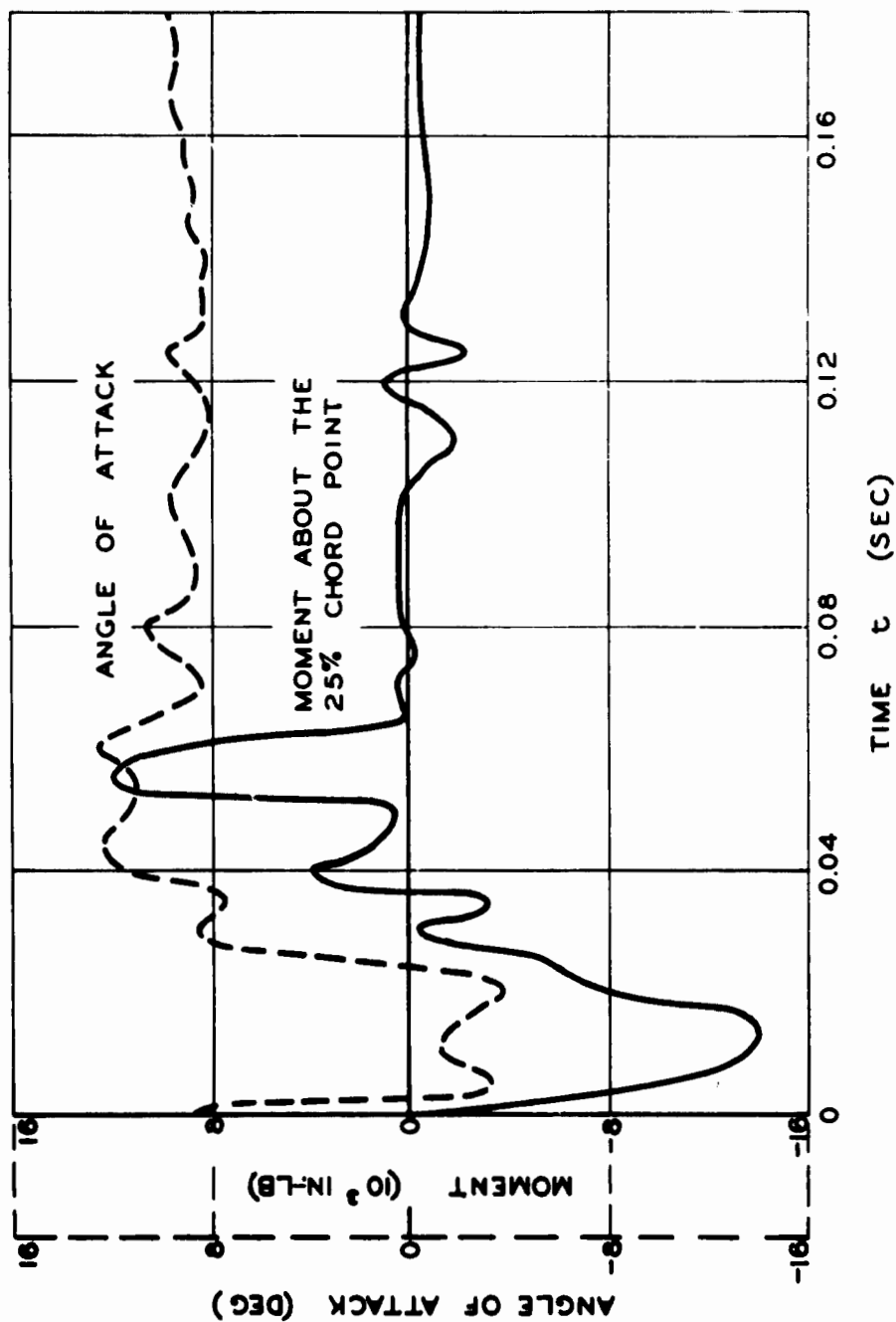


Fig. 5.29 Variation of Moment about the 25 Per Cent Chord with Time, Compared to the Variation of Angle of Attack for Rigid Wing 102. The angle of incidence was  $9^\circ$ , and the range was 4,020 ft, Engebli.

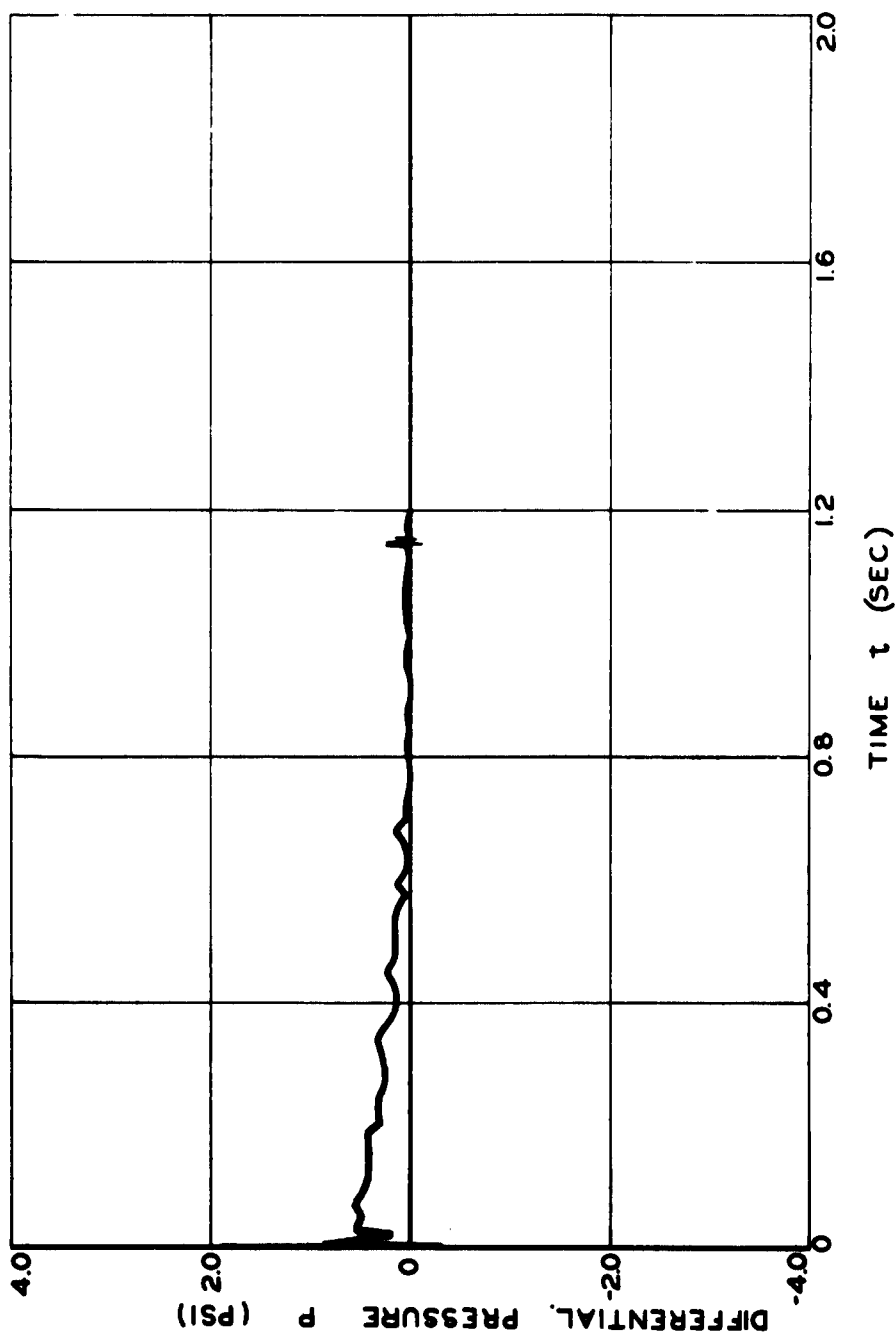


Fig. 5.30 Variation of Differential Pressure with Time at 10 Per Cent Chord of Rigid Wing 202. The angle of incidence was  $9^\circ$ , and the range was 6,878 ft, Muzin, indicating abrupt pressure variations 1,150 msec after passage of blast front.



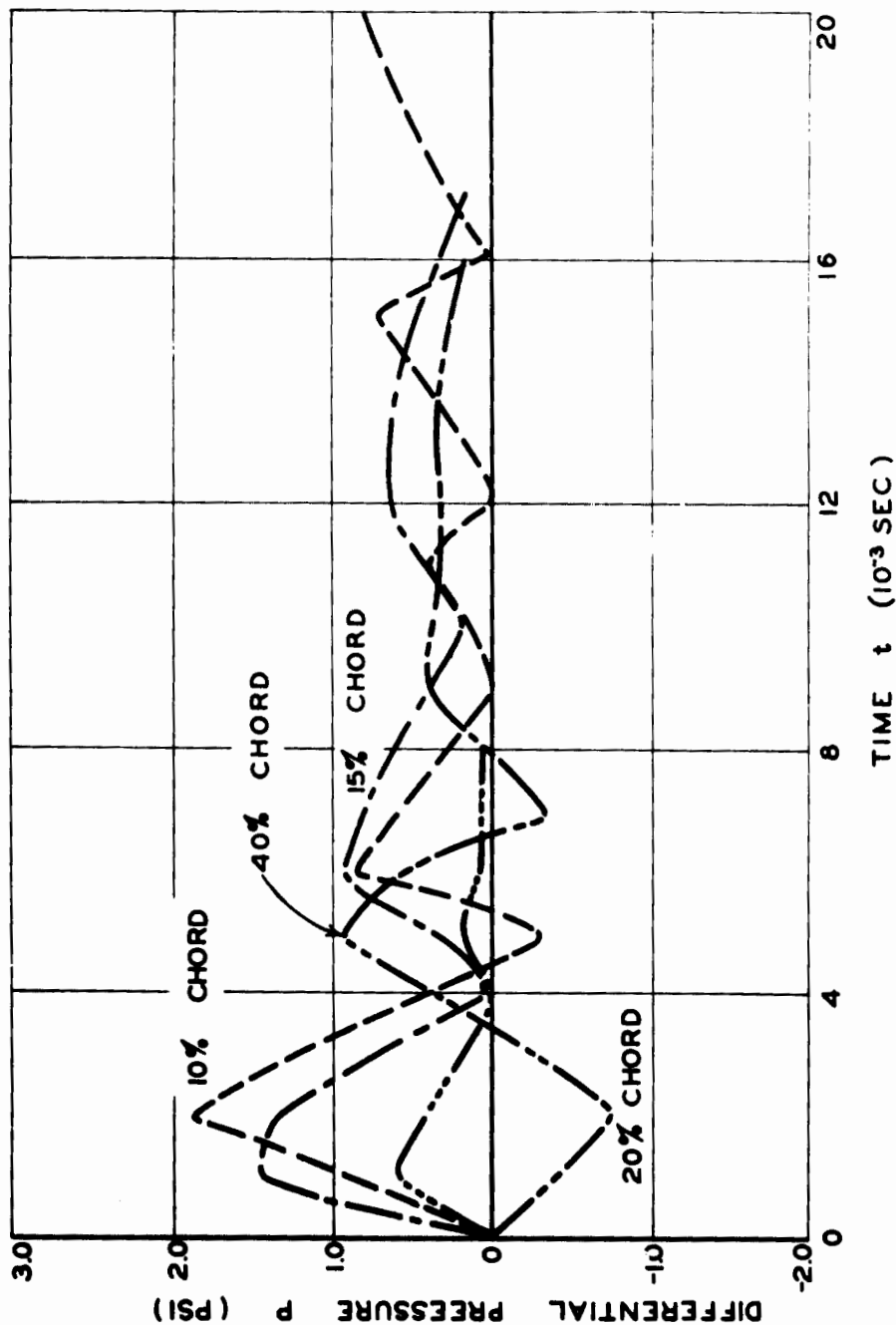


Fig. 5.31 Comparison during Initial Stages of the Variation of Differential Pressure at Four Chord Points of Rigid Wing 202. The angle of Incidence was  $9^\circ$ , and the range was 6,878 ft, Muzin.

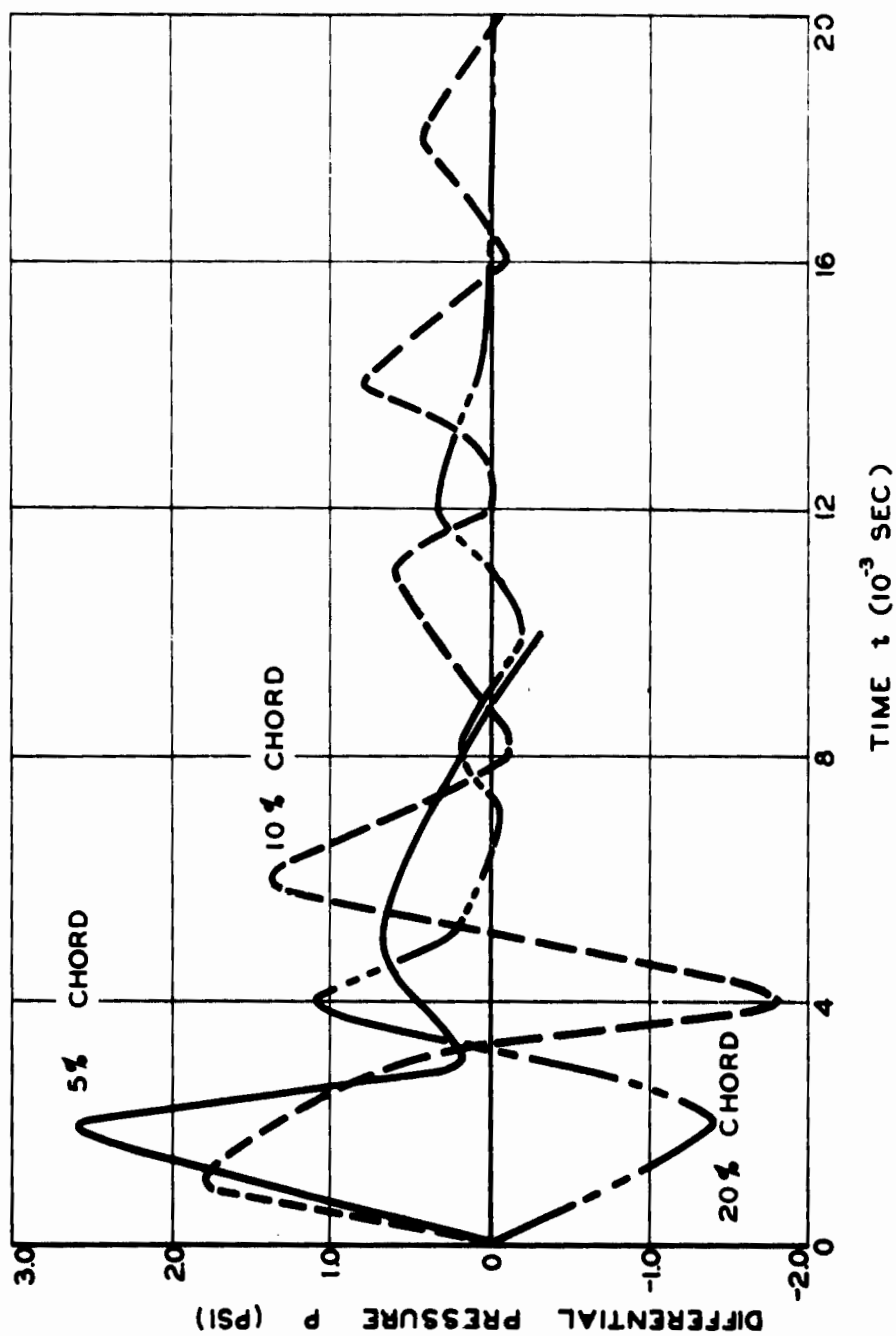


Fig. 5.32 Comparison during the Initial Stages of the Variation of Differential Pressure at Three Chord Points of Rigid Wing 203. The angle of Incidence was  $6^\circ$ , and the range was 6,878 ft, Muzin.

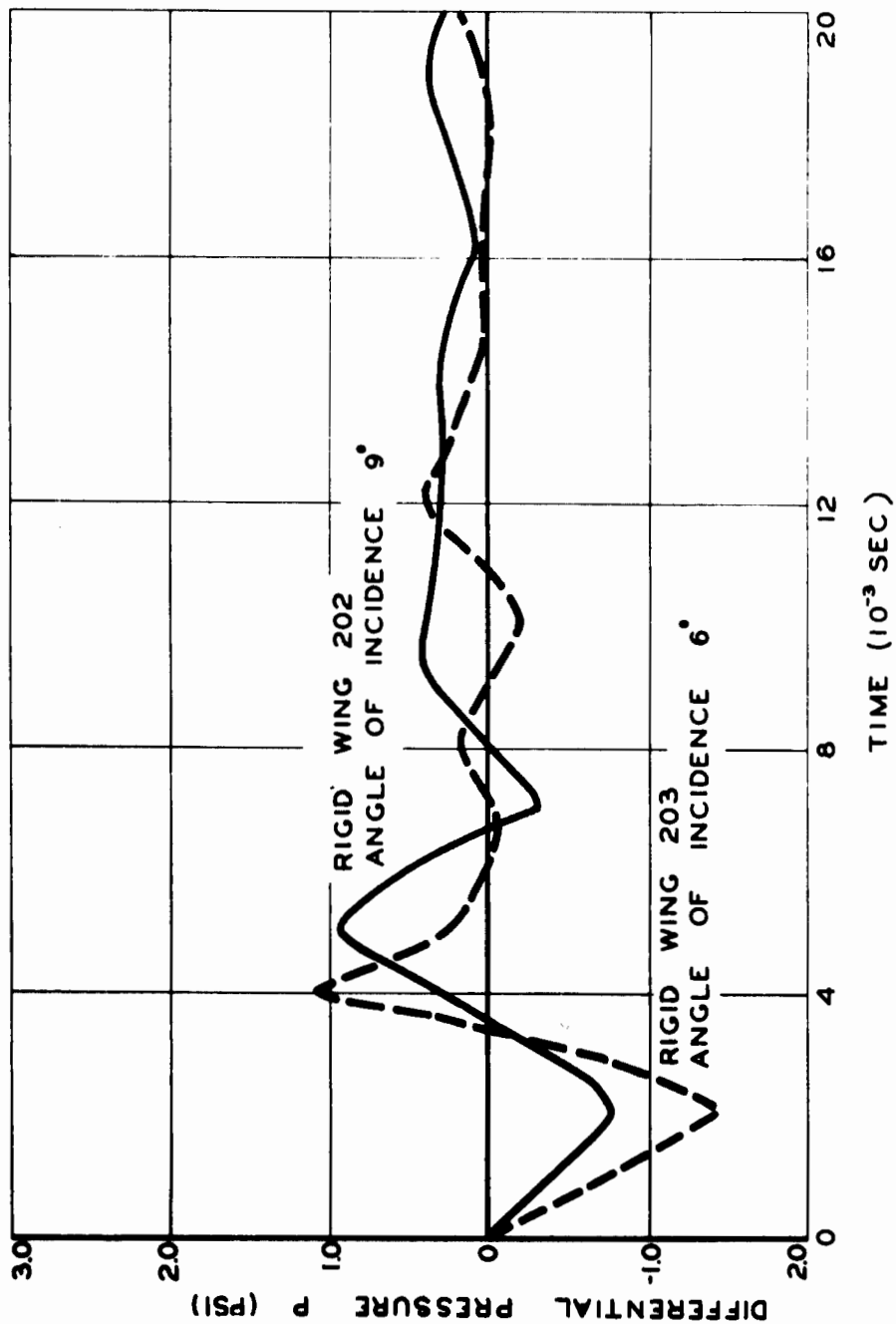


Fig. 5.33 Variation of Differential Pressure at 20 Per Cent Chord of Two Rigid Wings at Different Angles of Incidence. The range was 6,878 ft, Muzin.

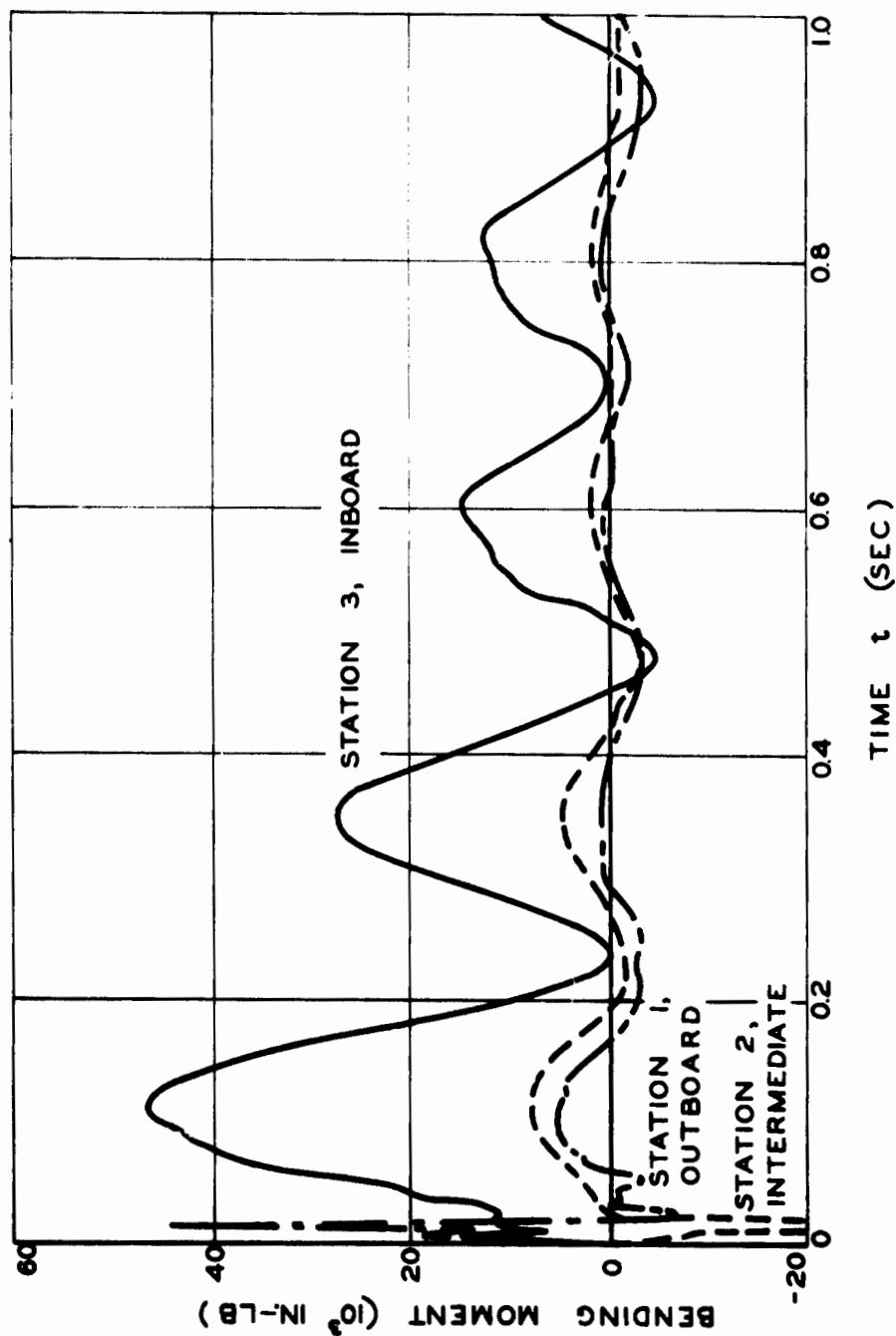


Fig. 5.34 Comparison of the Variation of Bending Moment with Time at Three Stations of Structural Wing 101. The angle of incidence was  $6^\circ$ , and the range was 4,020 ft, Engbeli.

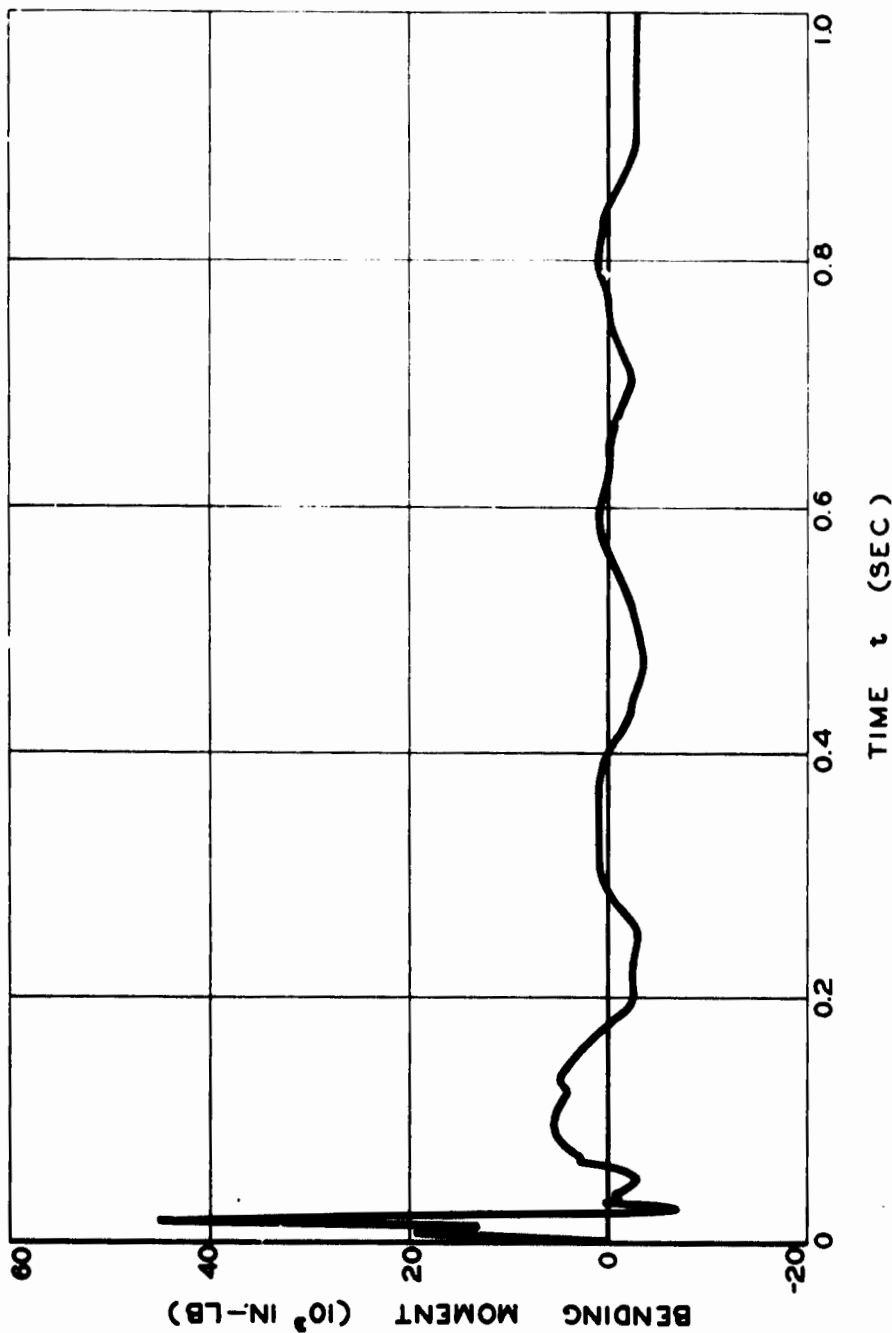


Fig. 5.35 Variation of Bending Moment with Time at Station 1, Outboard, of Structural Wing 101. The angle of incidence was  $6^\circ$ , and the range was 4,020 ft, Engbebi.

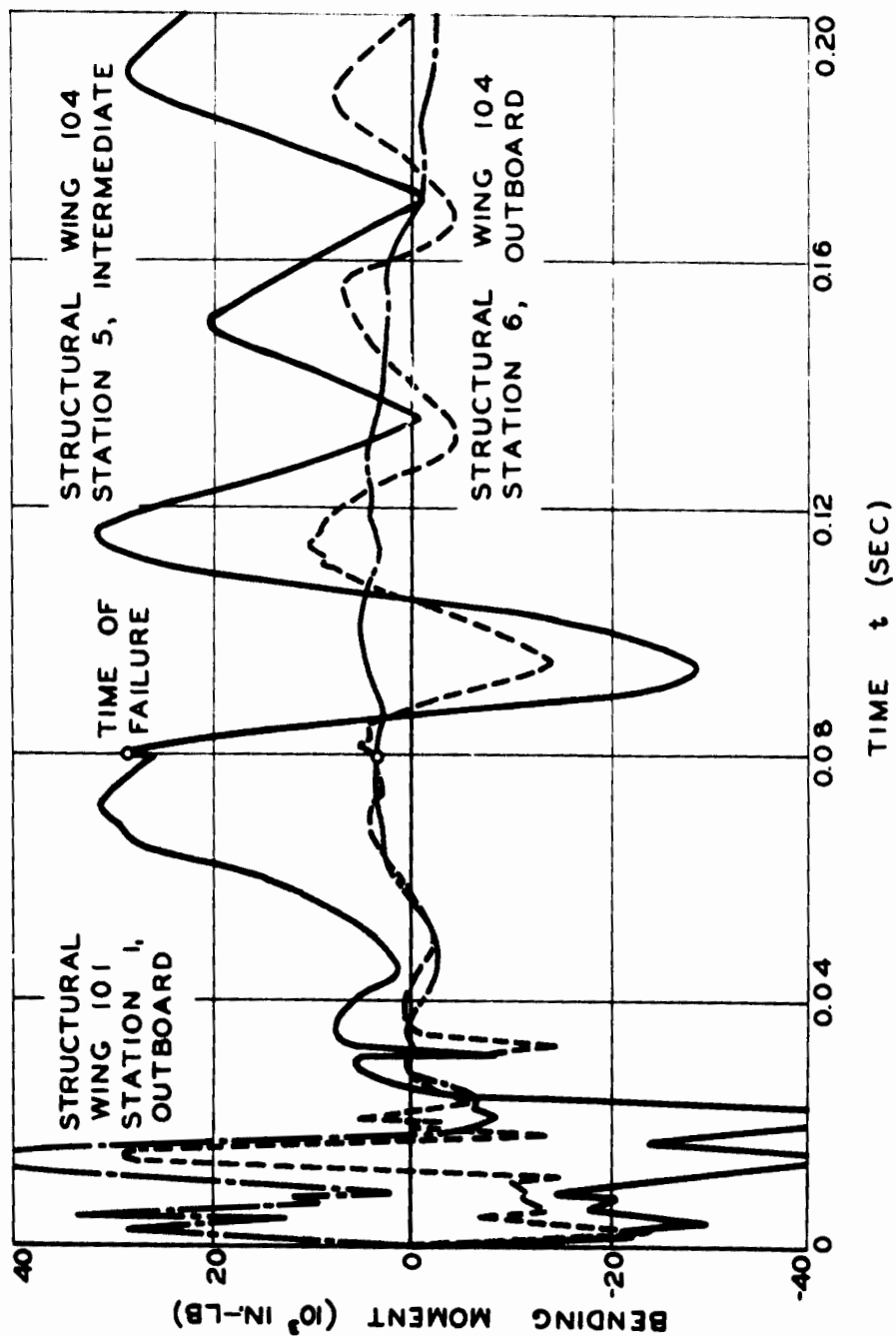


Fig. 5.36 Variation of Bending Moment with Time at Two Stations of Structural Wing 104, Angle of Incidence  $9^\circ$ , Compared with Bending Moment at One Station of Structural Wing 101, Angle of Incidence  $6^\circ$ , to Indicate Time of Failure of Wing 104. The range was 4,020 ft, Engcb.

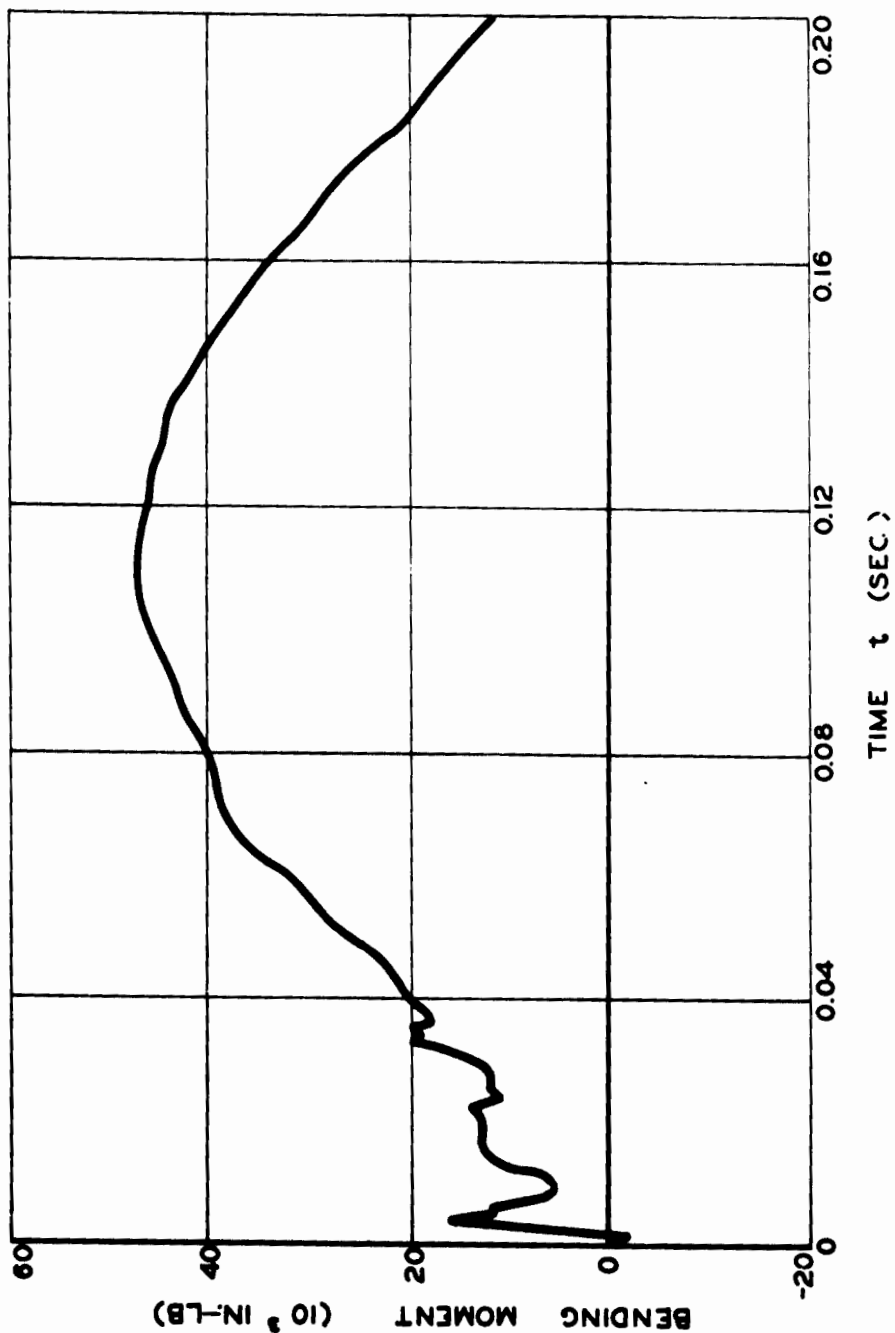


Fig. 5.37 Variation of Bending Moment with Time at Station 3, Inboard, of Structural Wing 101. The angle of incidence was  $6^\circ$ , and the range was 4,020 ft, Engbl.

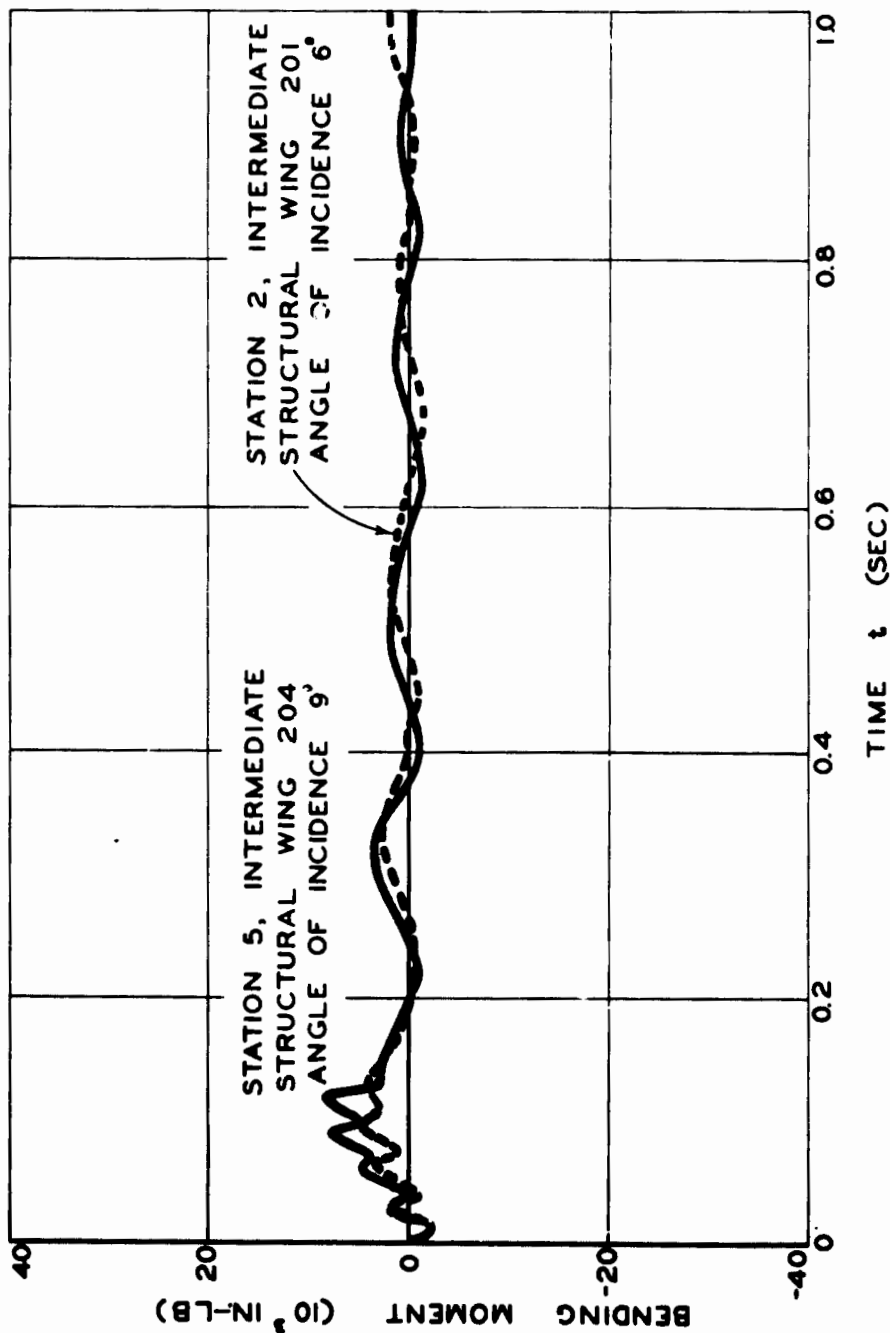


Fig. 5.38 Variation of Bending Moment with Time at the Intermediate Station of Two Structural Wings at Different Angles of Incidence. The range was 6,878 ft, Muzin.



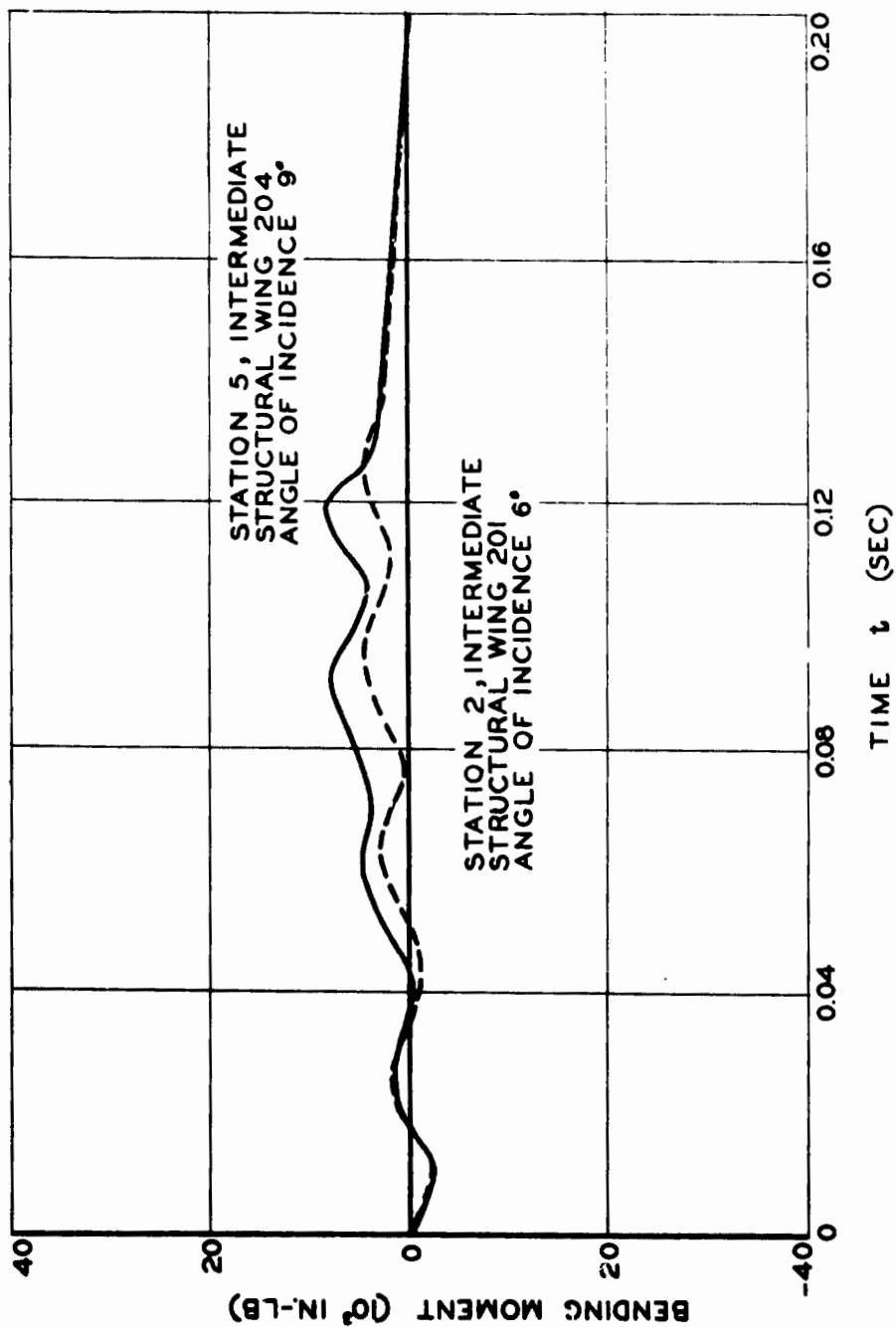


Fig. 5.39 Indication of Second-mode Bending Moment at the Intermediate Station of Two Structural Wings. The range was 6,878 ft, Muzn.

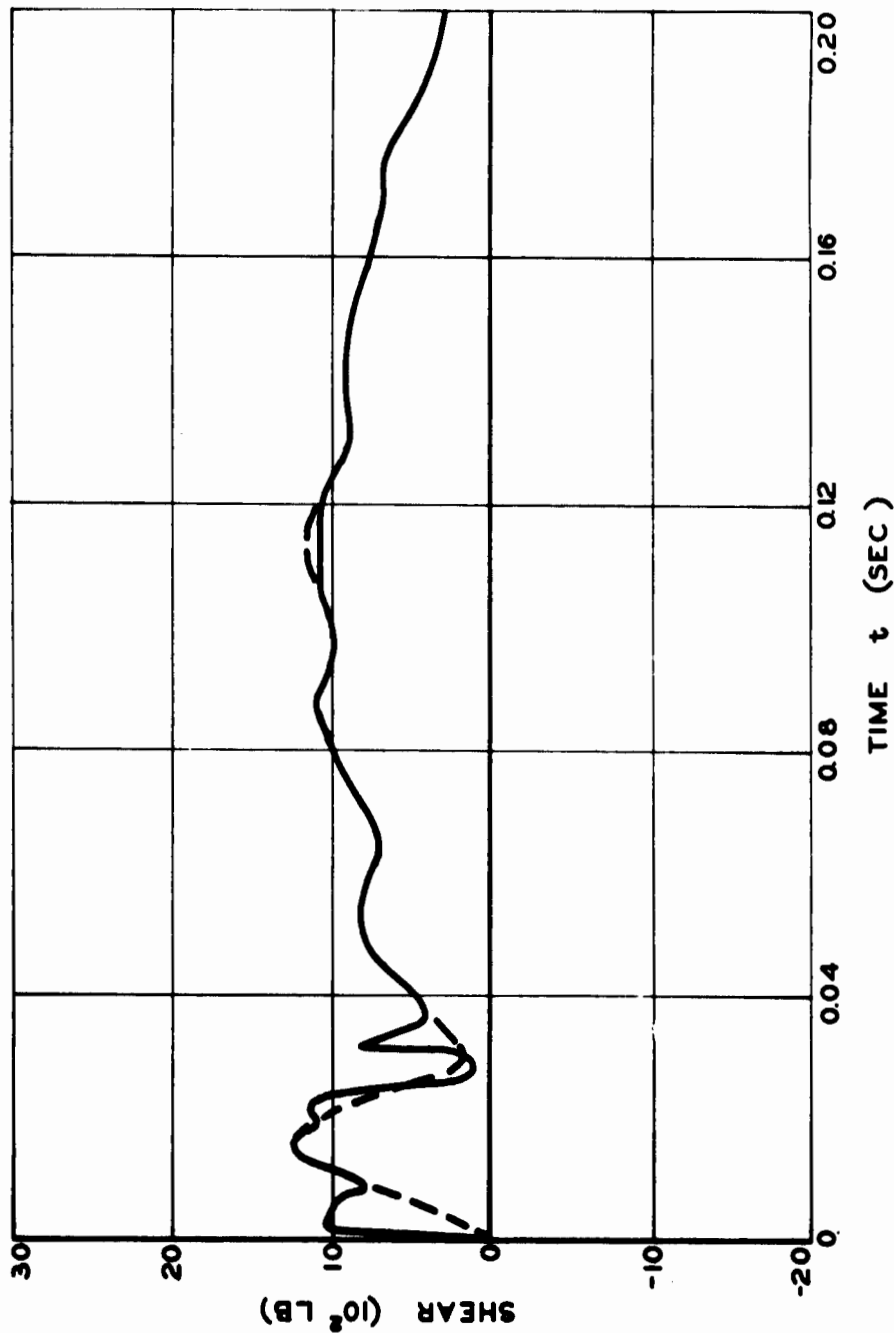


Fig. 5.40 Variation of Shear with Time at Station 3, Inboard, Structural Wing 101. The angle of incidence was  $6^\circ$ , and the range was 4,020 ft, Engbl.

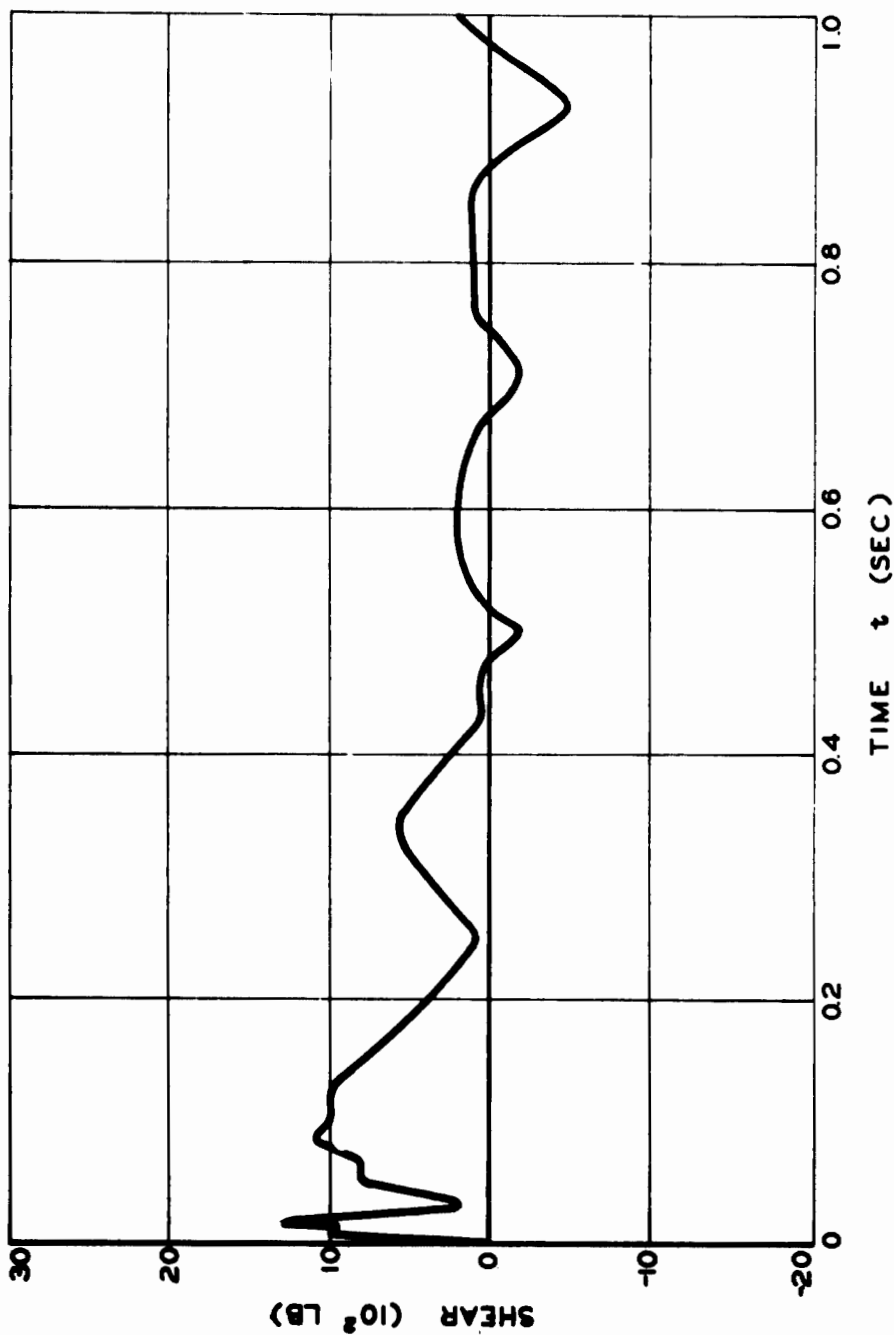


Fig. 5.41 Variation of Shear with Time at Station 3, Inboard, of Structural Wing 101. The angle of incidence was  $6^\circ$ , and the range was 4,020 ft, Engbbi.

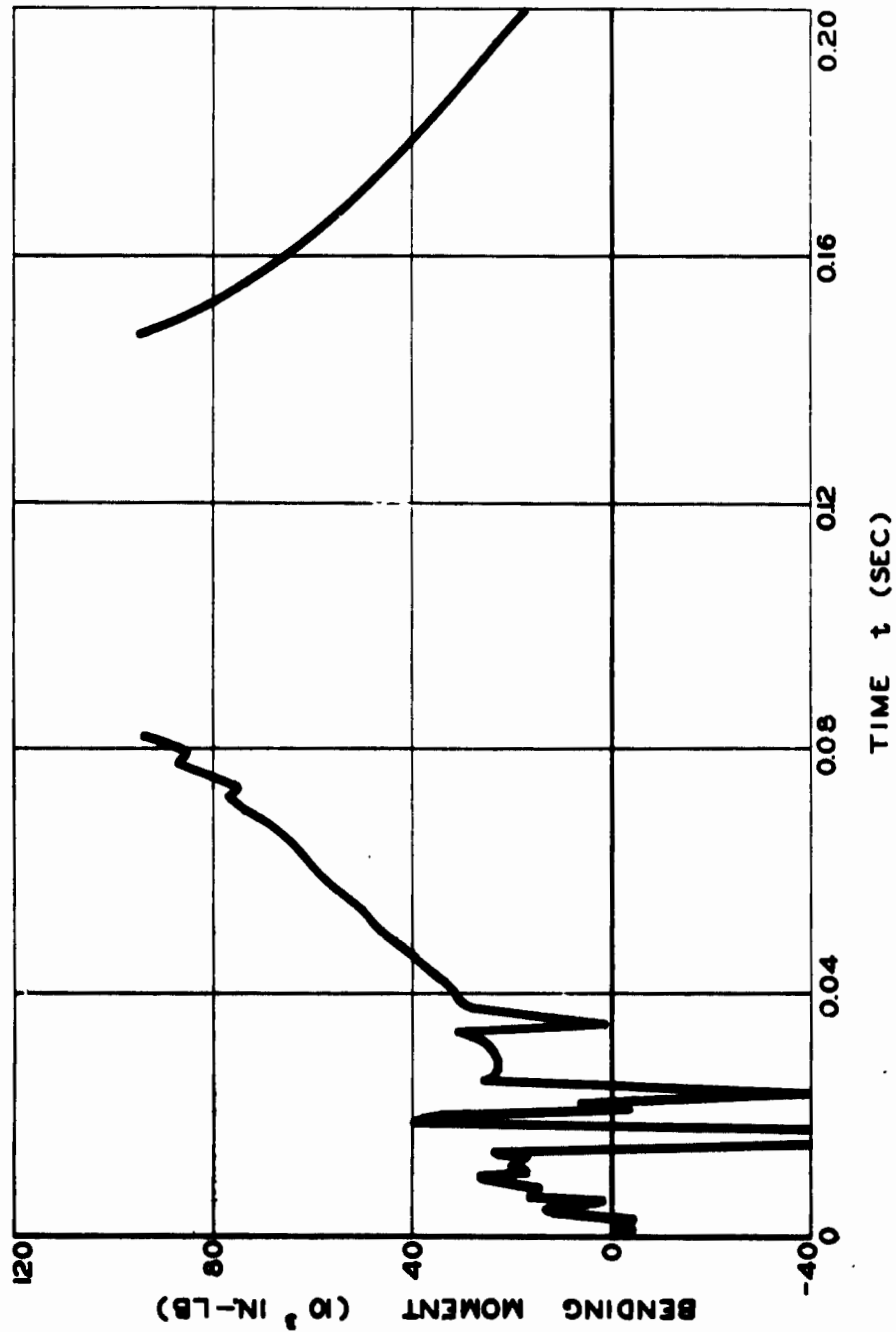


Fig. 5.42 Variation of Bending Moment with Time at Station 7, Inboard, of Swept Wing 105. The angle of incidence was  $8\frac{1}{4}^\circ$ , and the range was 4,020 ft, Engabl.

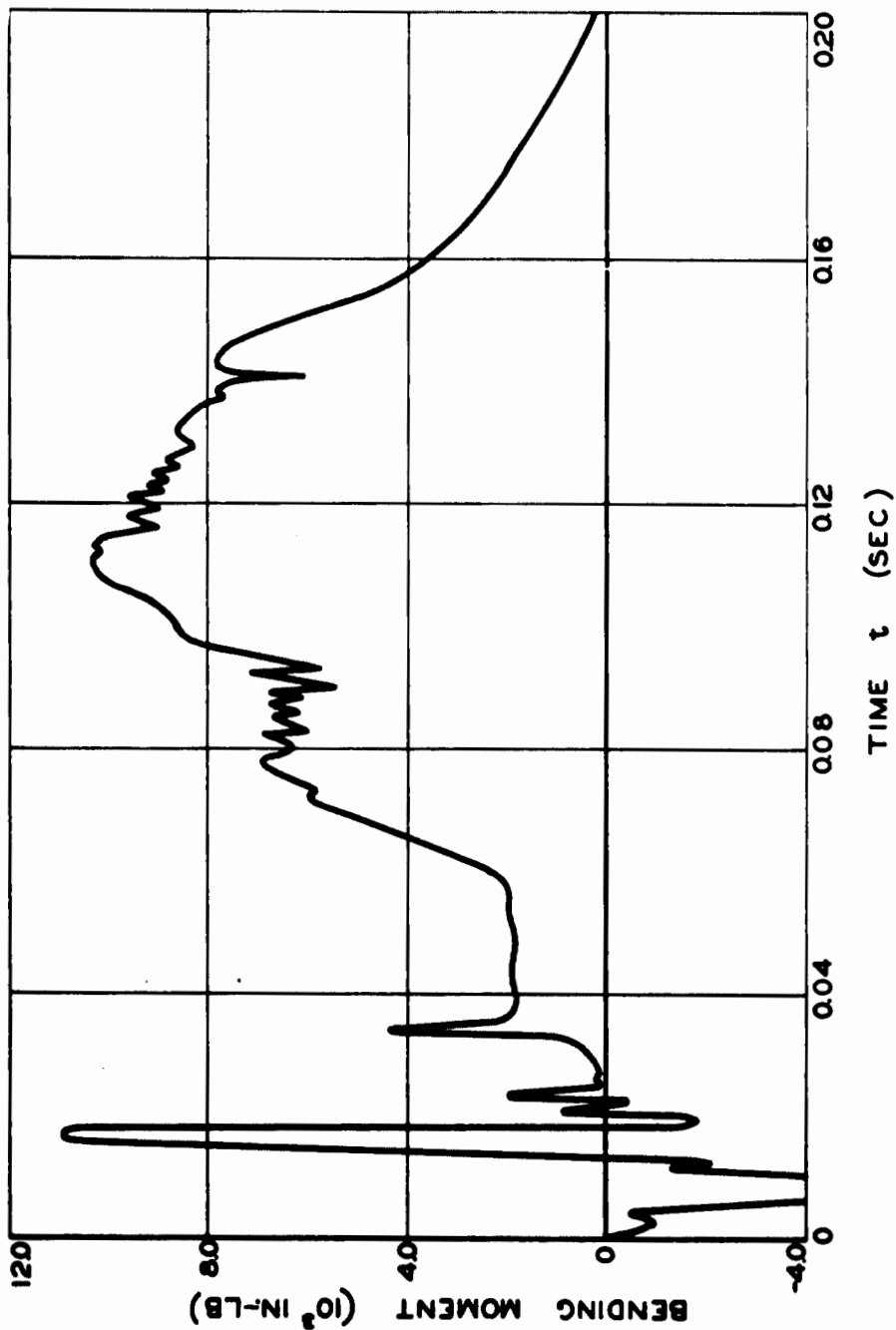


Fig. E.43 Variation of Bending Moment with Time at Station 8, Intermediate, of Swept Wing 105. The angle of incidence was  $8\frac{1}{4}^\circ$  and the range was 1,020 ft, Engel.

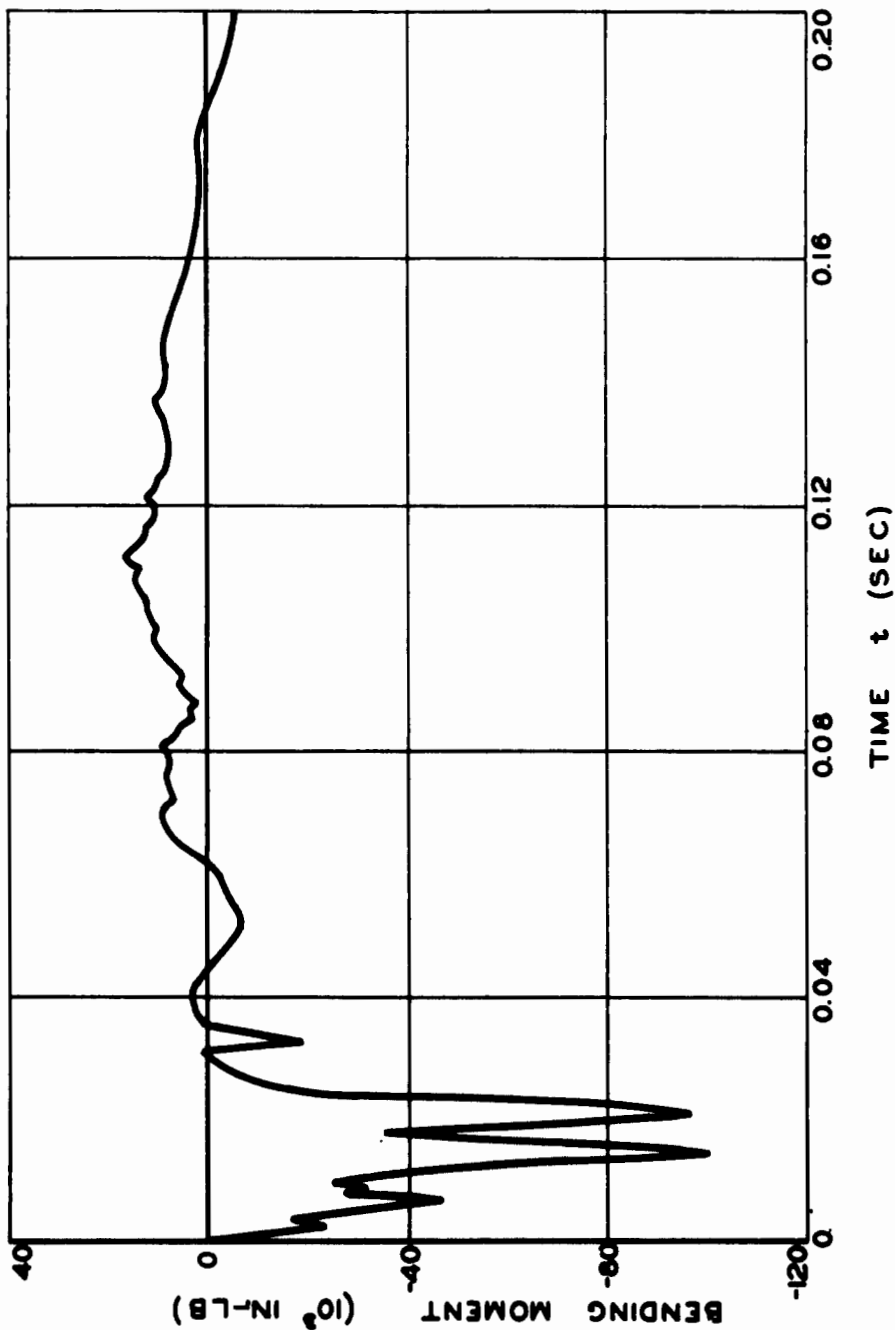


Fig. 3.44 Variation of Bending Moment with Time at Station 9, Outboard, of Sweep Wing 105. The angle of incidence was  $8\frac{1}{4}^\circ$ , and the range was 4,020 ft, Engelbl.

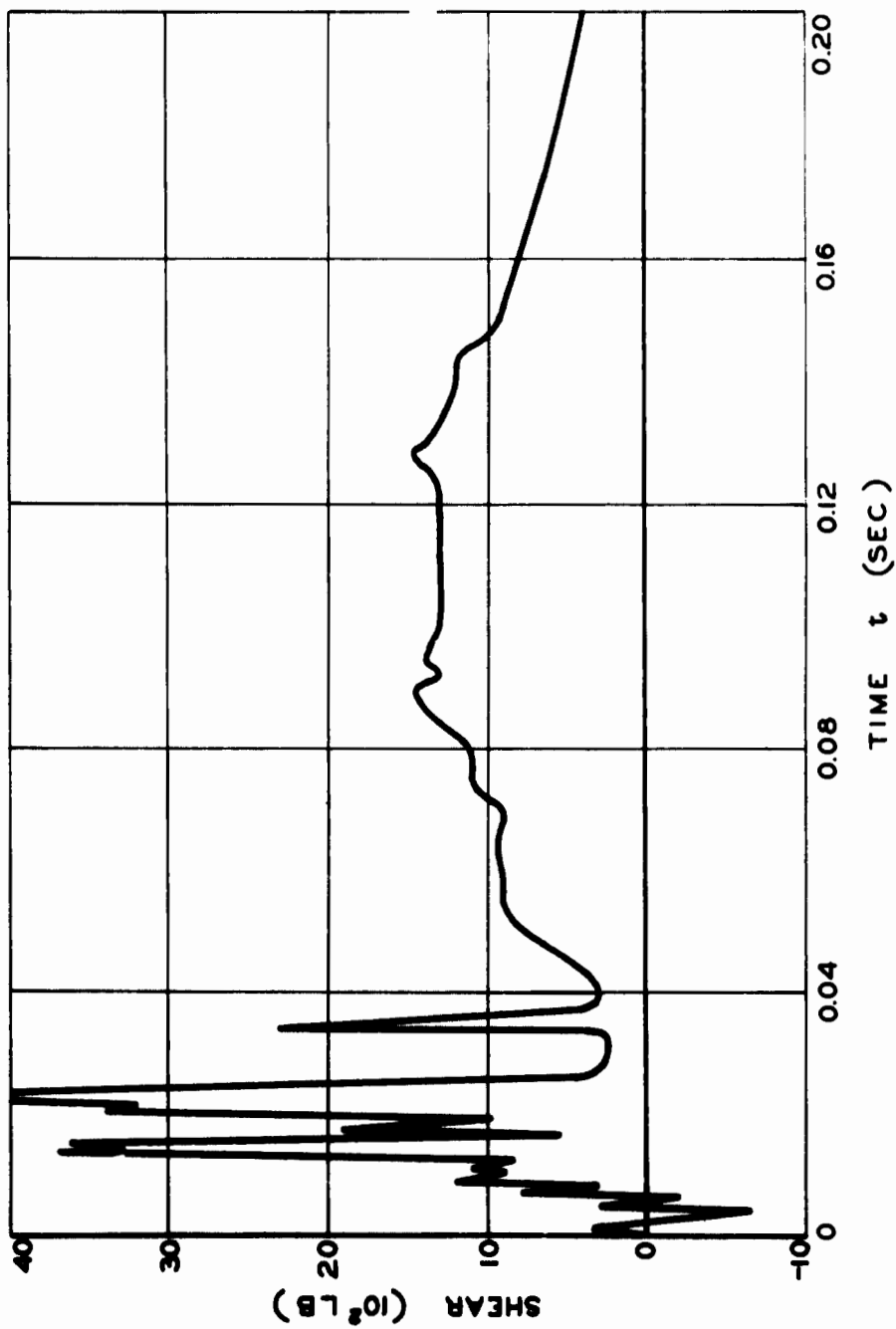


Fig. 5.45 Variation of Shear with Time at Station 8, Intermediate, of Swept Wing 105. The angle of incidence was  $8\frac{3}{4}^\circ$ , and the range was 4,020 ft, Engbl.

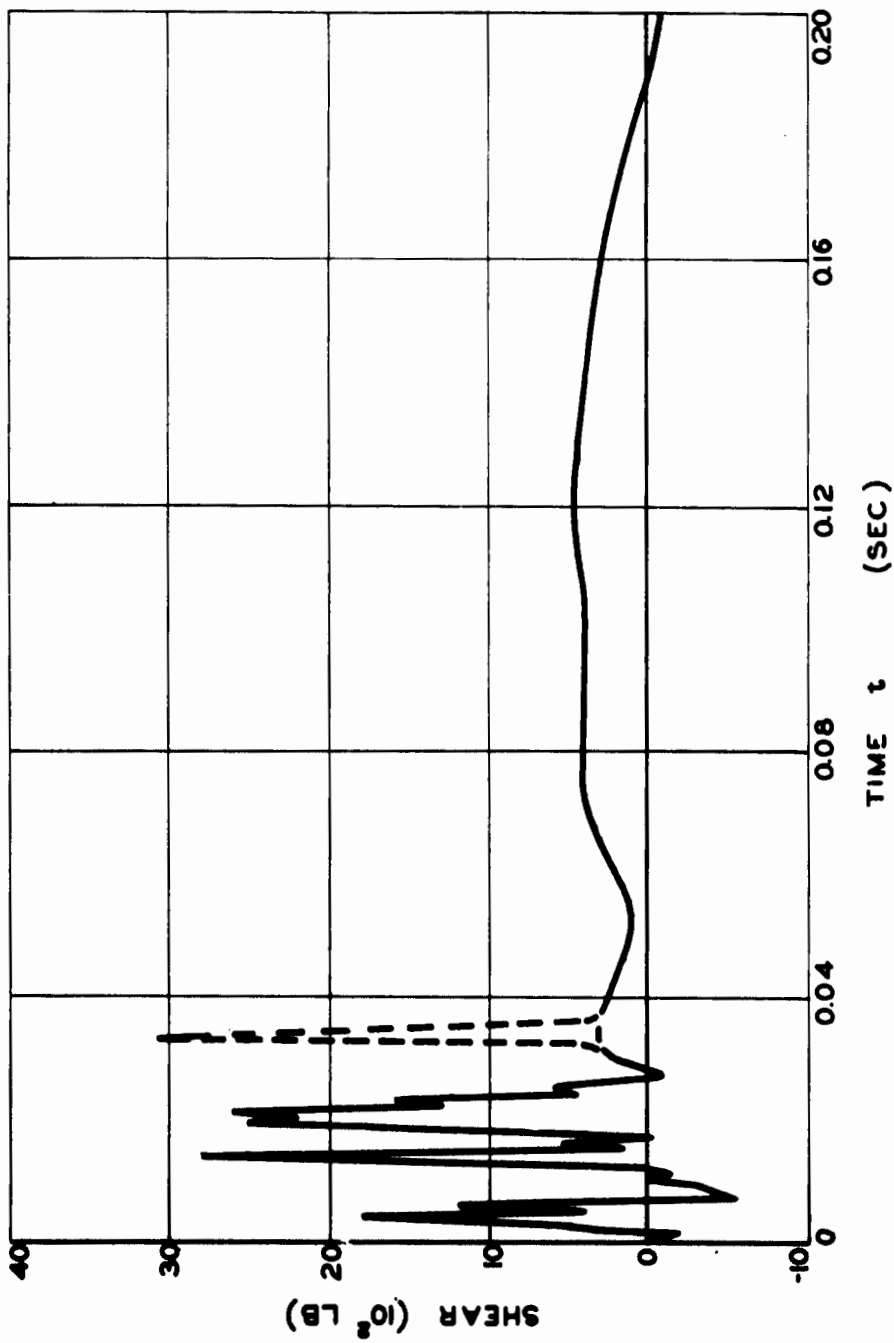


Fig. 5.46 Variation of Shear with Time at Station 9, Outboard, of Sweep Wing 105. The angle of incidence was  $8\frac{3}{4}^\circ$ , and the range was 4,020 ft, Engbl.



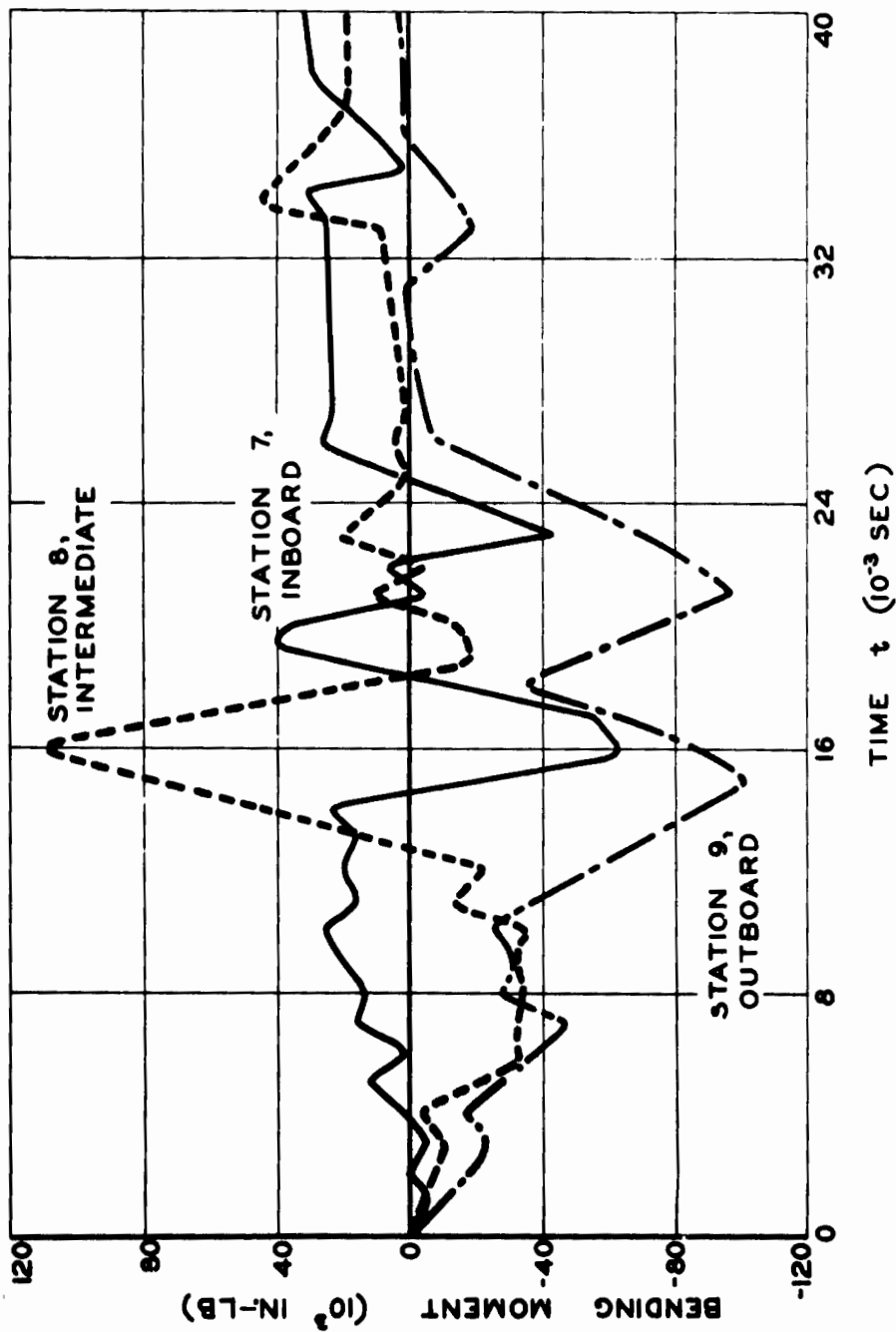


Fig. 5.47 Comparison during Initial Impulse of the Variation of Bending Moment with Time at Three Stations of Swept Wing 105. The angle of incidence was  $8\frac{1}{4}^\circ$ , and the range was 4,020 ft, Engebli.

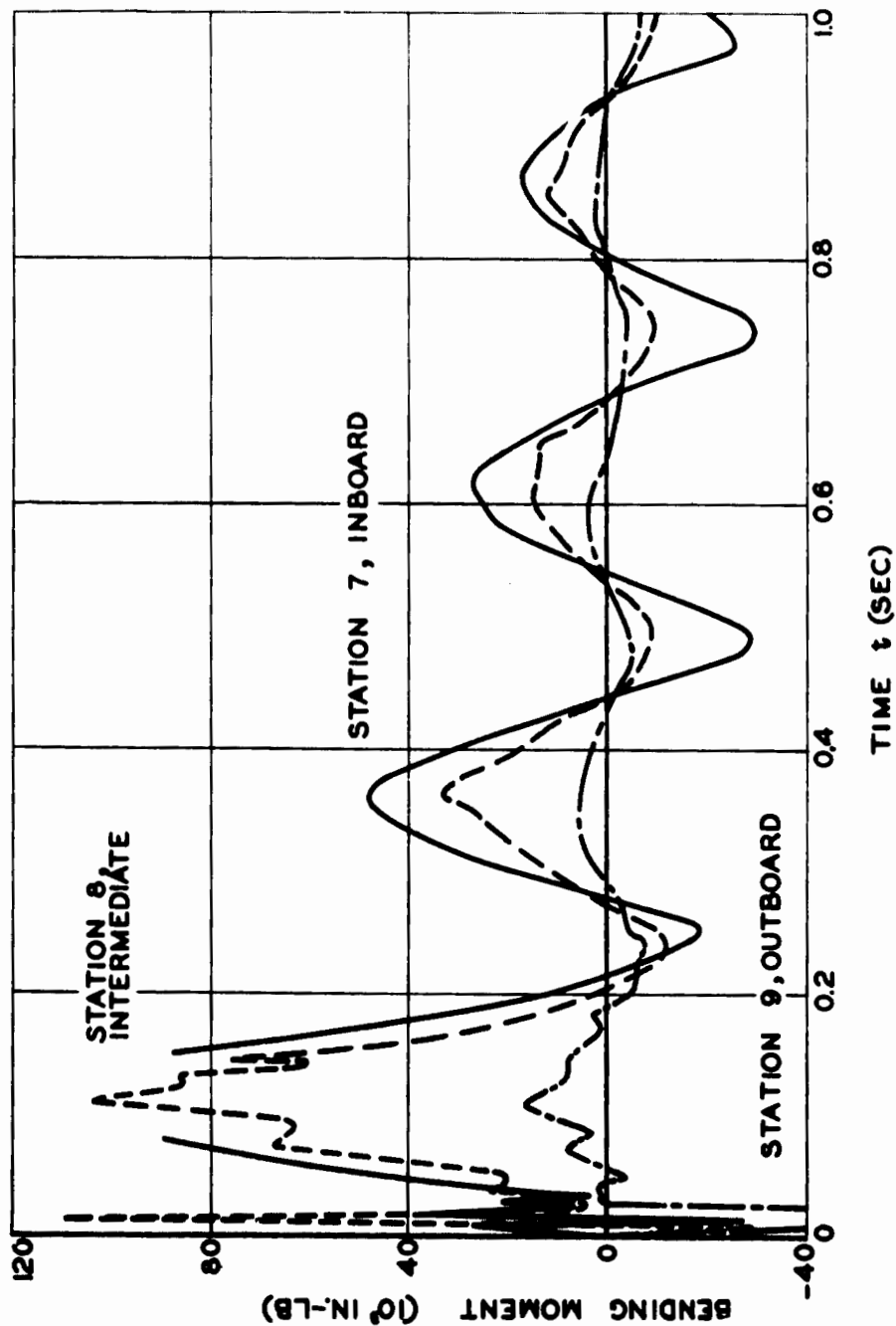


Fig. 5.48 Comparison of the Variation of Bending Moment with Time at Three Stations of Swept Wing 105. The angle of incidence was  $8^\circ 4'$ , and the range was 4,020 ft, Engbl.

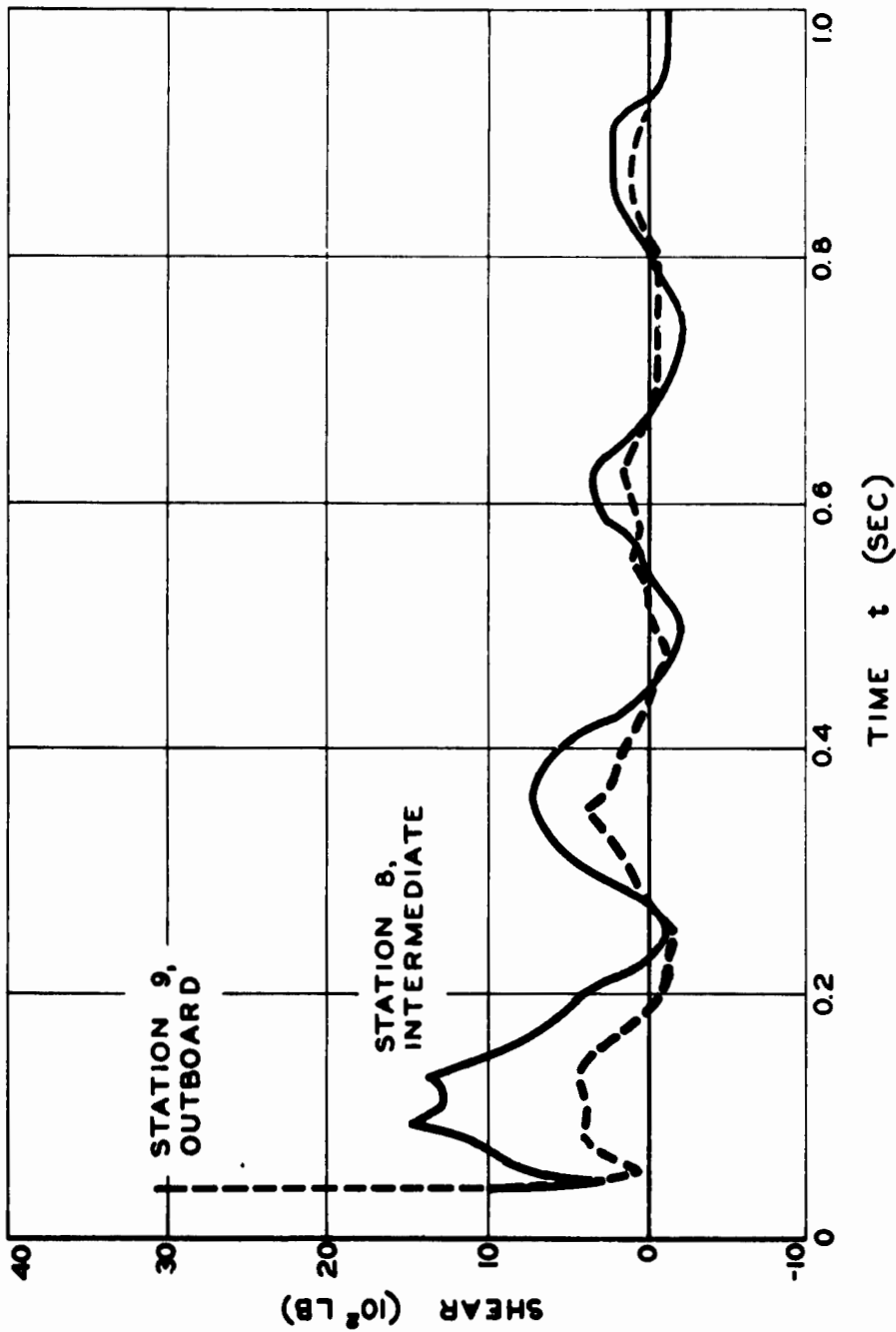


Fig. 5.49 Comparison of the Variation of Shear with Time at Two Stations of Sweep: Wing 105. The angle of incidence was  $8\frac{1}{4}^\circ$ , and the range was 4,020 ft, Engabl.

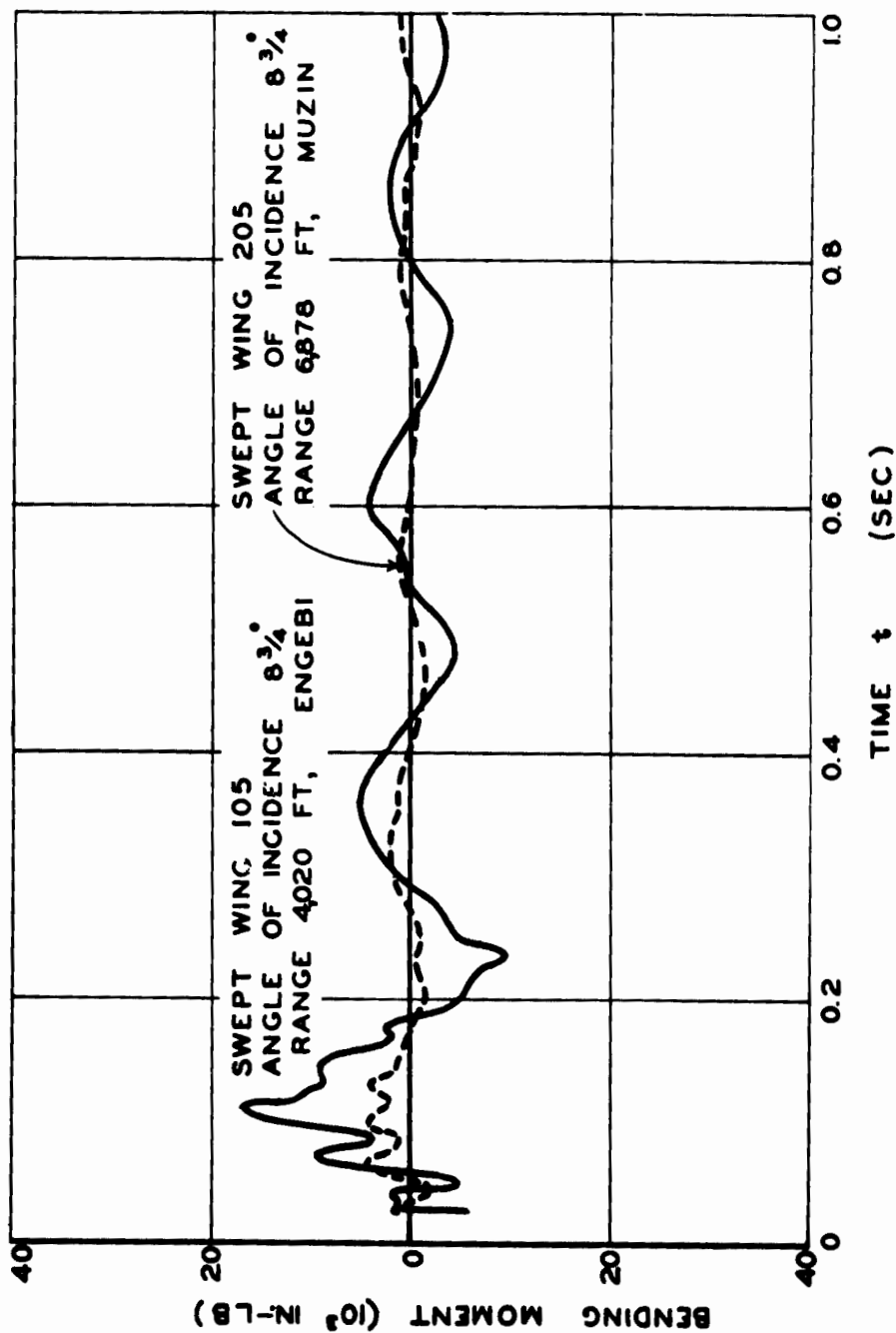


Fig. 8.50 Comparison of the Variation of Bending Moment with Time at Station 9, Outboard, for Two Swept Wings at Different Ranges

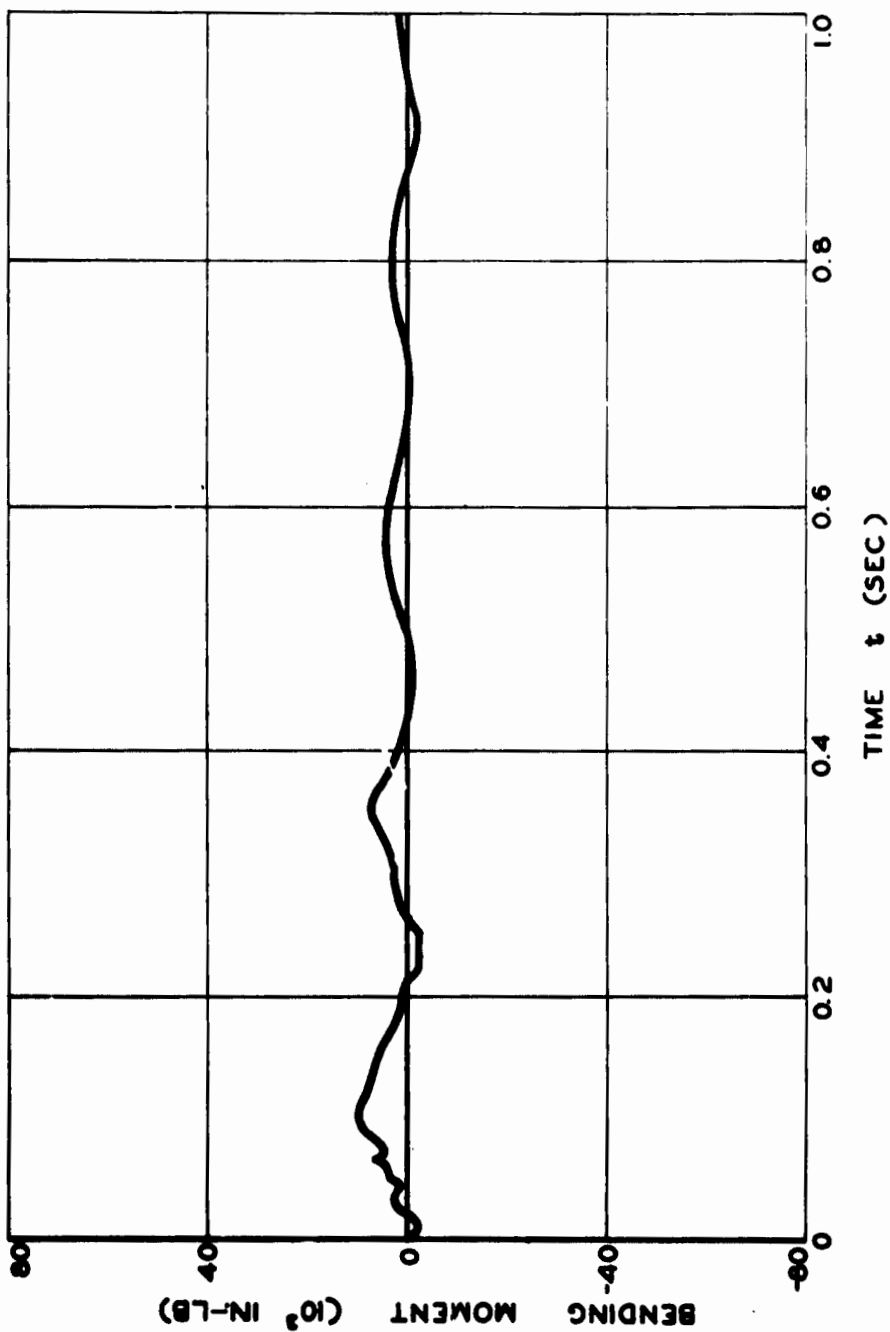


Fig. 8.61 Variation of Bending Moment with Time at Station 8, Intermediate, of Swept Wing 205. The angle of incidence was  $8\frac{1}{4}^\circ$  and the range was 6,878 ft, Muzila.

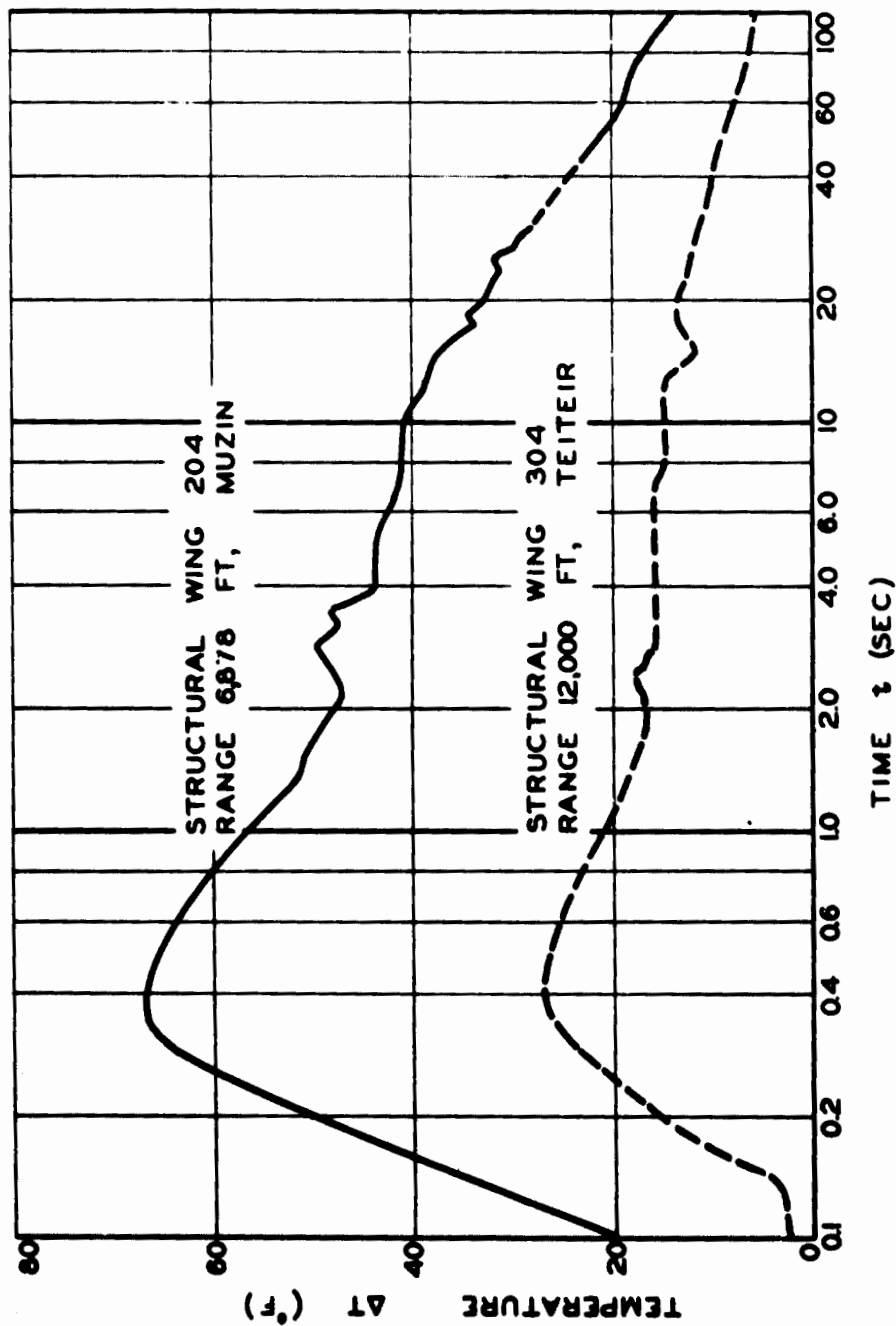


Fig. 8.82 Variation of Temperature Change with Time of an Outside-skin-surface Point on Each of Two Structural Wings at Different Ranges. The angles of incidence were  $25^{\circ}$ , and the ambient temperature was  $80^{\circ}$ F.

UNCLASSIFIED

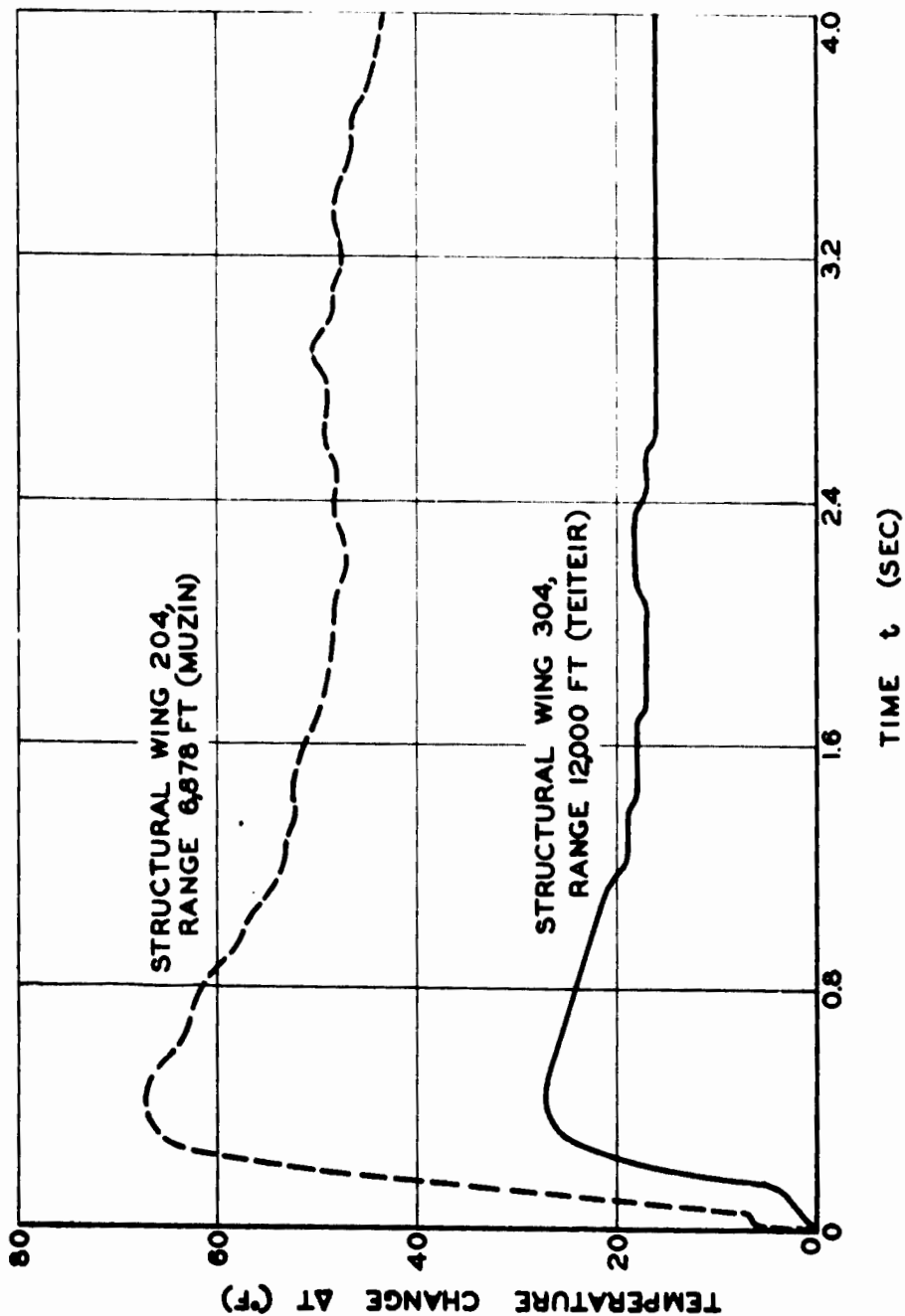


Fig. 5.53 Variation of Temperature Change with Time at a 25° Incidence Point on the Outside Skin Surface of Two Wings at Different Ranges

UNCLASSIFIED

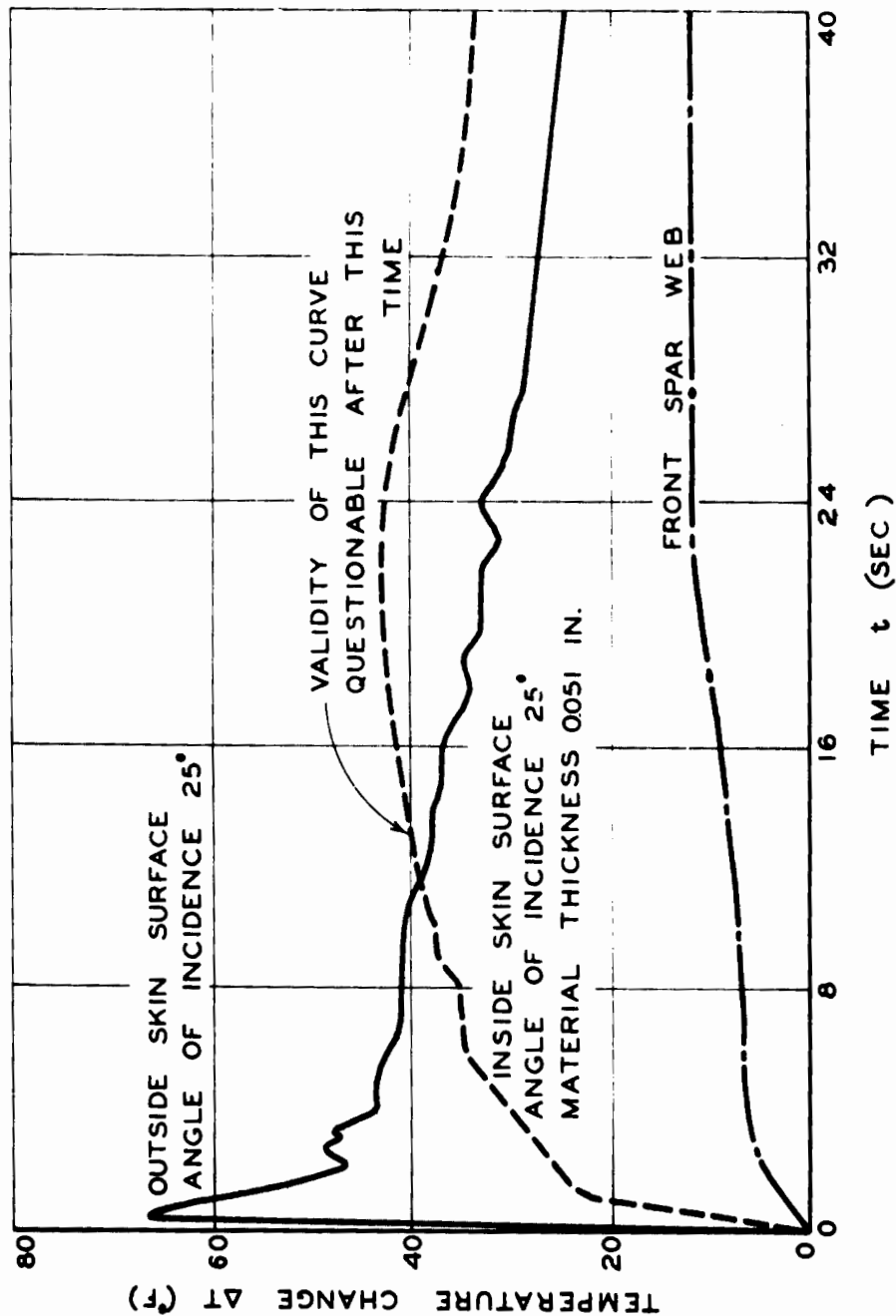


Fig. 5.54 Comparison of the Variation of Temperature Change with Time for Three Points of Structural Wing 204. The ambient temperature was 80°F, and the range was 6,878 ft, Muzin.



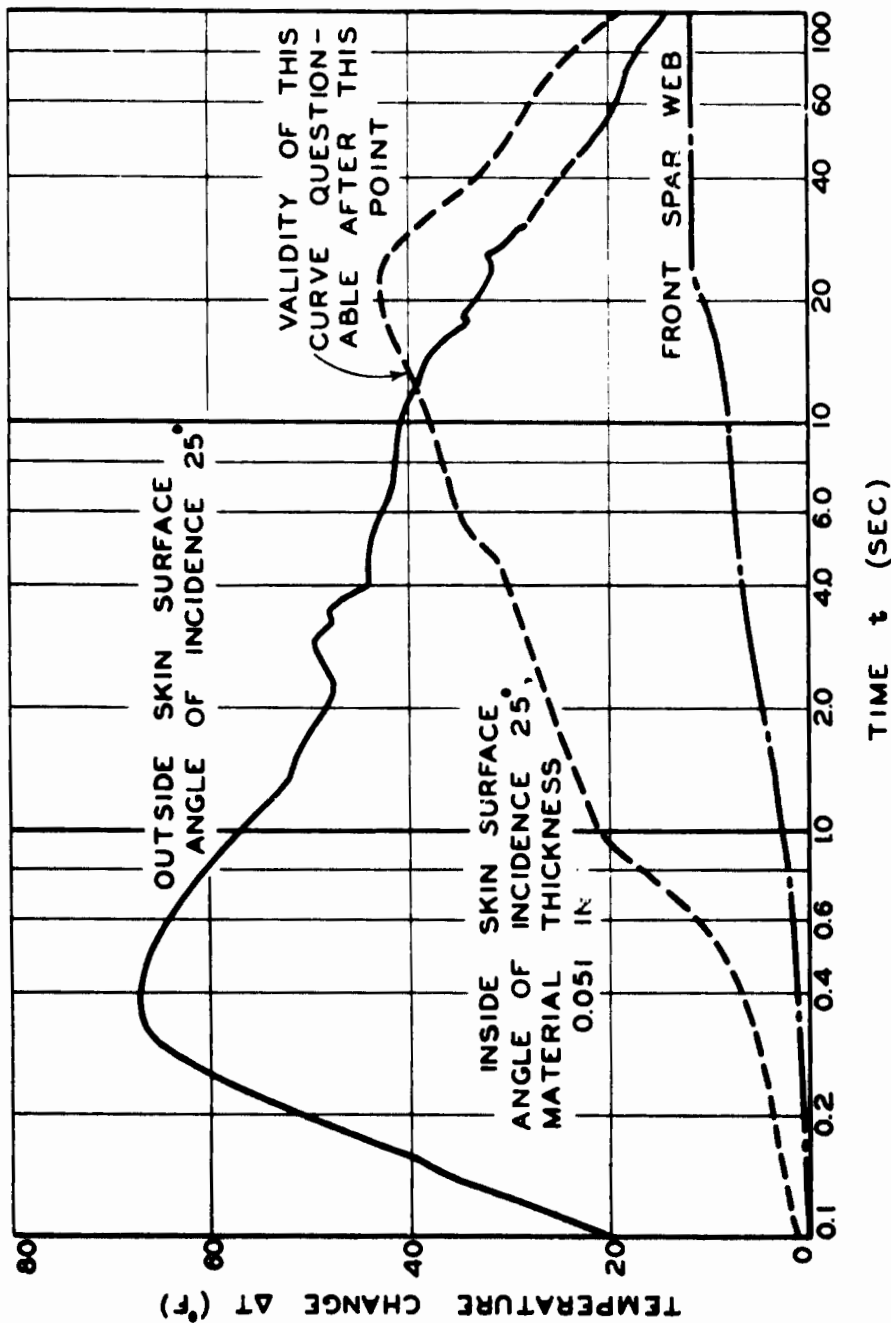


Fig. 5.55 Variation of Temperature Change with Time at Three Points of Structural Wing 204. The ambient temperature was 80°F, and the range was 6,878 ft, Muzlin.

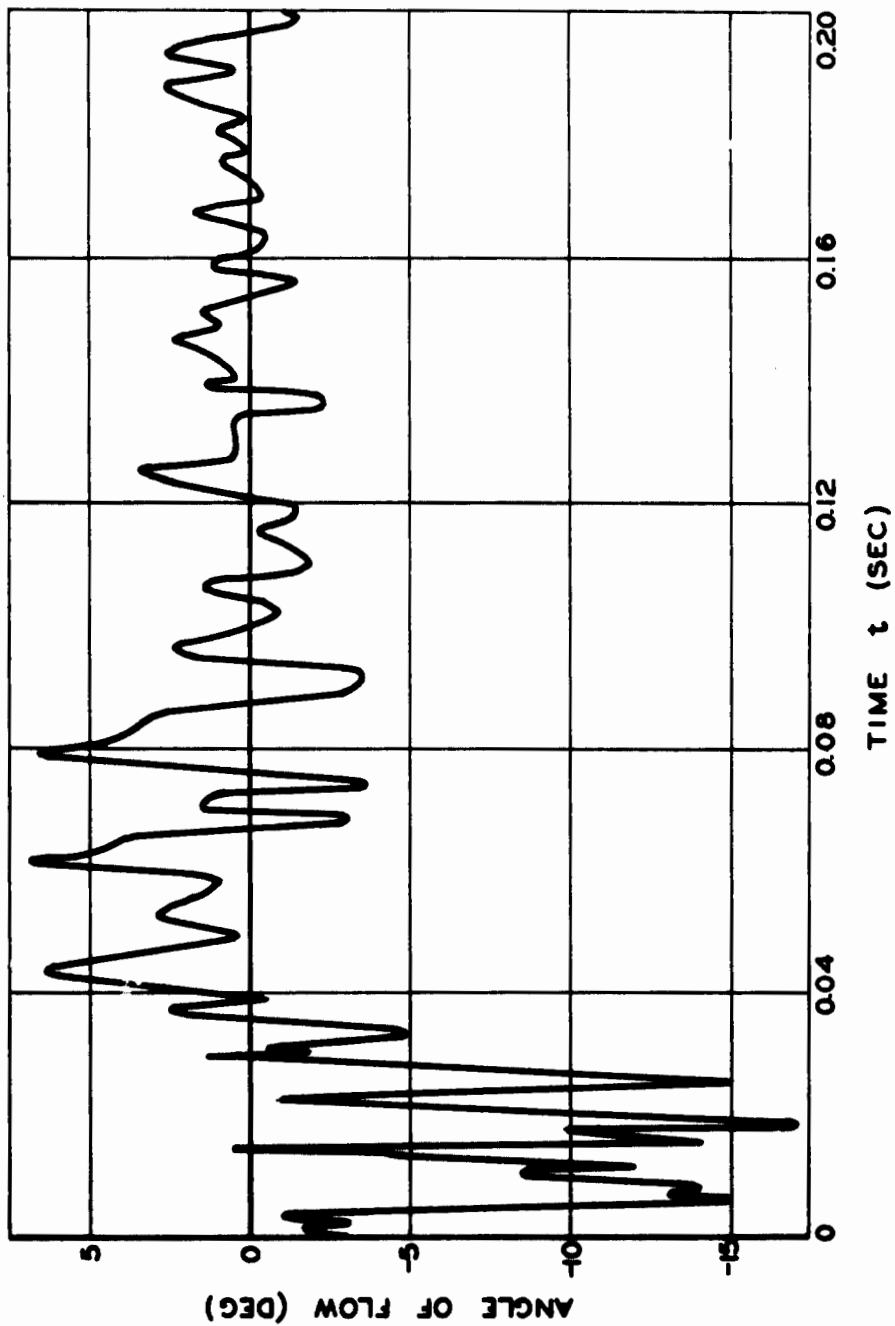


Fig. 5.56 Variation of Angle of Flow of the Advancing Air Mass with Time at 4,020-ft Range. Engbl

UNCLASSIFIED

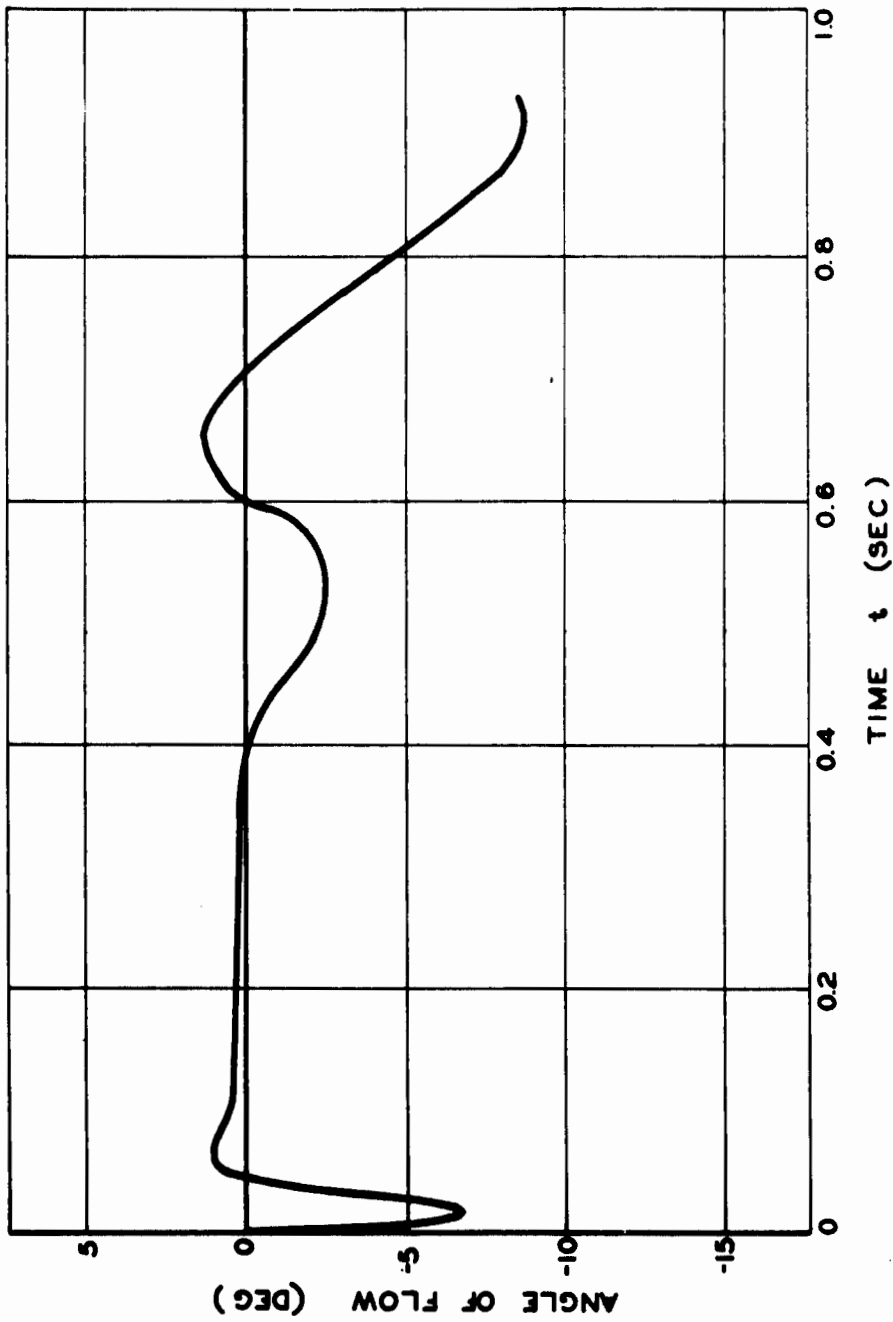


Fig. 5.57 Average Variation of the Angle of Flow of the Advancing Air Mass with Time at 4,020-ft Range, Engchi

UNCLASSIFIED



Fig. 5.58 Enlargement of Two Frames from 35-mm Roll B-35-100-714 from Fastax Camera Film Taken Just prior to Passage of Blast Front, Muzin, Range 6,878 Ft. These frames were taken for orientation purposes.



Fig. 5.59 Enlargement Same Film Roll as Fig. 5.60 Showing Probable Passage of Blast Front at Time That Shock Front Should Be Visible

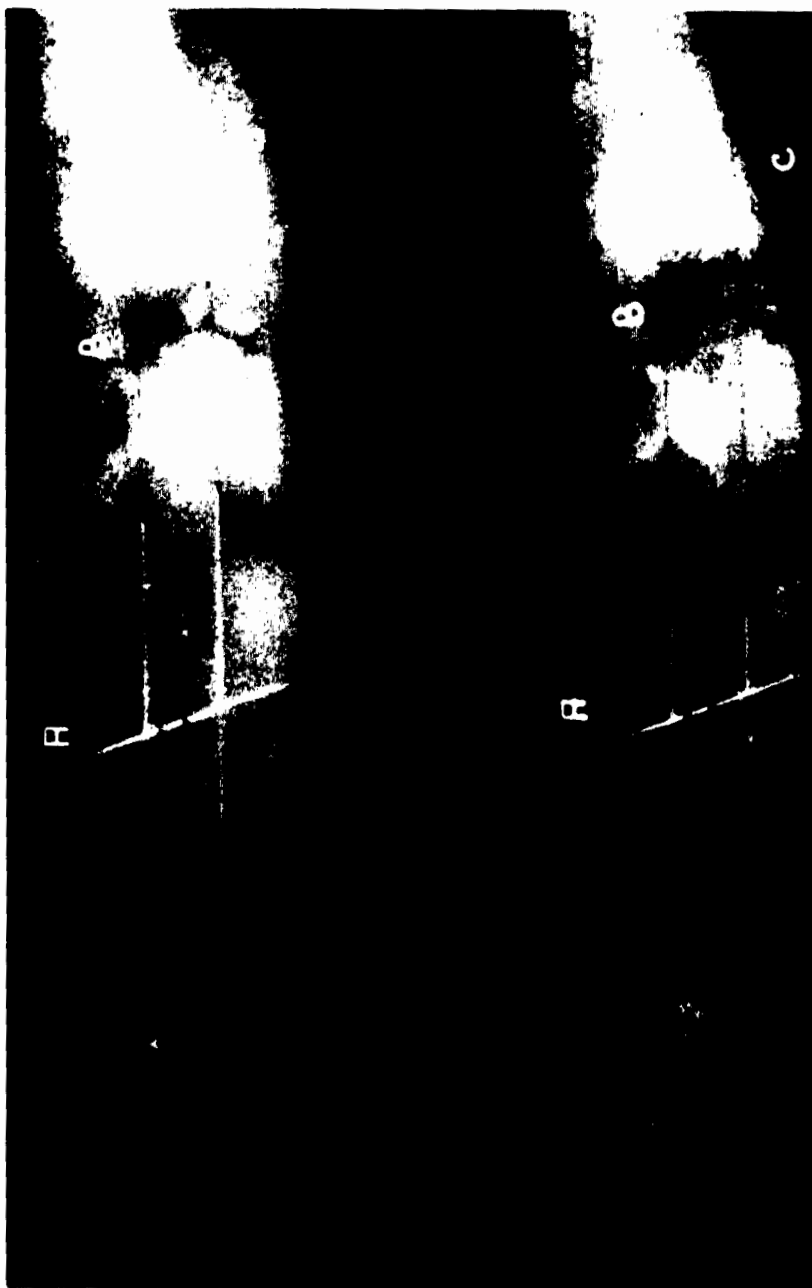


Fig. 5.60 Enlargement from 35-mm Fastax Camera on Muzin, Range 6,878 Ft, Illustrating Clouds and Their Movement

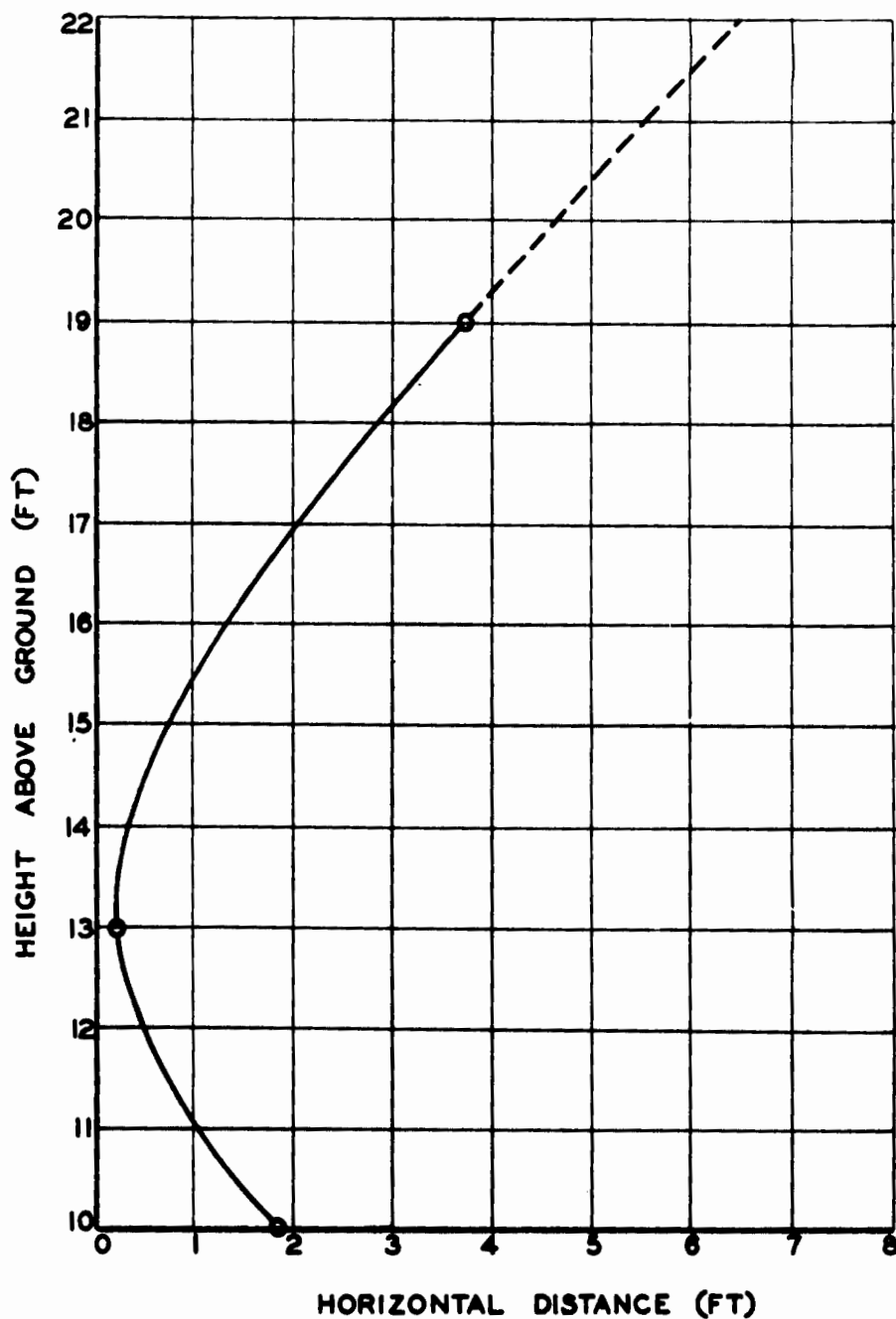


Fig. 5.61 Vertical Profile of Blast Front As Determined by Electronic Chronographs and Blast Switches

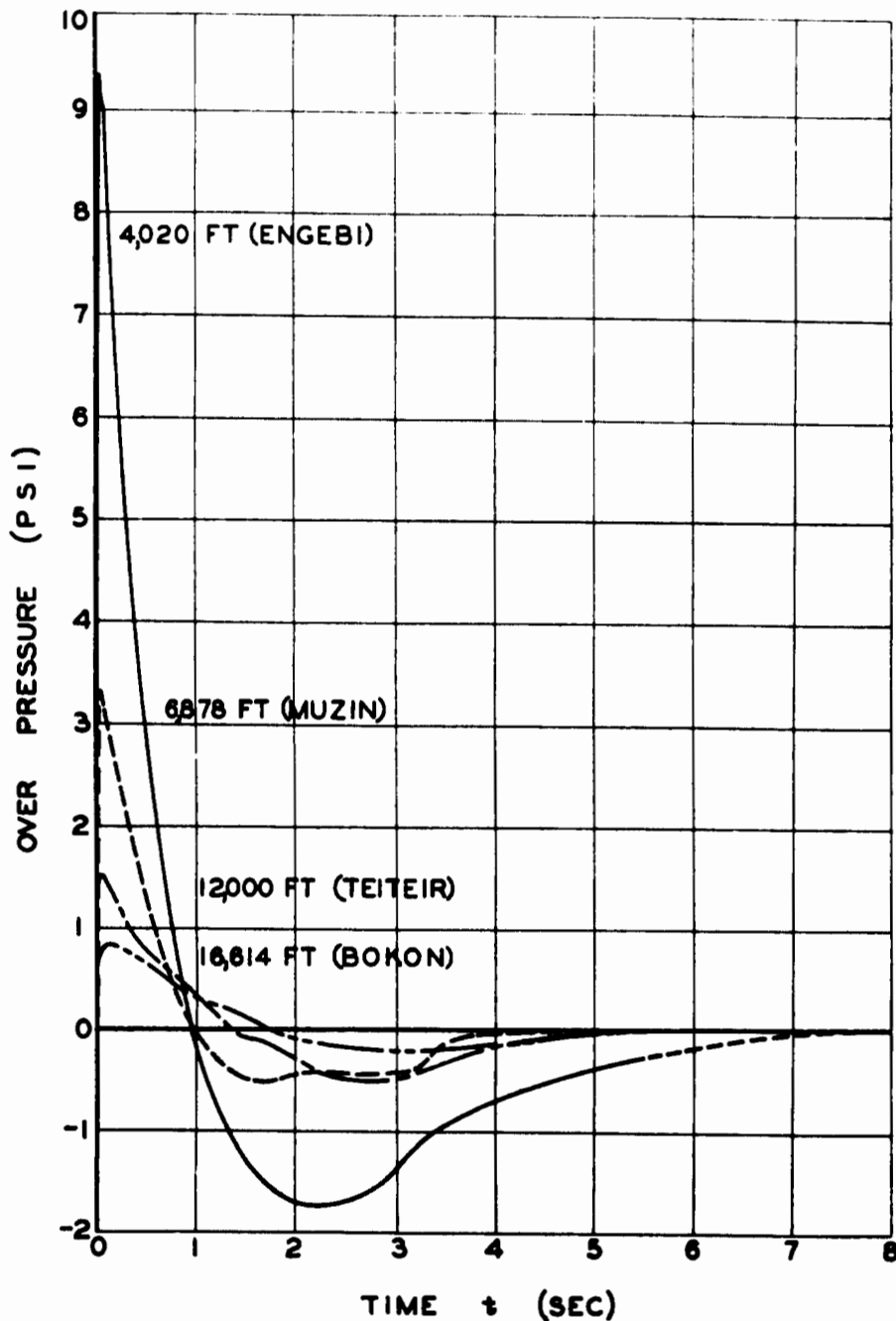


Fig. 5.62 Variation of Blast Pressure with Time at Each of the Four Test Sites As Determined from Interferometer Gauges



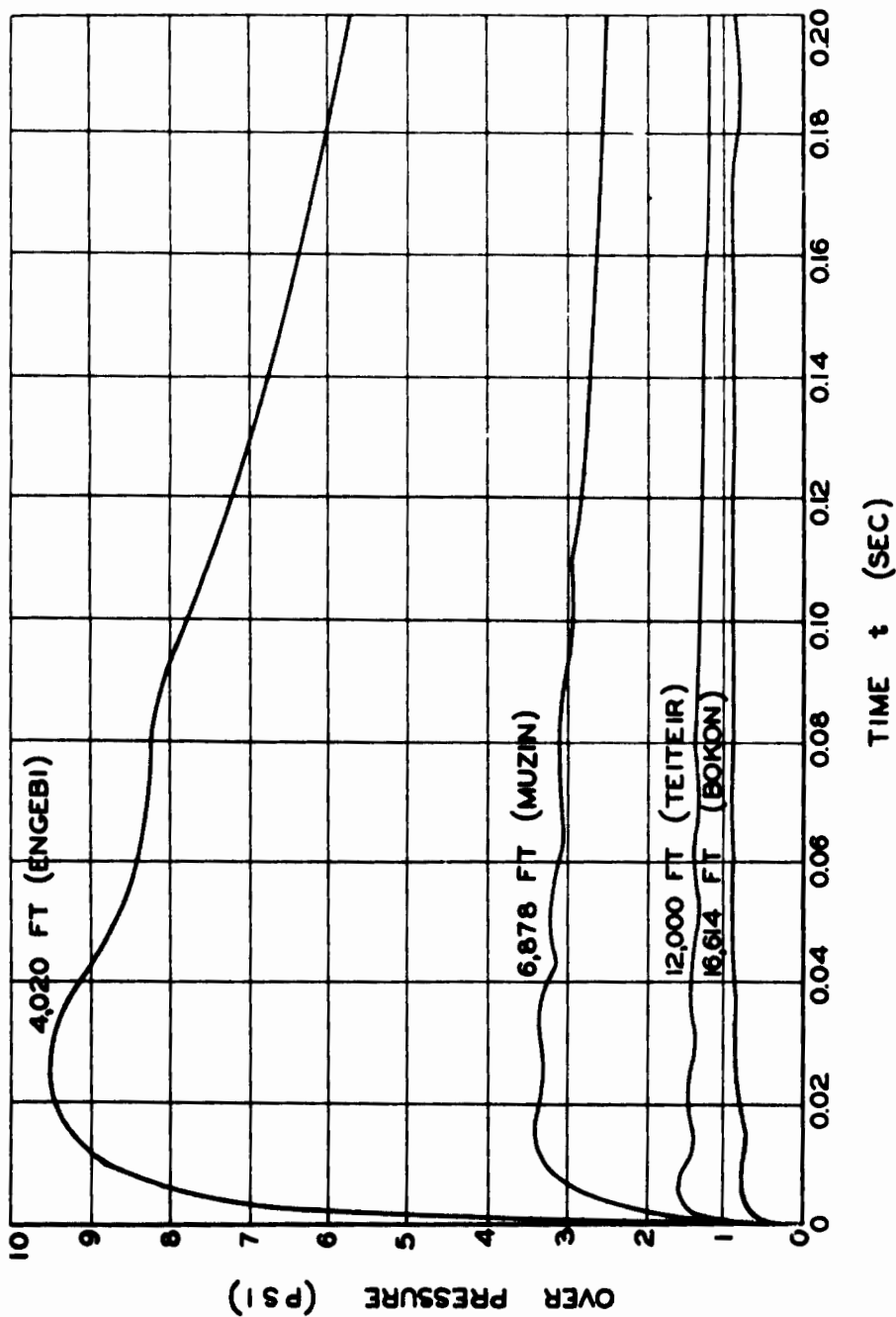


Fig. 5.63 Variation of Blast Pressure with Time for the First 200 Msec at Each of the Four Test Sites As Determined from Interferometer Gauges

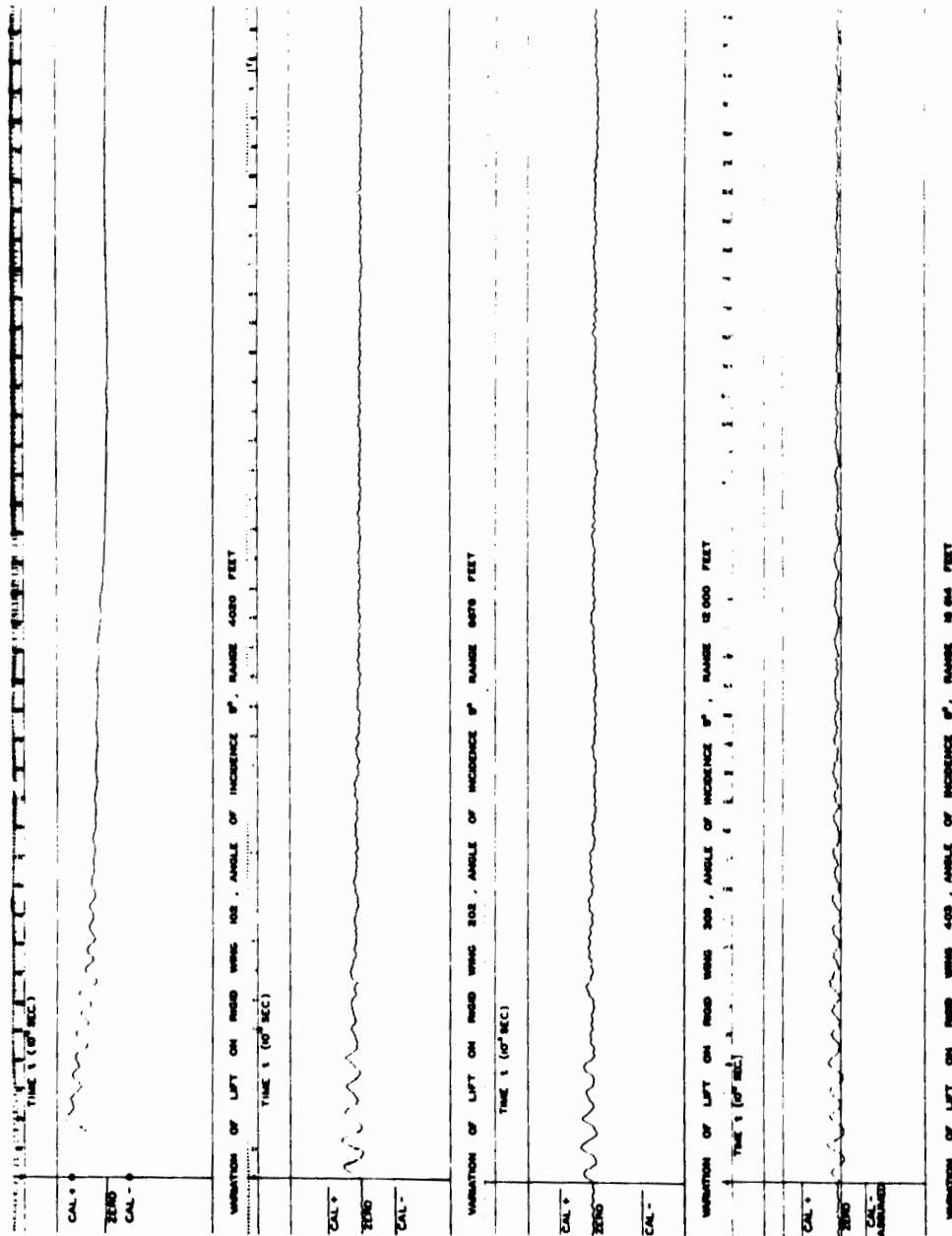


Fig. 6.1 Oscillograph Reproduction of the Magnetic-tape Record of the Lift for Four Wings

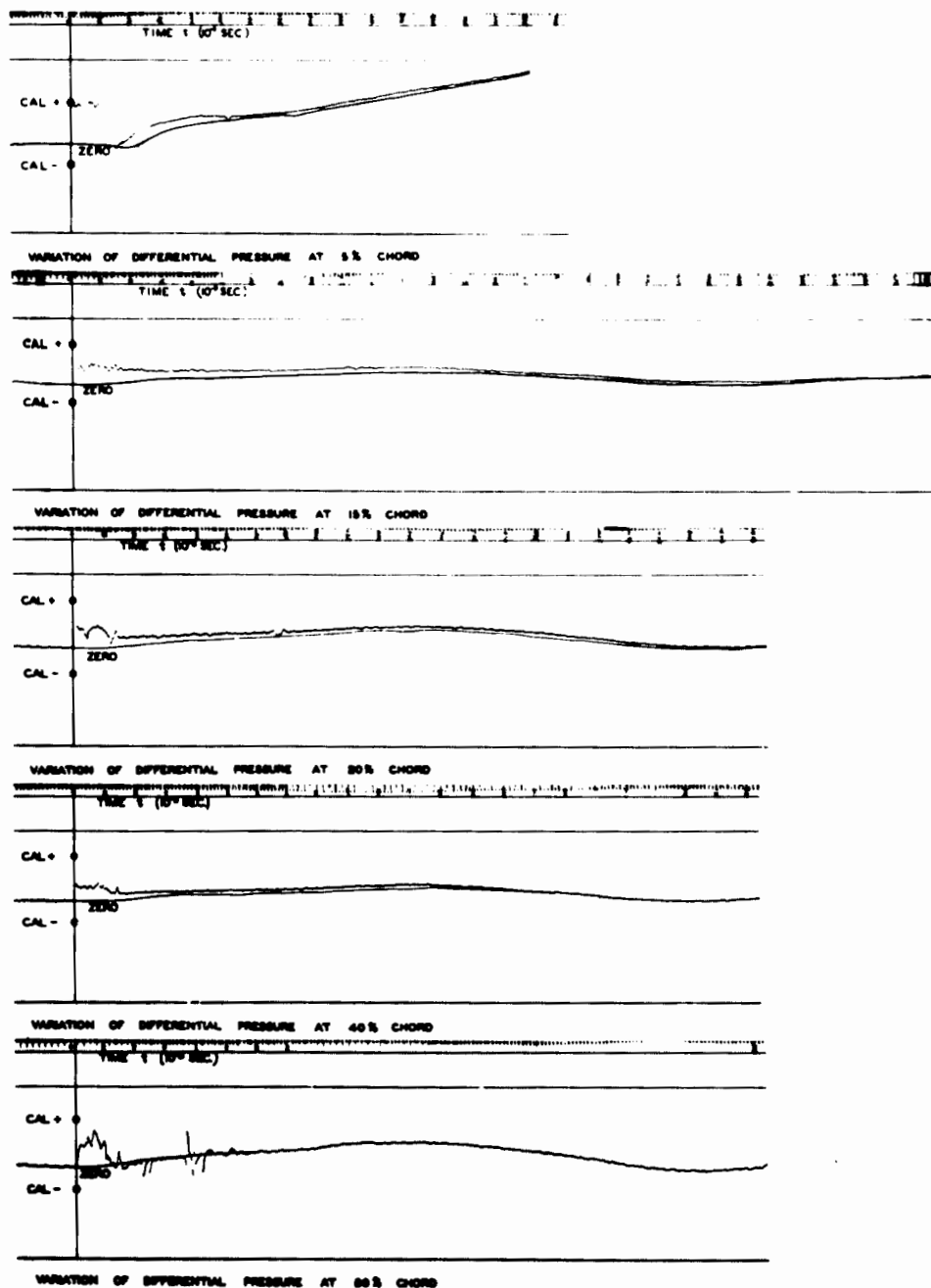


Fig. 6.2 Oscillograph Reproductions of the Magnetic-tape Record of the Variation of Differential Pressure with Time at Several Chordwise Stations of Rigid Wing 102, Angle of Incidence  $9^\circ$ , Range 4,020 Ft

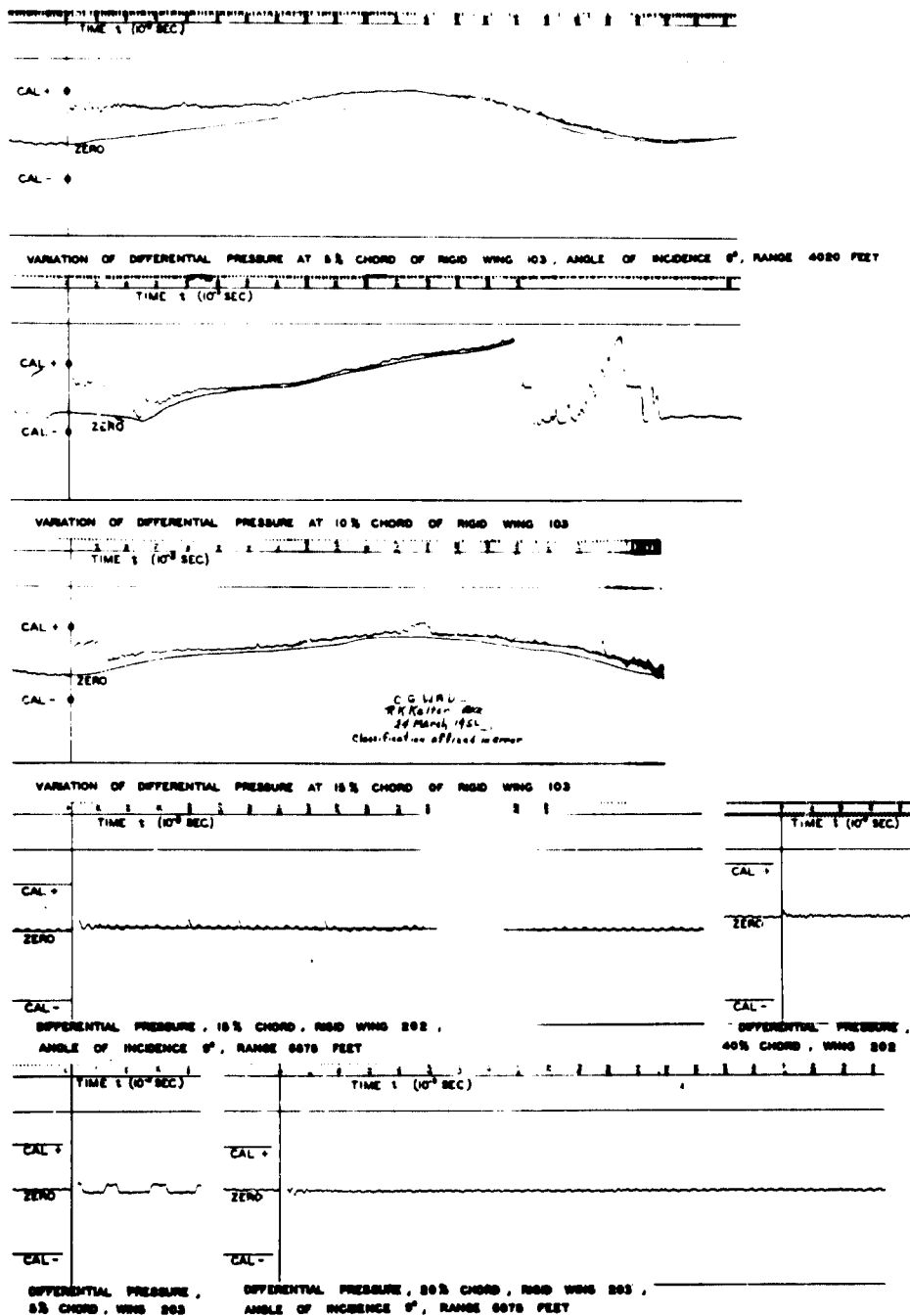


Fig. 6.3 Oscillograph Reproductions of the Magnetic-tape Record of the Variation of Differential Pressure with Time at Several Chordwise Stations of Rigid Wings 103, 202, and 203

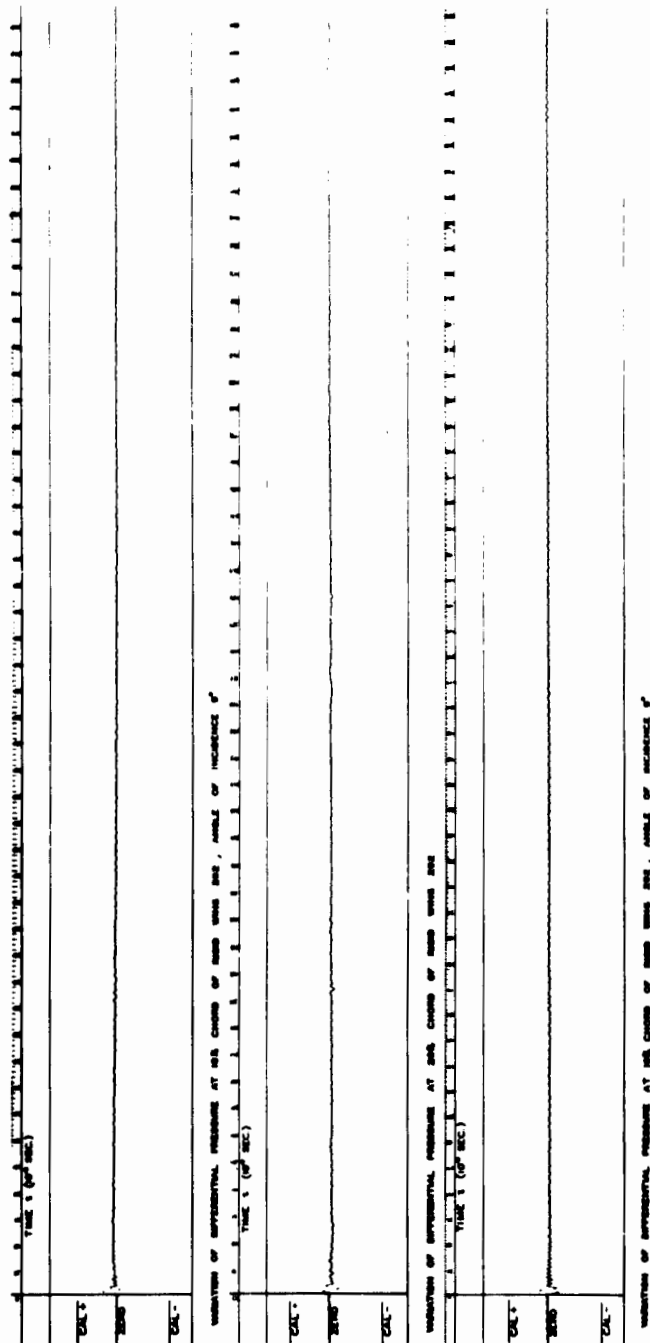


Fig. 6.4 Oscillograph Reproductions of the Magnetic-tape Record of the Variation of Differential Pressure with Time at Chordwise Stations of Rigid Wings 202 and 203, Range 6,878 Ft

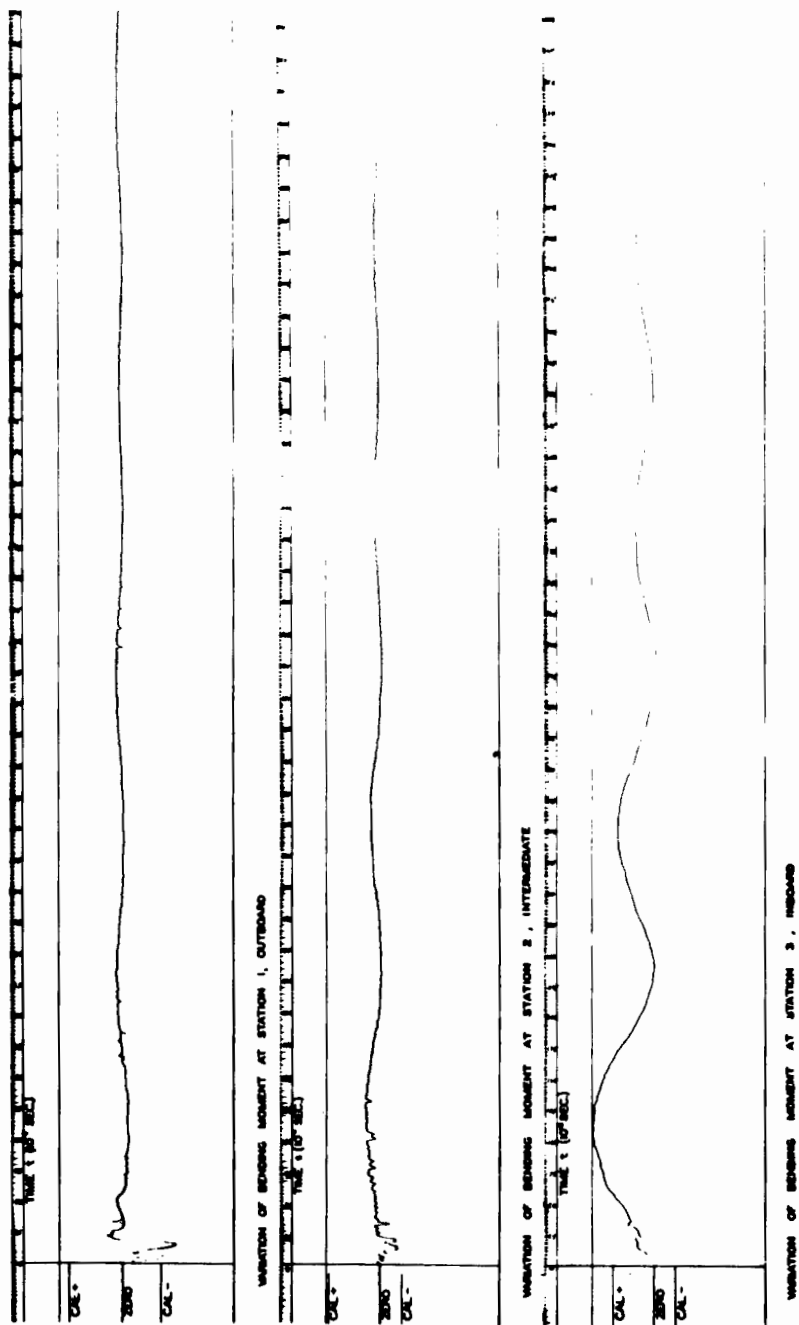


Fig. 6.5 Oscillograph Reproductions of the Magnetic-tape Record of the Variation of Bending Moment with Time at Three Stations of Structural Wing 101, Angle of Incidence 6°, Range 4,020 Ft

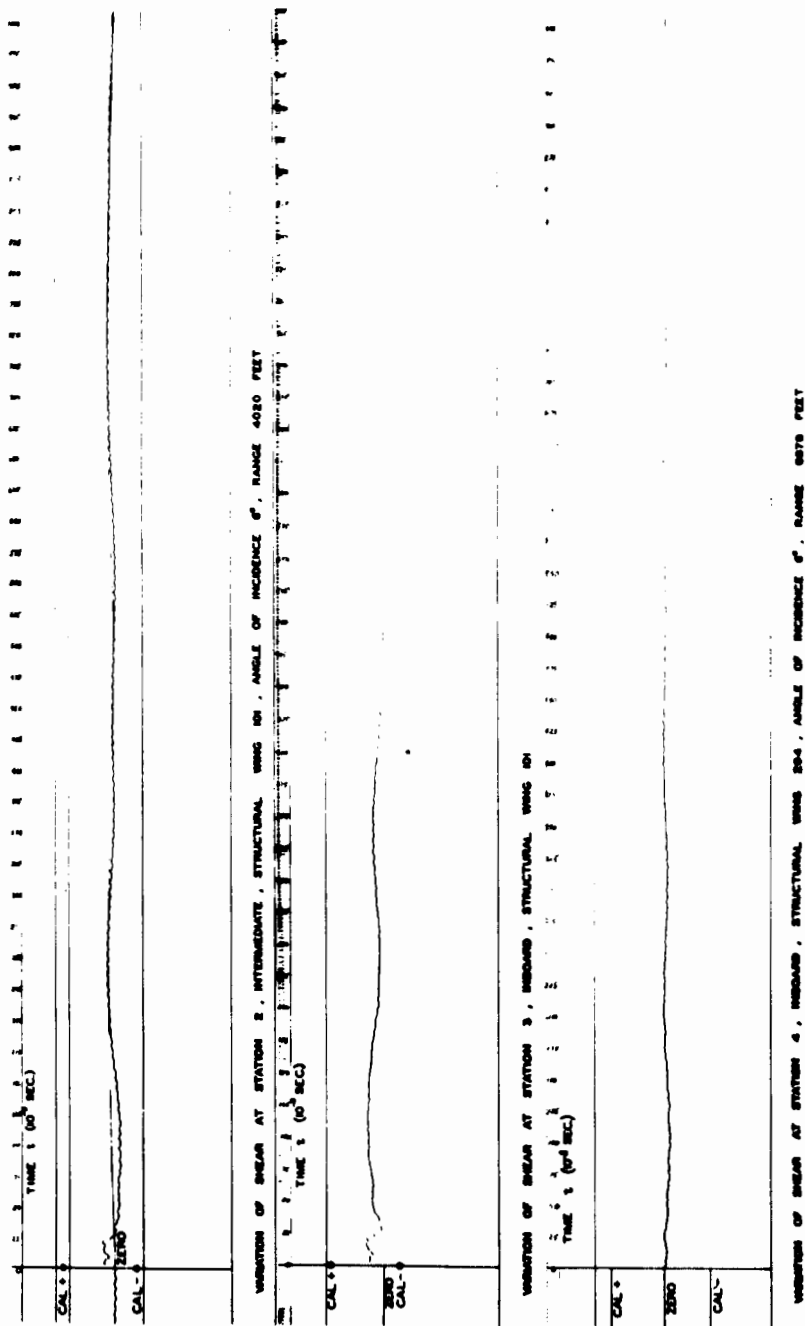


Fig. 6.6 Oscillograph Reproductions of the Magnetic-tape Record of the Variation of Shear with Time at Spanwise Stations of Structural Wings 101 and 204

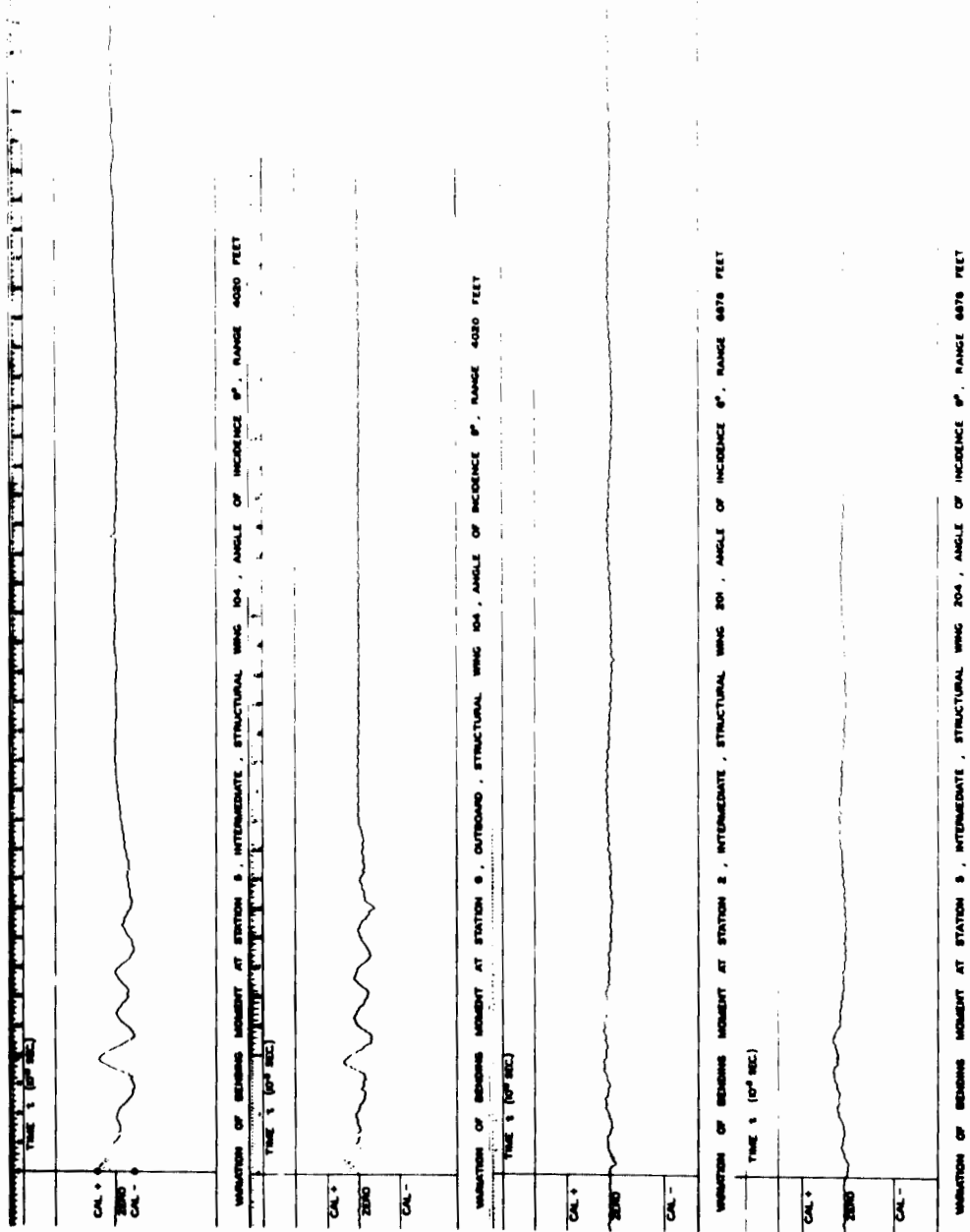


Fig. 6.7 Oscillograph Reproductions of the Magnetic-tape Record of the Variation of Bending Moment with Time at Spanwise Stations of Structural Wings 104, 201, and 204



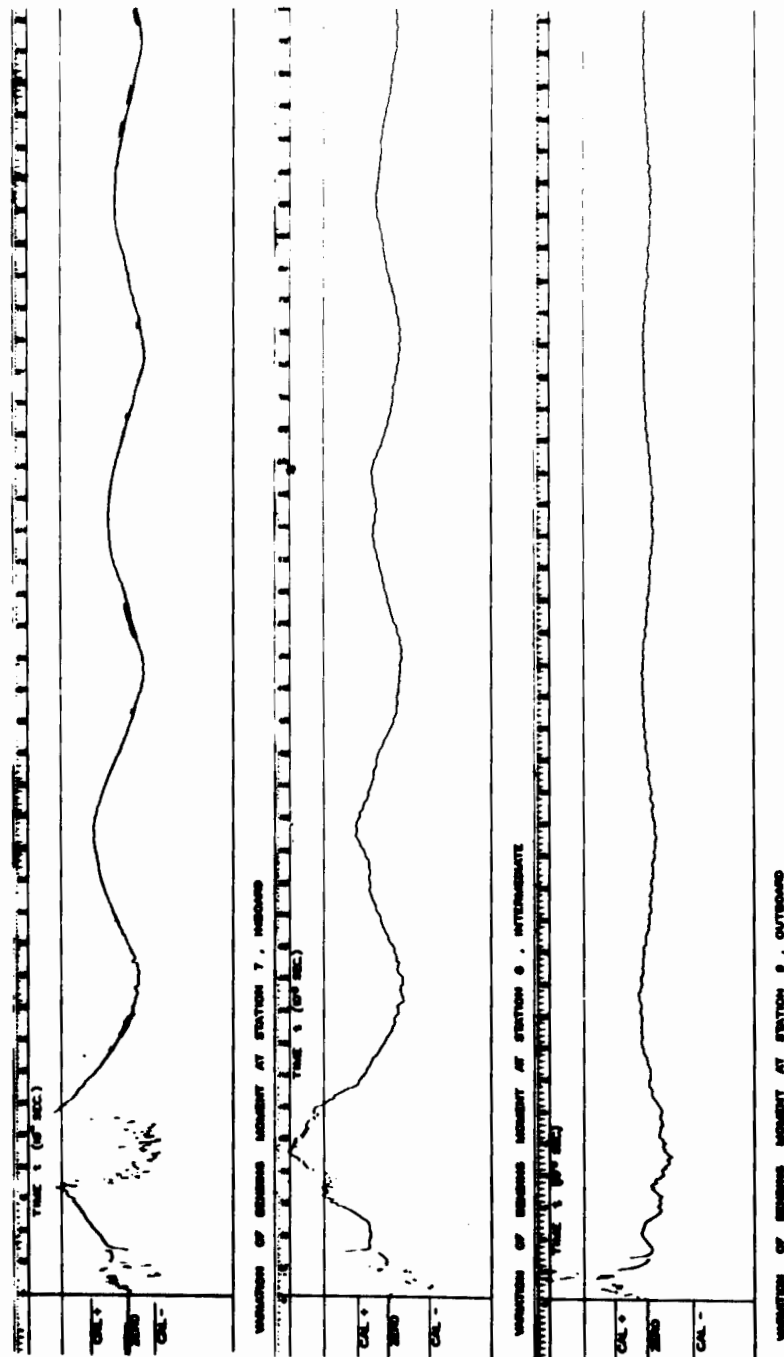


Fig. 6.8 Oscillograph Reproductions of the Magnetic-tape Record of the Variation of Bending Moment with Time at Three Stations of Swept Wing 105, Range 4,020 Ft

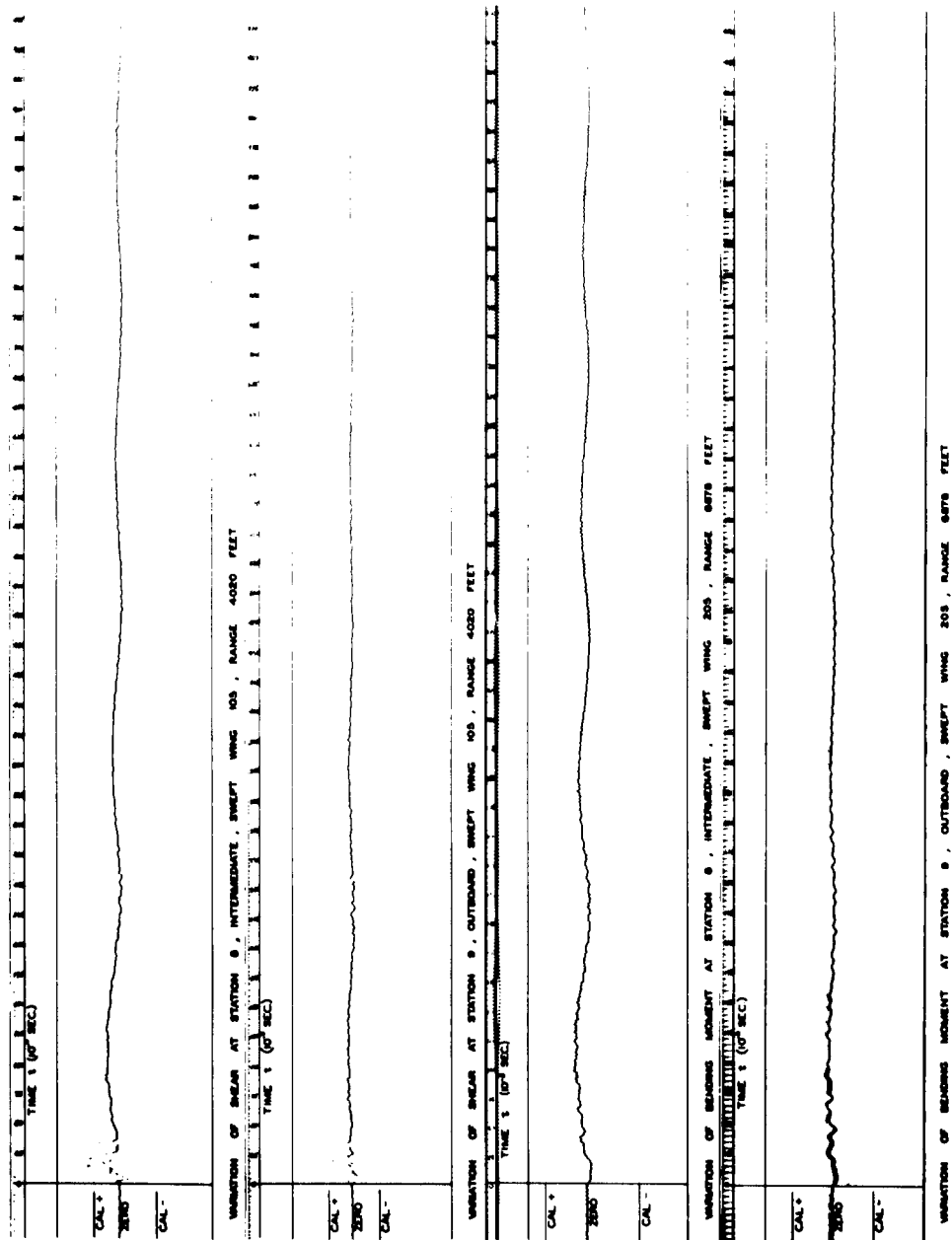


Fig. 6.9 Oscillograph Reproductions of the Magnetic-tape Record of the Variation of Shear with Time at Two Stations of Swept Wing 105; and of Bending Moment with Time at Two Stations of Swept Wing 205

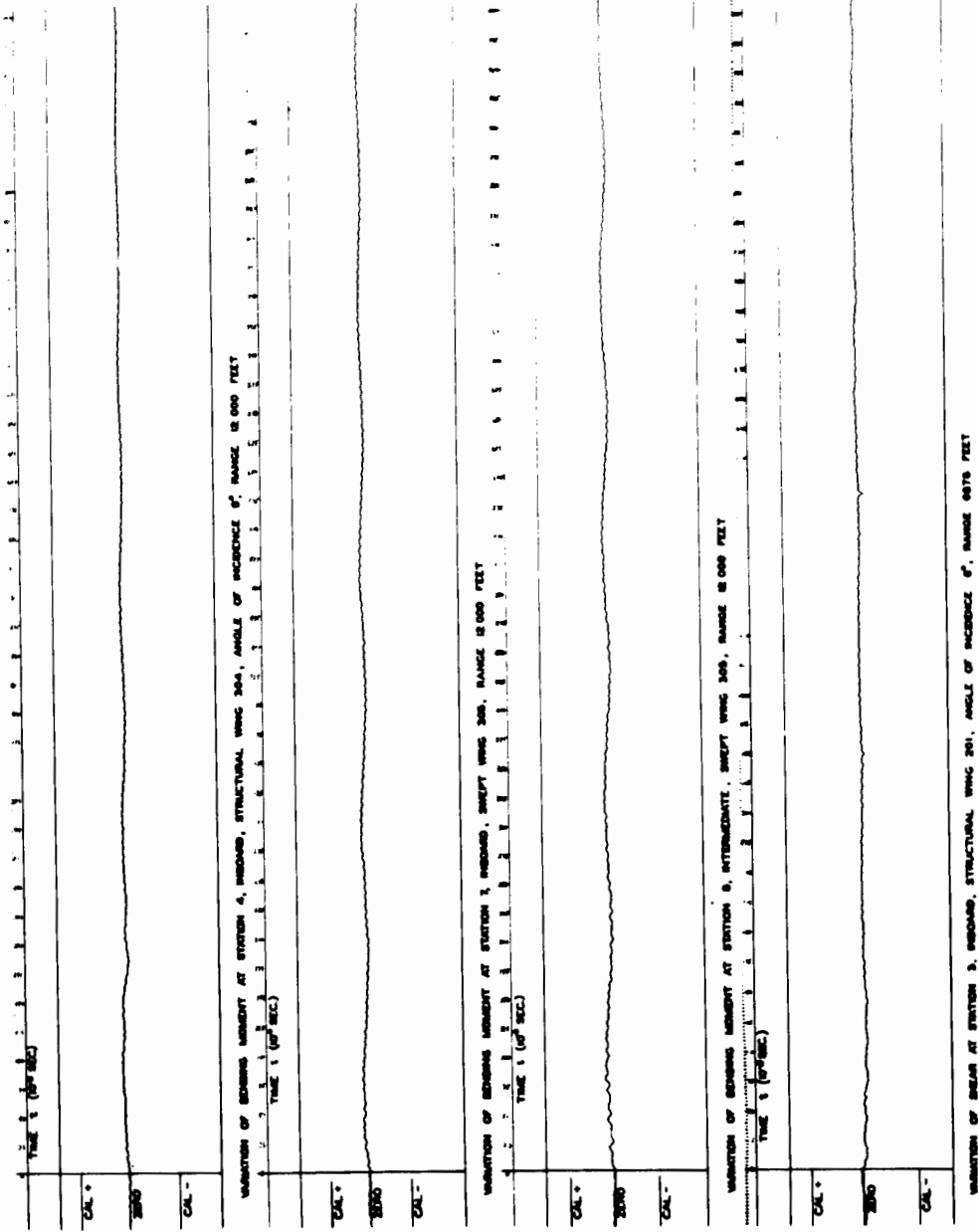


Fig. 6.10 Oscillograph Reproductions of the Magnetic-tape Record of the Variation of Bending Moment with Time at Station 4, Inboard, of Structural Wing 304; at Two Stations of Swept Wing 305; and of Shear with Time at Station 3, Inboard, of Structural Wing 201

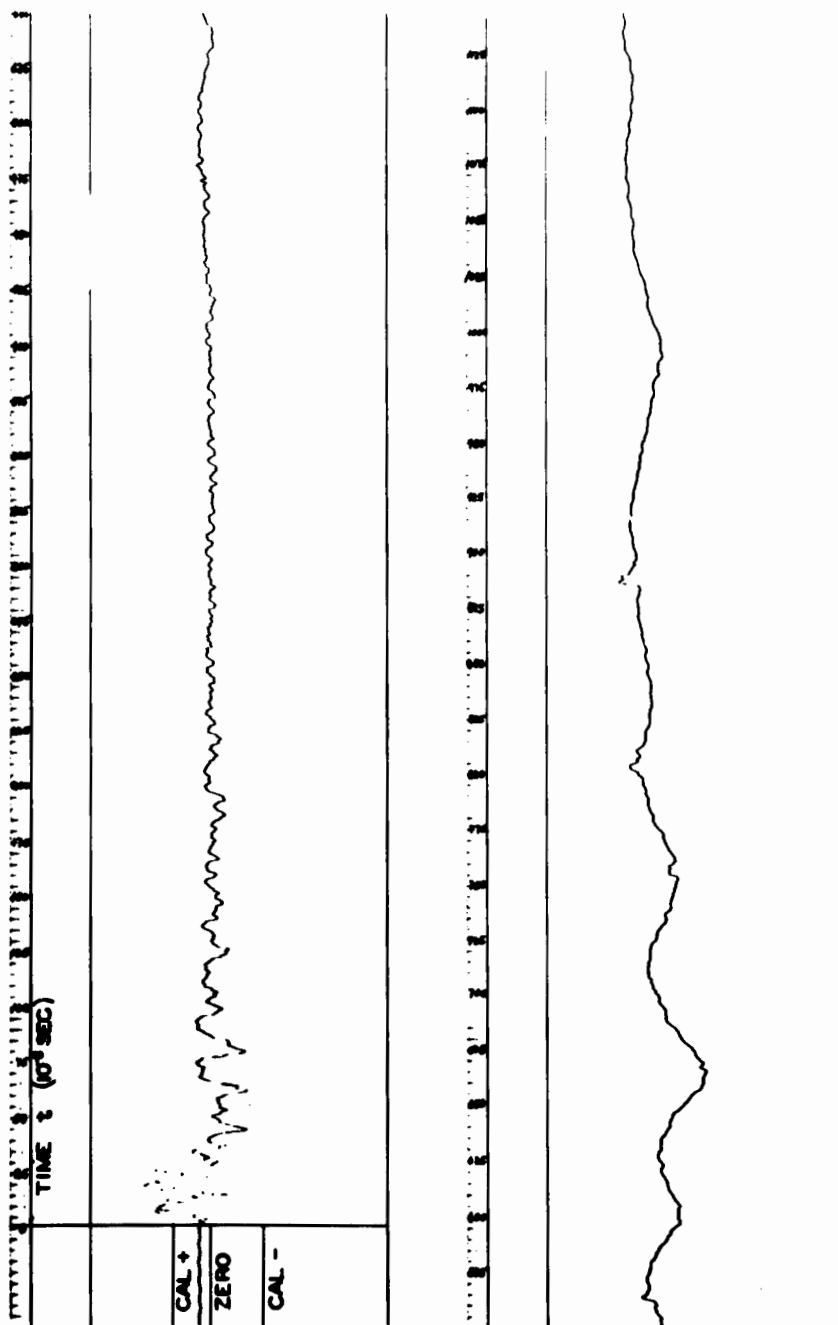


Fig. 6.11 Oscilloscope Reproduction of the Magnetic-tape Record of the Variation of Angle of Flow of the Advancing Air Mass at the 4,020-ft Range

UNCLASSIFIED

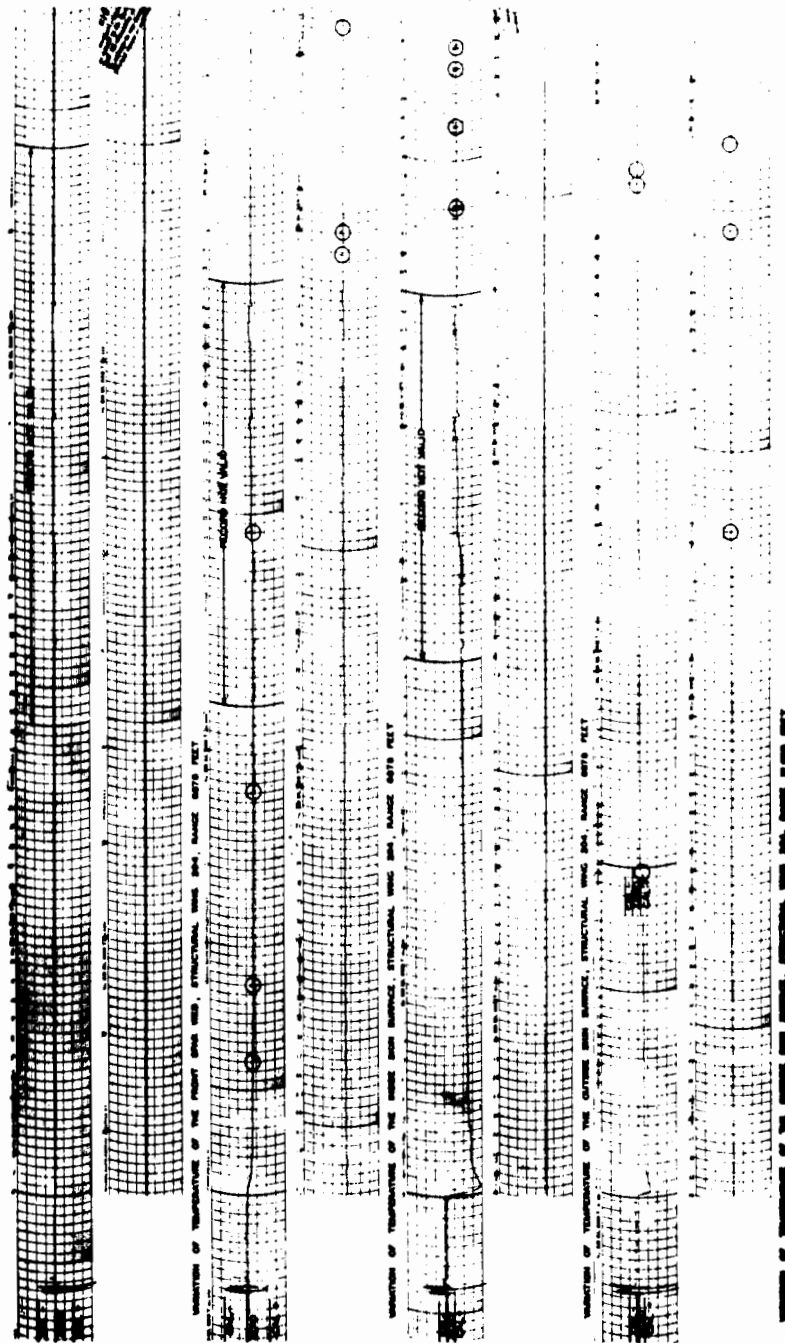


Fig. 6.12 Visual Reproductions of the Magnetic-tape Record of the Variation of Temperature Change with Time at Several Points on Structural Wings 204 and 304

UNCLASSIFIED

UNCLASSIFIED

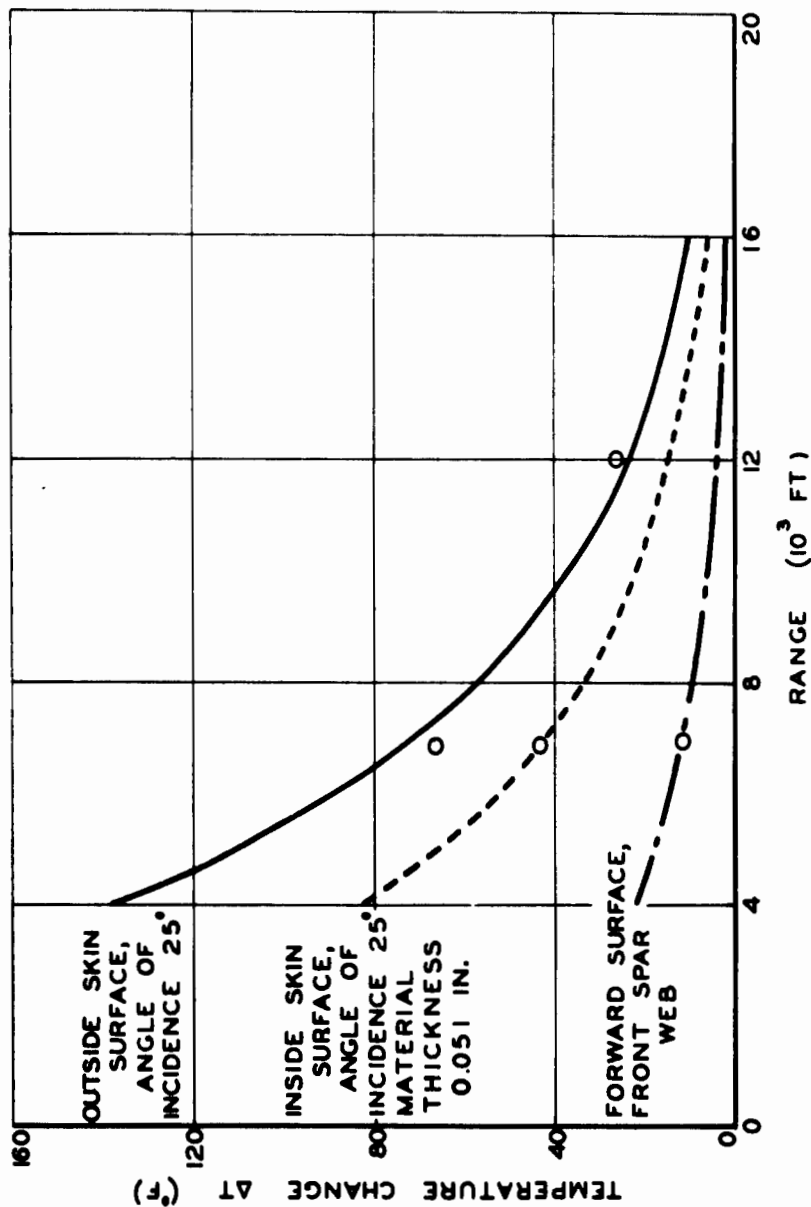


Fig. 6.13 Variation of Maximum Temperature Change with Range for Three Points on the Structural Wings

UNCLASSIFIED